OPTIMISING SPECTRAL AND 3D IMAGING FOR CULTURAL HERITAGE DOCUMENTATION USING CONSUMER IMAGING SYSTEMS

ELIZABETH KEATS WEBB

A thesis submitted in partial fulfilment of the requirements of the University of Brighton for the degree of Doctor of Philosophy

March 2020

Abstract

Cultural heritage objects can be recorded by a variety of 3D techniques. Accessible consumer imaging systems make it increasingly easy to capture image sets that can be processed to produce 3D reconstructions by heritage users who are not necessarily skilled in the process. The availability, flexibility, and automation that make image-based 3D reconstruction an accessible process increase the variability in the output models presenting new challenges in maintaining consistent, fit for purpose, 3D outputs. Conservation applications for image-based 3D reconstruction therefore require scientific rigour to establish reliable and accurate models, particularly for monitoring condition and measuring change over time. Widening access requires better, more accessible, investigative methods to improve image-based 3D reconstruction and thereby ensure consistent high-quality. Reconstructions are dependent on the geometric and photographic qualities of the input images and the methodology used in the reconstruction workflow.

This thesis identified and investigated two less well explored aspects for improving image-based 3D reconstruction through laboratory experimentation, both focused on the qualities of the input imagery. The first concerned the quantifiable scientific use of a modified camera combined with wavelength selection, while the second addressed a gap in the state of the art, seeking to quantify depth of field for 3D reconstruction with an associated automatic process of sharpness-based masking. The thesis demonstrated that a modified consumer digital camera can be paired with wavelength selection to improve image-based 3D reconstruction, demonstrating that reflected IR images can increase local image contrast and reduce wavelength specific specular reflections of a particular museum object to improve the consistency of the resulting 3D reconstruction. The imaging study and proposed wavelength selection workflow were informed by camera characterisation. The second approach experimentally quantified aspects of depth of field for 3D reconstruction of small to medium sized museum objects to inform imaging setup and acquisition combined with sharpness-based masking as part of an image pre-processing step to optimise the processing performance for 3D reconstruction.

Working at the intersection of collections photography, conservation documentation, and scientific imaging, this thesis provides methods of imaging processes that enable heritage specialists to quantify their imaging systems in order to produce accurate and reliable scientific 3D reconstructions of small to medium sized heritage objects. Developed processes are demonstrated throughout the thesis by iterative recording and 3D reconstruction of test and museum objects. The outcome is the optimisation of an image-based 3D reconstruction methodology to provide accurate and reliable scientific recording for conservation documentation while considering the accessibility to a wide range of users.

Table of Contents

List of Figures

List of Tables

List of Equations

Acknowledgements

Mel Wachowiak assumed the role as mentor when he accepted me as an intern at the Smithsonian's Museum Conservation Institute in 2009, which ultimately and unexpectedly led to the pursuit of a PhD focusing on scientific imaging of cultural heritage objects. We only had five years to work together, and Mel passed away shortly before I started the joint Master's and PhD through SEAHA. However, he is fully responsible for where I am today. Mel, a Senior Furniture Conservator turned Imaging Specialist, was passionate and enthusiastic about his work with conserving cultural heritage and with innovative conservation documentation. He is remembered by his kindness and generosity, his collaborative and collegial spirit, his meticulous conservation and imaging work, and his creative and personable demeanour.

David Arnold, founder of the Cultural Informatics Research Group and former professor at University of Brighton, was the reason that I signed up to pursue a PhD through SEAHA at the University of Brighton, but I did not have the opportunity to work as closely with him. I am appreciative of his vision and leadership and the impact that he had on the cultural heritage community.

I am grateful for these professionals and their invitations to be involved in this world of imaging and cultural heritage.

Without the support and funding from the Science & Engineering Arts Heritage & Archaeology (SEAHA) Centre of Doctoral Training, the Smithsonian's Museum Conservation Institute (MCI), the University of Brighton (UB), University College of London (UCL), and Analytik Ltd., none of this would have been possible. I would like to thank the supervisory team that supported this research: Roger Evans (UB), Stuart Robson (UCL), Robert Koestler (MCI), and Ian Laidlaw (Analytik).

A core group of people were instrumental in ensuring that I succeeded in completing the PhD. First, I am indebted to Stuart Robson who has gone above and beyond by taking me on as a student and for supporting this research. I am appreciative of his expertise, guidance, and patience. In addition to his role as supervisor, he provided an incredible example of kindness, support, guidance, and full attention. I have learned so much in the process of working with Stuart, and the thesis and research would not have taken the shape that it did without his guidance.

I am greatly appreciative for the support from Robert Koestler and Paula DePriest providing the opportunity and encouragement to pursue the PhD process that has included regular reminders about critical analysis and the role of persistence in addition to continued support, regular meetings, and patience while dividing my time between two places. I am grateful for the opportunity that they provided and the continual feedback from reviewing papers, presentations, and a full review of the thesis.

I am grateful for the role that Angela Benson willingly assumed as an unofficial advisor and strong advocate to navigate the university system and to ensure that I had what I needed to

conduct the research and complete the PhD. I appreciate her willingness to coach me through the process and provide feedback for a full review of the thesis.

I would like to express my sincere appreciation to colleagues at the institutions and organisations that supported this research:

- SEACH CDT: May Cassar (Director), Heather Viles (Co-Director), Matija Strlic (Deputy Director), and my fellow classmates of the first student cohort
- University of Brighton Cultural Informatics Research Group: Karina Rodriguez Echavarria, Corinna Hattersley-Mitchell, Dean Few
- University College of London classmates and colleagues from the Institute of Sustainable Heritage (ISH) and Civil, Environmental and Geomatic Engineering (CEGE): Lindsay MacDonald (Honorary Professor), Les Irwin (Research & Teaching Support Technician), Danny Garside (PhD Candidate), Ben Sargeant (PhD Candidate)
- Smithsonian American Art Museum: Amber Kerr (Chief of Conservation), Tiarna Doherty (Former Head of Conservation), Helen Ingalls (Retired Senior Objects Conservator), Ariel O'Connor (Objects Conservator)
- Smithsonian National Museum of American Indian: Marian Kaminitz (Head of Conservation), Emily Kaplan (Objects Conservator), and the other amazing staff and fellows
- Smithsonian Freer | Sackler Galleries: Ellen Chase (Objects Conservator), Claire Cuyaubere (Objects Conservator)
- Smithsonian Digitization Program Office: Jon Blundell (3D Program Officer)
- Institute of Applied Physics at the Italian National Research Council (IFAC-CNR): Marcello Picollo, Andrea Casini, Costanza Cucci, and Lorenzo Stefani
- Institute of Information Science and Technologies at the Italian National Research Council (ISTI-CNR) Visual Computing Lab: Roberto Scopigno, Marco Callieri, Matteo Dellepiane
- AICON3D: Dirk Rieke-Zapp and Lewis Homer

This endeavour involved living between two countries balancing work as a digital imaging specialist in Washington, DC and being a student in Brighton and London. An international community came together to support this research, including colleagues, friends, and family. It is not possible to list everyone, and this brief acknowledgement section will not adequately represent all those who were a part of this process challenging and supporting me. I have learned and grown as a researcher, scientist, and human being because of these connections, interactions, and relationships. I am grateful for the challenging questions, supportive words, encouragement shared over coffees, meals, whisky, and pies. Thank you to the friends and family who helped make this a reality!

Author's Declaration

I declare that the research contained in this thesis, unless otherwise formally indicated within the text, is the original work of the author. The thesis has not been previously submitted to this or any other university for a degree, and does not incorporate any material already submitted for a degree.

17 March 2020

1. Introduction

Can consumer imaging systems be optimised to improve the quality of image-based 3D reconstruction of museum objects? Can acquisition, processing, and assessment of 3D reconstructions of heritage objects generated from consumer digital cameras and automated workflows improve the consistency of the resulting 3D reconstruction, and what will this entail? This thesis examines the increasingly common use of 3D imaging for cultural heritage documentation, which is becoming a routine process supporting access, education, research, collections care, and conservation through the creation of digital and physical reconstructions. Cultural heritage objects can be recorded by a variety of 3D techniques that include active range-based technologies, such as laser and white light scanning, and passive image-based systems, such as photogrammetry. Accessible consumer imaging systems, comprising both mass market digital cameras and readily available automated processing software, make it relatively easy to capture image sets that can be processed to produce 3D reconstructions. As a result, a wider variety and quantity of cultural heritage objects are being recorded in 3D by an increasing number of heritage users who do not necessarily need to be skilled in the process. The accessibility, relative to cost and ease of use, results from the flexibility of the equipment that can be used, the methods for acquiring images, and the automation of the processing workflow.

The availability, flexibility, and automation that make image-based 3D reconstruction an accessible process also increase the challenges of maintaining consistent, fit for purpose, 3D output. As a result the internet connected world is becoming full of variable quality 3D models without the quality measures in place needed to understand model reliability and accuracy (Section 2.2.2). At one end of the scale, a 3D model could act as a catalogue entry of an object providing information about what an object looks like. Alternatively, a suitable 3D model can provide the condition of an object at a point in time, providing an invaluable record if the original object is stolen, lost, broken or degrades over time. However, scientific model usage requires scientific rigour to establish how reliable and accurate the information comprising the model is and in the case of a temporal analysis, what types and levels of change can be recorded. The research presented in this thesis isolates and evaluates critical stages in the 3D reconstruction workflow. Quantifiable measures designed to increase confidence in image acquisition, processing, and analysis of image-based 3D reconstruction data help to answer these questions of whether an object has changed over time (Chapter 4).

Widening access requires better investigative methods to improve image-based 3D reconstruction and thereby ensure consistent high-quality outputs. In order to understand

whether output images and models are fit for purpose, and if not, to what extent they need to be improved, the specific use of those outputs must be defined. Where 3D content is created to provide access and new engagement for the public to spin/rotate and generally navigate around an object, low geometric accuracy and low resolution are typically required. Conversely applications using models for visual displays aim to match the look of the original object placed side by side, or to enhance the scientific evidence and rigour of conservation observations concerning the change in an object over time. This thesis focusses on image-based 3D reconstruction for accurate and reliable scientific records for conservation documentation while seeking to maintain the accessibility of imaging and 3D model creation workflows. Since the quality of the output reconstruction is reliant on the quality and geometry of the input images, this research is directed towards scientific image acquisition specifically looking at local contrast, modified cameras and wavelength selection, sharpness, and focus.

Imaging using selected wavelengths within or beyond visible light can increase the image contrast of materials or features to provide an enhanced view. In turn, improved local detail and contrast through wavelength selection can be expected to improve image-based 3D reconstruction. While accurate and precise instruments exist for spectral imaging, these specialised devices can be out of reach for many heritage institutions, professionals, and collections in terms of cost and required expertise. Consumer digital cameras are optimised for visible light, colour photography but can be modified by removing internal filters to provide capabilities for spectral imaging and wavelength selection. Modifications take advantage of the silicon sensor's inherent sensitivity from the near ultraviolet (UV) to near infrared (IR), while maintaining a reasonably inexpensive, easy to use, portable, and high-resolution option. Modified cameras are being used by conservators for 2D conservation documentation to record the condition, inform the treatment, and increase the understanding of heritage objects through techniques like reflected IR imaging and UV-induced visible luminescence (Section 3.1.5).

The question arises whether sensor modification to consumer digital cameras impact their image quality. In this thesis both modified and unmodified cameras are characterised to assess the impact of modification on imaging performance resulting in the characterised camera becoming a scientific tool suited to investigation of wavelength selection and improved 3D reconstruction (Chapter 5). Furthermore, characterisation results paired with tests assessing the influence of wavelength on image quality can inform the selection of wavelength, imaging parameters, and 3D reconstruction workflow (Chapter 6).

Image-based 3D reconstruction processing tools assume sharp focus across the entire object being imaged, but depth of field (DOF), the range of acceptable sharpness, can be a limitation for 2D and 3D imaging of small to medium sized objects (Section 2.5). Aperture has a strong influence on lens quality and resulting image quality, so it is an important part of the investigation to improve image-based 3D reconstruction workflow. While DOF is well understood in the context of 2D imaging and it is considered with the acquisition of image-based 3D reconstruction, "acceptable" sharpness has not yet been quantified for image-based 3D reconstruction. Defining DOF in relation to 3D reconstruction can inform the setup and acquisition of an object in addition to sharpness-based masking as part of an image pre-processing step to optimise the processing performance for 3D reconstruction (Chapter 7).

This research emphasises the use of accessible, consumer imaging systems for improved image-based 3D reconstruction by heritage professionals, so it is important to clearly define these key concepts that will be used throughout the thesis. *Heritage professionals*, or *heritage users*, are distinguished from the general public as professionals working with cultural heritage and in heritage institutions. While they may be specialised in an area relating to heritage (not limited to conservators, curators, and museum specialists), they do not necessarily have a background in imaging or 3D reconstruction but are generally familiar with imaging as a means of making records. *Consumer imaging systems* include cameras and software that can be purchased off-the-shelf in a store or online and used by non-expert users. *Accessibility*, in the context of this research, is focused on the cost and complexity of the equipment and techniques. Consumer imaging systems tend to provide accessible solutions for heritage professionals, low cost and less complex, as compared to more expensive and specialised equipment.

1.1. Museum imaging

Imaging has a long history of object documentation for access, education, research, and conservation within museums and heritage institutions. Since early in its existence, photography has been used through a range of techniques as a non-destructive and portable tool to document cultural heritage objects. With the introduction of photography, the technique offered new ways of "measuring, collecting, and illustrating the modern world. Itself a marriage of technology and the advancing of sciences of chemistry and optics, photography also became nothing short of the most important record of the act of seeing" (Foresta, 2004, p. 12). Early photography was used at museums, like the Smithsonian Institution in Washington, DC, to aid in a mission of cataloguing and organising the world. Photographs offered a capability of preserving the past for the future that linked with the

aims of the Institution. In discussing the history of photography and the Smithsonian, Foresta (2004, p. 16) stated, "Photography though still in its infancy, was the perfect match for this progressive mission of collecting, knowing, and showing".

Photography has been used since early in its existence for museum imaging, and more recently digital imaging has caused a "step change" in this documentation (Verri, 2017). This "step change" comes from the versatility that digital cameras offer heritage research "by providing accessible tools that can address a variety of questions for conservators, curators, and scientists" (Verri, 2017). As digital technologies and advanced computing have developed more techniques do fall under the umbrella of *imaging*. *Imaging* is often used as a term to encompass the techniques and technologies used to document cultural heritage and has often been thought of in terms of photography; however, *imaging* has evolved beyond basic photography and can be considered as nearly any non-destructive investigation technique that records spatial distribution in more than one dimension (Verri, 2017). Imaging is about recording and visually mapping the spatial distribution of information across a surface and through time and relates to how we transfer and transmit information graphically which can include multidimensional information of a scene or object (Ballard et al., 2017; Verri, 2017). While *imaging* of cultural heritage does extend beyond photography and can include chemical mapping like hyperspectral imaging and XRF mapping, this research is focusing on camera-based, optical techniques recording information on conventional silicon detectors with their spectral response in the visible and near IR range.

Acknowledging the wide definition of *imaging,* Verri (2017) presented three categories that define the purpose of cultural heritage imaging: documentation, investigation, and visualisation/communication. *Documentation* is about creating a record for the future and can provide information to understand manufacture, materials, production technologies, history and use, and interventions in addition to providing a record of the condition. *Investigation* is about comprehending the cultural significance, visualising hidden information, understanding original and added material, looking at rates of change and decay mechanisms, and diagnosing and monitoring the condition. *Visualisation/communication* is about visualising the results of *documentation* and *investigation,* communicating complex ideas, and processing to improve visualisation.

This thesis presents another categorisation that focuses on the structure of museums or heritage institutions reflecting on where imaging takes place and why, with three main categories representing museum imaging: collections photography, conservation documentation, and scientific imaging. These categories are defined by different techniques, workflows, and applications, yet, similar to Verri's categories, they are interrelated and

overlap as illustrated in Figure 1-1. The categories of museum imaging are presented in order to:

- Define the context of this research which is positioned at the intersection of these three categories,
- Identify best practices and standards to inform the methods of improving image-based 3D reconstruction, and
- Provide examples of different uses of 3D output in order to understand the requirements of the results.
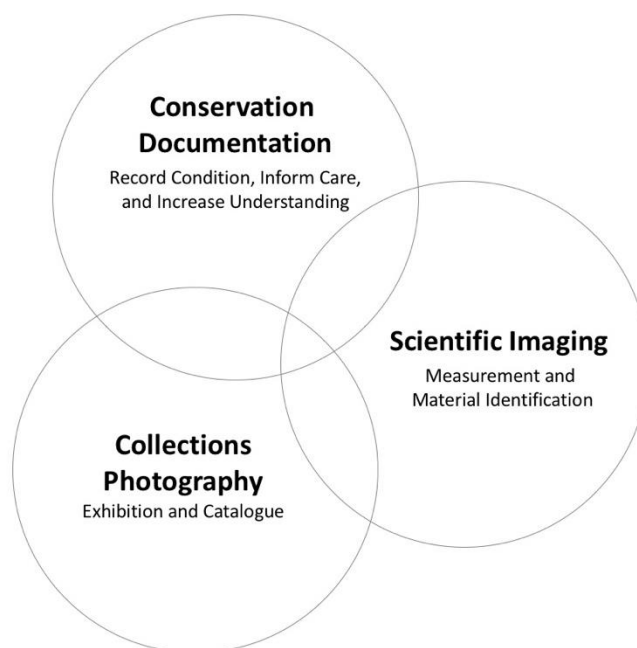
Figure 1-1. Diagram illustrating the categories of museum imaging: collections photography, conservation documentation, and scientific imaging.

1.1.1. Collections Photography

Collections photography is the documentation of collection objects for cataloguing and exhibition. A big part of collections photography has been the digitisation of full collections to broaden access, preserve collections, support education and enrich context as was set out in the Smithsonian 2010-2015 Digitization Strategic Plan (*Creating a Digital Smithsonian*, 2010). This digitisation strategic plan is an example of the trend of institutions recognizing that digital was having a "transformative effect on the delivery of their mission" (Tallon, 2017), and the Smithsonian's plan aimed to lay out how the institution could digitise its 137 million objects as a service to education and research (*Creating a Digital Smithsonian*,

2010). The trend has shifted from the digitisation process to how digitised collections can reach more audiences and provide new engagement. While "digital" incorporates more than just imaging, the heart of museums' digital strategies are the digital images of their collections.

Collections photography often results in public facing outputs and includes 2D visible light photography and more recently 3D models. Online access of collections including high-quality 2D images provides global access that can continue to grow over time, and these online catalogues are designed to share knowledge and to encourage new study, with examples including the Smithsonian's Freer|Sackler Galleries' 'Jades for Life and Death' (https://archive.asia.si.edu/publications/jades/default.php), and the Ancient Near East Seal Collection (https://archive.asia.si.edu/publications/seals/default.php). These catalogues include high-resolution 2D visible light photography of the jade and seal collections that are linked to the online catalogue information, essays, and archival material.

In addition to online access to 2D collection photography, examples of 3D collection documentation can be found in the cultural heritage section of Sketchfab (https://sketchfab.com/museums). Sketchfab is an online platform to publish 3D, augmented reality (AR), and virtual reality (VR) cultural content. Institutions can share 3D models of heritage objects that viewers can spin and rotate. The platform provides a means for artefacts to reach a wider audience especially for objects that may not otherwise be seen whether it is kept in storage or in a more extreme location like a shipwreck. In January 2017, Sketchfab announced over 500 cultural institutes from 51 countries using their platform to share 3D models of heritage objects and sites (Marchou, 2017) and in October 2019 they announced over 100,000 cultural heritage 3D models on their platform (Flynn, 2019).

The Smithsonian Institution is a good example of an institution adopting 3D. The Institution includes nineteen museums each of which have photographers, conservators, and researchers documenting the collection, and the 2010-2015 digitisation strategic plan was able to centralise the effort in a pan-Institutional approach to digitisation. The strategic plan resulted in the creation of an ongoing centralised digitisation programme, the Digitization Program Office (DPO), to develop and oversee digitisation strategies and to integrate digitisation into the core functions of the Smithsonian (*Creating a Digital Smithsonian*, 2010, p. 12).

One of the main programs of DPO includes 3D digitisation, which claims that 3D has already transformed the core functions of the Smithsonian museums: researchers are using 3D to document specimens and entire sites; curators and educators are using 3D for storytelling and "quests of discovery", and conservators are using 3D for recording the

condition and monitoring change ('Smithsonian Digitization Program Office: 3D Digitization', 2019). The Smithsonian has over 137 million objects which present a variety of challenges due to the range of shapes, sizes, surface properties, and condition. While 3D imaging efforts are taking place within the museums and units at the Smithsonian, DPO is working on institutional approaches to strategize, prioritise, and support the digitisation of the Smithsonian collections. Initially DPO focused on broad use-case explorations of 3D applications, but more recently they have shifted from "one-offs" to collections and the development of the Smithsonian 3D Open Source Pipeline and processes for high-throughput 3D digitisation ('Smithsonian Digitization Program Office: 3D Digitization', 2019; Rossi et al., 2019).

The motivation for the institutional digitisation is sharing the collections with new audiences in better ways to support the Smithsonian's mission of 'the increase and diffusion of knowledge'. Currently only 1% of the Smithsonian's collections are on exhibition at any given time, so digitisation, including 3D imaging, supports the vision of broadening access, preserving collections, supporting education, and enriching context. This also supports the more recent institutional five-year strategic plan "Smithsonian 2022: Greater Reach, Greater Relevance, Profound Impact" and the vision of engaging and inspiring more people "where they are, with greater impact" ('Smithsonian 2022', 2017).

This example of institutional prioritisation of 3D imaging by the world's largest museum and research complex provides evidence of the importance of 3D to museum imaging, an example of improving aspects of 3D imaging for cultural heritage applications and aims of increased automation with the 3D Open Source Pipeline.

Collections photography can include 2D and 3D imaging, but best practices cover mostly 2D imaging. Current best practices in 2D collections photography include the US-based Federal Agencies Digital Guidelines Initiative (FADGI) that has presented shared best practices and common digitisation guidelines (Section 3.2). The guidelines include the Digital Imaging Conformance Evaluation (DICE) consisting of image targets and analysis software to measure digital image performance and benchmark imaging systems for collections photography. While there are guidelines and best practices for 2D collections photography, these do not yet exist for 3D collections photography (Section 2.3).

1.1.2. Conservation documentation

Conservation documentation is the recording of the condition, informing the care and treatment, and increasing the understanding of an object. Documentation is an important part

of conservation and is considered basic to the ethical practice of conservators (Warda et al., 2011, p. 13). The American Institute for Conservation of Historic and Artistic Works (AIC) Code of Ethics outlined that documentation should be used for recording examination, sampling, scientific investigation, and treatment, and it further described the use of documentation to establish the condition, aid in the care and treatment, increase the understanding, and assist in the continued development of knowledge about an object ('AIC Code of Ethics and Guidelines for Practice', 1994). While conservation documentation encompasses standard visible light photography, it also includes the use of different setups, lights, and even cameras for the documentation and investigation of an object. Visible light photography can include normal, raking or transmitted illumination. The wavelengths used for illumination can extend beyond visible light to include UV and IR radiation for spectral imaging. In addition to 2D documentation, 2.5D techniques like Reflectance Transformation Imaging (RTI) and 3D techniques like image-based 3D reconstruction are also used for recording and investigating objects.

3D imaging has been used for conservation applications: white light scanning was used to create a physical copy and virtually recreating a missing piece (Wachowiak et al., 2009), laser scanning was used for virtual reconstruction and custom support production (Arbace et al., 2013), laser scanning was used for monitoring internal movement (Garland et al., 2015) and dimensional stability (Hess et al., 2015), and the integration of laser scanned data, photogrammetry and multimodal/multispectral data was used to assess the conservation state of paintings (Remondino et al., 2011a). In some cases, the accuracy of the colour and texture may be critical for the conservation question, whereas monitoring the dimensional shape will require more reliability and accuracy related to the geometry. The specific requirements for the resulting quality are going to be dependent on the object and the conservation question, so when planning a project, the scale, accuracy, and resolution need to be considered.

Guidelines and best practices for 2D conservation documentation have been provided in three editions of *The AIC Guide to Digital Photography and Conservation Documentation* by Warda et al. (2008, 2011, 2017) (Section 3.2). This guide was written by conservators with the purpose of assisting conservators to comply with the standards of the *Code of Ethics* that requires documentation of examination, scientific investigation, and treatment through the creation of permanent records and reports ('AIC Code of Ethics and Guidelines for Practice', 1994). Warda et al. (2011, p. 13) outlined the specifics of the digital photographic documentation workflow (photography setup, image capture, processing, management, and output) as a technical reference and manual for planning and

implementation of conservation documentation. Similarly, to collections photograph, while there are guidelines and best practices for 2D conservation documentation including spectral imaging, these do not yet exist for 3D conservation documentation.

1.1.3. Scientific imaging

Scientific imaging is the recording of objects for measurement and material identification. Scientific imaging, or applied photography, can be defined as "photography and imaging used as scientific tools to provide records that cannot be made in any other way" (Ray, 1999, p. 2). It is a process that provides "a means of extending imaging beyond the limits of human visual perception, producing permanent records for analysis and evaluation of the subject and process involved" (Ray, 1999, p. 2). Scientific imaging involves objectivity, absence of ambiguity, repeatability, and may require specialist equipment (Ray, 1999). As Verri (2017) presented, the expanded definition of *imaging* includes nearly any non-destructive investigation technique recording the spatial distribution in more than one dimension, and scientific imaging techniques can include hyperspectral imaging, XRF mapping, and Raman mapping.

There are similarities between 3D applications for conservation documentation and scientific imaging in that conservation documentation can also benefit from accurate measurement and therefore the resulting data, typically colour and shape, needs to be reliable and traceable to length and colour standards. As previously stated, the specific requirements for the resulting quality are going to be dependent on the object and the research question, so project planning requires consideration on selecting appropriate image geometry and lighting tailored to the dimensions and surface properties of the object being recorded.

Color & Space in Cultural Heritage (COSCH) was a European Cooperation in Science and Technology (COST) Action (2012-2016) that worked towards the enhanced understanding of material and helping its long-term preservation through promoting research, development, and application of spectral and spatial optical measurement techniques adapted to the needs of heritage documentation ('Colour and Space in Cultural Heritage (COSCH)', n.d.). The initiative included efforts in both spectral and 3D imaging. Working Group 1: Spectral Object Documentation worked towards standardisation and best practices of spectral imaging, specifically imaging spectroscopy, and Working Group 2: Spatial Object Documentation aimed to identify the main 3D techniques and to analyse and compare these techniques for cultural heritage applications. This cooperative initiative provides an example of 3D applications for scientific imaging of cultural heritage documentation (Hess et al., 2018).

The International Organization of Standards (ISO) provides standards that are used in scientific imaging that deliver specific principles and protocols for measuring aspects of imaging including resolution (ISO 12233:2017), principles of modulation transfer function (MTF) (ISO 15529:2010), and noise (ISO 15739: 2017). Additional ISO standards referenced in this thesis can be found in Section 11. These ISO standards focus on 2D imaging, and Section 2.3 will look at available best practices and standards for 3D imaging.

The identification of these three categories has come from both working in the field as a digital imaging specialist at the Smithsonian's Museum Conservation Institute (MCI) and in structuring the research for this thesis. It is a combination of observation and experience, research and reading, and collaborating and communicating with photographers, conservators, and scientists. At the most local level, identifying the categories is important for defining the research context where the intersection of the categories provides a focus for the rationale of this thesis. The process of categorising museum imaging involves looking at the techniques, applications, best practices, and standards for each area to understand how these relate and overlap. This process of identifying best practices and standards informed the borrowing of methods from the different areas to improve image-based 3D reconstruction as scientific records for conservation documentation.

The categorisation also helps to define the field, providing an understanding of future direction, development, and growth. This perspective is beneficial for working as a digital imaging specialist and for the wider field of museum imaging and cultural heritage documentation. Presenting the structure of museum imaging acknowledges the contributions from many fields for the continued development of the techniques and technologies, and it provides evidence for the multi and interdisciplinary nature of cultural heritage documentation. This builds a ground for understanding how these fields and categories connect and overlap to encourage development with the goal being the stewardship of our cultural heritage.

1.2. Research questions and objectives

The ease of creating 3D reconstructions using consumer imaging systems, both mass market digital cameras and readily available automated processing software, have brought 3D museum imaging into the mainstream. Techniques are highly flexible, giving the capability to work from image sources as varied as high resolution professional images to tourist snapshots. A direct result of this flexibility is that the quality of the output models is also highly variable ranging from compelling exhibition content to the exceptionally poor reconstructions. The target audience for this thesis is the museum professional with the

overall aim of improving image-based 3D reconstruction as a tool to make accurate and reliable scientific records of small to medium sized heritage objects for conservation documentation. The thesis addresses three research questions:

- How can consumer imaging systems be optimised to improve image-based 3D reconstruction of small to medium sized museum objects?
- Can photography with a modified consumer digital camera paired with selected illumination and filtration be used as a scientific method to better benefit the 3D reconstruction of museum objects for conservation documentation?
- How can the limitations of optical depth of field be mitigated using consumer imaging systems for the 3D reconstruction of small to medium sized museum objects?

The research objectives were:

- To optimise acquisition, processing, and assessment of image-based 3D reconstruction (Chapter 4),
- To characterise unmodified and modified consumer digital cameras (Chapter 5),
- To evaluate wavelength selection with a modified camera for improved 3D reconstruction (Chapter 6),
- To determine the acceptable image sharpness for 3D reconstruction (Chapter 7), and to integrate that process into the reconstruction workflow.

1.3. Methodology overview

This thesis is informed by the intersection of collections photography, conservation documentation, and scientific imaging which in combination give a structure against which the interdisciplinary nature of cultural heritage documentation can be mapped. The research draws upon methods from the three main areas of museum imaging to contribute to a future-proof protocol for producing 3D output with the goal of optimising image-based 3D reconstruction as a scientific conservation recording and documenting tool. The experimental design follows critical analysis such that individual steps in the reconstruction workflow can be assessed in detail, their key elements understood and standardised.

Two approaches for improving image-based 3D reconstruction are explored through laboratory-based experiments, both focus on the qualities of the input imagery. The first concerns the quantifiable scientific use of a modified camera combined with wavelength selection, while the second addresses a gap in the state of the art, seeking to quantify DOF

for 3D reconstruction with an associated automatic process of sharpness-based masking. These approaches are isolated and evaluated separately to reduce the variables being addressed. The photography was setup for the wavelength experiments so that DOF would not be a problem and vice versa. The specific materials and methods for the lab-based and practical experimental work are presented with each chapter.

Case studies with heritage objects provide intriguing results and can increase our understanding of the object and sometimes the potential and limitations of the techniques, but there is very limited control over the variables tested and acquiring reliable reference data can be problematic. Test objects and reference data are therefore essential for providing reliable and repeatable results for the quality assessment of the 2D images and 3D reconstructions. Test objects provide a better option for controlling parameters, assessing quality, and having more reliable reference data than heritage objects. The resulting imagery of a test object with known features describes how well the imaging system can reproduce those features.

The experimental approach is centred on a practical imaging study designed around purpose made test objects that can demonstrate the reconstruction process and some of its key challenges. Since there are many imaging configurations and software pathways that might be applied, for heritage professionals, the presentation of the method is as important as the results. Three test objects were used as part of the process of optimising the image-based 3D reconstruction workflow and the assessment of the results: the Panel test target (Figure 1-2), the Mango Vase (Figure 1-3), and the DICE target (Figure 1-4). The following section presents the test objects to provide information about the research methods implemented for this thesis.
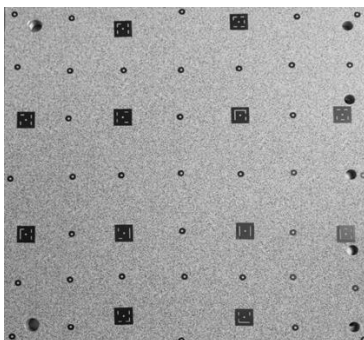
Figure 1-2. Panel test target (30.5 cm x 30 cm) used for assessing 3D reconstruction quality.

Figure 1-3. Mango Wood Vase test object (19 x 13 cm).

Figure 1-4. DICE device level target (17.9 x 25.4 cm) used for assessing 2D image quality and performance.

1.3.1.

1.3.1. Panel test target

The Panel test target (Section 4.1.1) is an engineering test object that has been optimised for image matching and can provide insight into the limitations of the imaging system. Sargeant et al. (2016) created this test object from a rigid aluminium plate (305 mm x 300 mm) coated with an Airbus designed wallpaper and a pseudo-random pattern designed to optimise the optical detection of surface strain with Digital Image Correlation (DIC) (Section 2.3.3.2). The pseudo-random pattern has a high local contrast and small features, which is beneficial for image matching and has been optimised to increase the sensitivity of the DIC measurement. The Panel was selected because it presented a practical surface for testing 3D imaging with the plane being a simple and known geometric shape that can be assessed by using a best-fit plane, or a flatness measure.

The Panel test target represents an optimised object for 3D reconstruction and provided a means of establishing the 3D geometric recording capabilities, or sensitivity, of the imaging system. The reconstruction accuracy achieved in this thesis aligned with engineering state of the art and provided evidence as to limitations of the available lens distortion models. To surpass the limitations of the imaging system, metrology-level instrumentation would be required.

While the use of the target is beneficial for establishing system sensitivity, the planar shape, high contrast surface, lack of sharp edge changes and discontinuities, cannot provide a full set of information as to system performance when documenting a similarly high contrast museum object in the round. Furthermore, the Panel test target is an engineering test object that was designed for 3D measurement and did not include capabilities for 2D image quality or spectral imaging assessment. While the Panel test target was selected as a flat surface, repeated measurement confirmed systematic unflatness in the surface, benefitting the thesis in introducing challenges with reference data and accuracy assessment (Section 4.1.3).

If the Panel test target is considered a target for assessing the performance of an imaging system and learning in the imaging science realm, then the Mango Vase test object is a reference object to illustrate how this can be applied to conservation documentation and museum imaging and is an example of learning in the museum realm.

1.3.2. Mango Vase

The Mango Vase (Section 4.2.1) links more closely with heritage objects and materials and provides insight for practical applications of recording heritage objects. Initially designed for the author's MRes research (Webb, 2015), it was modified for the research presented in this

thesis. It was intended as the primary test object; however, the research required a more fundamental test object to assess the performance of the imaging system and resulting quality, so the Panel test target was introduced and was able to assess the performance of the imaging system. The Mango Vase was designed to have a more complex geometry and similarities to a heritage object including materials and shape thus it will more closely relate to museum collections than the Panel test target.

The creation of the Mango Vase test object was informed by the painted panel target presented by George et al. (2017) and Cucci et al. (2019) as part of the COSCH Round Robin Test (RRT) (Section 3.2) and the considerations presented by Hess (2015a) in the creation of the Metric Heritage Test Object (Section 2.4.2). The Mango Vase (19 x 13 cm) included line patterns (graphite and ivory black), pigment patches (Prussian blue, azurite, malachite, madder lake, zinc white, and titanium white) and varnished areas (shellac and mastic) (Figure 1-5). These materials respond differently to different radiation sources (UV, visible, and NIR) including luminescence, reflection, absorption, and transmission (Figure 1-6). The line patterns were created using a ruler with 1 and 2 mm spacing as a sort of resolution reference. See Appendix 14.2 for more information about the creation of this test object.

Figure 1-5. Diagram indicating materials and location of materials on the Mango Vase.

Figure 1-6. Mango Vase enhanced with line patterns and pigment patches. Left to right: UV-induced visible luminescence image, visible light image, and reflected IR.

The Mango Vase presented challenges for assessing 3D reconstruction results due to the object's rotational symmetry and issues with alignment (Section 4.2). The rotational symmetry of the vase made alignment of the reference data with the 3D reconstruction results challenging and any offset in the alignment impacted the results of the comparison (Section 4.2.2). Accuracy of the alignment is critical and can significantly impact the resulting comparison and assessment of the 3D reconstruction results. Section 4.2.4 discusses challenges about the reliability of the reference data, which reiterates some of the issues initially discussed in Section 2.4 and challenges with the Panel test target elaborated on the discussion (Section 4.1.3). Section 4.2.5 further discusses reference data and assessing results through comparing 3D recording results, comparing image-based 3D reconstruction results, and overall assessment of 3D reconstruction results. While the Mango Vase was able to more closely represent a heritage object and had some features that took into account spectral imaging, the test object could not measure the limitations of an imaging system to the extent that the Panel test target and it did not have the capabilities of measuring 2D image quality.

1.3.3. DICE target

The Digital Image Conformance Evaluation (DICE) target (Section 5.2.1) is a commercial target for collections photography that provides metrics and criteria for assessing digital image performance. This target was used for the assessment of the 2D image quality and performance following the US-based Federal Agencies Digital Guidelines Initiative (FADGI) (further discussed in Section 3.2). The FADGI conformance program includes best practices and guidelines that are used for collections photography and take into account advances of imaging sciences and cultural heritage documentation (Rieger, 2016). Images of

the DICE target are analysed with the associated GoldenThread software (Section 12). The target and software were selected as a turnkey solution with metrics and criteria for measuring system performance capabilities that are already being used for collections photography to assess standard digitisation setups.

The DICE target was used to assess the image quality in several parts of the research. While the target and software provide an assessment of a full range of image quality parameters, this research focused on assessing noise, sharpness, and resolution using measures for noise, spatial frequency response (SFR), and sampling efficiency (Section 5.2.1.1). The target was used for the camera characterisation to understand the performance of the imaging system, and in the case of the modified camera, to better understand the impact of the modification (Section 5.2). The target was used as part of the investigation of improved 3D reconstruction and wavelength to assess the impact of wavelength on image quality (Section 6.1). It was also used as part of the investigation of improved 3D reconstruction and DOF to link 2D image quality with 3D reconstruction results to quantify and connect 2D DOF calculations with the range of acceptable sharpness for 3D and resulting 3D reconstruction quality (Section 7.1). Beyond this research, a target like the DICE target can provide metrics that could be used for comparing with other systems, which could be useful with monitoring an object over time and the changing technology.

This research has focused on accessible, consumer imaging systems and tools, so it needs to be noted that the DICE target and GoldenThread software are expensive ($2,950[1]). This cost may be prohibitive to some heritage professionals. With that said, despite the cost these are already being used by some collection photographers, which has been observed by the author as an imaging specialist working and communicating with collection photographers at different institutions. The research focused mostly on SFR analysis, which could also be done with slanted edge features and freely available software like *sfrmat3* and OpenDICE as discussed in Section 8.4. A benefit of the GoldenThread software is that it does not require any coding experience or a background in imaging science, and it provides several metrics to initially explore for the 2D image quality assessment. The FADGI guidelines and DICE target are limited to only the visible light range for 2D image quality assessment and they do not address spectral or 3D imaging.

---

[1] Price for the GoldenThread System (includes object-level target, device-level target and analysis software) from Image Science Associates (http://www.imagescienceassociates.com) accessed on 17 October 2019.

1.3.4. Methodology summary

The three test objects (Panel test target, Mango Vase, and DICE target) were selected or designed for 2D image and 3D reconstruction assessment based on specific requirements of the research. The three targets represent different areas of museum imaging a further indication of the methods borrowed from these areas to achieve the research goals. These test objects do not cover all aspects of the 3D recording process, but they provide a good start to understanding the performance of the imaging system. A significant aspect of 3D recording is the surface properties of the object. Replicating the surface properties of an object can be challenging and this might only be representative of a single object, so the use and implementation of test objects that can provide an understanding of the base level of accuracy present a good compromise because realistically test objects are limited. The advantages and limitations of the three test objects are discussed Section 8.4, which offers criteria and features for the creation of a new target that could deliver information to heritage professionals about the performance of their imaging system.

In summary, the methodology is an experimental approach based on scientific principles. The research has included lab-based experiments and practical experiments. The practical experiments and imaging study provide evidence of the applications of this research to museum imaging. As part of the methodology, test objects were essential for providing reliable and significant results for the 2D and 3D quality assessment and for providing evidence of improved image-based 3D reconstruction. Describing the three test objects further define the methods employed for this research. The specific materials and methods will be presented with each of the experimental chapters.

1.4. Structural summary of thesis

The following paragraphs give a structural summary of the thesis.

The thesis includes two literature review chapters providing separate reviews for image-based 3D reconstruction (Chapter 2) and spectral imaging (Chapter 3). Interconnection is more challenging than might be expected since 3D and spectral imaging have developed from different fields such that publications often do not overlap. Chapter 2 reviews the accuracy and reliability of image-based 3D reconstruction with a critique on available best practices and standards, metric 3D quality assessment, and DOF. The review provides a foundation for image-based 3D reconstruction and DOF exploration. Chapter 3 links spectral imaging with focusing on modified cameras, methods of characterising cameras, and best practice. This provides the basis for the use of a modified consumer camera as an accessible tool for spectral imaging and a foundation for characterisation of modified cameras.

Experimental work is introduced in Chapter 4, testing and refining aspects of acquisition, processing, and assessment to establish an optimised workflow for image-based 3D reconstruction built on best practices (Section 2.3). Methods that may be more widely applied outside of cultural heritage are highlighted to ensure breadth. The methods and results from this chapter inform the 3D reconstruction narrative throughout the document.

Experimental work on wavelength and improved 3D reconstruction is detailed in Chapters 5 and 6. Chapter 5 focuses on the lab-based camera characterisation of unmodified and modified consumer cameras that are essential for the use of consumer cameras as scientific tools. Chapter 6 includes the practical application of the modified camera presenting an imaging study and workflow using optical filters to select imaging wavelengths that enhance local surface contrast on the object in order to improve image-based 3D reconstruction. The outcome allows the selection of wavelengths that optimise the camera response, image quality, and object features to minimise the surface discrepancy for 3D reconstruction.

Chapter 7 focuses on the lab-based quantification of DOF, investigating the influence of sharpness on the output 3D reconstruction to better understand the effects of aperture, angle, and distance. The outcome provides evidence of the role of DOF in image-based 3D reconstruction and briefly presents masks from image content and depth maps as ways of optimising the processing in a structure from motion (SfM) and multiview stereo (MVS) workflow by removing unsharp image content.

Chapter 8 brings together the four experimental chapters, providing a critique on the methodology used and discussing recommendations. Placing the work in the context of the state of the art for each of the three categories of museum imaging (collections photography, conservation documentation, and scientific imaging) connects the research outcomes with the needs of the heritage professionals seeking to either use or benefit from image-based 3D reconstruction.

The thesis concludes with Chapter 9 summarising key findings and contributions and presenting directions for future work. This final chapter is followed by references (Section 10) and referenced standards (Section 11), a list of software used in the research (Section 12), the author's publications and presentations (Section 13), and Appendices (Section 14).

2. Image-based 3D reconstruction of cultural heritage objects

This research focuses on image-based 3D reconstruction as these techniques are being widely used as accessible methods for 3D object documentation that are portable and flexible resulting in high-resolution results for non-expert users (Section 2.1). The wide use of image-based 3D reconstruction also introduces a wide range of quality. Components that increase the accessibility and flexibility of imaging devices and workflows can contribute to challenges of maintaining reliability and accuracy of the 3D reconstruction results. With an aim of improving image-based 3D reconstruction as accurate and reliable scientific records of small to medium sized heritage objects for conservation documentation, this research focuses on accessible 3D imaging techniques, specifically structure from motion (SfM) and multiview stereo (MVS) (Section 2.2) and methods of assessing and improving accuracy and reliability. This review chapter will investigate best practices (Section 2.3), the assessment of the metric quality of 3D data (Section 2.4), and methods of optimising image-based 3D reconstruction looking at DOF and sharpness (Section 2.5).

2.1. 3D Imaging and cultural heritage documentation

3D imaging is used for cultural heritage documentation to record the surface geometry and texture of an object producing virtual and physical 3D models. 3D imaging allows digitisation to extend beyond the limitations of 2D object documentation and is being widely used to record heritage objects to monitor dimensional change, create virtual reconstruction, reduce handling and facilitate access, create custom mounts or repairs, and produce replicas (Hess, 2015a). The resulting 3D models are used for inspection, navigation, identification, visualisation, and animation with applications that include documentation for heritage at risk, virtual tourism and museums, and educational resources (Remondino and El-Hakim, 2006). 3D imaging has been used for conservation applications, for example, white light scanning to create a physical copy and virtually recreating a missing piece (Wachowiak et al. 2009); laser scanning for virtual reconstruction and custom support production (Arbace et al. 2013); laser scanning for monitoring internal movement (Garland et al. 2015) and dimensional stability (Hess et al. 2015); and the integration of laser scanned data, photogrammetry and multimodal/multispectral data to assess the conservation state of paintings (Remondino et al., 2011a). There are incredible examples of 3D imaging and repatriation with projects focused on education, cultural preservation, and security against loss (Hollinger et al., 2013), an example of 3D scanning and printing revealing functionality of a spear thrower ('atlatl') through field testing (Hollinger and Partridge, 2017), and the digital repatriation of a war canoe to the Western Solomon Islands (Hess et al., 2009). In

some cases 3D imaging can provide access to closed or limited access sites like an immersive virtual visitor experience of an Italian cave structure with Neolithic pictographs and 3D data that could be examined, measured, and compared for detecting and monitoring deterioration and enhancements for faded images (Beraldin et al., 2011). While this is by no means an exhaustive list, these examples provide evidence that 3D imaging is being used for a range of cultural heritage documentation.

A wide range of specialists from different institutions are using 3D imaging of cultural heritage for a variety of applications and questions as shown by an online survey conducted to better understand the adoption of 3D imaging technologies for cultural heritage documentation, priorities for 3D image quality, and ideas for future use (Hess, 2015b, 2015a). The survey results provide evidence of the use of 3D imaging to record cultural heritage objects by a range of specialists (archaeologists, anthropologists, palaeontologists, historians, computer scientists, surveyors, Egyptologist, museum scientists, biologists, engineers, conservators, etc.) from different workplaces (museums, universities, local authorities, national bodies, charities, commercial provider of services, self-employed/freelance/consultant). Over half of the participants were actively using 3D imaging at their workplace citing motivations ranging from digital documentation and the creation of digital surrogates to answering conservation questions, identifying/quantifying damage and monitoring change to interactive exhibitions, visitor engagement/experience, and teaching/educational purposes. The survey indicated that most of the objects that participants were working with were 1-60 cm, within close-range object imaging. Hess concluded that the results of this survey showed high interest in 3D imaging technologies across the museum sector; however, 3D digital documentation had not yet been adopted as a standardised procedure in museums or integrated in conservation workflows.

The previous paragraphs provide evidence of the wide use of 3D imaging for cultural heritage applications with references to smaller studies and specific projects; however, larger coordinated efforts of multiple institutions internationally show a higher level of interest and continued support in developing and integrating 3D imaging as standardised and routinely used documentation methods for cultural heritage applications. These include the International Committee for Documentation of Cultural Heritage (CIPA), a scientific committee of International Council of Monuments and Sites (ICOMOS) that was founded with the International Society of Photogrammetry and Remote Sensing (ISPRS) ('CIPA Heritage Documentation', n.d.), the 2008-2012 European project "3D COFORM: Tools and Expertise for 3D Collection Formation" to advance the state of the art in 3D cultural heritage documentation (Arnold, 2013), and the 2012-2015 European project 3D-ICONS focusing on

the digitisation of built heritage. These initiatives, in addition to Sketchfab (Section 1.1.1) and COSCH (Section 1.1.3) illustrate the interest and wider use of the techniques and technologies for cultural heritage documentation through establishing pipelines and digitising objects and sites; training and workshops; working towards best practices and standardized workflows; and providing sharing and visualisation tools.

Additional examples of coordinated efforts include the Community Standards for 3D Data Preservation (CS3DP) project ('CS3DP', n.d.) to develop standards for the preservation of digital 3D data, the IIIF 3D Community Group ('IIIF 3D Community Group', n.d.) to further interoperability and open standards for 3D, and the Europeana 3D Task Force ('3D Content in Europeana', n.d.) to inform, support, and encourage organisations who are creating 3D data. These examples of coordinate international efforts in addition to the online survey (Hess, 2015b, 2015a) provide evidence of the different levels of interest and support in the development and improvement of 3D imaging technologies for cultural heritage documentation. The international community is invested and engaged in developing 3D technologies and the research presented in this thesis complements efforts to support and improve 3D imaging for cultural heritage.

Cultural heritage objects can be recorded by a variety of 3D techniques that include active range-based technologies, such as laser and white light scanning, and passive image-based systems, such as photogrammetry. Range-based modelling directly captures 3D information of an object using active sensors that implement structured light or laser light to measure objects. Image-based methods use passive sensors to record 2D images and recover 3D surface information from mathematical models. Image-based methods include both photogrammetry and more automated methods from the field of computer vision, like SfM. Other 3D imaging techniques, such as computed tomography (CT) scanning and micro-CT scanning, use X-rays to record the shape and volume of an object, and 3D digital microscopy records geometry at the micro scale. Reviews of 3D imaging techniques for cultural heritage applications include Wachowiak and Karas (2009), Engel (2011), and Remondino (2011a, 2011b, 2011c).

The wide range of 3D techniques and technologies that are available provide many options to choose from when planning the documentation of a heritage object or site. Advantages and limitations of these techniques and instrumentation relate to surface characteristics of the object, required documentation accuracy, object properties, location considerations, and project budget (Remondino and Menna, 2008). The selection of 3D techniques can be influenced by factors like the costs, ease of use and usability, portability, operator

experience, location considerations, object properties, and the overall aim of the documentation (Remondino and Menna, 2008).

The availability of a variety of low-cost and open source software systems combined with high-quality, high-resolution consumer digital cameras have made image-based 3D reconstruction popular and more accessible to cultural heritage (Remondino et al., 2014). In addition, the increased automation of software does not require an expert user and the equipment required is flexible and minimal contributing to the popularity and accessibility. Image-based 3D reconstruction methods offer advantages including (Remondino, 2011a, p. 133):

- the image data contains the information needed (geometry and texture) for both 3D modelling and documentation,
- archived images can be processed even if the object has changed or has been lost,
- the acquisition of images is faster and easier than range-based techniques, and
- the tools are generally cheap, portable, easy to use, and offer the potential of high accuracy.

Image-based 3D reconstruction techniques are considered accessible, portable, and flexible and can provide high-resolution results to non-expert users, and therefore, heritage users have adopted these techniques for 3D recording.

Image-based 3D reconstruction is being widely used for cultural heritage with many publications presenting research and results. These range from small scale to large scale objects including case studies on micro and macro scale for rock art (Plisson and Zotkina, 2015), coins (Hess et al., 2018), and small archaeological objects (5-10 cm) (Clini et al., 2016; Sapirstein, 2018) to medium sized sculptures (Menna et al., 2016) and larger scale archaeological excavations (Dellepiane et al., 2013), archaeological sites (Green et al., 2014; Nocerino et al., 2014; Sapirstein, 2016), a 300 m cave corridor (Beraldin et al., 2011) and 40 km of historic porticos (Remondino et al., 2016). Image-based techniques have been used for conservation and monitoring (Robson et al., 2004; Remondino et al., 2011a; Dellepiane et al., 2013; Abate et al., 2014), underwater applications and submerged surfaces (Guery et al., 2017; Menna et al., 2018), documenting of rock art (Lerma and Muir, 2014; Noya et al., 2015; Plisson and Zotkina, 2015; Jalandoni et al., 2018), recording archaeological sites (Nocerino et al., 2014; Sapirstein, 2016) and excavations (Dellepiane et al., 2013; De Reu et al., 2014; Galeazzi, 2016), built heritage and architecture (Green et al., 2014; Toschi et al., 2014; Remondino et al., 2016), and the creation of a virtual museum (Marziali and Dionisio, 2017). There have also been many publications and projects comparing 3D techniques,

software, and instrumentation in addition to assessing acquisition and processing methods (Kersten and Lindstaedt, 2012; Remondino et al., 2012; Skarlatos and Kiparissi, 2012; Green et al., 2014; Jalandoni et al., 2018). While these examples are far from an exhaustive list, it provides evidence of the wide use of image-based 3D reconstruction for cultural heritage documentation.

There has been a "democratisation" of 3D documentation as image-based techniques have become more automated and flexible (Hollinger et al., 2013; Lerma and Muir, 2014; Remondino et al., 2017). Nearly any digital camera and lens (including mobile cameras) can be used to acquire images of scenes or objects ranging in scale with different lighting conditions from close up to far away. Mobile apps are available to create 3D models using the cameras in mobile phones (examples: Qlone[2], Trnio[3], and Scann3D[4]). The available software tools are automated and require little knowledge and input and can produce models that "look good". Consumer imaging systems, both the consumer digital cameras and automated processing software, are off-the-shelf options that are readily available for non-expert heritage users and can be used for 3D imaging of cultural heritage objects providing an accessible option for 3D recording. The accessibility results from the flexibility of the equipment that can be used, the methods for acquiring images, and the automation of the processing workflow.

Accessibility is a critical advantage of SfM-MVS methods, but the features that make the method accessible also can impact accuracy and reliability. Having a model that "looks good" does not mean that it can be used for metric applications. Hess (2015a) noted that 3D data of museum and archaeological objects can be highly inconsistent including variation in geometric accuracy, resolution, and colour, and while it might appear to be a good visual representation, the results might not be scientifically traceable. The flexibility and automation that make image-based 3D reconstruction more accessible also increase the challenges of maintaining consistent 3D output. In turn, the wider use of image-based 3D reconstruction introduces a wider variety of resulting quality.

The wide variety of resulting quality is a growing problem that calls for investigating methods to improve the consistency of 3D output. The online survey conducted by Hess (2015b, 2015a) addressed priorities for 3D imaging quality; however, it did not establish the

---

[2] Qlone: https://www.qlone.pro/ [Accessed 16 October 2019]
[3] Trnio: http://www.trnio.com/ [Accessed 16 October 2019]
[4] SCANN3D:
https://play.google.com/store/apps/details?id=com.smartmobilevision.scann3d&hl=en_US [Accessed 16 October 2019]

quality of the 3D models being produced. There are studies that have discussed the variability in quality of the resulting 3D reconstructions from automated processes (Hess and Robson, 2012; Nocerino et al., 2014). Remondino et al. (2017, p. 591) described this variability stating that conference presentations are filled with image-based 3D models, but the presentations do not necessarily address or investigate the distortions, deformations, and scaling issues. The automated processing makes it easier for anyone to create a 3D model of an object, but this does not ensure accurate or reliable reconstructions. In fact, there is a lack of standards and guidelines for evaluating data (Hess and Robson, 2012; Toschi et al., 2015) in addition to an insufficient knowledge about the process and software being used (Remondino et al., 2017) (Section 2.2.2). While Hess' survey (2015b, 2015a) indicated an interest in accuracy and reliability by participants identifying the extreme importance of correct overall geometry and metric accuracy, detailed surface geometry recording, and recording of surface features, this interest and emphasis does not ensure a consistent quality across the museum sector. Due to the high variability there is a need for improved consistency of 3D output, and this thesis aims to provide methods of optimising image-based 3D reconstruction focusing on accessible, consumer imaging systems and on workflows that can be made available and inform best practices for 3D imaging of heritage objects.

In discussing 3D imaging and museums, Robson et al. (2012) provided a useful analogy. The authors point out that within a museum there are a range of photographic records of museum objects from blurred snap shots from visitors to professional images by collection photographers. This is also the case with 3D imaging. The specific use of the 3D outputs must be defined in order to understand whether the output images and models are fit for purpose, and if not, to what extend they need to be improved (Robson et al., 2012). This thesis focusses on image-based 3D reconstruction for accurate and reliable scientific records for conservation documentation while seeking to maintain the accessibility of imaging and 3D model creation workflows.

2.2. Photogrammetry and structure from motion (SfM)

Photogrammetry is often used as a general term to present and discuss image-based 3D reconstruction for cultural heritage documentation and is sometimes considered a new technique. However, photogrammetry has a long history that parallels photography (Luhmann et al., 2014), and there are a range of methods used that relate to photogrammetry but may be better described using other or additional terms. The interdisciplinary nature and wide use of image-based 3D reconstruction in different fields can result in the misuse of terminology or the unclear definition of meanings (Remondino et al., 2017). Consequently, this section will briefly look at the fields of photogrammetry and computer vision and the

development of image-based 3D reconstruction techniques to better define some of the terminology being referenced by heritage users. While there is an importance to clearly defining terminology in an interdisciplinary field, this discussion is also important to provide insight into the investigation on accuracy and reliability of the techniques.

Photogrammetry is one of the specialisms of geomatics, or surveying, a scientific field for the collection, analysis, and interpretation of survey data relating to the earth's surface. Photogrammetry is focused on making accurate 3D measurements. Initially it was used for architectural measurement before applications in mapping, and the first examples of cultural heritage and preservation applications were as early as 1858 (Luhmann et al., 2014, p. 18). Luhmann et al. (2014, pp. 17–27) provides more information about the development and history of photogrammetry tracking the start of *analytical photogrammetry* in the 1950s, a shift into *digital photogrammetry* in the 1980s, and a significant expansion of photogrammetric measurement technology due to the increased resolution of digital cameras in the 1990s.

The fundamentals of photogrammetry and its underlying principals are provided by Luhmann et al. (2014, pp. 7–9). Photogrammetry is based on a pinhole camera model where an object point corresponds to an image point with this line defining an image ray that passes through the perspective centre. The shape and position of an object are determined by central projection imaging by reconstructing the bundle of rays passing through the perspective centre. The intersection of at least two spatially separated image rays can locate an object point in three dimensions. The *interior orientation* defines the imaging geometry within the camera, while *exterior orientation* defines the spatial position and orientation of the camera. While photogrammetry is based on a pinhole model, in practical cameras the imaging geometry will differ. Each camera must therefore be calibrated to correct for systematic departures from the pinhole model that would otherwise cause error. The principle procedures for close-range photogrammetry include: recording, pre-processing, orientation, and measurement and analysis (Luhmann et al., 2014, pp. 11–12).

Photogrammetry encompasses numerous techniques and there are several ways to specify and categorise the method and measurement. This includes categorisation by camera position and object distance (i.e., aerial and close-range photogrammetry); by number of measurement images (i.e., single-image and stereo photogrammetry); by method of recording (i.e., analogue, analytical, and digital photogrammetry); by availability of measurement results (i.e., offline and online photogrammetry); and by application or specialist area (i.e., architectural, industrial, and forensic photogrammetry) (Luhmann et al., 2014, p. 6).

Computer vision has a more modern history with its beginnings in 1970s and initial investigations into the visual perception aspect of providing robots with intelligent behaviour that mirrored that of human intelligence (Szeliski, 2011, p. 10). Computer vision involves mathematical techniques for the recovery of 3D shape and appearance focusing on automation and differing from the aims of the precise measurement of photogrammetry (Szeliski, 2011).

Photogrammetry and computer vision both start from 2D images in order to extract 3D information, but the approaches can be different. Photogrammetry has focused on accuracy and reliability for mapping, cartography, and monitoring, while computer vision has focused on automation for robotics and inspection (Remondino et al., 2012). The integration of computer vision methods has included a self-calibration approach leading to SfM. SfM is an approach that simultaneously and automatically determines the camera parameters and the geometry of the scene using image matching and bundle adjustments (Remondino et al., 2012; Granshaw, 2016). MVS relies on the use of multiple images for the identification of correspondences for the image matching. While *photogrammetry* is often the term used, the image-based 3D reconstruction widely used for cultural heritage is the automated and flexible method based on SfM paired with MVS.

While the previous paragraphs may give the impression that photogrammetry and computer vision remain entirely separated, computer vision techniques build from photogrammetry principles and current tools have become an integration of the two. It was worth clearly defining the two and discussing the fields as the intention and aims of technique development are different, which can inform the applications and limitations. While the previous paragraphs defined the fields and techniques separately, the current state of art involves the integration of photogrammetry and computer vision algorithms (James and Robson, 2014; Remondino et al., 2017).

2.2.1. SfM software

There are a variety of low-cost and open source software options available that implement SfM and MVS. Commercial software packages include Agisoft PhotoScan and Pix4d, while more open solutions are available. Bundler is a freely available tool for SfM (Snavely et al., 2006) that can be paired with MVS tools like Patch-based MVS (PMVS) (Furukawa and Ponce, 2010), which was extended by Clustering Views MVS (CMVS). VisualSFM (Wu, 2013) is a freely available SfM option that can be integrated with PMVS/CMVS or other tools. Another free, open-source solution for SfM and MVS is MICMAC developed by National Institute of Geographic and Forestry Information (IGN) and the National School of

Geographic Sciences (ENSG) (Rupnik et al., 2017). There are several other software solutions that may not be listed here. The technology continues to develop at a fast pace, so the software solutions available in a few years may be different from current options.

While the software examples provided above have been used for cultural heritage documentation, Agisoft PhotoScan is widely used as a commercial option for heritage applications that incorporates both SfM and MVS. Agisoft, founded in 2006, is a Russian company that has focused on computer vision technologies to develop applied tools for digital photogrammetry ('Agisoft', 2019). As a commercial software it is being actively maintained and updated incorporating new processes, applications, and new users in different fields. PhotoScan provides an "end-to-end solution" while many of the open source options for SfM tend to require different software solutions for components of the processing, or a "multi-package workflow" (Green et al., 2014). Open source software tends to be the result of research-oriented projects solving specific research questions that do not usually provide an end-to-end solution, while commercial software is answering a need and not a research question. The open source software has the advantage of allowing more control over each step of the process, but the automation and single software solution that PhotoScan offers is appealing and advantageous as an accessible option especially for non-expert heritage users. PhotoScan was selected for this research because it provides a single software solution that is widely used by heritage professionals. There are limitations with using a commercial tool with high automation. While there is some control over the process, the software is still considered a "black box" with unknowns about the actual algorithms and processing.

Several cultural heritage studies have used PhotoScan as the primary software selected (Verhoeven, 2011; Koutsoudis et al., 2013, 2014; De Reu et al., 2014; Clini et al., 2016; Sapirstein, 2016), other studies have used PhotoScan for interior and exterior camera parameters paired with Australis PhotoModeler for the bundle adjustment (Nocerino et al., 2014; Menna et al., 2016); and other studies have compared the results and performance PhotoScan to other software options (Kersten and Lindstaedt, 2012; Remondino et al., 2012, 2017; Alsadik and Remondino, 2013). This is not an exhaustive list of cultural heritage projects using PhotoScan, but it provides evidence that the software is widely used.

The discussion differentiating traditional photogrammetry and automated methods like SfM was included because the term *photogrammetry* is often used to generally reference image-based 3D reconstruction without consideration for the selected approach and the resulting quality. This differentiation is not widely acknowledged by heritage users. Traditional photogrammetry involves precision, accuracy, and critical analysis to ensure a known

quality for metric survey, and most of the image-based 3D reconstruction of heritage objects does not have this accuracy and precision. In addition, it is especially important to clearly define terms in an interdisciplinary field to ensure clear communication, including the appropriate comparison of techniques and the complete understanding of the results (Remondino et al., 2017). This discussion about terminology and how it relates to the fields and applications ties directly into the discussion about the accuracy and reliability of the resulting 3D models.

2.2.2. Accuracy and reliability

Accessibility is an important advantage of SfM-MVS methods allowing non-expert users to be able to implement these methods, but the features that make the method accessible also can impact the accuracy and reliability. Accessibility results from the flexibility of the equipment that can be used, the methods for acquiring images, and the automation of the processing workflow. Nearly any digital camera and lens (including mobile cameras) can be used to acquire images of scenes or objects ranging in scale with different lighting conditions from close up to far away. The available software tools require little knowledge and input. While the resulting model may be a fairly complete reconstruction that resembles the recorded object or scene, a model that "looks good", the use of the model will be limited if there is not information about the data (acquisition, processing, etc.) and if the quality and reliability cannot be assessed. The specific use of the 3D output must be defined in order to understand whether the models are fit for purpose or accurate and reliable for the application on hand. This thesis is focused on the use of image-based 3D reconstruction for scientific records for conservation documentation providing capabilities for monitoring and measuring change over time while also maintaining the accessibility of imaging and 3D model creation workflows.

Tools like PhotoScan are widely used because they are powerful and cheap; however, most users may not be aware of its strengths and weaknesses (Remondino et al., 2017). According to Remondino et al. (2017), the trend of the increased ease of use from a high level of automation is leading to the risk of insufficient knowledge of the processing and tools and the increased confidence in the 3D results even though the results include object distortions and deformations, scaling problems, and non-metric artefacts. Remondino et al. insisted that users better understand acquisition principles, data processing algorithms, and standard metrics in addition to defining the most common terms to improve the ability of assessing and comparing data. The challenges of easy to use software that provide 3D models that "look good", the risk that this poses to non-expert users, the limitations of the results for metric applications, and the need for assessing the accuracy of the results are reiterated by

several sources (Remondino et al., 2012; Dellepiane et al., 2013; Green et al., 2014; Nocerino et al., 2014; Sapirstein, 2016). This provides evidence of the questioning of the accuracy and reliability of 3D reconstruction furthering the point that a model that "looks good" may be limited in its metric capabilities and its use as a scientific record.

In addition to the studies questioning the accuracy and reliability of SfM methods, others examined the development of the methods and the accuracy and resolution of image-based modelling as compared to range-based techniques. For example, Remondino et al. (2014, p. 146) concluded that image-based techniques can result in 3D models that are comparable to laser scanning, and Menna et al. (2016) reported that image-based techniques can attain the accuracy and resolution of range-based techniques and provide "valid alternative" depending on the quality of the images and camera network. Part of this difference in reporting on the accuracy and reliability could be attributed to the development of the processing algorithms and software, but it could also be attributed to the range of resulting quality, the lack of standard acquisition and processing protocols, and the lack of standard analysis tools for assessing quality.

As emphasised with the discussion about photogrammetry and computer vision, terminology is important especially when describing and assessing 3D quality. As Remondino et al. (2017) were concerned about the misuse of terminology and the lack of clear meanings and measures, the authors presented definitions of common terms including those relating to the assessment of 3D quality; the following list of terms and definitions were presented by Remondino et al. and consequently, provide an important foundation for discussing accuracy and reliability.

- Determining the *accuracy* generally requires reference coordinates or measures, and the relative accuracy is represented by the relation of the achieved object measurement accuracy and the maximum dimension of the measured object.
- *Precision* is "a quantitative measure of variability of results and is indicative of random errors, following a Gaussian or normal distribution (Granshaw, 2016)" (Remondino et al., 2017, p. 595). This can be calculated as a standard deviation and should be reported with its coverage factor (e.g. 3 sigma).
- *Reliability* is "a measure of how outliers (gross or systematic errors) can be detected and filtered out from a set of observations in an adjustment process" and is dependent on redundancy and network configuration (Remondino et al., 2017, p. 595).
- *Residuals of image coordinates*, or *reprojection error*, provide the deviation between the values of the image observation and the computed values from the

adjustment process. This is the Euclidean distance between the measured image point and the back-projected position of the corresponding 3D point. Reprojection error can result from noise, inaccurate camera poses, and unmodeled lens distortion (Remondino et al., 2017, p. 594).

- The *standard deviation σ* is the square root of the variance, and the *variance* is the mean of the squared deviation of a variable from its mean value μ. While *σ* represents the spread, or variability, of a set of numbers from the mean value μ, the *Root Mean Square (RMS)* represents how much the differences, or the residuals, are on average from zero. The RMS is "the square root of the mean of the squared differences between the variable and its most probable value" while *RMS Error (RMSE)* requires a reference measurement as opposed to the most probably value (Remondino et al., 2017, p. 594).

SfM is widely used for cultural heritage documentation; however, the question arises whether the method is providing accurate and reliable results. This research aimed to create accurate and reliable scientific records for conservation documentation, and while focusing on accessible 3D imaging techniques, specifically SfM-MVS, there is a need for investigating methods of assessing and improving the quality of the resulting 3D reconstruction. The discussions based on questioning the accuracy and reliability of image-based 3D reconstruction methods and software leads in a few directions: establishing available best practices and standards (Section 2.3), assessing the accuracy of 3D data (Section 2.4), and methods of optimisation specifically looking at DOF and sharpness (Section 2.5).

2.3. Best practices and standards

This section focuses on best practices and standards to provide a foundation for the acquisition, processing, and assessment presented in this thesis. The first step in improved image-based 3D reconstruction is establishing the available best practices and standards. Best practices are important for ensuring or improving quality data acquisition and use for a specific field, and standards aim at influencing a community to improve outcome and are the result of science, technology, and experience (Beraldin et al., 2011). As a field grows and has enough users beyond the initial technological innovators and early adopters, best practices are essential for making the technology mainstream (Beraldin et al., 2011, p. 2). Similarly, standards are needed with the growth of new users who are not familiar with the techniques and require clear statements and information to understand whether the system satisfies specific requirements (Remondino, 2011a).

For several years best practices and standardisation for image-based 3D reconstruction in cultural heritage have been called for to provide both advantages and limitations of systems and solutions (Remondino, 2011c), to standardise the acquisition for archaeologist (Dellepiane et al., 2013), to evaluate the resolution, repeatability, and reproducibility (Toschi et al., 2014), and to support responsible archaeological recording for precision, accuracy, and sustainability (Sapirstein and Murray, 2017). In addition to the call for best practices and standardisation, others provided best practices for specific objects, materials, sites, and projects and general overviews for the use of image-based 3D reconstruction and heritage applications. Examples include best practices provided for documenting a cave structure (Beraldin et al., 2011), comparing 3D imaging techniques to define an overall methodology of recording an archaeological excavation (Galeazzi, 2016), and the decision making for archaeological field work (Sapirstein and Murray, 2017). With the wider use of the techniques, there are now available "best practices" for different objects and applications, but there is not yet standardisation for image-based 3D reconstruction for cultural heritage applications.

The previous paragraph provided examples of best practices for specific objects, materials, sites, and projects, which may not be helpful for or relevant to unrelated objects or sites. The following section will look at more general examples of best practices for a non-expert audience in order to establish a starting workflow for the research presented in this thesis.

2.3.1. Image-based 3D digitisation pipeline

Remondino et al. (2013, p. 140) provided guidelines based on a critical review of the digitisation pipeline targeting the non-expert user and covering the process from sensor selection through planning, acquisition, processing, and visualisation. These design and implementation guidelines include key actions for image-based 3D reconstruction (Remondino et al., 2013, p. 137):

> *1. Site overview and planning or object examination.*
>
> *2. Selection of the appropriate technology and parameters, or combination of multiple technologies.*
>
> *3. Data collection positions planning and configuration design.*
>
> *4. Data acquisition workflow based on best practice.*
>
> *5. Selection of data processing tools, 3D model representation method and suitable file formats.*
>
> *6. Selection of software tools able to handle all processing and visualisation needs.*

The data acquisition best practice (Remondino et al., 2013) is expanded upon by including an adapted version of the 3x3 Rules, originally from Waldhäusl and Ogleby (1994). These best practices were adapted and modified for the use of digital cameras and to provide guidelines for image-based 3D reconstruction (Table 2-1). The authors recommended separating the camera calibration from the orientation, using the largest DOF and lowest ISO to achieve the minimum noise and maximum sharpness, selection of medium lens focal length (around 50 mm), ensuring consistent colour settings between images and overall even and diffuse light, and planning the image ground sampling density (GSD) to reflect the project needs and imaging system.

Table 2-1. *Modified 3x3 Rules for photogrammetric documentation using digital cameras from Remondino et al. (2013)*

GEOMETRIC	PHOTOGRAPHIC	ORGANISATIONAL
Acquire control / ground information	Keep a constant interior geometry of the camera	Make proper sketches
Multiple & convergent image coverage with adequate B/D ratio	Keep homogeneous illumination	Write proper protocols and keep metadata
Separate calibration & orientation	Select a stable combination of large format camera & lenses	Perform a final check

Historic England has produced two documents relating to best practices and 3D: *Metric Survey Specifications for Cultural Heritage* (Andrews et al., 2015) and *Photogrammetric Applications for Cultural Heritage: Guidance for Good Practice* (2017). The first of these is a second edition to the standard specifications for English Heritage that have been used for metric survey for the nine years prior to this edition (Bryan et al., 2009), which focused on metric survey fit for purpose for heritage management, specifically built heritage, to connect the information user to the information supplier to ensure the success of the survey. The second document focused on SfM techniques and the "practical application of photogrammetry". The document included basic principles, general considerations, scales and applications, and case studies to provide a comprehensive resource for SfM applications for cultural heritage but does not cover all aspects of photogrammetry in depth. A general workflow was provided, see Figure 2-1 (2017, p. 15), with an emphasis on metadata at all stages and general considerations for image acquisition, equipment selection, camera settings, and lighting.
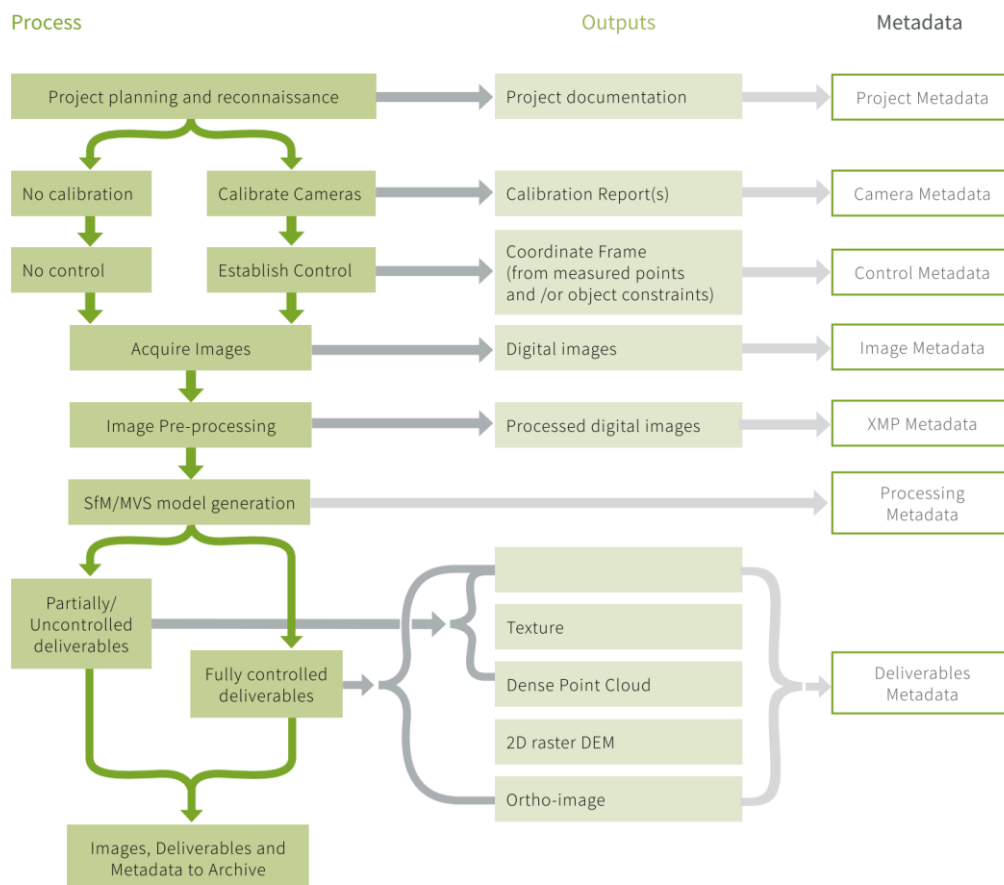
Figure 2-1. Basic elements to a photogrammetric workflow (*Photogrammetric Applications for Cultural Heritage: Guidance for Good Practice*, 2017, p. 15)*.*

Taking into consideration the general workflows from multiple sources, such as *Guidance for Good Practice*, Remondino et al. (2013), and Menna et al. (2016), Figure 2-2 outlines a combined general workflow for a starting point for the research (Chapter 4) and the workflow is developed in Chapter 6 as part of the wavelength selection workflow (Section 6.3). The first stage of the project is the design or planning phase, which involves examining the object and establishing the object characteristics: dimensions, materials, surface characteristics, and features of interest and dimensions of those. This information will help to guide the planning, set the project requirements, and establish the technology and parameters required.
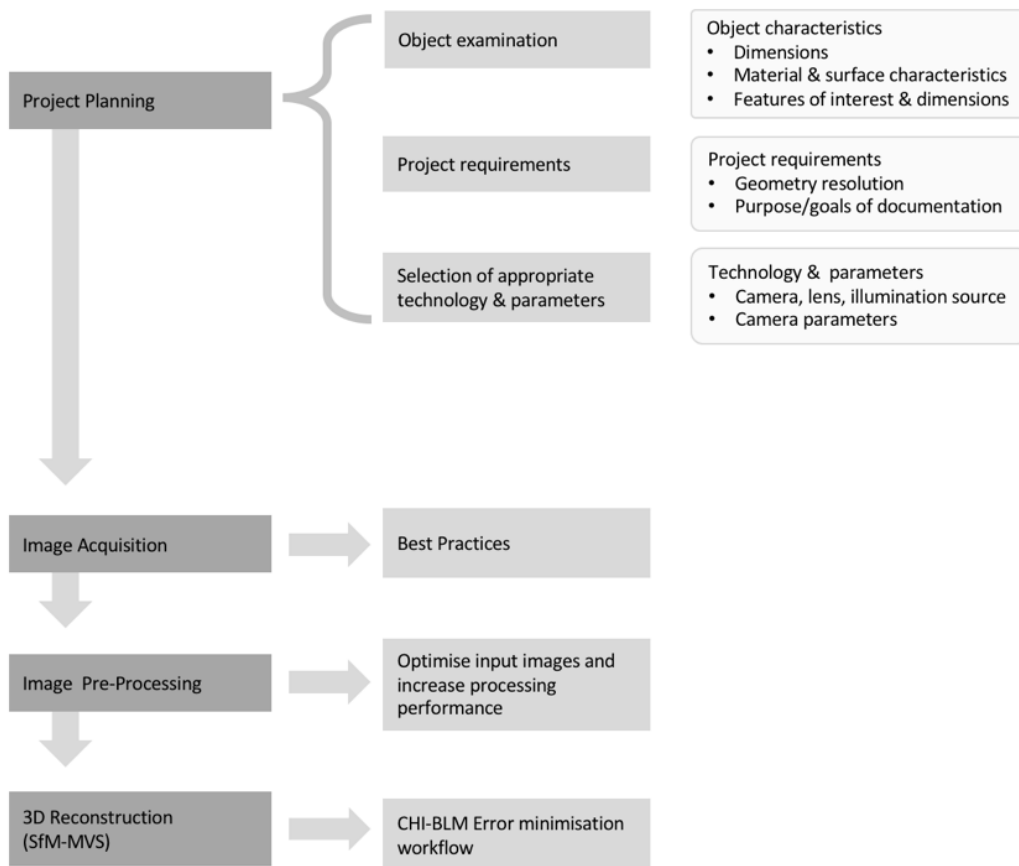
Figure 2-2. General workflow for image-based 3D reconstruction..

The project requirements for resolution and quality need to be identified in order to inform the selection of the best technology and parameters including camera, lens, illumination, and camera parameters. The ground sampling density (GSD) can be used to understand the parameters required for recording the smallest detail that needs to be resolved. The GSD is the size of an object or feature in object space represented by a single pixel in the image space and it is calculated by dividing the camera-object distance H by the focal length f and multiplying this by the pixel size p as given by the following equation (Andrews et al., 2015):

$$GSD = \frac{H}{f} \times p \tag{2.1}$$

The GSD needs to be 2-3 times smaller than the smallest detail that needs to be resolved (Remondino et al., 2013). While this can be a useful tool for planning, it is only representative of the geometry of a single image and imagery taken perpendicular to the subject surface (*Photogrammetric Applications for Cultural Heritage: Guidance for Good Practice*, 2017).

As with other image-based 3D reconstruction projects, there needs to be planning for the camera positioning and configuration design. The defined project requirements and selection of technology/equipment during the planning phase (selected based on the object size and the size of the features of interest) will inform the positioning (camera-object distance). A strong camera network is important and can impact the resulting geometry (further discussed in Section 2.3.3.2). The planning stage is followed by the image acquisition, image pre-processing, and 3D reconstruction. The following section informs the image acquisition and 3D reconstruction aspects of the image-based 3D reconstruction workflow.

2.3.2. Cultural Heritage Imaging (CHI) and error minimisation workflow

Cultural Heritage Imaging (CHI) is a non-profit organisation, founded in 2002, dedicated to advancing digital technologies for recording cultural heritage, focusing mostly on Reflectance Transformation Imaging (RTI) and image-based 3D reconstruction. CHI has collaborated with the US Bureau of Land Management (BLM) to create an *error minimisation workflow* for "practical, scientific use of photogrammetry in cultural heritage" (Schroer et al., 2017b). Additional information about the origins of this method are provided by Mudge et al. (2008) and Matthews (2008). CHI provides 4-day photogrammetry training that covers the optimised processing workflow targeting heritage professionals including photographers, conservation and preservation professionals, archaeologists, anthropologists, historical preservationists, classicists, epigraphers, and natural scientists. These are considered "non-expert" and non-technical users.

The CHI workflow uniquely includes an *error minimisation workflow* that iteratively removes bad points and optimises the alignment and calibration removing significant errors and producing higher quality results. The training and workflow include assessing the quality of the results by looking at the metric model quality indicators, and best practices are presented for different image capture scenarios including complex geometries and turntable setups. While Agisoft PhotoScan Pro is used with the training, the workflow is software independent.

The workflow uses CHI calibrated scale bars with coded and non-coded targets. The scale bars were designed by US BLM photogrammetry experts, printed on DIBOND (composite material with 2 aluminium sheets bonded to a solid polyethylene core), and individually calibrated to 0.10 mm or better accuracy (Cultural Heritage Imaging, 2015). The 18 cm and 5 cm scale bars include 2 non-coded, circular cross-type targets, which were used in this thesis for scaling image-based 3D reconstruction models.

The effectiveness and influence of the CHI training and best practices can be understood by observing the adoption and wide use of Reflectance Transformation Imaging (RTI) for heritage documentation especially within conservation. CHI initially focused on training and development of RTI including the processing and viewing software. Ten years after CHI's first RTI training workshops, the computational technique is commonly known and widely used in conservation, it is incorporated in conservation training programs in the US, and it is included in the guide for conservation documentation (Warda et al., 2017).

The CHI-BLM *error minimisation workflow* is the processing workflow that is used for the research (Chapter 4). This workflow was introduced to the author initially during a 4-day training with CHI in 2014, and the author has also hosted the training workshop at the Smithsonian's Museum Conservation Institute in 2017. The training and workflow provided an emphasis on scientific accuracy and reliability and best practices to improve the resulting 3D quality.

2.3.3.   Additional methods for improved image-based 3D reconstruction

Beyond best practices and standards there are additional methods for improving the results for image-based 3D reconstruction. This section will specifically look at the use of targets (Section 2.3.3.1), the importance of image configuration (Section 2.3.3.2), and the risk of over-parameterisation for camera models (Section 2.3.3.3), which tie into the experimental setup and results of this thesis.

2.3.3.1.   Targets

Targets are widely used for photogrammetry outside of cultural heritage and are essential for measurement applications. As listed by Luhmann et al. (2014, p. 221), targets are used:

- *to identify natural object feature points which cannot otherwise be identified accurately,*
- *as uniquely defined points for comparative measurements,*
- *as control points for geodetic measurement,*
- *for automatic point identification and measurement,*
- *for accuracy improvement.*

Targets can be different shapes and materials; the selection is dependent on the application, imaging configuration, and illumination. These can include retro-reflective targets, circular targets, spherical targets, patterned targets, and coded targets (Luhmann et al., 2014, pp. 221–233).

Targets were not initially considered for this research, but targets present an option related to setup and acquisition that could improve the alignment of 3D reconstructions. References stated that targets cannot be used for cultural heritage because the targets should not be adhered to the surface of an object due to disturbances and damage (Wachowiak and Karas, 2009; Barazzetti et al., 2010; Remondino et al., 2011b, 2012; Simon Chane et al., 2013). However, targets have been used around heritage objects (Robson et al., 2004; Gallo et al., 2014; MacDonald et al., 2014; Sapirstein, 2018). Targets have also been used with built heritage (Nocerino et al., 2014; Sapirstein, 2016) and archaeological sites (Sapirstein and Murray, 2017). Andrews et al. (2015), in the metric survey specifications for Historic England, used targets for documentation, but they acknowledged that the historic fabric may be too fragile for the application of targets.

Non-coded circular and patterned targets and coded targets may present the best options for heritage applications and related test objects. Retro reflective targets may be useful for a control field around an object or adhered to a test object, but the setup and acquisition of the targets is not consistent with what is required for documentation of a heritage object (since the targets are recorded and not the object). The use of coded targets could greatly improve the ease of aligning datasets, but a challenge remains when considering the acquisition and comparison of multi-temporal data. Once the object moves in relation to the targets, the targets cannot be used to align the datasets and there is still the challenge of aligning 3D data for comparisons. This is further discussed in the context of the research results in Section 4.2.2.1.

2.3.3.2. *Image configuration*

Proper image configuration, or camera network geometry, is important for the acquisition of image-based 3D reconstruction as it determines the calibration quality and defines the image geometry (Remondino and El-Hakim, 2006, p. 276; Nocerino et al., 2014). While network issues were addressed years ago, the importance of camera network geometry is often overlooked in cultural heritage applications (Nocerino et al., 2014, p. 465). Following the trend pointed out by Nocerino et al., this research initially overlooked the importance of the camera network geometry, but the results in Section 4.1.2 reiterated the importance of image configuration and network design.

Normal image configuration can result in systematic errors observed as 'doming' (either a dome or bowl shape). This error can be attributed to an inaccurate estimate of radial lens distortion from self-calibration bundle adjustments (Wackrow and Chandler, 2008; James and Robson, 2014). The simulated examples for both Wackrow and Chandler (2008) and

James and Robson (2014) clearly showed a dome or bowl shape while the practical test from Wackrow and Chandler resulted with concentric radiating circles as a dome. Wackrow and Chandler (2008) and James and Robson (2014) provided evidence that a convergent image configuration minimised the systematic error surfaces resulting from an inaccurate model of radial lens distortion with the self-calibration procedures. Remondino and El-Hakim (2006) and Nocerino et al. (2014) also recommended using convergent images to strengthen the camera network, reduce deformation, and improve the geometry.

An Imaging Network Design Robot (INDRo) was presented by Sargeant et al. (2013) and Hosseininaveh Ahmadabadian et al. (2014) for studies involving robot calibration and network design. INDRo consisted of two perpendicular linear motion stages mounted to an optical table with the object placed on a rotary motion stage (Sargeant et al., 2013). Hosseininaveh Ahmadabadian et al. (2014) used an iteration of the INDRo for studying and optimising the design of imaging networks. The proposed system and process for recording complex objects included the creation of an approximate model of an object, designing the imaging network from the approximate model, and capturing images from the designed network through by using the INDRo. The INDRo allowed for specific camera positioning based on the robot calibration (Sargeant et al., 2013) and the Imaging Network Designer (IND) software designed to define a network based on satisfying specific criteria (Hosseininaveh Ahmadabadian et al., 2014).

The research presented in this thesis required an imaging geometry that could reproducibly position the camera to capture the network needed for the 3D reconstruction of a test object, which resulted in the *camera positioning robot* (Section 4.1.1.1) that was built with Sargeant from components of the INDRo.

Network design was also important for Sargeant et al. (2016) in a study of sensor placement for optical measurements specifically focusing on Digital Image Correlation (DIC). DIC is a photogrammetric technique that relies on surface matching for measuring strain and looking at localised deformation over time. While Sargeant et al. were interested in network configuration, their work with DIC and target-based tracking for the high accuracy recording of large volumes is not fully relevant for the 3D reconstruction of small to medium sized museums objects. However, Sargeant et al. created a test object from a rigid aluminium plate coated with an Airbus designed wallpaper with a pseudo-random pattern originally designed to optimise the optical detection of surface strain with DIC (Figure 1-2). The target included circular retro-reflective targets that were measured using photogrammetry with a Nikon DSLR and Brunson scale bars. Patterns with high local contrast and small features, like the pseudo-random pattern on the test object, provide a high sensitivity for DIC measurements

and the patterns can be optimised to increase the sensitivity of the measurement (Bossuyt, 2013; Bomarito et al., 2017).

This test object used by Sargeant et al. (2016) for DIC was also used as a test object for the image-based 3D reconstruction presented in this thesis (Section 1.3.1 and 4.1.1). The Panel test target provided a planar surface with a medium spatial frequency and a local high contrast ideal for surface matching that could be used for the optimisation for image-based 3D reconstruction. The panel is used throughout the experimental work presented in Chapter 4, 5, 6, and 7.

2.3.3.3.   Camera models and parameter selection

Image-based 3D reconstruction using SfM-MVS relies on self-calibration and the estimation of the camera model during the bundle adjustment through self-calibration. This process can model the principal distance, position of the perspective centre, radial distortion, tangential distortion, and affinity and shear of the image coordinate system. The estimates for the camera model are based on correction functions for deviations from the ideal central perspective model, which otherwise result in imaging errors. The correction functions have been standardised and correct for the effects of radial and tangential distortion and affine and shearing errors (Luhmann et al., 2014, p. 152). The principal point coordinates in PhotoScan are labelled as cx and cy.

- Radial distortion is one of the major sources of error for most camera systems resulting from variations in refraction with the different lens components and is dependent on wavelength, aperture, focal length, and object distance (Luhmann et al., 2014, p. 153). The second radial distortion parameter has its main effect at the edges of the image and the third radial distortion parameter is useful for modelling lenses with large distortion at the edges of the image (Luhmann et al., 2014, p. 155). The radial distortion parameters in PhotoScan are labelled as K_1, K_2, K_3, and K_4.

- Tangential distortion is also known as decentring distortion and is caused by decentring and misalignment of lens elements. This is generally not significant with high quality lenses, but may be a consideration for low-cost lenses (Luhmann et al., 2014, p. 157). The tangential distortion parameters in PhotoScan are labelled as P_1, P_2, P_3, and P_4.

- Affinity and shear describe deviations of the image coordinate system and relate to orthogonality and scale, which may be the case for digital systems that do not have a regular grid of light-sensitive elements or they are rectangular and not square

(Luhmann et al., 2014, p. 157). The parameters for affinity and shear in PhotoScan are labelled as B_1 and B_2.

Over-parameterisation of the camera model during the self-calibration procedure can cause deformation of the resulting model, processing artefacts, and increased spatial variability of error (James et al., 2017). Over-parameterised is defined as a solution with too many parameters that cannot be determined accurately because of the strong correlations between parameters (Granshaw, 2016, p. 237). Despite over-parameterisation being a well-known issue in the photogrammetry community, it may not be considered in other SfM-MVS applications as presented by James et al. (2017) for geoscience applications. While this issue is brought up in this geomorphology study, it was not something that seemed to be addressed in cultural heritage documentation studies and was initially overlooked for this research. A central argument for the study presented by James et al. (2017) was based on the high variability of the results using SfM-MVS and a lack of reporting on the processing and parameters being used. The lack of reporting meant that the cause of variability could not be fully understood. The authors demonstrated the sensitivity of the models to the camera parameters, which had not been previously published in geomorphological literature. It is important to consider camera models and parameter selection for cultural heritage applications, and this is further discussed as a part of the experimental work presented in Section 4.1.4.2 and 4.2.3.

2.4. Assessing 3D metric quality

As 3D imaging technologies are becoming more widely available and used, there are projects investigating the "best" technology comparing different 3D techniques and assessing the accuracy. There are no clear standards for assessing accuracy (Toschi et al., 2014), so the available studies include a range of comparisons, metrics, and results. The main methods that have been used for accuracy analyses include: (1) comparing results with higher accuracy techniques mostly range-based; (2) assessing reconstruction of known geometric shapes; and (3) comparing results with a model averaged from multiple acquisitions as was seen in studies like Remondino et al. (2014) and Toschi et al. (2014).

2.4.1. Higher accuracy techniques for reference data

A method commonly used for assessing techniques is to compare the resulting model with a 3D model obtained by another higher accuracy 3D technique. Several studies have compared models to reference data acquired by range-based techniques and several have used measurements from survey instruments and control points for assessing their accuracy.

When comparing 3D models, the results tend to include RMS and standard deviation values and sometimes surface discrepancy maps showing the distance differences between the models using a colour scale from negative to positive distances.

While this is a regularly implemented approach, there are several limitations using data acquired by another 3D technique. Image-based 3D reconstruction is often selected for documentation because it is low-cost, accessible, and portable, so it may not be an option in terms of cost, complexity, and portability to acquire a reference dataset of an object or site with a range-based scanning method. In some cases, the instrumentation used to acquire the reference data or the resulting reference data may have errors that exceed that of the technique being tested (Sapirstein, 2016), and the reference data is seldom questioned (Toschi et al., 2014). According to Remondino et al. (2014, p. 146) range-based techniques can be considered "black boxes" as "they lack well-defined procedures to assess quality on an individual project basis". With range-based techniques there can be a lack of a traceability chain (Toschi et al., 2014): manufacturers of 3D imaging systems provide customers with datasheets and calibration information but these are not linked back to international standards and are instead linked only to internal guidelines from the manufacturers.

Reference data needs to have a higher accuracy than the technique being tested. According to Remondino et al. (2014), the reference data needs to be two to three times more accurate, and according to Toschi et al. (2014), who referenced ISO 14553, the uncertainty of the instrument acquiring the reference data needs to be at least four times smaller than the technique being tested. Establishing a reference dataset with an accuracy two to three times better than the results is not always straightforward and is complicated by defining what should actually be compared and evaluated (the full object, a small area or single points) (Remondino et al., 2014). Reference sets are generally required but may not always be available for cultural heritage applications (Remondino and Menna, 2008). Results presented and discussed in Chapter 4 further support the challenges of reference data presented in the literature (Section 4.1.3 and 4.2.4).

2.4.2. Known geometric features

Another method for assessing accuracy is recording known geometric shapes (like planes, spheres and cubes) and using evaluation parameters defined by VDI/VDE (Remondino et al., 2014; Beraldin et al., 2015). Using known geometric shapes can have better metrological traceability than using reference data acquired by a range-based technique (Toschi et al., 2014). Examples include assessing flatness measurement error of a cube or plane using a

best-fit (Remondino et al., 2014), measuring the diameter of a sphere (Skarlatos and Kiparissi, 2012), and measuring sphere-spacing error between spheres (Beraldin et al., 2015).

The Metric Heritage Test Object, a purpose-built test object, was developed by Hess (2015a) for evaluating the performance of 3D imaging systems and the metric 3D recording of heritage objects. The 3D geometric plate of the test object included known geometric features: spheres with calibrated diameter, step artefacts, angle artefacts, and length control. A goal for creation of the object was to address a gap in guidelines and best practices of close-range 3D recording relating to heritage applications. With engineering metrology being founded on quantification and some previously established best practices and standards, this field provided a framework to develop the metric test object, to evaluate 3D imaging sensors, and to deliver a workflow and guidelines. The Metric Heritage Test Object was optimised for range-based sensors and is not widely available for heritage professionals to use, but the research, considerations, and resulting discussions are important in continuing the discussion about image-based 3D reconstruction and assessing accuracy.

While known geometric shapes provide a method for accuracy assessment, they may not have the same material properties as the object being documented. Different material properties and the complexity of a shape will influence the resulting accuracy of the technique. While the shape can provide a comparison of different recording techniques on the same test object, it cannot provide an accuracy assessment that can carry over to an object with different material properties. This method may provide a better means of comparing different imaging systems than assessing the performance of an imaging system for a particular object or collection.

2.4.3.   Averaging data and repeatability testing

In addition to the two previously presented approaches for assessing accuracy and reliability, there is also the potential of averaging datasets and repeatability testing when reference data may not be available. These do not constitute independent reference datasets with higher accuracy, but can be used for highlighting differences (Remondino et al., 2014). Examples include averaging four independently generated models into a reference model for archaeological objects (Sapirstein, 2018) and repeatability testing of an excavation of an archaeological site with two datasets processed independently and compared to provide an indication of the minimal change that could be detected in the spatio-temporal analysis (Dellepiane et al., 2013). The cost and challenge of getting higher-precision scanning equipment on site to acquire reference data can be unrealistic for some projects. The

advantage of averaging data and repeatability testing is that it is an option when reference data is not available; however, this does not provide an external check for the data.

2.4.4. Discussion

Accuracy assessment is accepted as a known challenge for image-based 3D reconstruction. A component of this is the lack of standard quality analysis tools for evaluating the quality (Remondino et al., 2017). The previous paragraphs looked at recent studies to better understand the options for assessing the accuracy of 3D reconstructions with variations of "reference data". Another component of this may be a gap between knowledge, experience, and literature within traditional photogrammetry and what is available to cultural heritage users.

Even though photogrammetric principles are integrated into the automated SfM-MVS workflows, the processing and workflow still requires quality assessment to better ensure the accuracy and reliability associated with traditional photogrammetry. James et al. pointed out that quality assessment tools for rigorous photogrammetric analysis are generally not provided by SfM-MVS software (2017, p. 52). James et al. emphasised the importance of considering the underlying photogrammetry methods to improve resulting reconstructions. While the integration of photogrammetry and computer vision algorithms in current tools implies less of a gap between the two fields, there is still a gap between non-expert users and the photogrammetric principles to ensure the reliability and accuracy of the results.

James et al. (2017) identified a gap between SfM-MVS geomorphology applications and traditional photogrammetric protocols, specifically accuracy assessment, which has similarities and relevance for the documentation of heritage objects. While James et al. focused on unmanned aerial vehicle (UAV) topographic surveys, the study is important for SfM-MVS-based workflows and is still valid and beneficial for cultural heritage documentation despite the large physical scale differences in aerial land survey compared to cultural heritage object documentation. According to James et al. (2017), SfM-MVS greatly facilitates UAV topographic surveys, but there is also a high variability in the published studies in geomorphology and a lack of information provided about the processing details to understand the sources of variability. The authors were able to build on a previous study showing the high variability of published results in geomorphological studies. While an equivalent study is not available for cultural heritage documentation, similar variation is likely present since SfM-MVS is also facilitating the wider documentation of heritage objects without the understanding of the underlying photogrammetric processes. The user-friendly SfM-MVS software makes the technique more accessible. However, there is a lack

of understanding of the sources of error in the studies in addition to the software generally not providing the quality assessment capabilities required for rigorous photogrammetric analysis (James et al. 2017, p. 52).

James et al. stated that some issues are well-known to the photogrammetry community, but these have not necessarily been considered in SfM-MVS geoscience applications, for example camera model over-parameterisation (2017, p. 54). The study aimed to address underlying photogrammetric processes that are important for understanding and improving the survey quality and consistency. The authors addressed photogrammetric processes and best practices that have not carried over to geomorphology applications and publications in order to improve repeatability and accuracy and minimise error. They suggested that processing details need to be included with published results as a means of reducing processing errors and promoting confidence in SfM-based surveys in geomorphology. While James et al. (2017) was speaking to the field of geomorphology, this carries over to cultural heritage. The knowledge, experience, and literature within traditional photogrammetry is disconnected from the heritage field, so there is a gap associated with the accuracy and reliability of image-based 3D reconstruction.

2.5. Depth of field (DOF) and sharpness

3D reconstruction processes assume that an object is "acceptably" sharp throughout the input image set, but limited depth of field (DOF) is an issue with close-up 2D and 3D imaging of three-dimensional objects especially smaller objects. The range of acceptable sharpness both in front of and behind the point of focus, or DOF, can be quantified and calculated for 2D imaging. While the DOF is understood for 2D imaging, an "acceptable" sharpness has not yet been quantified for image-based 3D reconstruction in the photogrammetric and computer vision communities (Verhoeven, 2018).

Sharpness can be considered subjectively as the perceptual impression on an observer and objectively through measurements made in the image (Allen and Triantaphillidou, 2011, p. 9). Objectively sharpness is the ability of a system to record edges, or transitions, and is dependent on the contrast reproduction of an imaging system, specifically high frequencies (Allen and Triantaphillidou, 2011, p. 443).

There is an acceptance of some image degradation that is permissible allowing for objects to not be sharply in focus (Allen and Triantaphillidou, 2011, p. 111). DOF is essentially based on an arbitrary specification, the perception of blurriness and what is deemed "acceptable". With a practical imaging system, light does not focus into a point but into a spot that is

referred to as the circle of confusion, or blur circle (Luhmann et al., 2014, p. 116). The circle of confusion is considered the parameter of acceptable blurriness (Nasse, 2010, p. 7) or the criterion of permissible unsharpness (Allen and Triantaphillidou, 2011, pp. 110–111). An observer views an object point in an image as sharp if the diameter of the circle of confusion is under the resolution limit (Luhmann et al., 2014).

The diameter of the circle of confusion relates to the point spread function of the imaging system (the smallest element of an image) and can be regarded as the smallest element that a digital imaging system can resolve. A widely used circle of confusion diameter is 0.03 mm for the 35 mm image format (or full frame 24 x 36 mm). This relates to the smallest details that can be resolved by a human observer and are separated by a visual angle of one arc minute. If a 120 x 180 mm image is being viewed at a distance of 250 mm, then a visual angle of one arc minute represents 1/3000 of the diagonal of the image. A circle of confusion twice as large, or 1/1500 of the diagonal, provides "satisfying sharpness" and corresponds to the standard measure of 0.03 mm used for the 35 mm format (Nasse, 2010). Appendix 14.1 includes a table of references and selected values for the circle of confusion that differ from the routinely used measure of 0.03 mm. The values range from 1 pixel up to nearly 8 pixels. While the diameter of the circle of confusion does change the DOF and the measured range of acceptable sharp focus, changing the value of the diameter alters the acceptance criteria rather than physically changing image formation.

For 3D reconstruction correlations between image patches rather than viewer acceptance are required. The questions arose: what is an appropriate value to substitute for the for the circle of confusion in DOF tables and how accurate does the value need to be? How does this value change for different 3D reconstruction applications?

DOF can be calculated using similar triangles and the geometry of image formation illustrated in Figure 2-3 from Ray (2002, p. 218). The following equations for the far and near limit (S and $R)$ and depth of field (T) can be derived where u is the focused distance, f is the focal length, N is the relative aperture, and C is the diameter of the circle of confusion (Ray, 2002, p. 218).

Figure 2-3. Diagram of the geometry of image formation for DOF. Figure from Ray (2002, p. 218).

$$S = \frac{uf^2}{f^2 - NCu}$$

(2.2)

$$R = \frac{uf^2}{(f^2 + NCu)}$$

(2.3)

Depth of field (*T*) can be defined as $T = S - R$, so

$$T = \frac{2f^2u^2NC}{f^4 - N^2C^2u^2}$$

(2.4)

Based on the information presented with the parameters that define DOF and the equations to calculate the range of acceptable sharpness, it would be reasonable to consider a small aperture diameter which would provide a larger DOF. Reducing the diameter of the aperture increases the DOF and decreases some lens aberrations; however, it also increases the effect of diffraction which reduces the image quality. *Diffraction* relates to the wave nature of light and the 'bending' of light around the edge of an obstacle like an aperture, and it is dependent on the size of the aperture and the wavelength of light (Allen and Triantaphillidou, 2011, p. 32).

DOF, as the range of acceptable sharpness, can be measured as a function of sharpness. Sharpness is a spatial image attribute that ties into 2D image quality (Section 3.3.2). Image sharpness is influenced by contrast, noise, and tone reproduction, and sharpness and resolution are closely related. Sharpness and resolution can be measured using the Modulation Transfer Function (MTF) and Spatial Frequency Response (SFR). The MTF is

used to describe the performance of an imaging system and is the modulus of the optical transfer function or the 2D Fourier transform of the imaging system's point spread function. The MTF is "a function describing the reproduction of micro-image contrast at all available spatial frequencies and falls to some threshold value, which is considered as the limiting system resolution" (Allen and Triantaphillidou, 2011, p. 347).

ISO 15529:2010 specifies MTFs and outlines techniques for its measurement through two classifications: wave recording and edge methods. Wave recording methods rely on sine-wave or square-wave targets with a range of spatial frequencies. The edge method is conceptually one of the simplest approaches requiring an image of an edge across which image intensity gradients are calculated. The derivative of the edge spread function is then computed to provide the line spread function. MTF is calculated from the Fourier transform of the line spread function. This method is not easily used with digital systems as the orientation of the edge to the sensor array structure will produce variations in the resulting measures because of aliasing and phase effects limiting the calculation of MTFs up to the Nyquist frequency, or Nyquist limit (Allen and Triantaphillidou, 2011, p. 447). The Nyquist frequency is the highest frequency that can be reliably reproduced without aliasing, and it is the half-sampling frequency or 0.5 cycles/pixel. Spatial frequencies below the Nyquist frequency will be faithfully reproduced, but frequencies above the Nyquist frequency will be aliased (Burns and Williams, 2008; Allen and Triantaphillidou, 2011).

The slanted edge technique was developed to overcome edge alignment limitations to provide a Spatial Frequency Response (SFR). SFR measures the contrast loss as a function of spatial frequency and provides information about an imaging system's ability to maintain contrast as image details get smaller. ISO 12233:2017 provides a technique for calculating SFR in which the region of the slanted edge is first located and then the edge spread function and its derivative, the line spread function, is calculated. The SFR is then derived from the Fourier transform of the line spread function (ISO 12233:2017). Whilst SFR is readily calculated with available software tools, it does not take into account the spatial frequency content of the edge target and does not separate the system components as is possible with MTF (Allen and Triantaphillidou, 2011, p. 447). SFR results are reported by plotting the modulation level versus spatial frequency. The SFR at the 10% modulation provides a measure for the limiting resolution of the system, and the SFR at the 50% modulation provides a threshold as a sharpness indicator (ISO 19264-1:2017). The limiting resolution is the smallest distance between image points that can still be resolved (Burns and Williams, 2008). With both the 10% SFR and 50% SFR, the aim is to achieve the highest frequency but to not exceed the Nyquist limit.

The sampling efficiency provides a convenient single value measure for comparing multiple SFR results (Burns and Williams, 2008; ISO 19264-1:2017). The sampling efficiency measure is the ratio of the limiting resolution to the sampling resolution and feature. The limiting resolution is the frequency that the SFR falls to 10% which can be calculated from the SFR of a slanted edge.

The DICE target is used in this thesis to provide an accessible means of measuring sharpness through SFR analysis and calculating sampling efficiency. The target and associated software are described in Section 1.3.3 along with its use in collections photography. The 2D image quality assessment using the DICE target and sharpness measures provide a method in this thesis of relating 2D DOF to 3D reconstruction quality working towards defining "acceptable" sharpness to image-based 3D reconstruction.

2.5.1. DOF and image-based 3D reconstruction

DOF is problematic when recording small objects and fine details. When documenting small objects, the focusing distance may be decreased and/or the focal length increased in order to maximise magnification and fill the frame with the view of the small object, both of these parameters decreasing the DOF. Macro lenses offer an optimised lens option for close-up photography allowing for a smaller focusing distance, but do not alter the limited DOF. While decreasing the lens aperture increases the DOF, it also reduces image quality as the aperture becomes small and the effect of diffraction increases. While this is the case for 2D imaging of small objects, image-based 3D reconstruction relies on the image quality of the 2D input images. A limited DOF makes image matching more difficult, it can increases the noise level and the topological errors, and also result in some of the final texture being out of focus (Nicolae et al., 2014).

Verhoeven (2018) discussed the challenges related to DOF and sharpness for image-based 3D reconstruction noting that it is assumed that an object's surface can be reconstructed if the physical object falls within the DOF and therefore the DOF needs to be "scene-encompassing". If the object falls outside of the DOF resulting in out of focus areas, then the reconstruction will likely be partial and inaccurate. Verhoeven pointed out that DOF is a perceptual quantity (the idea of "acceptable" sharpness) without a direct relation with image-based 3D reconstruction, and there is not an accepted value for the circle of confusion threshold to calculate a DOF for 3D imaging applications. The fields of photogrammetry and computer vision have not yet quantified "acceptable" sharpness for image-based 3D reconstruction. The challenges of limited DOF for 3D reconstruction are further discussed in studies recording small heritage objects with conclusion that the biggest limitations relate to

the loss of spatial resolution and blurring with small aperture diameters and the effect of diffraction (Gallo et al., 2012; Menna et al., 2012; Percoco et al., 2017; Sapirstein, 2018).

2.5.2. Improving DOF and increasing sharpness

As solutions for DOF challenges, there has been research on extending DOF and increasing overall sharpness with efforts focusing on accessible commercial software, hardware solutions, and processing algorithms that will be reviewed in the following paragraphs.

Commercial software like Zerene Stacker (Zerene Systems LLC, n.d.; Gallo et al., 2014) and Helicon Soft (Helicon Soft Ltd, n.d.; Gallo et al., 2012) include options for acquiring and processing image stacks for focus stacking solutions. Focus stacking involves the acquisition of a set of images with varying focal positions and the processing of the image set to produce an image with an increased DOF, or extended DOF. Focusing stacking has been used for the 3D reconstruction of small archaeological objects (Gallo et al., 2014; Clini et al., 2016) and samples of encrustation from a marble statue (Gallo et al., 2014). However, the composite image is problematic for self-calibration and the determination of the interior and exterior orientation for image-based 3D reconstruction, which was acknowledged as a limitation (Gallo et al., 2014; Clini et al., 2016). Any change in the camera geometry impacts the interior orientation and needs to be taken into account (Luhmann et al., 2014, p. 150). The increase in the number of images and increased acquisition and processing times for this approach have also been cited as reasons that focus stacking was not selected (Gallo et al., 2014; Marziali and Dionisio, 2017; Verhoeven and Missinne, 2017; Sapirstein, 2018).

Hardware solutions are available for extending DOF from focus stacking rails to new digital camera modes and 3D digital microscopes. Focus stacking rails provide an automated solution for moving the camera to different focal positions (Nobel, 2017). Camera manufacturers are including modes to aid in acquiring image sets with different focal positions, live composite, and focus stacking modes in the Olympus OM-D E-M1 Mark II (Olympus America Inc., 2016), post focus simulation and focus stacking capabilities (Panasonic, n.d.), and focus shift capabilities in the Nikon D850 (Nikon, 2017). Three-dimensional digital microscopes are available that provide focus stacking capabilities including Leica offering a multifocus mode (Bauer and Rottermann, 2010) and Keyence and Hirox offering 3D digital microscopes with capabilities for extended DOF for 2D and 3D imaging.

Light field imaging and plenoptic cameras offer an option for extended DOF in a single exposure and even the possibility of 3D reconstruction. Levoy (2006) provided a survey of

the theory and practice of light field imaging. Light fields can be recorded by moving a single camera through a scene, creating an array of cameras, or by creating an array of lenses. There are only a few examples of light field imaging and heritage documentation (Ng et al., 2012; Berrier et al., 2015). The limited number of examples suggest challenges with the complexity and nature of the equipment, processing, and amount of data. The technique requires a specific camera and while these are available commercially, they are not yet widely available or accessible to heritage users.

The development of new processing algorithms has also been an active area of research for extending DOF. Computer vision researchers have been investigating the involved challenge of depth estimation including the development and refinement of Shape From Focus (SFF). The technique, first introduced by Nayar and Nakagawa (1994), provided a solution for shape recovery that used focus analysis to compute depth maps. Local focus variations can be used as depth cues while focus measure operators can compute the focus level for each pixel in the image. The method derives shape from a sequence of images of the same scene with variation in the focus. It is used widely in computer vision as a method for passive depth recovery (Pertuz et al., 2013). Generally, SFF has been used for a single view, micro imaging; however, Pertuz et al. (2013) and Billiot et al., (2013) attempted to extend its use from the well-controlled scenarios of microscopy to complex, real scenes using conventional cameras.

2.5.3. Methods for masking

Pre-processing is used to optimise images and reduce processing times for the computationally intensive dense image matching step in 3D reconstruction (Barazzetti et al., 2010; Remondino et al., 2016). Pre-processing can be used to enhance image features that are important for the 3D reconstruction by improving local image feature contrast using a Wallis filter (Barazzetti et al., 2010; Gaiani et al., 2016; Remondino et al., 2016) or reducing noise with an adaptive smoothing filter (Remondino and El-Hakim, 2006; Barazzetti et al., 2010; Gaiani et al., 2016).

Another widely explored pre-process is to mask out the background or non-essential features (Barazzetti et al., 2010; Gallo et al., 2012, 2014; Koutsoudis et al., 2013; Guidi et al., 2014; Nicolae et al., 2014; Troisi et al., 2015; Abate et al., 2016; *Photogrammetric Applications for Cultural Heritage: Guidance for Good Practice*, 2017; Marziali and Dionisio, 2017; Sapirstein and Murray, 2017). Masking can improve the quality of the image alignment (Abate et al., 2016) and decrease the reconstruction processing time by reducing the quantity of input image data and removing unwanted 3D content outside of the volume of the object

of interest (Gallo et al., 2012; Koutsoudis et al., 2013; Troisi et al., 2015). Gallo et al. (2014) reported that using background masks could reduce the computational time by up to 75%. In some cases, masking can be a time-consuming manual process (Koutsoudis et al., 2013; Abate et al., 2016) or a more automated process. Using a homogeneous background like a black cloth can facilitate the background masking (Nicolae et al., 2014; Troisi et al., 2015; Porter et al., 2016). Most studies have masked out the background and non-essential features; very few have discussed masking related to sharpness and DOF. The Historic England *Guidance for Good Practice* recommends masking areas that are out of focus indicating that some photogrammetric processing software provides this option although specific software is not mentioned (*Photogrammetric Applications for Cultural Heritage: Guidance for Good Practice*, 2017).

Verhoeven (2018) provided the most extensive study on looking at sharpness and DOF for masking image sets for image-based 3D reconstruction. Verhoeven (2018) investigated defocus estimating algorithms for automatic masking based on sharpness to speed up the reconstruction process and produced a Matlab toolbox that included fifteen working methods for mapping defocus blur and reported on three edge-based methods assessing accuracy, running time, and robustness. Verhoeven recognised that there was a potential for some of the edge-based methods for masking out homogenous areas and those without edges, which might include skies or studio backgrounds, and concluded that additional improvements were required for future implementation.

PhotoScan, the 3D reconstruction software used extensively in this thesis, includes a feature that estimates the image quality for each input image based on the sharpness of the most focused part of the image ('Agisoft PhotoScan User Manual', 2018, p. 19). Even though PhotoScan has this feature, the results are not used by the algorithms but are provided to inform the user whether to disable or remove images with a low quality value from the 3D reconstruction processing. Posts in the PhotoScan community forum have discussed a feature to mask images based on sharpness or lack of sharpness, but this is not a current feature of the software.

2.6. Chapter summary

3D imaging is being widely used to document heritage objects. While accurate and precise instruments exist for 3D imaging, these specialised devices can be out of reach for many heritage institutions, professionals, and collections in terms of cost and complexity. Accessible devices and workflows are being adopted by non-expert heritage users for more routine and wider use of 3D imaging. Consumer digital cameras paired with computational

approaches, specifically SfM-MVS, provide automated and flexible image-based 3D reconstruction workflows. A range of low-cost and open source software options are available, increased automation of software does not require an expert user, and the equipment required is flexible and minimal making image-based 3D reconstruction popular and accessible. The wide use of image-based 3D reconstruction also introduces a wide range of quality. Accessibility is a critical advantage of SfM-MVS methods, but the features that make the method accessible also can impact the accuracy and reliability.

Section 2.2 focused on differentiating photogrammetry, computer vision, and SfM, as *photogrammetry* is often used as a general term for image-based 3D reconstruction. While it is necessary to clearly define terminology in an interdisciplinary field, this discussion is also important to provide insight into the investigation on accuracy and reliability of the techniques. Accuracy and reliability are key topics for the research, and this chapter focused on available standards and best practices (Section 2.3), the assessment of metric quality of 3D data (Section 2.4), and methods of optimising image-based 3D reconstruction investigating DOF and sharpness (Section 2.5).

Section 2.3 referenced best practices for specific objects, materials, sites, and projects, in addition to the more general best practices. While there still are not standards for image-based 3D reconstruction of cultural heritage objects, there are a variety of best practices available that can improve the performance and quality of image-based 3D reconstruction. Section 2.3.2 presented CHI's comprehensive workflow that is situated between conservation documentation and scientific imaging. This is an example of making scientific techniques more available for conservation documentation and non-expert users, which is an area of interest for this research. The best practices and workflow provided by CHI focus on an audience of non-expert users with an emphasis on the scientific accuracy and reliability of the 3D reconstruction by using rule-based data acquisition, good geometry and scale, and the *error minimisation workflow*. Section 2.3.4 specifically discussed additional methods for improved image-based 3D reconstruction including targets, image configuration, and camera models and parameter selection that will be further discussed with the iterations, results, and discussion in Chapter 4. Components of the INDRo and the Panel test target (Section 2.3.3.2) have been incorporated into the experimental setup and assessment for the research presented in this thesis.

There is a lack of standard quality analysis tools for evaluating the quality of 3D reconstructions and accuracy assessment is an identified challenge for image-based 3D reconstruction. Section 2.4 reviewed the metric quality assessment of 3D data identifying three main methods of accuracy assessment and providing advantages and limitations for the

methods: (1) comparing results with higher accuracy techniques mostly range-based; (2) assessing reconstruction of known geometric shapes; and (3) comparing results with a model averaged from multiple acquisitions. These methods will inform the accuracy assessment of the 3D reconstructions for the experimental chapters. Another component of the challenges of accuracy assessment could be attributed to a gap between knowledge, experience, and literature within traditional photogrammetry and what is available to cultural heritage users, similar to what was presented by James et al. (2017) for the field of geomorphology.

The final section of the review focused on DOF and sharpness for improving output of image-based 3D reconstruction (Section 2.5). The 3D reconstruction processes assume that an object is "acceptably" sharp throughout the input image set, but limited DOF is an issue with close-up 2D and 3D imaging of three-dimensional objects especially smaller objects. DOF is well understood in the context of 2D imaging and it is considered with the acquisition of image-based 3D reconstruction, but "acceptable" sharpness has not yet been quantified for image-based 3D reconstruction in the photogrammetric and computer vision communities. Section 2.5.2 investigated options for improving DOF including research on extending DOF and increasing overall sharpness through commercial software, hardware solutions, and processing algorithms. One option for optimising image-based 3D reconstruction is image pre-processing and masking based on DOF and sharpness (Section 2.5.3). Image pre-processing can optimise images and increase the processing performance for 3D reconstruction, and the examples presented focused mostly on background masking (Section 2.5.3). Similarly, image pre-processing using sharpness-based masking might be expected to improve image-based 3D reconstruction.

3. Spectral imaging of cultural heritage objects

This research investigated spectral imaging as a method of optimising image-based 3D reconstruction using consumer imaging systems. Spectral imaging techniques are used as standard, non-invasive investigation tools for conservation documentation and also as scientific imaging methods for material identification and measurement (Section 3.1). While accurate and precise instrumentation of spectral imaging exists, the cost and complexity can keep it out of reach for many heritage institutions, professionals, and collections. Non-expert heritage users are using modified digital cameras as accessible devices for spectral imaging, and these devices offer inexpensive, easy to use, portable, and high-resolution options for conservation documentation (Section 3.1.5). Available best practices and standards will be reviewed to inform the setup, acquisition, and processing of spectral image data (Section 3.2). As there are limited references assessing the performance of modified cameras and the influence of the modification on the camera, options for camera characterisation will be reviewed focusing on 2D image quality assessment and measuring spectral response (Section 3.3).

3.1. Spectral imaging techniques and instrumentation

Spectral imaging records the interaction of radiation with materials and can include broadband and multiband, multispectral and hyperspectral data within the ultraviolet (UV), visible, and infrared (IR) regions of the electromagnetic spectrum. Spectral imaging techniques can detect changes in composition, show past conservation treatments, visualise faded or obscured details, provide manufacture information, reveal underdrawings, and characterise, differentiate, and identify materials.

This section will focus on spectral imaging techniques and instrumentation that are used for conservation documentation and scientific imaging. By providing the context of the techniques and devices being used for conservation documentation and scientific imaging, we can see where accessible devices and workflows for spectral imaging fit into museum imaging.

3.1.1. Ultraviolet radiation and photo-induced luminescence techniques

UV-induced visible luminescence (UVL), also referred to as UV-induced visible fluorescence, is an established conservation investigation and documentation tool. A variety of materials luminesce when exposed to UV radiation. This property can be used as a tool for the examination and documentation of cultural heritage objects to characterise and

differentiate materials, to establish the condition of an object, and to reveal past treatments. This can aid in characterising pigments and resins, uranium glass, tidelines, mould, optical brighteners, and some minerals (McGlinchey Sexton et al., 2014). The forthcoming chapter by Webb (2020) further discusses the application of UVL for conservation documentation and the developments and limitations of the technique including the need for standardisation and targets. The technique does not require a specialised or modified camera and the availability of UV lamps make it an accessible technique.

Reflected UV (RUV) records the varying reflection, transmission, and absorption of UV radiation by materials present in an object. RUV can be used for characterising and differentiating materials, establishing the condition, and revealing past treatments. RUV requires a camera sensitive to UV radiation, either a specialised camera or a modified camera, which has limited the conservation applications (Warda et al., 2011).

In addition to UVL being included in this section as a standard spectral imaging technique for conservation documentation and as part of the discussion on applications and instrumentation, there is the consideration of UV radiation being used to improve image-based 3D reconstruction. The imaging results for UVL tend to be dark depending on the materials that luminesce in relation to the overall object and the strength of the luminescence. Generally, UVL will not provide improved local detail and contrast due to the generally dark image results and would not be expected to improve image-based 3D reconstruction. However, RUV has the potential of an enhanced view of an object or detail depending on the materials, and UV radiation could be considered as part of the wavelength selection process (Chapter 6).

UVL is a photo-induced luminescence technique, and other such techniques that have been used for conservation documentation are visible-induced IR luminescence (VIL) (Verri, 2008, 2009b; Dyer and Sotiropoulou, 2017) and visible-induced visible luminescence (VIVL) (Dyer and Sotiropoulou, 2017; Dyer et al., 2018). These techniques aid in the spatial characterisation of luminescent materials such as Egyptian blue and rose madder lake. VIL requires the use of a camera with sensitivity to IR radiation, and VIL and VIVL require the use of filters to block and pass specific wavelengths. These two techniques are briefly mentioned as spectral imaging techniques requiring specific camera sensitivity and filtration, and modified cameras (Section 3.1.5) have been used for these techniques.

3.1.2. Reflected infrared and infrared reflectography imaging

IR radiation has been used for cultural heritage documentation since the 1930s when film sensitive to near infrared (NIR) radiation (up to ~ 900 nm) became available (Warda et al., 2011). IR imaging records the varying reflection, transmission, and absorption of IR radiation by the materials present in an object. Following the terminology outlined in Warda et al. (2011), *reflected IR* refers to imaging that uses wavelengths in the NIR region (700-1000 nm) and corresponds with the sensitivity of IR films and digital cameras with silicon detectors, and *IR reflectography (IRR)* refers to imaging that uses wavelengths in the short-wave infrared (SWIR) region (1000-2500 nm) and requires specialised sensors (Fischer and Kakoulli, 2007; Warda et al., 2011).

Reflected IR imaging and IRR are established investigative tools for painting and paper conservation for detection of features beyond visible light. Early reflected IR imaging was used to investigate the artist's technique to reveal guide lines (Keck, 1941) and to provide clearer documentation of a painting obscured by aging varnish (Rawlins, 1942). In the 1960s, Van Asperen de Boer (1969) extended the sensitivity of reflected IR imaging from NIR to SWIR by introducing the use of the Vidicon system as a tool for detecting underdrawings in paintings. IR imaging has continued to develop with the advancement of digital imaging and the development of various sensors with IR sensitivity in the NIR and SWIR (Cucci et al., 2019). These sensors include standard silicon charged-couple device (CCD) and complementary metal-oxide semiconductor (CMOS) sensors and more specialized sensors made from platinum silicide (PtSi), indium gallium arsenide (InGaAs), indium antimonide (InSb), and mercury cadmium telluride (HgCdTe or MCT), which have greatly improved the IR imaging techniques and documentation for cultural heritage (Fischer and Kakoulli, 2007).

A couple of examples of applications and these sensors include Arslanoglu et al. (2013) using an InGaAs camera for IRR to complement X-ray radiography of paintings in the investigation of working methods and materials, and Gavrilov et al. (2013) also using an InGaAs detector for IRR to compare NIR, SWIR, and thermographic imaging for paintings inspection to look at working methods, changes in composition, and structural defects. An IRR system, the SIRIS (scanning infrared imaging system) camera was developed by the National Gallery in London, UK (Saunders et al. 2006), and is now commercially available as the OSIRIS and APOLLO camera models from Opus Instruments ('OSIRIS Camera', n.d.).

3.1.3. Multispectral and hyperspectral imaging

The continued development and use of IR imaging and related instrumentation ties into imaging spectroscopy: multispectral imaging (MSI) and hyperspectral imaging (HSI). Imaging spectroscopy, the integration of spectroscopy and digital imaging, was originally developed for remote sensing, but it has presented advancements in the field for non-invasive analytical tools for cultural heritage documentation.

Initially, MSI was used for qualitative comparisons of different bands for characterising and identifying materials, degradation, past conservation treatments, underdrawings, and improving colour accuracy and measurement (Liang, 2012, p. 309). As the techniques were developed, the number of bands increased, the acquisition became faster, and the capabilities expanded to pigment identification through the extraction of reflectance information (Liang, 2012, p. 309). Imaging spectroscopy provides a better understanding of the materials used by the artists and the distribution of the materials, which can inform conservation treatment and also provide information about the artists' process (Delaney et al., 2010). Reviews for MSI and HSI and cultural heritage applications have included Fischer and Kakoulli (2007) and Liang (2012).

As early as the 1980s, researchers became interested in MSI of paintings due to the higher colour accuracy and the possibility to estimate spectral reflectance (Saunders et al., 2006, p. 521). European projects in the 1990s and early 2000s contributed to the hardware and software development of spectral imaging technology for cultural heritage documentation (George et al., 2017, p. 143) including the Visual Arts System for Archiving and Retrieval of Images (VASARI) project (Saunders and Cupitt, 1993; Martinez et al., 2002), the Methodology for Art Reproduction in Colour (MARC) project (Martinez et al., 2002), and CRISATEL (Ribés et al., 2005).

A couple of examples of more recent MSI setups include the system at the Library of Congress (Washington, DC, US) and the UCL Department of Digital Humanities (London, UK). A prototype EurekaVision system was assembled for the spectral imaging of the 1507 Waldseemüller World Map and was further developed into the system being used by the Preservation Research and Testing Division of the Library of Congress in Washington, DC (Christens-Barry et al., 2009). The spectral imaging system based on a 39-MP monochrome camera and LED-based narrowband illumination includes reflected, transmitted, and raking illumination and the use of 12 spectral bands for preservation research and scholarly studies. Components of the system, acquisition, and processing are based on the multispectral imaging and analysis of the Archimedes Palimpsest (Knox,

2008). The UCL Digital Humanities setup (RB Toth Associates) is based on a 60-MP achromatic camera and 12-band LED lighting panels (370 to 940 nm) (Equipoise Imaging LLC, USA) (Gibson et al., 2018).

In the 2000s, technological advances made HSI possible, and the "Nello Carrara" Institute of Applied Physics of the Italian National Research Council (IFAC-CNR) in Florence, Italy (Casini et al., 2005) and the National Gallery of Art in Washington, DC (Delaney et al., 2010) pioneered the use of HSI for documenting paintings, specifically using custom-built pushbroom imaging spectroscopy systems (George et al., 2017, p. 143). In both cases, the devices being used by IFAC-CNR and the National Gallery of Art have been developed and customised for the uses in their labs enabling the development and application of HSI for recording cultural heritage (Cucci et al., 2016).

Specialised research labs are developing spectral imaging instrumentation for cultural heritage applications. The Imaging & Sensing for Archaeology, Art History and Conservation (ISAAC) research group at Nottingham Trent University (Nottingham, UK) developed the Portable Remote Imaging System for Multispectral Scanning (PRISMS) designed for in situ high-resolution spectral and 3D documentation system for wall paintings to identify pigments and reveal faded writing and details of drawings (Liang et al., 2014). The system included modular components for long and close range distances in addition to a filter wheel with nine interference filters (400-880 nm) for VIS-NIR acquisition and an Acousto-Optic Tunable Filters (AOTF) and InGaAs detector (900-1700 nm) for SWIR acquisition. Systems like PRISMS are experimental instrumentation that push the field of scientific imaging and the recording of heritage objects, but these devices are not available or accessible to support routine recording in a conservation lab.

HSI has been used for the identification and mapping of material (Mounier and Daniel, 2015; Cucci et al., 2016; Delaney et al., 2016) including watercolour pigments (Mulholland et al., 2017) and the identification and mapping of paint binders in paintings and illuminated manuscripts (Ricciardi et al., 2012; Dooley et al., 2013). The technique has also been used for identifying non-original material in the case of two Pablo Picasso paintings (Delaney et al., 2016). HSI in the NIR and SWIR range can improve the visualisation of underdrawings and subsurface paint layers (Cucci et al., 2016; Delaney et al., 2016). Analytical and quantitative capabilities of the techniques are continuing to be developed and refined including the use of HSI for the non-invasive identification of red lake pigments (Vitorino et al., 2015) and the potential of NIR HSI for quantitative chemical mapping of the composition of Islamic paper (Mahgoub et al., 2017).

This section aimed to provide some of the history and applications of spectral imaging for cultural heritage documentation touching on the instrumentation being used. The techniques were broadband and narrow band techniques from UV through visible and into the NIR and SWIR. These techniques are being used for conservation documentation and scientific imaging with a variety of instrumentation being used from low cost to expensive and from accessible to specialised and custom-built. To provide insight and a summary of the state of the art in spectral imaging the following section will provide a closer look at a recent European initiative.

3.1.4. Colour & Space in Cultural Heritage (COSCH): Instrumentation and users

Color & Space in Cultural Heritage (COSCH) and the Working Group 1 (Section 1.1.3) worked towards standardisation and best practices of spectral imaging. The increased number of available spectral imaging systems and the diverse experience and backgrounds of the user community emphasised the importance of the reproducibility and comparability of the resulting data. The working group initiated a Round Robin Test (RRT) of imaging five objects using different imaging and imaging spectroscopy systems as a coordinated research effort to better understand the instrumentation, elements of data acquisition, and the effects of the instruments and methodology on the accuracy and reliability of the data.

The COSCH RRT initiative provides insight into the state of the art in imaging spectroscopy for cultural heritage documentation and analysis in Europe by reflecting on the participating institutions, the instrumentation used, and the data received.[5] The initiative included datasets received from eleven countries and sixteen institutions. The participating institutions were predominately universities (56%) and national research labs (25%) with one heritage institution and two commercial companies producing HSI systems. The datasets received included both MSI and HSI results covering a range of visible (400-700 nm), NIR (700-1000 nm), and SWIR (1000-2500 nm). The received datasets include 31% MSI and 69% HSI data with 42% in the visible and NIR (VNIR) range and 27% in the SWIR.

The RRT did not include every institution using MSI and/or HSI for cultural heritage documentation at the time of the initiative, but it is interesting to note the institutions and devices represented. The study showed a combination of commercial devices and experimental instruments, and most of the spectral imaging was being conducted within

---

[5] The information provided in this section is a summary from a COSCH Short Term Scientific Mission (STSM) completed by the author in March 2016 at IFAC-CNR. The STSM focused on summarising the data received, explored the variations observed with the resulting datasets, and presented suggestions for future research to conclude the coordinated research initiative.

universities and research labs. This may reflect on the nature of the instrumentation and the specialisation and expertise required to support the equipment and research. With the exception of the recently introduced mobile hyperspectral camera assessed in a feasibility study by Cucci et al. (2017), most hyperspectral systems have included specialised and expensive equipment. To further support this, George et al. (2017) presented results from the RRT using a subset of four spectral imaging systems (two MSI and two HSI). The systems are categorised by complexity, portability, and cost. The two MSI systems are categorised as medium complexity, high portability, and medium cost (€30,000-€50,000), while the two HSI systems are categorised as high complexity, low or no portability, and expensive (more than €80,000). The medium and high costs put these instruments out of reach of some heritage professionals and institutions in addition to the complexity of the instrumentation. While the cost may be coming down for some of the equipment, there are also challenges related to calibration, processing, analysis, and interpretation with one example being the availability of software for processing and analysis of MSI and HSI data. The COSCH study showed that most people were using ENVI and Matlab for processing spectral imaging; both are commercial software packages that have a high cost, especially for institutions that are not universities receiving educational discounts.

The COSCH RRT participants were from mostly universities and national research labs using commercial devices and experimental instruments that are considered high complexity and expensive. This provides evidence similar to 3D imaging that accurate and precise instrumentation for spectral imaging exists, but the cost and complexity can keep it out of reach for many heritage institutions, professionals, and collections. In contrast, the next section will investigate the use of modified cameras by non-expert heritage users as accessible devices for spectral imaging.

3.1.5.   Modified cameras

Heritage professionals are already using consumer digital cameras for 2D and 3D documentation. Silicon sensors, at the heart of consumer digital cameras, are inherently sensitive to near UV and NIR radiation but are optimised for visible light, colour photography by incorporating an IR blocking filter and a colour filter array (CFA) on the sensor. The top layers of the sensor include microlenses, the CFA, and photodiodes. Microlenses above each pixel focus the light to increase effective sensitivity, and the CFA introduces an array of red, green, and blue filters such that some pixels become more sensitive to specific wavebands, and this allows the reconstruction of a full colour image through a process called demosaicing. The IR filter blocks IR radiation which would, in normal colour photography, lead to reduced contrast, and impact tone and colour balance of

images. By modifying consumer digital cameras, these devices can provide capabilities for spectral imaging while retaining the same user-friendly properties and interfaces to a wide range of photographic accessories and software.

The main types of camera modifications available are single wavelength, full-spectrum, and monochrome conversions (Davies, 2018):

- Single wavelength conversion: This conversion includes the removal of the IR blocking filter and replacing it with a bandpass filter that reduces the sensitivity to a single range of wavelengths in the UV, visible or IR regions of the sensor's sensitivity. The CFA is still in place and the transmission of the red, green, and blue filters impact the sensitivity of the camera.

- Full-spectrum conversion: This conversion includes the removal of the IR blocking filter and then filtering the light reaching the camera sensor through mounting filters on the lens or filtering the light source. By placing an IR blocking filter on the lens, the camera can also take visible light images, so this conversion provides a highly versatile modification and a wide range of filters can be used. Similarly, to the single wavelength conversion, the CFA is still in place and the transmission of filters impacts the overall sensitivity of the camera.

- Monochrome conversion: This conversion includes the removal of about 5 µm of the sensor surface layers, including the microlenses and CFA in addition to the IR blocking filter ('MaxMax Cameras' and D. Llewellyn, personal communication, March 11, 2016). Similar to the full-spectrum conversion, the light reaching the camera sensor can be controlled by mounting filters on the lens or filtering the light source.

The two primary US-based companies that offer camera modifications are MaxMax LDP LLC (https://maxmax.com/) and LifePixel (https://www.lifepixel.com/). MaxMax offers UV-VIS-IR (i.e., full-spectrum), IR-only, and monochrome conversions. For the monochrome conversion MaxMax uses decommissioned semiconductor fabrication equipment to remove 5 µm from the surface including the microlenses and CFA[6]. LifePixel does not offer the monochrome conversion but does include IR and full-spectrum conversions both as a service for a camera previously purchased or as the purchase of a new camera with the modification. Examples of prices are included in Table 3-1 with current Canon models that would be comparable to the Canon 5D Mark II that was used in the research presented in this thesis. LifePixel's full-spectrum and IR conversions are $275-350

---

[6] Information included on MaxMax's website (https://maxmax.com/faq/camera-tech/monochrome-manufacturing) accessed 14 November 2019.

for many of the DSLR models if the service is purchased as opposed to the purchase of a converted camera.[6]

Table 3-1. Available services for camera modifications.

	MaxMax		LifePixel[7]
	Full-Spectrum and IR Conversions[8]	Monochrome Conversion[9]	Full-Spectrum and IR Conversions
Canon 5DS	$4,100	$6,175	$3,849
Canon 5D Mark IV	$3,312	$5,810	$2,849
Canon 6D	$1,975	$4,380	$1,079

Cameras can be modified with DIY ("Do It Yourself") methods, but this runs a high risk for breaking the camera and causing injury. LifePixel includes tutorials for specific camera models on IR DIY conversions (https://www.lifepixel.com/tutorials/infrared-diy-tutorials). However, they do warn against doing the conversion yourself and advertise that the tutorials are designed for informational/educational purposes only. There are also videos online for monochrome conversions including one where a wooden tool is used to physically scratch off the CFA (https://youtu.be/N1Lgju9L23c). The description of the video includes the statement "there's is a very high risk of damaging the sensor but in this case it worked fine".

Modified cameras are being used for UV and IR photography in several fields including zoology, medicine, dermatology, forensics, botany, entomology, agriculture, forest management, and mapping of water bodies (Verhoeven et al., 2009; Davies, 2018). In the medical field, a study investigated the use of NIR transillumination and the use of a modified camera for the diagnosis of *Maxillary Sinusitis* (Coughlan et al., 2016). In the field of forestry and agriculture, modified cameras are being used for colour IR imaging for detection of pest infestation in forests (Lehmann et al., 2015). In the field of forensics, a study investigated NIR photography for on-site detection of bloodstains on dark textiles (Sterzik and Bohnert, 2016).

Modified cameras are also being used for cultural heritage and archaeology applications. The introduction of modified cameras provided an inexpensive, easy to use, portable, and high-resolution option for spectral imaging of cultural heritage objects (Falco, 2009). Guides

---

[7] Prices accessed from https://www.lifepixel.com/shop on 14 November 2019.
[8] Prices accessed from https://maxmax.com/shopper/category/9256-canon-uv-vis-ir and https://maxmax.com/shopper/category/9249-canon-ir-only on 14 November 2019.
[9] Prices accessed from https://maxmax.com/shopper/category/9274-canonmonochrome on 14 November 2019.

for conservation documentation included modified cameras for reflected UV and NIR imaging of cultural heritage objects with primarily examples of paintings and paper objects (Warda et al., 2011; Dyer et al., 2013). Falco (2009) tested a modified camera for reflected IR imaging with examples of underdrawings revealed in paintings and distinguishing materials in a suit of armour. Verhoeven (2008) provided examples of the use of an IR modified camera for aerial archaeological imaging, ceramic sherds, and obscured writing, and Verhoeven et al. (2009) presented its use as a flexible and low-cost approach for aerial archaeological reconnaissance. Webb (2017) used a modified camera for reflected IR imaging of three-dimensional objects investigating the potential integration of IR and 3D imaging for object documentation. In addition to reflected IR imaging, modified cameras are being used for VIL and VIVL imaging to detect Egyptian blue and madder lake (Verri, 2009b; Kakoulli et al., 2017; Dyer et al., 2018).

The published literature does not fully represent the use of modified cameras by heritage professionals, and only a few published examples are available as presented in the previous three paragraphs. Despite limited representation through publications, modified cameras are being used by heritage professionals. As a digital imaging specialist using a modified camera for conservation documentation, the author of this thesis has received at least seven professional inquiries from conservators and photographers interested in purchasing a modified camera or already working with one. In addition to personal communications, discussions on ImageMuse, an international discussion group on cultural heritage imaging (http://www.imagemuse.org/), have included the topic of modified cameras for IR imaging with responses including at least eight heritage professionals using modified cameras and in addition to recommendations for camera modifications.

3.1.6. Wavelength selection

In addition to the camera, spectral imaging requires a method of wavelength selection, which can be categorised into three methods: electronically tunable filters, tunable light sources, and optical filters (Simon Chane, 2013). Electronically tunable filters allow for wavelengths to be selected electronically. These filters include Liquid Crystal Tunable Filters (LCTFs) that transmit wavelengths in the visible and Acousto-Optic Tunable Filters (AOTFs) that extend the transmission into NIR and SWIR. LCTFs and AOTFs are used for MSI and HSI. Electronically tunable filters offer quicker acquisition compared to optical filters and the flexibility for the number of bands acquired. However, LCTFs have low transmission rates, and AOTFs have higher transmission rate but require collimated light (Simon Chane, 2013). Incorporating electronically tunable filters does increase the cost of the setup and the complexity of the setup and processing.

Tunable light sources allow for different wavelengths to illuminate the object. An example of a MSI setup with narrow-band LEDs is the Library of Congress (Washington, DC) setup for the documentation of books and paper documents (Christens-Barry et al., 2009). Tunable light sources are gaining popularity because of the rapid development and availability of LED technologies (Simon Chane, 2013). Using tunable lights can minimise the impact of light to the object as it is only being exposed to the wavelength being recorded instead of broadband spectrum of light (France et al., 2010). In addition, since LEDs are cooler than incandescent lighting, they reduce the risk of increasing the temperature and causing dimensional change of an object (Christens-Barry et al., 2009).

Another means of filtering wavelengths recorded by the camera are optical filters that can be mounted on the lens or in filter wheels to pass or block specific wavelengths from being recorded by the sensor. Optical filters can be used for multiband and MSI acquisition using a variety of bands, bandwidths, and regions of the electromagnetic spectrum. The number of bands and the spectral resolution can be restricted based on the number of slots in the filter wheel and the transmission of the filters. While there are advantages and limitations for the different methods of wavelength selection, optical filters provide an accessible solution for multiband and multispectral imaging for heritage professionals especially with the availability of modified cameras.

3.1.7. Discussion

In the early days of MSI and HSI, European projects and research labs were focusing on the development of MSI capabilities, which continued to develop and expand into HSI capabilities. While some research labs and universities have continued to increase the spectral and spatial resolution developing HSI systems and capabilities, components of MSI have become more available to non-expert users. In a sense, we are seeing a second wave of MSI, but with more accessible devices.

While the specialised and custom-built equipment is essential for the development of spectral imaging capabilities and the application for scientific imaging of cultural heritage, there is also an interest and demand for imaging systems that are more accessible in terms of cost and complexity for conservation documentation. Modified cameras with optical filters offer an option for more accessible imaging systems for multiband and multispectral imaging. This thesis will focus on the use of a modified camera with optical filters as an accessible option for acquiring spectral images as part of the investigation of wavelength and improved image-based 3D reconstruction.

MSI was cutting edge technology in scientific imaging of artworks 20-30 years ago, and early publications are important for informing components of the instrumentation and process including the characterisation of instrumentation. As an example, Casini et al. (1999) presented an early study into the use of imaging spectroscopy for the identification and mapping of pigments. Casini et al. characterised the imaging system in order to fully present the limitations of the device for its intended use. Despite being published twenty years ago, this is an important example of the use of characterisation to define the limitations of a device for scientific imaging applications. Camera characterisation will be revisited in Section 3.3 after first looking at best practices and standards in spectral imaging.

3.2. Best practices and standards

Best practices are important for ensuring or improving quality data acquisition and use for a specific field, and standards aim at influencing a community to improve outcome and are the result of science, technology, and experience (Beraldin et al., 2011) (Section 2.3). In order to improve and ensure the recording of quality data, this section will review the available best practices and standards for spectral imaging spanning the three categories of museum imaging (conservation documentation, collections photography, and scientific imaging). This will inform the setup, acquisition, and processing of spectral image data in addition to the best options for scales and references.

Guidelines and best practices for conservation documentation have been provided in three editions of *The AIC Guide to Digital Photography and Conservation Documentation* by Warda et al. (2008, 2011, 2017). This guide was written by conservators with the purpose of assisting conservators to adhere to the standards of the *Code of Ethics* that requires documentation of examination, scientific investigation, and treatment through the creation of permanent records and reports ('AIC Code of Ethics and Guidelines for Practice', 1994). Warda et al. (2011, p. 13) outlined the specifics of the digital photographic documentation workflow (photography setup, image capture, processing, management, and output) as a technical reference and manual for planning and implementation of conservation documentation.

In an effort to address the challenges of reproducibility and comparability of spectral data, Dyer et al. (2013) developed a user manual aimed at establishing a set of "widely-accessible methods and protocols" for MSI. The user guide was developed to optimise methodologies of image acquisition and processing for the documentation of art objects focusing on readily available equipment and user-friendly resources. The guide includes both theory about acquisition and post-processing and practical details for setup, equipment, and acquisition

('CHARISMA: Technical Imaging', 2017). With the aim of maximising the value of the information gained from these imaging techniques, the tools presented in the guide improve the consistency of the processing to aid in the comparison and interpretation (Dyer et al., 2013, p. Foreword).

Federal agencies in the United States initiated a collaborative effort in 2007 to assemble shared best practices and to develop common digitisation guidelines as the Federal Agencies Digital Guidelines Initiative (FADGI). The Still Image Working group compiled shared best practices into the "Technical Guidelines for Digitization of Cultural Heritage Materials" originally presented in 2010 and revised in 2016 (Rieger, 2016). The current version aligns with the Netherlands equivalent, Metamorfoze (van Dormolen, 2012), and takes into account the advances of imaging sciences and cultural heritage documentation. The document includes the 3-element FADGI conformance program: technical guidelines and parameters, best practices, and Digital Imaging Conformance Evaluation (DICE). Consisting of image targets and analysis software, DICE provides metrics and criteria for assessing digital image performance for resolution, tonality, colour, registration, uniformity, and noise, and for measuring system performance capabilities.

The DICE device level target (Figure 1-4) and GoldenThread software are produced by Image Science Associates (Rochester, NY). The DICE target includes colour patches that are identical to the GretagMacBeth ColorChecker, spectrally neutral grey patches, L*a*b* value annotations for colour and grey patches, vertical and horizontal slanted edge features to calculate the spatial frequency response (SFR), visual spatial resolution targets, and bidirectional rulers (metric- and English-based). The associated GoldenThread software automatically provides measurements for sampling rate (dpi), resolution, colour, tone, noise, and colour channel misregistration.

While FADGI is US-based and Metamorfoze is Netherlands-based, ISO 19263-1:2017 and 19264-1:2017 offer an international specification. ISO 19264-1:2017 defines a method for analysing imaging systems quality for the digital image capture of cultural heritage material. It includes best practices for cultural heritage documentation and combines the related ISO standards for imaging systems quality analysis. The document specifies the measurement characteristics, how they are measured, and the presentation of the results. The specification, like FADGI and Metamorfoze, is limited to two-dimensional originals and visible light imaging using scanners and digital cameras.

The COSCH Working Group 1 (WG1) (Section 3.1.4) worked to address the need for spectral imaging best practices and standardisation resulting from the expanded use of MSI

and HSI, the increased number and variety of instruments being used, and the introduction of a mixed user community ('Colour and Space in Cultural Heritage (COSCH)', n.d.). The Round Robin Test (RRT) was carried out as a coordinated research effort to better understand the instrumentation, the elements of data acquisition, and the effects of the instruments and methods (acquisition and processing) to the accuracy and reliability of the data (George et al., 2017). A summary of the RRT initiative and findings by George et al. (2017) illustrated the challenges and complexities of assessing and comparing different datasets with a considerable variation in the data resulting from the equipment (MSI vs HSI, manufacturer, specifications), the users (museums, universities, research laboratories), and data processing (procedures and workflow). The recognition of this variation in the data was important in informing best practices and working towards standardised methodologies. This emphasised the importance of heritage users understanding calibration (spectral, radiometric, and spatial calibration), accuracy, precision, the limits of the system, and the importance of routine calibration, validation, and testing of the imaging system.

The best practices and standards presented in this section are derived from the main categories of museum imaging (conservation documentation, collections photography, and scientific imaging). The *AIC Guide to Digital Photography and Conservation Documentation* (Warda et al., 2011, 2017) represents the current best practices and guidelines for conservation documentation. The guide did not include targets that go beyond visible light, colour photography, and the workflows related to spectral imaging are limited. It is important to acknowledge the wide use of this guide by conservators in the US especially considering its approachability and accessibility. It is a comprehensive guide covering the full pipeline for documentation in an approachable and accessible way. The guide has provided a successful example for conservation documentation, and future guides and workflows would benefit from reflecting on the successes of this guide in the conservation community, a consideration when developing workflows and encouraging implementation within the conservation community.

The CHARISMA user manual (Dyer et al., 2013) is an example of working at the intersection of the museum imaging categories of conservation documentation and scientific imaging. The authors aimed to make components of scientific imaging more accessible through the guide and software. Dyer et al. (2013) provided a great resource for the community that worked to address the issues of reproducibility and comparability of reflected and luminescence imaging for cultural heritage documentation. The manual included a strong emphasis on readily available equipment and open access software taking into consideration the required components of accessibility for non-technical users, a strong

advantage to the document. While open access software can be advantageous for heritage users providing a low cost option when paired with the readily available equipment, open access software can also be unsustainable especially when long-term funding is not included for the maintenance after the project is completed (Geffert et al., 2018). For the document and software to continue to be a resource for the community, there is a need for additional funding and support in order to update and maintain both. The CHARISMA user manual is included to inform the imaging processing in this thesis and as an example of pulling methods from imaging science over to conservation documentation in order to improve the reproducibility and comparability of imaging results.

FADGI, Metamorfoze, and ISO 19264-1:2017 are focused on collections photography, but take into account image sciences and build on established ISO standards. Based on the experience of the author in the US, the FADGI guidelines and DICE target are used for collections photography but are not as widely used for conservation documentation. The DICE target provide several measurement capabilities for assessing image quality and system performance that the other targets presented in Warda et al. (2011) do not offer. The DICE target and software provided a turnkey solution with metrics and criteria for measuring system performance capabilities that are already being used in museum imaging to assess standard digitisation setups, which is why these were selected for the image quality assessment included in this thesis.

The COSCH initiatives and the focus on imaging spectroscopy are more closely linked to scientific imaging. The summary of the RRT initiative and findings presented by George et al. (2017) are important to emphasise in relation to the camera characterisation and overall best practices, which include heritage users understanding calibration, accuracy, precision, the limits of the system, and the importance of routine calibration, validation, and testing of the imaging system. The COSCH RRT informed the characterisation presented in this thesis and the creation of the custom-built target, the Mango Vase test object (Section 1.3.2 and 4.2.1).

Working at the intersection of collections photography, conservation documentation, and scientific imaging, the research aims to borrow methods from these areas to improve the recording of scientific records for conservation documentation. This summary and review of best practices and standards illustrates how the different categories of imaging can inform the setup, acquisition, and processing of image data for the recording of heritage objects with this discussion specifically linking to the FADGI guidelines, the DICE target and software, and the image processing presented in the CHARISMA user manual that inform the methods presented in this thesis..

3.3. Camera characterisation

Modified cameras are being used as accessible tools for spectral imaging and conservation documentation (Section 3.1.5). The examples of modified cameras being used for cultural heritage applications are mostly IR conversions with the IR blocking filter removed and either replaced with an IR pass filter or a clear filter. These cameras are still using the red, green, and blue channels for recording the image, and the resulting IR images are dependent on the IR transmission for these colour filters. This research uses a camera with the monochrome conversion that includes the removal of 5 μm from the surface of the sensor, an invasive and destructive process, resulting in a camera that records from near UV to NIR without the impact of the transmission of the CFA. Since the consumer digital cameras are produced for visible light, colour photography, the questions for this thesis are: does the modification impact the resulting spectroradiometric and geometric image quality and can these devices be used as scientific devices for cultural heritage documentation?

Characterising the camera would provide a better understanding of the modification and also the spectral capabilities for optimal use such as the "new" spectral bands presented by Verhoeven et al. (2009). Characterisation is used to define the nature of the imaging system assessing its performance. Image quality measurement, a means of assessing the performance, quantifies the relationship between the input, or the scene, and the output, the image (Allen and Triantaphillidou, 2011). The characterisation can include measuring the spectral sensitivity or response in addition to resolution, contrast, noise, and other image quality attributes. This section will review methods that inform the characterisation of an unmodified and modified camera for this thesis (Chapter 5).

Camera characterisation is more widely practiced for scientific applications, and there are limited examples within cultural heritage applications, specifically conservation documentation. Early MSI studies like Casini et al. (1999) offer an important example for characterising imaging systems to define the limitations of a device for scientific imaging applications. The studies presented by Falco (2009) and Verhoeven et al. (2009) included characterisation and assessment of the modified cameras being used for cultural heritage and archaeological applications. In both cases the IR blocking filter had been removed and replaced with a filter that blocked visible light and passed IR radiation and the CFA had been left in place. Falco (2009) characterised a modified camera by estimating the relative and total transmission of the CFA, discussing resolution by visually assessing the camera's ability to resolve small features, and discussing contrast and noise. Verhoeven et al. (2009) measured the spectral response of the modified camera and used this measurement to take advantage of the unequal spectral transmission in the NIR of the red, green, and blue filters

and to calculate new spectral bands for aerial archaeological reconnaissance. Falco and Verhoeven provide examples characterising a modified camera for heritage applications.

This section discusses camera characterisation focusing on measuring image quality and spectral response to assess the performance of imaging systems. One primary consideration of the characterisation and the resulting performance of the imaging system is the image handling and how the images are recorded and processed. Before discussing methods of measuring image quality and spectral response, the acquisition and processing of RAW files will be discussed.

3.3.1. RAW processing workflow

Capture and workflow based on RAW files is recommended for optimum image quality (Allen and Triantaphillidou, 2011, p. 467) and specifically for conservation documentation (Warda et al., 2011) and scientific imaging (Verhoeven, 2010). RAW files are proprietary image formats that contain unprocessed, or minimally processed, image data originating directly from the acquisition device. RAW capture and workflow provide a higher degree of control for imaging and processing, editing capabilities that are non-destructive, and an increased potential image quality specifically with tonal range (Allen and Triantaphillidou, 2011). A RAW workflow allows the user to maintain control over the white balance, colorimetric interpretation, gamma correction, noise reduction, anti-aliasing, and sharpening (Dyer et al., 2013). In addition, RAW files have an archival advantage with the non-destructive editing process leaving the file unchanged and available for reprocessing at any given time.

RAW files are non-standardised, proprietary image formats and require image processing or RAW conversion for a 'finalised' image file (Allen and Triantaphillidou, 2011). There is a range of RAW file formats from the different camera manufacturers in addition to a variety of conversion software. The various RAW converters include propriety rendering algorithms and therefore do not render images consistently, so the same image can be processed and look different with different RAW converters. The RAW converters will generally perform demosaicing, colour space mapping, gamma correction/curve shaping, white balance, noise reduction, anti-aliasing, and sharpening (Allen and Triantaphillidou, 2011, p. 322; Dyer et al., 2013). The RAW image is acquired as a single channel (grayscale) with each pixel capturing information for only one channel and the values for the two other channels are interpolated for that specific pixel location (Allen and Triantaphillidou, 2011, p. 270). Demosaicing is the interpolation process needed to produce colour images. Currently, there

is no standard demosaicing algorithm for converting the RAW data, so the results can vary depending on the processing method (Allen and Triantaphillidou, 2011, p. 322).

Adobe Camera RAW (ACR) is an attempt to solve these rendering inconsistencies, like demosaicing, by providing a generic converter that is widely used and supports many different RAW formats. The ACR RAW conversion includes a single step and applies a variety of built-in processing that can include demosaicing, encoding gamma correction, white balance, colour space mapping, and noise reduction. Adobe Photoshop and ACR, considered the industry standard, are part of a routine conservation documentation workflow that is included in the AIC imaging guidelines although some free software alternatives are available (Warda et al., 2011).

While a RAW workflow is important, consumer digital cameras are made for "aesthetically pleasing" images and not necessarily scientific documentation with some built-in adjustments introducing unwanted modifications that can impact the reliability, reproducibility, and comparability of images (Dyer et al., 2013). Emphasising the importance of image processing on the interpretation and analysis of spectral imaging, Dyer et al. presented a methodology to produce device-independent images that focused on understanding the experimental factors, optimising the experimental procedures, and developing freely available image calibration and correction protocols.

Understanding the experimental factors includes recognising the limitations of commercially available equipment and the physical phenomena that impact the resulting images or contribute to device-dependent issues. This includes experimental factors and correction protocols like spatial inhomogeneities resulting from non-uniform illumination and requiring flat field correction, the spectral density of the radiation source and non-linear camera response, and camera response (colour calibration for visible-reflected images only) (Dyer et al., 2013, pp. 10–22). Figure 3-1 provides an example of the processing methodology presented by Dyer et al. for reflected images.

Flat fielding can correct for spatial inhomogeneities and is an important consideration for this research and the RAW processing workflow presented in Section 5.1. This process includes recording an image of a uniformly reflective board parallel to the object surface with the same parameters as the reflected image. The reflected image is divided by this flat field image of the board, which corrects for the non-uniform illumination in addition to variations in pixel-to-pixel sensitivity and distortions in the optical path.
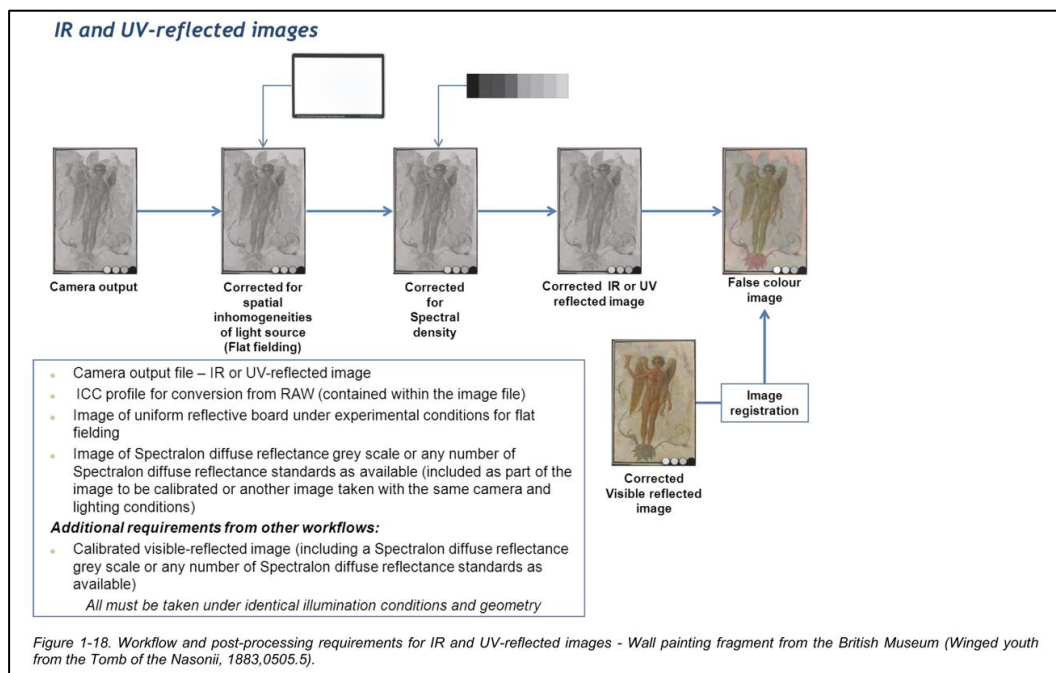
Figure 3-1. Processing methodology for reflected IR and UV images from Dyer et al. (2013, p. 22).

The spectral density of the radiation source is described by its spectral power distribution (SPD) and is the intensity of the radiation output by wavelength. Radiation sources are not homogenous across wavelengths, and there are a variety of radiation sources with different spectral densities impacting the comparability of images. In addition to spectral density, the camera response is a device dependent issue. Dyer et al. (2013) recommended RAW file acquisition and provided Adobe Photoshop in the example for RAW conversion to 16-bit TIFFs. While the sensors used in DSLR cameras are linear, images are often corrected with the application of gamma (a non-linear correction) to accommodate for the sensitivity of the human eye. However, linear data is important for comparable images. The application of gamma correction is included in many RAW conversion software packages. In the methodology presented by Dyer et al., Spectralon reflectance standards (Labsphere, Sutton, NH, USA) can be used to compensate for the camera-applied gamma and the spectral density of the radiation source.

The previous paragraphs focused on the experimental factors and correction and calibration protocols presented by Dyer et al. (2013) as these highlight important considerations and steps of a RAW processing workflow for spectral imaging that are not addressed by Warda et al. (2011) and not specified with the standard RAW processing using only ACR. These experimental factors and correction protocols inform the RAW processing workflow in Section 5.1.

3.3.2. 2D Image quality assessment

Image quality assessment of 2D images can provide information about the performance of an imaging system as part of characterisation. The five main image quality attributes that impact the resulting image are tone (or contrast), colour, resolution, sharpness, and noise (Allen and Triantaphillidou, 2011). Table 3-2 combines two tables from Allen and Triantaphillidou (2011, pp. 347–348) and provides the visual description and measures for the five image quality attributes. While colour is listed as one of the main attributes, colour reproduction is not relevant in the characterisation of a monochrome camera. Therefore, the discussion of colour and colour reproduction will not be included as part of this research. This section will address each of the other image quality attributes and the following section will discuss image quality measurement to inform the 2D image quality assessment used to characterise the unmodified and modified cameras in this thesis (Section 5.2).

Table 3-2. *Image attributes with associated perceptual attributes and imaging performance measures. Table combined from two tables in Allen and Triantaphillidou (2011, pp. 347–348).*

IMAGE ATTRIBUTE	VISUAL DESCRIPTION	MEASURES
Tone	*Macroscopic contrast* or reproduction of *intensity*	Characteristic curve, density differences, transfer function and OECF, contrast, gamma, histogram, dynamic range
Colour	Reproduction of *brightness* or *lightness, colourfulness* or *chroma* and *hue*	Spectral power distribution, CIE tristimulus values, colour appearance values, CIE colour differences
Resolution	Reproduction of *fine detail*	Resolving power, imaging cell, limiting resolution
Sharpness	*Microscopic* contrast or reproduction of edges	Acutance, ESF, PSF, LSF, MTF
Noise	Spurious information	Granularity, noise power spectrum, autocorrelation function, total variance (σ^2_{TOTAL})

Tone reproduction is the reproduction of original intensities and intensity differences from an original scene to the resulting image. Tone reproduction is the most important image quality attribute, as it is an important factor of the subjective impression of an image (Allen and Triantaphillidou, 2011). In addition, contrast directly impacts other image quality attributes, such as colour, resolution, and sharpness, and the measurement of these attributes relies on good tone reproduction (Allen and Triantaphillidou, 2011). Tone reproduction can be assessed objectively or subjectively. Objective tone reproduction relates to the measured relationship between input and output intensities of an imaging device or system, while subjective tone reproduction accounts for viewing conditions. Transfer functions describe

the relationship between input-to-output intensities, and the transfer function used for acquisition devices is the opto-electronic conversion function (OECF). ISO 14524:2009 provides methods for measuring OECFs for a digital camera.

Resolution, as a spatial image attribute, is the capability of an imaging device to record fine detail (i.e., high spatial frequency information) and relates to the smallest element of an image, the point spread function (Allen and Triantaphillidou, 2011). Resolution can refer to spatial, radiometric, temporal or spectral details (Ray, 1999, p. 327), and it is often incorrectly interpreted referencing the number of pixels of a camera system (ISO 12233:2017). Resolution has a significant impact on image quality. Lens and sensor array impact the resolution of a system, and the resolution of a lens is influenced by aperture, wavelength, and subject distance (Ray, 2002, p. 145). Resolution can be limited by diffraction or aberration and is influenced by contrast.

Sharpness is also a spatial image attribute, and it was previously discussed in relation to DOF (Section 2.5). Sharpness can be considered subjectively and objectively and is related to the definition of edges. Image sharpness is influenced by contrast, noise, and tone reproduction and can be measured by MTF and SFR. Further discussion of measuring sharpness and related standards and targets is included in Section 2.5.

Noise is unwanted variation in light intensity in an image that can impact the reading of the signal. Noise can be caused throughout the imaging chain and by a range of sources, and it can be a significant limitation affecting an imaging system and resulting image quality. While noise can be introduced at various stages, there are several types of noise related to electronic system noise and digital sensors including photon shot noise, dark current, readout noise, pixel response non-uniformity, and fixed pattern noise. More information about these types of noise can be found in references like Allen and Triantaphillidou (2011, pp. 433-434,441-443).

Test charts and targets are used to objectively measure image quality and evaluate the performance of an imaging system providing known (measured) values that can be compared with the recorded values. These charts and targets are calibrated in a way that they have known and constant properties that are either provided by the manufacturer or can be measured in a lab setting (Allen and Triantaphillidou, 2011, p. 353). Several of the ISO standards referenced include specifications for targets or preferred targets used to measure the image quality attributes. For example, ISO 12233:2017 includes preferred charts for edge-based and sine-based SFR and ISO 14524:2009 includes test charts for OECF.

The descriptions outlined here of image quality attributes and measures included aspects associated to ISO standards. These provide standardised definitions and means of measurement but are not focused on cultural heritage documentation. FADGI, Metamorfoze, and ISO 19264-1:2017 provide technical guidelines, parameters, and best practices used for collections photography to assess image quality and system performance.

FADGI defines a four-star rating system as a quality indicator of acceptability for the documentation of cultural heritage materials. The star system aligns with the three-tier Metamorfoze system with both systems including metrics that can be traced to ISO standards (Rieger, 2016). The lowest rating, one-star, is defined as only informational with the quality not being sufficient even for optical character recognition (OCR). A two-star rating is defined as only being appropriate when three- or four-star is not achievable, and these images would also only be informational and may or may not be useful for OCR and other processing techniques. A three-star rating signifies a very good professional image that can be used for most applications, and a four-star rating represents the state of the art in image capture and the top imaging quality available. The FADGI guidelines recommend digitising at a three-star or higher quality (Rieger, 2016).

The ISO standards relating to image quality measurements and the cultural heritage documentation best practices (FADGI and Metamorfoze) are limited to the documentation of two-dimensional objects using standard, visible light imaging. None of these directly address the documentation of three-dimensional objects or image-based 3D reconstruction. While it is accepted that the quality of the input image for 3D reconstruction is important, the 2D image quality metrics have not been implemented as part of the 3D reconstruction assessment. In addition to not addressing 3D imaging, these best practices in cultural heritage documentation are limited to standard, RGB imaging with visible light. Most of the image quality measures addressed by the ISO standards included so far can be applied to monochrome or colour cameras, and they do not necessarily specify the range of radiation. The questions for this thesis are: How do the best practices and quality assessment for cultural heritage documentation correspond with the quality of image-based 3D reconstruction? How can the cultural heritage documentation best practices and ISO standards be used for image quality measurement of a modified camera that has a sensitivity beyond visible light?

The DICE target and GoldenThread software were selected for the research presented in this thesis as a turnkey solution with metrics and criteria for measuring system performance capabilities that are already being used for collections photography to assess standard digitisation setups. The FADGI star rating system provides a point of reference to link the

2D image quality to the 3D reconstruction as part of the investigation of DOF and improved image-based 3D reconstruction (Chapter 7). By focusing on metrics like noise, sharpness, and resolution, these could be measured beyond visible light to assess the camera's performance and to understand the impact of the modification.

Standards and test targets exist for characterising imaging systems (ISO 12233:2017, ISO 19264-1:2017), but these do not represent the materials found in a museum object or the system's ability to detect specific features. As stated in ISO 19264-1:2017, ideally the target would include similar materials as that of the object being documented, but often this is not the case due to the wide range of original heritage materials. The performance when recording specific objects or materials can only be verified if the targets are made of the same material (ISO 19264-1:2017, p. v). As discussed in Cucci et al. (2019), custom built targets can be useful—testing the usability of an imaging system for specific collections or materials. Cucci et al. (2019) and George et al. (2017) described a custom made test target using medieval Tuscan panel painting techniques with seven pigments and five underdrawing materials to create different layering and line patterns that was used to test the quality and performance of MSI and HSI systems specifically for the documentation of paintings. The painted panel test object inspired and informed the development of the Mango Vase as a custom built test object (Section 1.3.2 and 4.2.1) to assess the optimisation of image-based 3D reconstruction.

This section focused on image quality attributes and measures tying in best practices for cultural heritage, specifically discussing the FADGI rating system. Image quality assessment provides one method of measuring the performance of an imaging system, but it does not address the sensitivity, or the spectral response, of an imaging system.

3.3.3.   Spectral response measurements

Spectral response is the relative sensitivity of an imaging system as a function of wavelength (Bongiorno et al., 2013). Measuring the spectral sensitivity of a device is important if the camera is to be used for measurement purposes (Manakov, 2016). Camera manufacturers do not provide spectral sensitivity data, and this sensitivity varies even if the camera is made by the same manufacturer (Darrodi et al., 2015). Spectral characterisation of digital cameras is used for a range of applications in several fields: colour processing, colour measurement, colour accuracy, and colorimetric applications. Similarly understanding the spectral response can support colour vision applications of MSI, colour constancy, and spectral reflectance recovery (Jiang et al., 2013a). Beyond colorimetry and computer vision, cameras have been characterised for aerial archaeology (Verhoeven et al., 2009), remote sensing to

monitor vegetation (Berra et al., 2015). Pike (2011), to study of animal colouration (Pike, 2011), for colour correction in underwater environments (Bongiorno et al., 2013), and forensic examination (Garcia et al., 2014) and facial recognition (Gernoth and Grigat, 2010).

The spectral response of a camera relies heavily upon the materials that make up the imaging sensor and the silicon substrate (Allen and Triantaphillidou, 2011). Silicon, used for CCD and CMOS sensors, is inherently sensitive to near UV and NIR radiation up to about 1100 nm, but the CFA and IR blocking filter influence the resulting sensitivity of the system (Allen and Triantaphillidou, 2011).

The output of an unmodified, colour sensor, $O_i(\lambda)$, can be calculated by the following equation:

$$O_{j,i} = \sum_{\lambda=380}^{780} L(\lambda)R_i(\lambda)s_j(\lambda) \tag{3.1}$$

where: $L(\lambda)$ is the SPD of the light source; $R_i(\lambda)$ is the spectral reflectance of the object; and $s_j(\lambda)$ is the sensitivity of jth channel with the maximum number of channels being eight (ISO 17321-1:2012). This equation shows the influence of the illumination source, the reflectance of the object, and the sensitivity of the colour channel for calculating the sensor output.

There are several methods for measuring and estimating the spectral response of a camera system. Two standards exist for characterisation, one produced by the European Machine Vision Associations (EMVA) and one published by ISO. The EMVA Standard 1288 (2012) works to define a unified method for the characterisation of the sensitivity, linearity, and temporal noise of monochrome and colour digital cameras for machine vision applications. While the EMVA standard can be used for monochrome cameras, the ISO standard focuses only on colour measurement and therefore is used for characterising only colour cameras. ISO 17321-1:2012 for colour characterisation for digital still cameras provides two characterisation methods to measure colour performance: a spectral method and a target method. The spectral method uses a monochromator and integration sphere to measure colour performance, while the target method uses a colour test target under specified lighting.

The methods presented by these standards include measurements that require complex, expensive equipment, like the use of a monochromator, that would mainly be available to specialised labs (Bongiorno et al., 2013; Prasad and Brown, 2013; Berra et al., 2015; MacDonald, 2015). Even the ISO 17321-1:2012 acknowledged the complexity and expense

of some of the presented methods and stated that it may not be practical for characterisation of individual digital cameras. Manakov (2016) categorised the approaches for determining spectral response as physics-based and computational methods, and stated that the main limitations of physics-based spectral response measurements are the specialised and expensive equipment required.

There has been active research to find easier, quicker, and more accessible methods for measuring and estimating spectral sensitivity of cameras. These include the use of interference filters to restrict the wavelength range of the illumination source or camera (Bongiorno et al., 2013; MacDonald, 2015), the use of a single image and a linear variable edge filter (Bongiorno et al., 2013), and the use of a single image of an LED panel with 36 narrow band interference filters (Hawkins and Green, 2008). Other estimation methods are computational methods that used colour charts and unknown illuminates (Prasad and Brown, 2013), images of the sky (Kawakami et al., 2013), and a transparent target for characterisation for high dynamic range imaging (Kim and Kautz, 2008). Some of the methods are focused on the visible range and colour and do not extend into the NIR, like the LED panel (MacDonald, 2015) and the linear variable edge filter (Bongiorno et al., 2013). Other methods extend beyond visible characterising cameras sensitive into the UV and NIR using a monochromator and spectrometer (Verhoeven et al., 2009; Garcia et al., 2014; Berra et al., 2015).

An alternative method to using a monochromator is the use of interference filters to restrict the wavelength range of the illumination source or camera (Bongiorno et al., 2013; MacDonald, 2015). Both the monochromator and filter methods require the acquisition of images at each wavelength band over a range of wavelengths, so easier and quicker approaches look to reduce the number of images required. Using filters is "notionally easier" than a monochromator-based approach, interference filters are expensive, and both approaches require significant lab-based measurements (Darrodi et al., 2015). The study by MacDonald (2015) included a filter-based method in the visible range using a set of transmission filters, but the method could be extended into the UV and NIR by incorporating additional interference filters beyond the visible. In the study, a set of narrow bandpass filters was used to acquire a sequence of images of a white target illuminated by tungsten halogen lamps. The light source and transmission of the filters were measured with a spectrometer. The mean RGB value was extracted from the image set and corrected with the integral power transmitted through each filter. The results were compared to measurements acquired using a monochromator. MacDonald concluded that the transmission filter method

provided results comparable to the measurements with a monochromator, which informed the use of a filter-based method for measuring spectral response in Section 5.3.

Spectral response and variations in measurements

The spectral sensitivity of consumer cameras is largely influenced by the sensitivity of silicon, in addition to the CFA and IR blocking filter. For a standard, unmodified camera the spectral sensitivity can be visualised with three curves representing the relative sensitivity of the red, green, and blue channels within the visible range, about 400 to 700 nm, with cut off at 700 nm due to the IR blocking filter.

For IR and full-spectrum converted cameras, the CFA is still in place and the camera records three channels, but the sensitivity extends beyond visible and into the UV and NIR. Verhoeven et al. (2009) provided results for spectral sensitivity measurements of an IR converted camera, and with the visible light blocked, the sensitivity of the red, green, and blue channels fall between 700-1000 nm (Figure 3-2). Berra et al. (2015) provided results for measurements of a full-spectrum conversion without the visible light blocked, so the sensitivity of each of the channels extends into the NIR (Figure 3-3). With the monochrome conversions (the modified camera used for this thesis), the CFA is removed and the spectral sensitivity is represented with a single curve instead of the three curves.
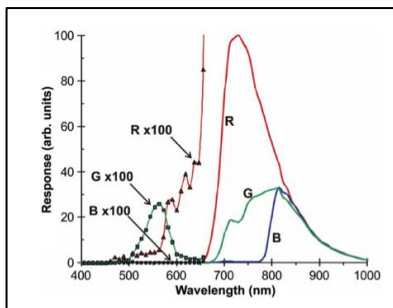
Figure 3-2. Relative spectral response of a modified Nikon D50 with a visible block filter in front of the sensor (400-1000 nm) (Verhoeven et al., 2009).
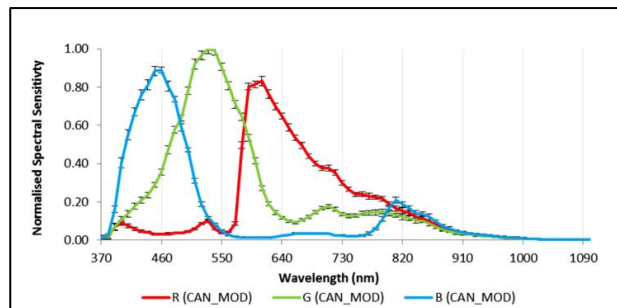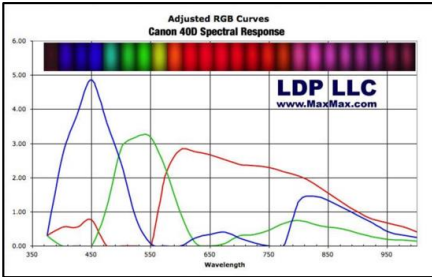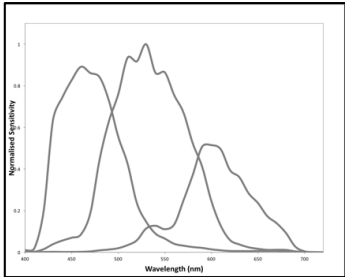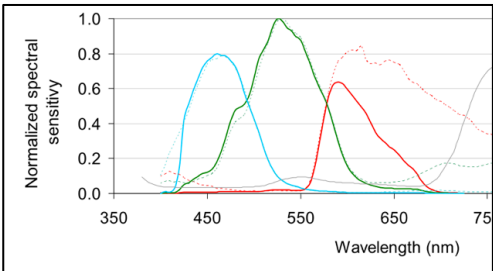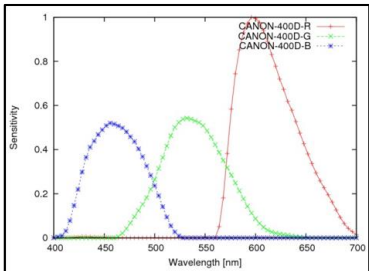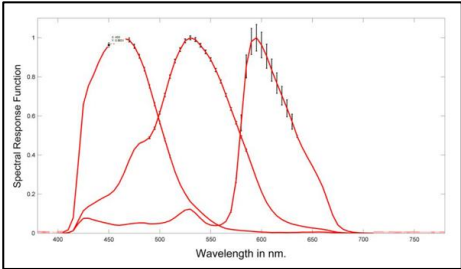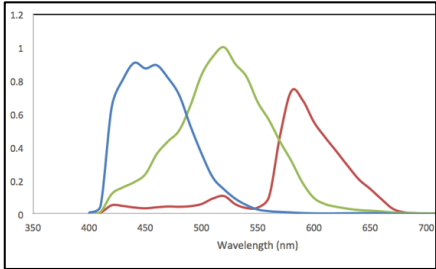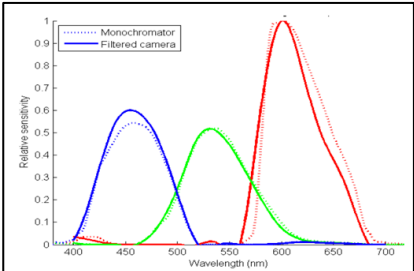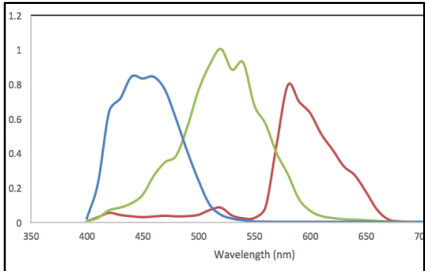
Figure 3-3. Spectral response for a modified Canon camera (370-1090 nm) (Berra et al., 2015). According to the authors, the results are normalised to the peak of the green channel.

Figure 3-4. Spectral response measures for four cameras

Canon 40D	*Modified Canon 40D* *Figure from MaxMax ('MaxMax Cameras', n.d.)* *Measurement: Monochromator; Range: 375-1000 nm*	*Measurement from Jiang et al. (2013b)* *Measurement: Spectrometer & monochromator with integrating sphere; Range 400-720 nm, 10 nm interval*
Canon 400D	*Figure from Lebourgeois et al. (2008)* *Measurement: Method not included except monochromatic source used and references Déliot et al. (2006) and Labbé et al. (2007); Range: ~400-700 nm*	*Figure from University of Tokyo ('Spectral Sensitivity Database', n.d.)* *Measurement: Spectrometer & monochromator; Range: 400nm-700nm, 4nm interval*
Nikon D5100	*Figure from Darrodi et al. (2015)* *Measurement: Double monochromator; Range: 380-770 nm, 5nm interval*	*Measurement from Jiang et al. (2013a, 2013b)* *Measurement: Spectrometer & monochromator with integrating sphere; Range 400-720 nm, 10 nm interval*
Nikon D200	*Figure from MacDonald (2015)* *Measurement: Monochromator; Range: 380-780 nm, 5nm interval; Filtered camera; Range: 400-700 nm, 20 nm interval*	*Measurement from Jiang et al. (2013a, 2013b)* *Measurement: Spectrometer & monochromator with integrating sphere; Range 400-720 nm, 10 nm interval*

Cameras have different spectral responses even if they are the same manufacturer and model (Ji and Rhodes, 2011). This difference is due to variations in materials, manufacture, optics, and in-camera processing, as the overall spectral sensitivity of a camera system includes the sensor sensitivity, the transmission of the CFA, and in-camera processing (Bongiorno et al., 2013). Figure 3-4 illustrates the difference between camera models and the same manufacture (Canon 40D and 400D, Nikon D5100 and D200); the difference between manufacturers (Canon vs Nikon); and even the variation in measurements by including spectral response measurements of four cameras (two Canon, two Nikon) with two measurements per camera. A comparison of data from Jiang et al. (2013a, 2013b) shows the difference between models of Canon cameras (Figure 3-5) and the difference between two comparable models of Canon and Nikon cameras the Canon 5D Mark II and the Nikon D3X (Figure 3-6).
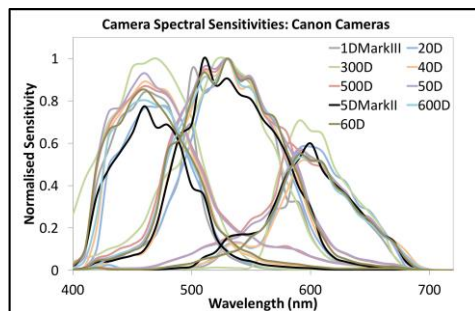
Figure 3-5. Spectral sensitivities of nine different models of Canon cameras. This shows the variation in spectral response for the different models of cameras despite being made by the same manufacturer (Jiang et al., 2013b).
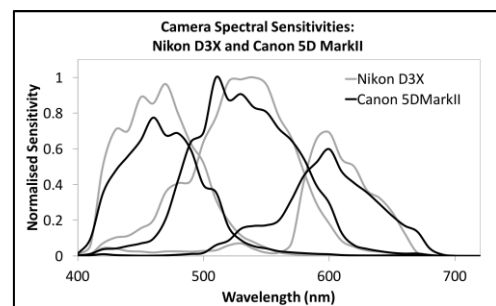
Figure 3-6. Spectral sensitivities of the Nikon D3X and the Canon 5D Mark II, comparable models of cameras made by two different manufacturers. One of the most significant differences is the red channel (right peak) with the Nikon having a sharper slope around 550 nm and the Canon having a more gradual slope between 500 and 600 nm (Jiang et al., 2013b).

Processing can influence the results of the spectral response measurements. According to MacDonald (2015), the amplitudes of the curves can be attributed to white balance and illumination source. Tests indicated that the white balance settings do not impact the image data in a RAW file; however, RAW conversion programs can apply these settings, which can result in what appears to be a change in the spectral sensitivity (Figure 3-7).
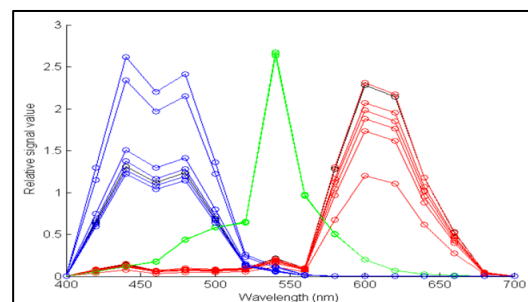
Figure 3-7. Comparison of spectral sensitivity with varying mean RGB values for six white balance settings. Figure from MacDonald (2015).

In addition to the inherent differences in cameras and processing, there is also the question of the measurement methods and the resulting accuracy and reliability. The literature relating to measurement and estimation of spectral sensitivity does not fully address the reliability and accuracy of the results. A limited number of studies have discussed the uncertainties and accuracy of measuring and estimating spectral response (Darrodi et al., 2015; Manakov, 2016). Manakov cited methods and measurements for spectral characterisation and acknowledged that none of the methods listed provide information about the resulting accuracy of the characterisation. Darrodi et al. is one of the few publications that discussed the uncertainty and error associated with the measurement of spectral sensitivity. Darrodi et al. acknowledged the complications and complexities of measuring spectral sensitivity of a camera; however, they pointed out that most of the related studies do not discuss the uncertainties and errors involved with the measurements and results. There are calibration procedures that are being used with a simpler setup that increase ease and speed, but these setups reduce the control of the variations and errors of the system and uncertainties cannot be reported. Darrodi et al. provided ground truth data for two cameras (Nikon D5100 and Sigma SDMerill). However, this ground truth cannot be used as a reference for the Canon 5D Mark II measurements for the research presented in this thesis due to the variation of the spectral sensitivity of different makes and models of cameras.

3.4. Chapter summary

Spectral imaging techniques are used for both conservation documentation and scientific imaging to document and analyse heritage objects. While spectral imaging can provide complementary information for 3D imaging, selected wavelengths within or beyond visible light can improve contrast and provide an enhanced view of an object or features. There is the potential of using wavelength selection to record improved 2D images of an object to optimise image-based 3D reconstruction for conservation documentation, which could be useful for objects that would otherwise be problematic to document.

This review chapter focused on spectral imaging with the first section presenting spectral imaging techniques and instrumentation within conservation documentation and scientific imaging (Section 3.1). While accurate and precise instrumentation for spectral imaging exists, the cost and complexity can keep it out of reach for many heritage institutions, professionals, and collections. Non-expert heritage users are using modified digital cameras as accessible devices for spectral imaging (Section 3.1.5). These devices offer inexpensive, easy to use, portable, and high-resolution options for conservation documentation. Modified

cameras can be paired with optical filters, which provide a solution for wavelength selection and multiband/multispectral imaging for heritage professionals (Section 3.1.6).

Consumer digital cameras are optimised for visible light, colour photography, so the question arises whether the modification impacts the resulting image quality both radiometrically and geometrically. While MSI was cutting edge technology in scientific imaging of artworks 20-30 years ago, these early publications are important for informing components of the instrumentation and process including the characterisation of instrumentation. Characterising the camera would provide a better understanding of the modification and the use and limitations of the device for scientific imaging.

Best practices and standards were reviewed in Section 3.2 to improve and ensure the recording of quality data. The available best practices and standards reflect the three categories of museum imaging: collections photography, conservation documentation, and scientific imaging. This is a good example of the placement of the research at the intersection of the museum imaging categories and the benefit of borrowing methods from these areas to improve the recording of scientific records of conservation documentation.

A combination of the best practices will inform the setup, acquisition, and processing of image data within the experimental chapters of this thesis. The *AIC Guide to Digital Photography and Conservation Documentation* (Warda et al., 2011, 2017) represents the current best practices and guidelines for conservation documentation. The CHARISMA user manual is included to inform the image processing and as an example of pulling methods from imaging science over to conservation documentation in order to improve the reproducibility and comparability of imaging results. The COSCH RRT informed the characterisation presented in this thesis and the creation of the custom-built target, the Mango Vase test object.

Section 3.3 discussed RAW processing (Section 3.3.1), 2D image quality assessment (Section 3.3.2), and spectral response measurement (Section 3.3.3) to inform the characterisation of the modified camera. Image quality assessment measures the relationship between the scene (the input) and the image (the output), and how well the imaging system can reproduce the scene. Measuring image quality is used to understand the performance of an imaging system and can be used to understand the modification of a consumer digital camera. The FADGI guidelines and DICE target offer a turnkey solution with metrics and criteria for measuring system performance capabilities that are already being used in museum imaging to assess standard digitisation setups, which is why these were selected for the image quality assessment included in this thesis.

Measuring the spectral response of a camera, or the responsivity of the sensor as a function of wavelength, is important if the camera is to be used for measurement purposes and to understand the resulting sensitivity of a modified consumer digital camera. While there are several methods for measuring and estimating spectral response, the filter-based method used by MacDonald (2015) presented an available option that could include measurements into the NIR for a modified camera. MacDonald compared four methods of measuring spectral response, and the filter-based method was found to have good correspondence with data acquired using a monochromator. Optical filters provide a solution for wavelength selection and multiband/multispectral imaging for heritage professionals especially with the availability of modified cameras.

4. Optimising image-based 3D reconstruction

Consumer imaging systems paired with automated workflows lead to the wide use of image-based 3D reconstruction techniques like SfM-MVS for the 3D recording of heritage objects in addition to the high variability of the resulting quality. Chapter 2 discussed accessibility and variability, presented the questioning of the accuracy and reliability, and explored best practices. This first experimental chapter introduces methods to improve acquisition, processing, and assessment of image-based 3D reconstruction that address the research question "How can consumer imaging systems be optimised to improve image-based 3D reconstruction of small to medium sized museum objects?" These methods build on current best practice and 3D reconstruction workflow (Section 2.3) using two purpose developed test objects to support quantitative assessment (Section 2.4).

4.1. Panel test target

4.1.1. Materials and methods

The Panel test target is a rigid (305 mm x 300 mm) aluminium plate coated with an Airbus designed wallpaper with a pseudo-random pattern originally designed to optimise the optical detection of surface strain with Digital Image Correlation (DIC) (Figure 4-1). The panel was the test object created by Sargeant et al. (2016) and discussed in Section 2.3.3.2. While the
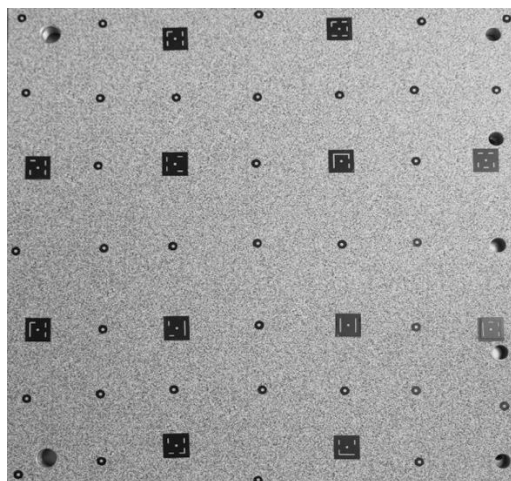
Figure 4-1. Panel test target used for assessing 3D reconstruction quality.

Panel test target is not usually used for depth reconstruction, it provided a planar surface with a medium spatial frequency and a high local contrast for surface matching ideal for investigating the optimisation of image-based 3D reconstruction.

A planar surface provides a known shape for testing 3D imaging techniques and results can be assessed by using a best-fit plane, or a flatness measure. The flatness measurement error is a quality parameter used to measure form and evaluate the performance of 3D systems and is part of national guidelines and international standards for 3D measurements (Beraldin et al., 2015; Hess, 2015a). It is "the range of the signed distances of the measured points from the best-fit plane calculated using the least- squares method" (Beraldin et al., 2015, p. 8). The guidelines and standards relating to this measure require planes with a certified flatness

providing traceability for the measurement systems. The Panel test target is not a certified flat plane, but it presented a practical surface for testing 3D imaging with the plane being a simple and known shape that can be assessed using plane fitting (Section 2.4.2).

The panel includes circular retro-reflective targets and Ben Sargeant (UCL CEGE PhD candidate) supplied reference coordinates for these targets generated photogrammetrically using a Nikon D700 DSLR and Brunson Scale bars (Sargeant et al., 2016). These reference coordinates were used for the scaling and alignment in PhotoScan. Additional information about the processing using PhotoScan will be discussed later in this chapter.

4.1.1.1.   *Camera positioning robot*

An experimental imaging geometry was required that could reproducibly position the camera to capture the image networks needed for the 3D reconstruction of the Panel test target while maintaining the same relationship between the target and illumination. The *camera positioning robot* (Figure 4-2-Figure 4-4) was built with Sargeant from components of an earlier Imaging Network Design Robot (INDRo) (Sargeant et al., 2013; Hosseininaveh Ahmadabadian et al., 2014) (Section 2.3.3.2). Unlike INDRo, the linear stages were stacked allowing the camera to be positioned in an area 300 x 600 mm with the camera height staying constant. The target could be moved up and down to allow different imaging viewing angles. The target was mounted on a Hepco section using a target plate that could be moved up and down and be locked in place along the section, which in turn was attached to the optical table and provided an object-camera distance of 600 mm. Instead of using the rotary stage for the object being recorded, the rotary stage was included in the camera positioning robot and stacked on the two linear stages. The camera was mounted on a 3-way pan/tilt tripod head on the rotating stage allowing for the camera angle to change in relation to the object.

The camera positioning robot was setup on an optical table in the Advanced Structures Lab in the Civil, Environmental and Geomatic Engineering (CEGE) department at the UCL. The lab included a window and overhead lights both of which are problematic for photographic setups. There was no option to move the entire setup to another lab with a more controlled lighting environment. The best option to mitigate stray radiation effects was to use a powerful illumination source and short shutter speed. Continuous illumination, such as fluorescent or tungsten sources, would not be able to out power the stray radiation, while flash sources could. Off-camera flashes provided a compact option for flash illumination, however, the repeatability testing discussed (Sections 5.3.4 and 5.3.5) showed that studio strobes with power mains were more consistent than off-camera flashes. Therefore, studio

strobes with umbrellas as diffusers were used to provide even illumination for the image acquisition. To test if stray radiation was impacting the resulting imagery, an image was acquired with the same camera settings but with the flash turned off to ensure that no image data was being recorded.
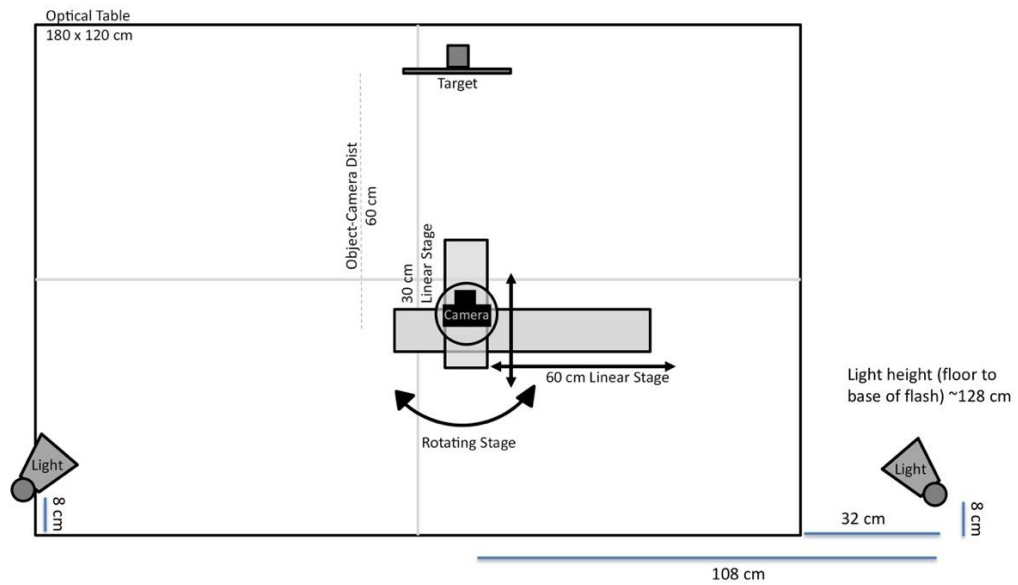
Figure 4-2. Diagram of the camera positioning robot setup (overhead view).
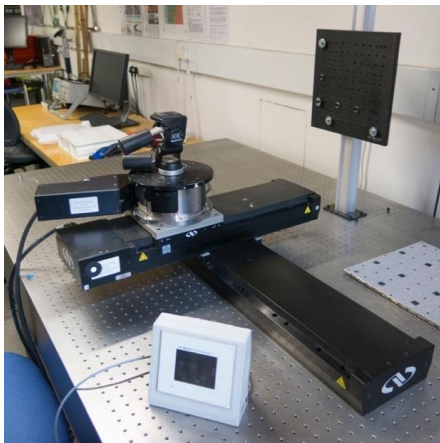
Figure 4-3. Image of camera positioning robot setup. Two linear stages are stacked with rotational stage and tripod head on top, and a Hepco section mounted to optical table with platform for mounting the target.

Figure 4-4. Image of camera positioning robot with camera, DICE target, and Bowens studio strobes in place.

The image sets of the Panel test target were acquired using an unmodified Canon 5D Mark II camera. This camera has a full-frame CMOS sensor (36 x 24 mm) with a maximum resolution of 21.1 MP (5,616 x 3,744 pixels) and a pixel pitch of 6.4 μm (Table 4-1). A Coastal Optics 60 mm f/4 UV-VIS-IR apochromatic macro lens was used with the unmodified camera. This is a high performing lens used for forensics, science, and fine art

imaging with low aberration and distortion and no focus shift from UV through IR. Two Bowens Gemini GM400Rx studio strobes (Bowens International Ltd.) with umbrellas were used to illuminate the object. The ISO and shutter speed were consistent for each image set (ISO 100 and 1/100 sec shutter speed), and Table 4-2 provides the information about the changing aperture and corresponding flash power. The camera was focused at the same position for each aperture set using Live View at 200% magnification viewing the pattern at the centre of the Panel test target.

Table 4-1. Reference list for camera and lens information

	Name	Make and Model	Serial No.	Specifications
Cameras	*Canon*	Canon 5D Mark II (Canon U.S.A. Inc., Melville, NY, USA)	2321303956	Full-frame CMOS sensor (36 x 24 mm), maximum resolution of 21.1 MP (5,616 x 3,744 pixels) and 6.4 μm pixel pitch
	mCanon	Canon 5D Mark II + monochrome conversion by MaxMax LDP LLC (Carlstadt, NJ)	0652304598	
Lenses	*60 mm*	Coastal Optics 60 mm f/4 (Jenoptik Optical Systems, Jupiter, FL, USA)	108223	UV-VIS-IR Apochromatic (APO) macro lens
	50 mm	Canon 50 mm f/2.5 Compact Macro	354556	Compact macro lens
	24 mm	Canon 24 mm f/2.8	963000576	

RAW images were acquired and processed using the RAW processing workflow with Adobe Camera RAW (ACR) (workflow: Section 5.1, software: Section 12). The image sets were batch-processed for a greyscale conversion using an Adobe Photoshop Action script (Section 12). Greyscale images were used as input for the 3D reconstruction for a more comparable assessment in later sections between the unmodified and modified camera.

Table 4-2. Camera and flash settings for the image sets Panel

Aperture	Flash Power
f/5.6	1
f/11	3
f/32	6

4.1.1.2. *Image-based 3D reconstruction processing*

The image-based 3D reconstructions were processed using SfM-MVS through Agisoft PhotoScan Pro version 1.3.3 (Section 12). The processing followed the CHI *error minimisation workflow* (Section 2.3.2). The processing incudes an initial alignment of the images and the creation of a sparse point cloud. The optimised workflow is an iterative process of gradually selecting and removing points while performing bundle adjustments to refine the alignment of the images and sparse point cloud and to determine a better camera calibration. The final steps include building a dense point cloud and generating a mesh and texture model. The 3D file formats processed were STL (Stereolithography) for geometry data and PLY (Polygon File Format) for texture and geometry data.

4.1.1.3.   Assessment of 3D reconstruction

Standards are not available for assessing the accuracy and resulting quality for image-based 3D reconstruction, which is discussed in Section 2.4. The section presented three main options for accuracy analyses: (1) comparing results with higher accuracy techniques mostly range-based; (2) assessing reconstruction of known geometric shapes; and (3) comparing results with a model averaged from multiple acquisitions. One of the challenges for assessing accuracy is the availability and quality of reference data, which is especially challenging for cultural heritage documentation. This is discussed in Section 2.4, but the research and results in this thesis also illustrate and reiterate these challenges found in the literature, specifically in this chapter.

The resulting 3D reconstructions were assessed using certified GOM Inspect software (Section 12). The 3D reconstructions for the Panel test target were assessed using plane fitting. GOM Inspect was selected because it is a free version of a software produced by GOM, a company focusing on precise industrial metrology. While the free version of the software has limitations, it maintains strong support and development as part of a commercial company with software and hardware solutions in metrology. It is certified by PTB and NIST[11] and can be used as a traceable product for quantitative analysis. Surface deviations are visualised through colour scaled discrepancy maps with a histogram indicating the distribution of the discrepancies. These enable systematic and random error to be identified.

4.1.2.   Network configuration

Initially images of the Panel were acquired with a normal image configuration with the camera moved parallel to the target surface. A network of seven images was acquired from three target heights and three camera positions with near parallel viewing directions (Figure 4-5, left column). The angle of the camera was not changed.

The normal image configuration 3D reconstructions exhibited systematic errors observed in the surface discrepancy maps as concentric circles radiating from two central areas (Figure 4-6). This error can be attributed to an inaccurate estimate of radial lens distortion from self-calibration bundle adjustments (Wackrow and Chandler, 2008; James and Robson, 2014)

---

[11] PTB, the Physikalisch-Technische Bundesanstalt, is the national metrology institute of Germany, and NIST, the National Institute of Standards and Technology, is part of the United States Department of Commerce.

(Section 2.3.3.2). The systematic error surfaces seen in the practical test results of Wackrow and Chandler (2008) more closely resemble the errors observed in the figures on the top row of Figure 4-6 with concentric circles radiating from two central locations than the simulated examples that clearly show a dome or bowl shape.
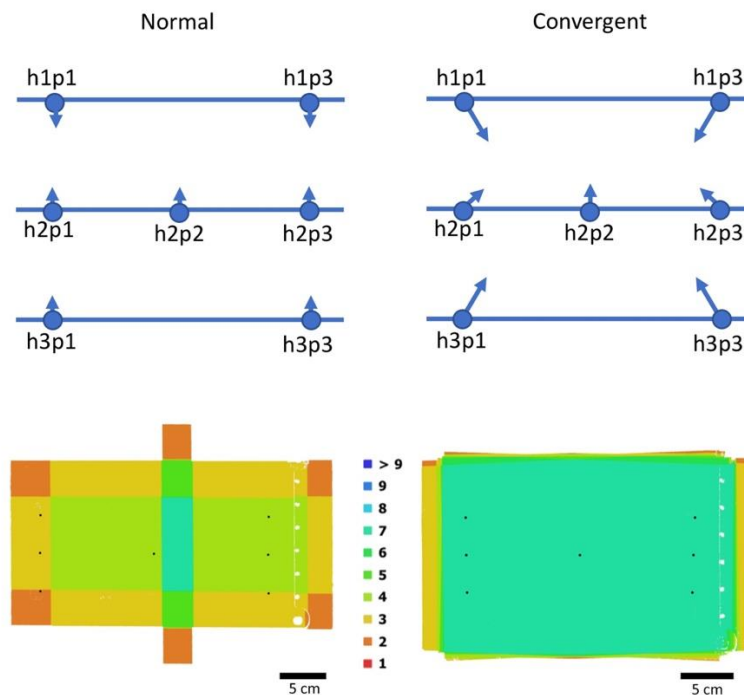
Figure 4-5. Diagram illustrating normal vs convergent image configurations. The top row includes positioning and angling of camera from three heights ('h') and three positions ('p'). The bottom row includes camera locations and image overlap figures from PhotoScan to show the difference in overlap between the configurations. The colour corresponds with the number of overlapping images.

An additional set of images was acquired in a convergent image configuration to compare with the normal configuration and to confirm the best camera network. The convergent image configuration included seven images acquired from three target heights and three camera positions with the camera pointing towards the centre of the target and converging slightly behind the object plane (Figure 4-5, right column). The camera was angled to -10° and 10° at position 1 and 3 (*p1* and *p3*) from position 2 (*p2*) at 0°. When the target was positioned at height 1 (h1) the camera was angled down approximately 5° and at height 3 (h3) the camera was angled up approximately 5°. The angling for *p1* and *p3* was done using the rotational stage providing more precise and repeatable angling than the positioning for *h1* and *h3,* which was done manually using a 3-way pan/tilt tripod head and an angle-o-meter.
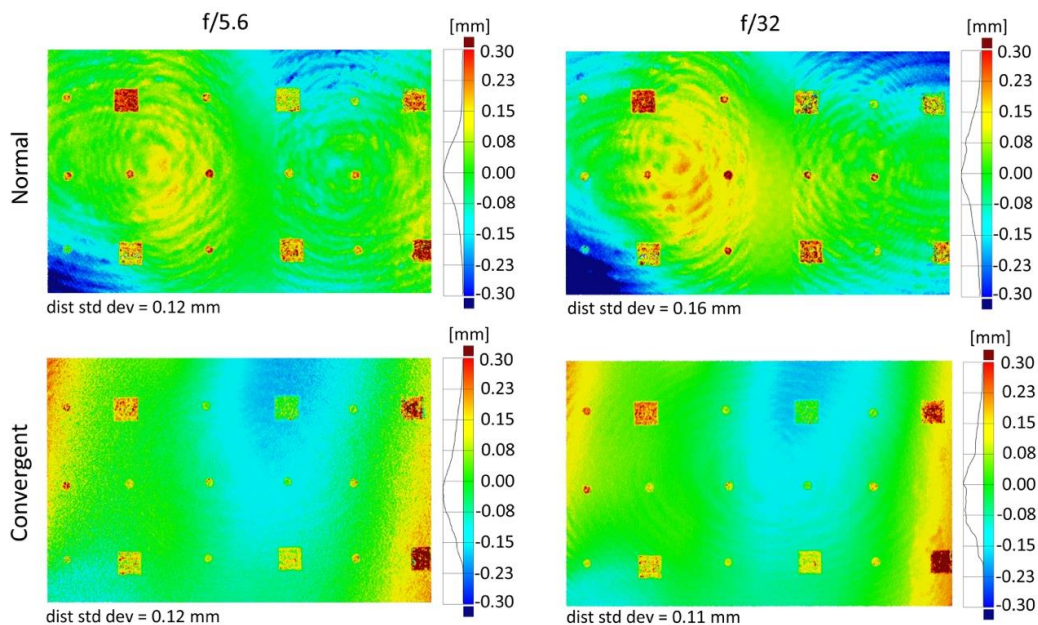
Figure 4-6. Surface discrepancy maps from 3D reconstruction results of normal and convergent image configuration. The figure includes surface discrepancy maps of the 3D reconstructions assessed using plane fitting for a normal (top) and convergent image configuration (bottom) for image sets acquired with apertures f/5.6 (left column) and f/32 (right column). The normal image configuration results show systematic error from unmodeled lens distortion, and the convergent image configuration reduces the impact of this error. The square and circular local surface anomalies observed in this figure are the photogrammetric targets attached to the panel surface.

The resulting 3D reconstructions showed that the convergent image configurations had improved geometry as compared to the normal image configurations (Figure 4-6). These results confirm that the resulting geometry is improved when using a convergent network. The convergent image configuration minimised the effect of the systematic error from the inaccurate model of lens distortion observed with the normal image configuration. This comparison of normal and convergent image configurations further supports Remondino and El-Hakim (2006) and Nocerino et al. (2014) and the emphasis on the importance of proper camera network geometry discussed in Section 2.3.4.2. Including convergent images strengthens the geometry and helps to avoid global deformation in the 3D reconstruction results. The results presented for the assessment of normal and convergent image configurations further supports the discussion about the importance of camera networks for cultural heritage documentation.

These results for the documentation of the Panel, as a planar surface, are important for the consideration when documenting paintings and other relatively two-dimensional objects. It would be beneficial to document a painting with a combination of normal and convergent networks since the normal will provide a better texture and the convergent will provide a

better geometry. The documentation of a more three-dimensional object would require a different network and recording in the round, but the convergent configuration is mimicked by recording a series of surface patches with optimal camera geometry that are combined to record the entirety of the object.

4.1.3. Reference data

The results from the convergent image configuration (Figure 4-6) showed a feature that was consistent throughout the results despite different apertures highlighting that the panel was not flat to the order of +/- 0.15 mm. A test was run to confirm that the feature observed in the 3D reconstruction results was a function of the shape of the panel and not necessarily the imaging system or calibration. The Panel test target was documented at three orientations rotating the target 90° for each orientation (0°, 90°, 180°). A convergent image configuration of seven images (Section 4.1.2) was acquired with the target rotated 90° and then 180°. The target was removed from the platform, rotated 90°, and repositioned on the platform, while the camera positions remained consistent with each of the image sets. This was repeated for the 180° target orientation. The results (Figure 4-7) showed that the error rotated with the panel rotation indicating that the -0.15 mm surface discrepancy (the light blue area) was a function of the shape of the plate and not a function of the measurement system and image configuration.

The Panel test target had been selected because it presented a practical surface for testing 3D imaging with the plane being a simple and known geometric shape that can be assessed using plane fitting. As a result, the analysis is more complex than it would be in using a flat reference surface as an independent check. With the systematic unflatness of the surface, the plane fitting was no longer the best option for assessing the performance of the system and measuring error. In the absence of an independent measurement of better capability, averaging a few 3D reconstructions of the panel were used to generate a reference surface (Section 2.4.3).

Geomagic Wrap[12] (Section 12) was used to average four meshes of the Panel test target to create a reference mesh and to accommodate for the shape of the panel. The reference mesh was created from resulting meshes from the DOF-Sharp-SFR test (f/5.6 position 0 mm and

---

[12] Geomagic Wrap offered a straightforward and quick method for aligning and averaging the meshes. It is a commercial software tool for 3D models that includes surface editing and analysis features and has a feature for averaging meshes. The Smithsonian's Digitization Program Office was able to provide access to a license for the software, so a few datasets could be processed and tested.

10 mm, f/11 position 0mm and 5 mm) (Section 7.1.2). The meshes were cropped to a central rectangle of the target (removing the target platform and edge of the target). The meshes were then globally registered and averaged. The resulting averaged mesh was assessed by comparing the shape to a best-fit plane (Figure 4-8). The surface discrepancy map shows the systematic unflatness of the panel was retained in the averaged mesh as would be expected with the edges about +0.15 mm (orange-red areas) and the central depression about -0.15 mm (light blue areas).
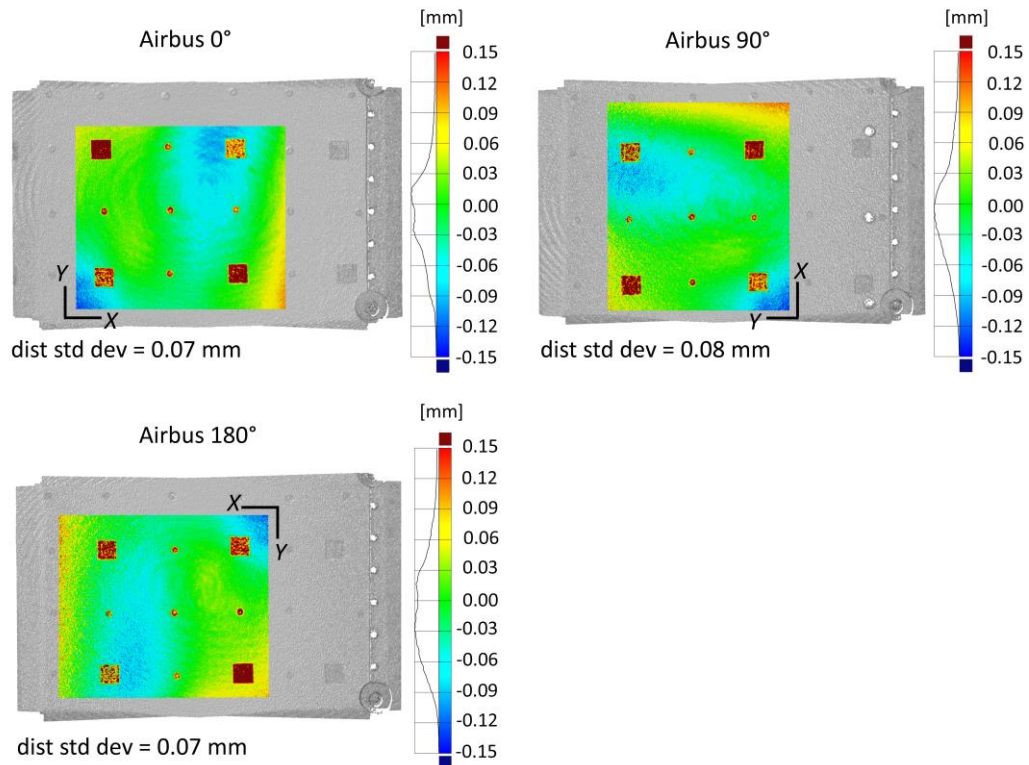
Figure 4-7. Assessment of flatness of Panel. Surface discrepancy maps of the 3D reconstruction results from rotating the Panel to check its flatness. The figure includes surface discrepancy maps of the 3D reconstructions assessed using plane fitting for three target orientations (0°, 90°, 180°). The results show that the error rotates as the Panel is rotated providing evidence that the error is a function of the shape of the panel and not a function of the imaging system or image configuration.

Assessing the 3D reconstructions with the average reference mesh, GOM Inspect was used for alignment and comparison. The 3D reconstruction result being assessed was aligned with the average reference mesh in GOM Inspect using the prealignment function, a global best-fit alignment and a subsequent local best-fit. The
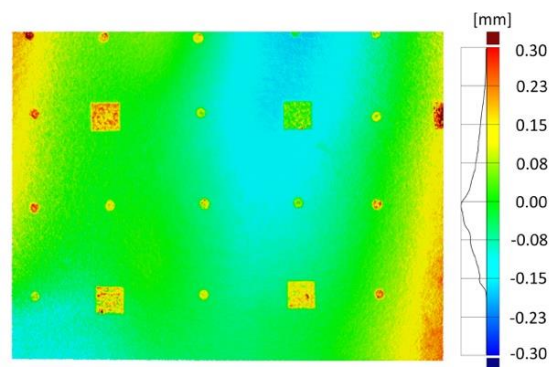
Figure 4-8. Surface discrepancy map assessing averaged mesh with a best-fit plane.

surface deviation was calculated by computing the direct perpendicular distance of each polygon point between the two datasets ('GOM Inspect Professional V8 SR1 Basic Manual: Inspection 3D Metrology', 2015, p. 50). These deviations are visualised through colour scaled discrepancy maps with a histogram indicating the distribution of the discrepancies.

The averaged mesh was used to assess the 3D reconstruction from an f/11 image set and then compared to the previous option of plane fitting (Figure 4-9). The surface discrepancy map assessing the f/11 dataset with the averaged mesh did not include the systematic unflatness of the panel indicating that this systematic error was corrected for. However, the histogram for the averaged mesh comparison was bimodal rather than a Gaussian distribution indicating another error was present (Figure 4-9).

The scale of the surface discrepancy map was reduced to a smaller range of represented discrepancies (+/- 0.05 mm) (Figure 4-10), and the error showed up as concentric circles radiating from the centre of the reconstruction. The pattern had similarities to that observed with the normal image configuration (Section 4.1.2). While the convergent image configuration minimised the effect of the inaccurate model of lens distortion, there was still a systematic error observed at a fine scale (+/- 0.02 mm).
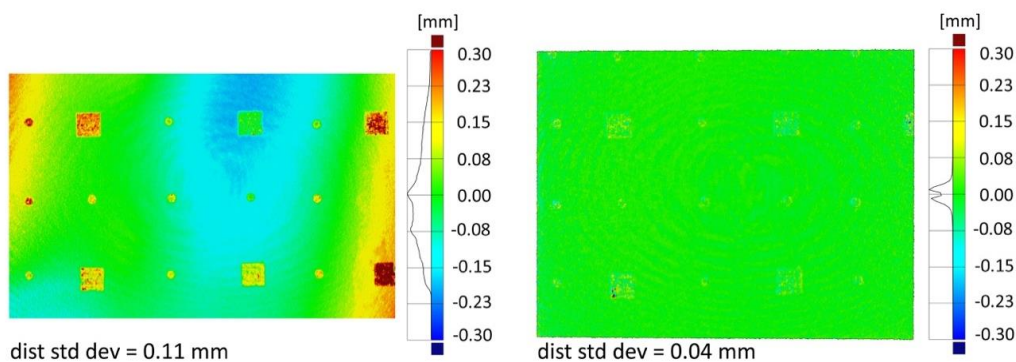
Figure 4-9. Surface discrepancy maps comparing assessment with plane fitting and an averaged mesh. The 3D reconstructions of an f/11 image set was assessed using plane fitting (left column) and an averaged mesh (right column). The comparison using the averaged mesh showed the systematic unflatness of the panel was no longer dominating the assessment of the resulting 3D reconstruction.

The largest discrepancies in the comparisons (Figure 4-10) are in the areas of the dark square and circular targets on the Panel. These deviations are generally beyond the scale of the comparison and sometimes registering as greater than +/- 5mm. The areas of large deviations were due to noise from a lack of signal returning from the dark square and circular photogrammetric targets on the panel surface. Removing the areas of the highest deviations allowed the resulting comparison to provide a better assessment of the performance of the imaging system (Figure 4-10, right).

dist std dev = 0.04 mm   dist std dev = 0.02 mm
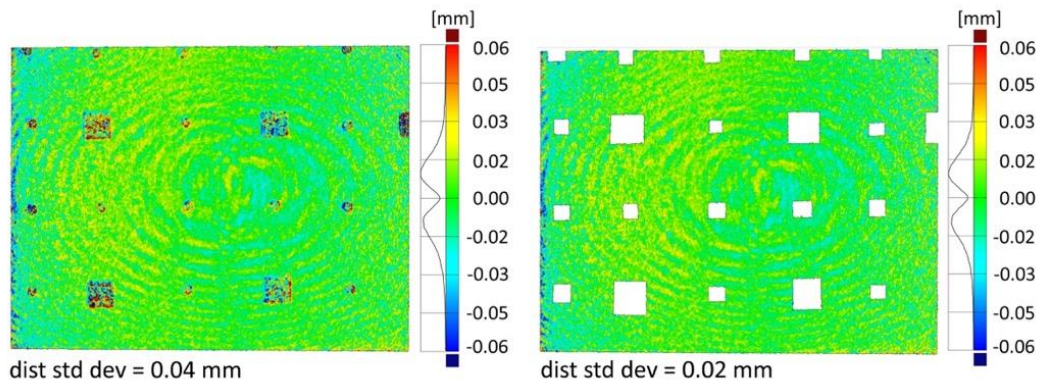
Figure 4-10. Surface discrepancy maps highlighting the systematic error observed as a ripple pattern and the bimodal distribution of the histogram. The surface discrepancy map is comparing the 3D reconstruction of the f/11 dataset and the averaged reference mesh. The removal of the dark targets from the comparison provides a better assessment of the performance of the imaging system.

The bimodal distribution typically indicates a systematic error. In this case, it resulted from the default selection of a feature 'Collect local deviation peaks' in the GOM Inspect surface comparison calculation found under 'Expert parameters'. When selected, this feature enhances the high and low deviations in the data which increases the visual appearance of the residual lens distortion pattern (Figure 4-11, left), and when deselected the results provided a normal distribution without enhancing the local deviation (Figure 4-11, right).

dist std dev = 0.02 mm   dist std dev = 0.01 mm
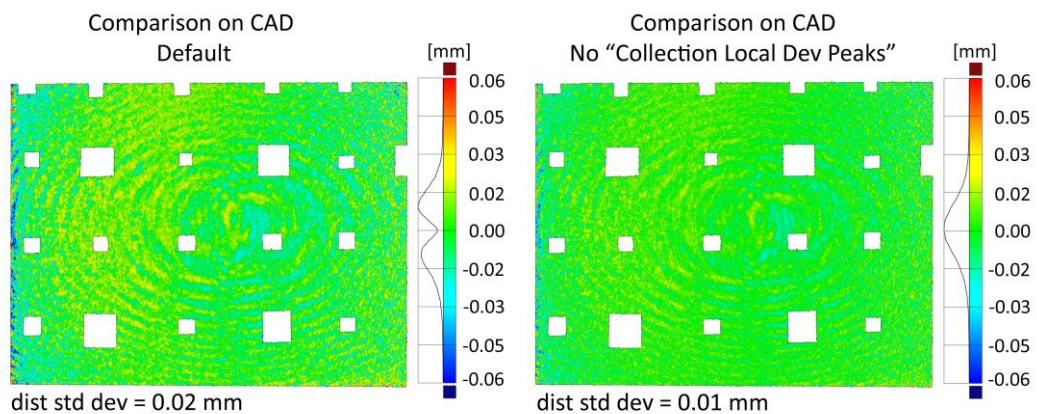
Figure 4-11. Surface discrepancy maps comparing results with different GOM Inspect parameters. A default setting in the surface comparison calculation enhances local deviation peaks resulting in bimodal distribution (left), while deselecting this default parameter provides a normal distribution (right).

4.1.4. Investigation of systematic error resulting in ripple pattern

The previous sections started to illustrate the process of identifying systematic errors and correcting those errors in order to get to the level of random errors which can provide an indication of the limitation of the imaging system. The systematic errors have included the unmodeled lens distortion from the normal image configuration and the unflatness of the

Panel test target. Despite correcting for these systematic errors, the assessment of the 3D reconstruction with the averaged reference mesh resulted in another systematic error becoming apparent; this was a ripple pattern with an amplitude of about +/- 0.02 mm.

The ripple pattern was thought to be caused either by the pattern on the Panel test target or an optical issue. One hypothesis was that the source of the ripple pattern was caused by an artefact from the pseudo-random pattern of the Panel test target. Two tests explored this. The first looked at frequency response analysis involving the Fourier transform of image details of the Panel test target—results suggested that the pattern would not be the cause. The second test involved documentation of a flat surface without the pattern. A wood panel was documented, but the plane fitting with the resulting 3D reconstruction indicated that it was not flat enough to provide evidence of whether or not the pattern was contributing to the ripple systematic error.

The second hypothesis for the cause of the ripple pattern pointed to an optical source. Two investigations explored whether the lens or the camera model were a source the systematic pattern: (1) lenses and camera-object distances, and (2) camera models and calibration parameters.

4.1.4.1. *Lenses and camera-object distances*

A comparison of image sets acquired with different lenses was assessed to establish whether the ripple pattern was resulting from the camera model not properly modelling the distortion for the 60 mm lens. Image sets acquired with the 24 mm and the 50 mm lenses (Table 4-1). The images for the three lenses were acquired at a camera-object distance of 60 cm with the same seven image convergent configuration. Another image set was acquired with the 60 mm lens and a camera-object distance of 40 cm to see if the change in magnification would influence the ripple. The ripple was still present for the 24 mm and 50 mm lenses (Figure 4-12). The noise for the 60 mm at 40 cm camera-object distance was a little higher, but at the edges there was still a hint of the ripple, which was not as prominent as the three lenses at 60 cm.

4.1.4.2. *Camera models and parameter selection*

Image-based 3D reconstruction using SfM-MVS relies on self-calibration and the estimation of the camera model during the bundle adjustment through self-calibration. Section 2.3.4.3 discussed camera models and parameter selection. The CHI *error minimisation workflow* recommends initially solving for the default PhotoScan parameters (f, cx cy, k1-,3, p1-2) using the iterative process of gradually selecting, deleting and optimising, and completing

this optimisation process by solving for all the parameters (f, cx cy, k1-4, b1-2, p1-4). However, James et al. (2017) discussed the risk of over-parameterisation and the errors that it might introduce into the resulting model if too many parameters are selected.

In order to better understand whether the parameter selection, the camera model optimisation was investigated to see if over-parameterisation was causing any of the error observed with the Panel test target results. Following the procedures demonstrated by James et al. (2017), the influence of the camera model parameter sets were assessed using an image set with sequentially more complex camera model parameter sets. These sets are presented in Table 4-3, and the first four (A-D) were presented by James et al. Three additional sets were included (E-G). PhotoScan v.1.3.3 allowed for optimisation with one or two radial distortion parameters at a time, which was not possible for the version (v.1.1.6) of the software used by James et al.
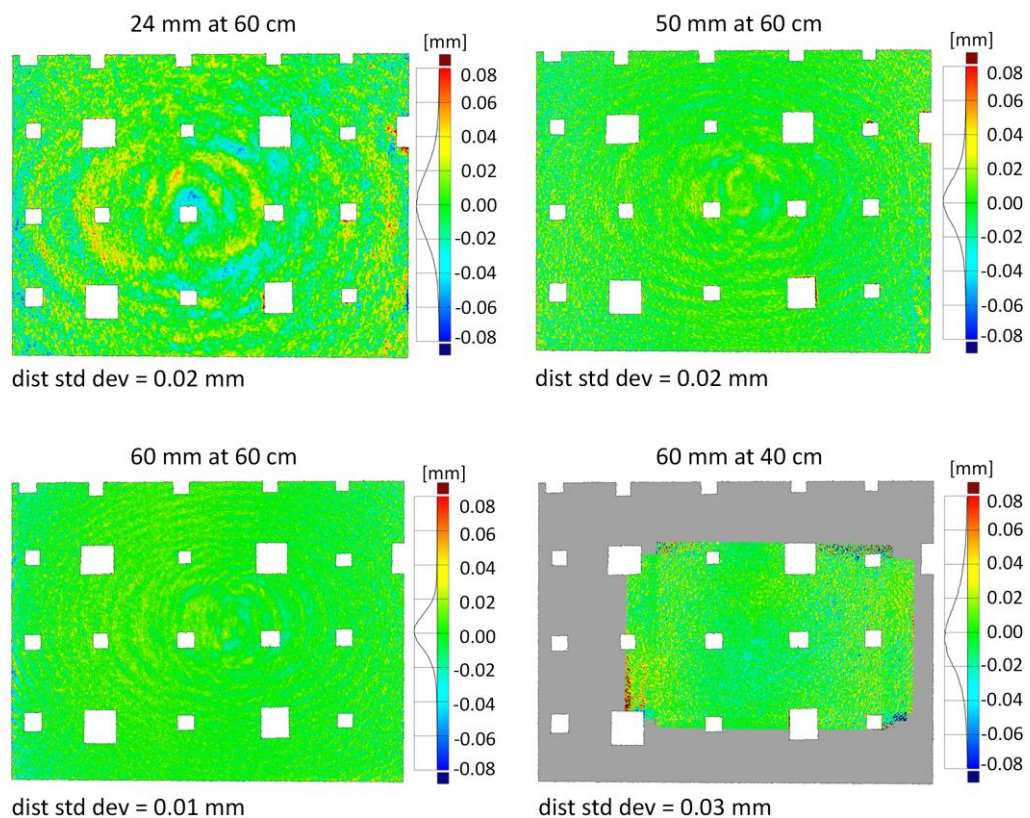
Figure 4-12. Surface discrepancy maps comparing different lenses and camera-object distances. The surface discrepancy maps compare the 3D reconstructions from three lenses (24 mm, 50 mm, 60 mm) at a camera-object distance of 60 cm and the 60 mm lens at 40 cm.

The results for the different camera parameter sets were assessed by comparing the 3D reconstruction with the averaged reference mesh (Figure 4-13). Set A serves as the control—no parameters for radial or tangential distortion, affine or shearing errors were selected. The

results showed the doming effect discussed by Wackrow and Chandler (2008) from unmodeled lens distortion (Section 4.1.2). With the exception of Set A, the results showed some similarities between several of the parameter sets. Solving for two radial distortion coefficients and two tangential distortion coefficients (Set G) reduced slight doming and wave effect seen in Set E and some of the noise that was appearing at the edges of Set D and F. While the camera model parameters can be selected to improve the resulting model (Figure 4-13), the different parameter sets did not eliminate the ripple pattern, which was most notable with Set E but still present for Sets B, C, D, F, and G.

These results of the Panel test target did not show significant deformation, processing artefacts, and increased spatial variability of error for this particular object and scale. However, James et al. (2017) reported significant error with geomorphology applications and made an important argument that processing details need to be reported with results. Camera model parameters and over-parameterisation need to be considered when processing 3D reconstructions of heritage objects.

It is also important to note that looking at the processing results and statistics from the processing does not expose systematic error (James et al., 2017). James et al. described the importance of reporting the statistical description of the model error, but that this needs to be supplemented by the visualisation of the spatial distribution of the error to catch hidden and potentially complex systematic errors.

Table 4-3. Camera models and their parameters. A-D from James et al. (2017)

Camera model	Parameters included
A	Focal length *f*
B	Focal length, principal point, radial distortion (three parameters) *f, cx cy, k1, k2, k3*
C	Focal length, principal point, radial distortion (three parameters), tangential distortion (two parameters) *f, cx cy, k1, k2, k3, p1, p2*
D	Focal length, principal point, radial distortion (four parameters), tangential distortion (two parameters), aspect ratio, skew *f, cx cy, k1, k2, k3, k4, p1, p2, b1, b2*
E	Focal length, principal point, radial distortion (one parameters) *f, cx cy, k1*
F	Focal length, principal point, radial distortion (two parameters) *f, cx cy, k1, k2*
G	Focal length, principal point, radial distortion (two parameters), tangential distortion (two parameters) *f, cx cy, k1, k2, p1, p2*
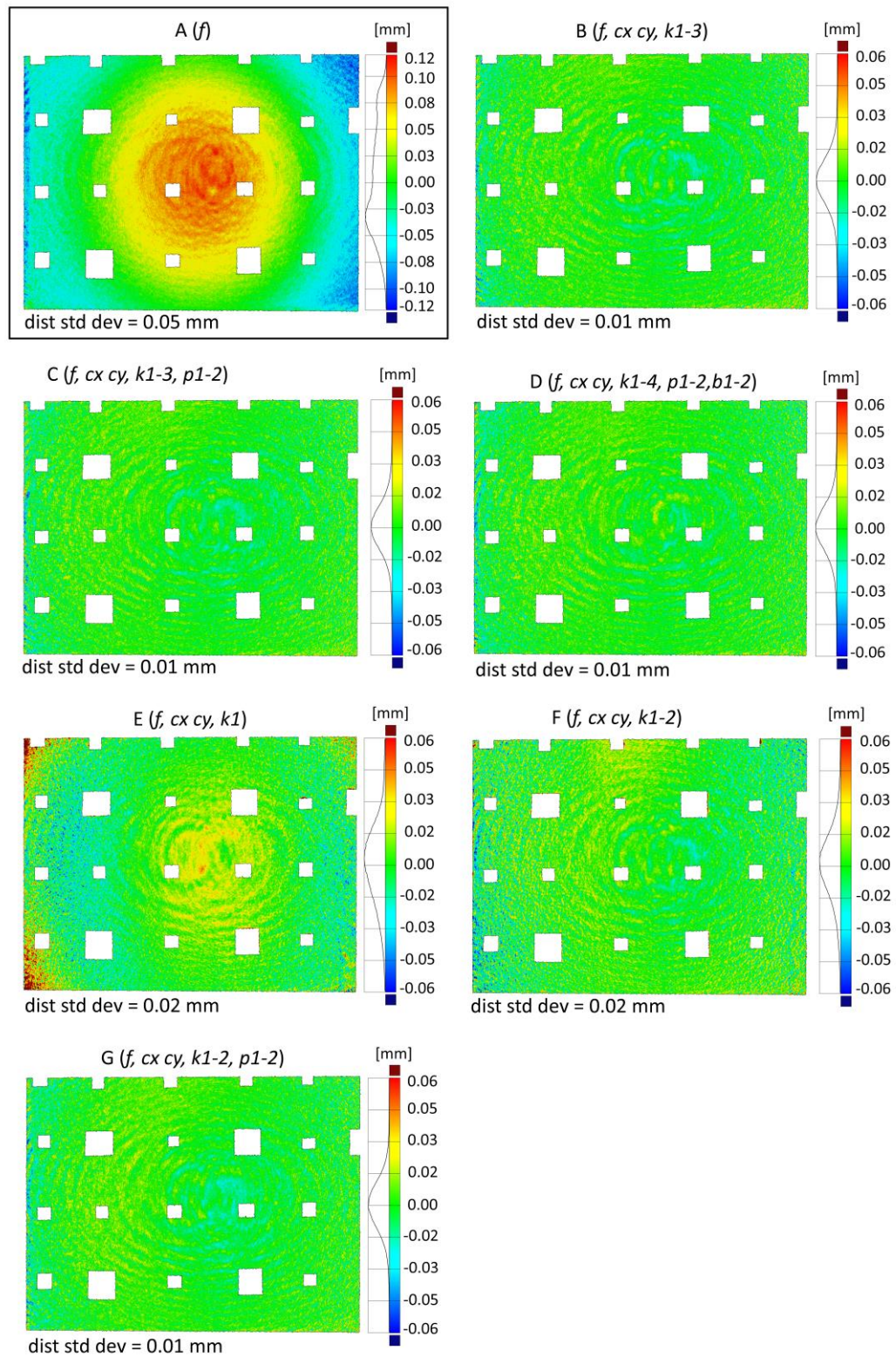
Figure 4-13.Surface discrepancy maps of 3D reconstruction results testing different camera parameter sets. The first four sets (A-D) are from James et al. (2017) and the remaining sets were testing additional parameter set combinations.

4.1.5. Independent reference

Despite different investigations to identify the source of systematic error observed as a ripple pattern, the source was not identified. As the final step for the optimisation of the acquisition, processing, and assessment for the image-based 3D reconstruction of the Panel test target, an independent reference dataset was acquired. Ten images were acquired handheld with a convergent configuration and a camera-object distance of 81.5 cm (estimated from PhotoScan) by Stuart Robson, February 2019, using a Nikon D600 camera and 35 mm lens. The ground resolution was calculated as 0.131 mm/px.

The dataset acquired with the Nikon camera provided a measure of the Panel test target that was independent of the Canon camera system used elsewhere in this thesis; however, the resulting data was not two to three times more accurate than the 3D reconstructions that were assessed so it was not considered a ground truth. It did provide a measurement from a different imaging system (camera and lens) and different camera-object distance. The GSD was lower than that of the 3D reconstructions acquired with the Canon and 60 mm lens. The final systematic error observed with the Canon imaging system had an amplitude of 0.06 mm indicating that imaging system could resolve features greater than 0.06 mm. The Nikon data had a noise level of about +/- 0.06 mm indicating that that imaging system could resolve features greater than 0.12 mm.
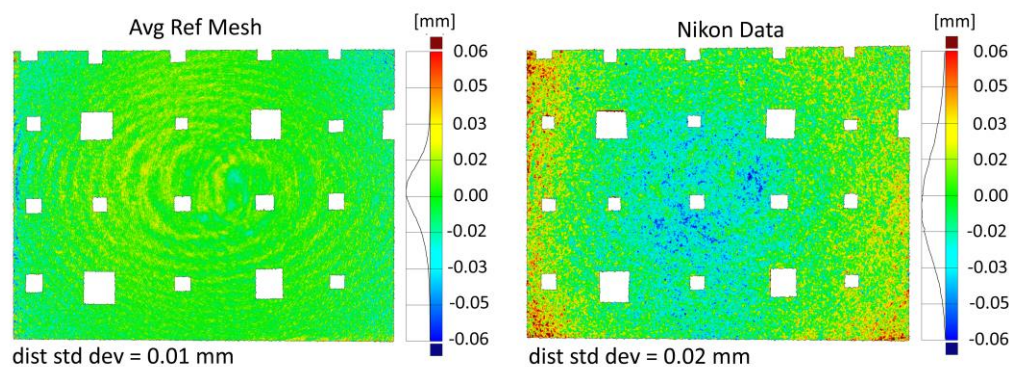
Figure 4-14. Surface discrepancy maps comparing the averaged reference mesh and the Nikon data. The figure includes surface discrepancy maps of the f/11 a1 3D reconstruction (Section 7.1) compared to the averaged reference mesh (left) and the Nikon data (right). The f/11 a1 data set has been processed using a camera model with two radial parameters and two tangential parameters (k1-2, p1-2).

The averaged reference mesh is not an independent reference and had accumulated the systematic errors of the 3D reconstructions used to create the mesh. By using this as the reference data, the systematic error observed as the ripple pattern was actually exaggerated when the 3D reconstructions with the systematic error were compared to the reference, in some cases creating an increased amplitude of the error. Since the ripple pattern became a feature in the averaged model, the assessment of the 3D reconstructions would result with

the ripple pattern whether or not it originated in the 3D reconstruction being assessed. The use of an averaged reference mesh in this research had been intended as a means of assessing accuracy, but the results of this chapter indicated the limitations of the averaged model as reference data and emphasised the need for independent measures for assessing the results.

4.2. Mango Vase

The Mango Vase test object (Figure 4-15) was initially designed as the primary test object for the research. However, the research required a more fundamental test object to assess the performance of the imaging system and resulting quality, so the Panel test target was introduced and was able to assess the performance of the imaging system. The Mango Vase was designed to have a more complex geometry and similarities to a heritage object including materials and shape thus it will more closely relate to museum collections than the Panel.

Figure 4-15. Mango Wood Vase test object.

While the Panel presented differences with acquisition, processing, and assessment, methods from Section 4.1 could be applied to the documentation of the Mango Vase and museum collections. The optimisation process with the Panel test target demonstrated the challenges and considerations for the reference data and the approach of identifying systematic errors and correcting and calibrating for these in order to establish the sensitivity of the imaging system for surface recording of an object.

4.2.1. Materials and methods

4.2.1.1. Mango Vase

The creation of the Mango Vase test object was informed by the painted panel target presented by George et al. (2017) and Cucci et al. (2019) (Section 3.3.2), and the considerations presented by Hess (2015a) in the creation of the metric test object. The Mango Vase (19 x 13 cm) included line patterns (graphite and ivory black), tempera pigment patches (Prussian blue, azurite, malachite, madder lake, zinc white, and titanium

white) and varnished areas (shellac and mastic) (Figure 4-15). These materials respond differently to different illumination (UV, visible, and NIR) including luminescence, reflection, absorption, and transmission. (See Appendix 14.2 for more information about the creation of this test object.)

The reference data for the Mango Vase was acquired using a structured light scanner at AICON 3D Systems GmbH (Meersburg, Germany) in February 2016. This structured light scanner, the stereoSCANneo, had two 16 MP monochrome cameras and a digital light projector with 3 LED diodes. The field of view was 550 mm and the scanner were calibrated at the beginning of the acquisition (calibration value of 5.88 μm). The acquisition settings included 4 grabs, 12 views per rotation, and an averaging value of 8. The alignment RMS was 11μm. The data was acquired by Lewis Homer and Dirk Rieke-Zapp from AICON 3D. As discussed in Section 4.1.1.3 the resulting 3D reconstructions were assessed using GOM Inspect to compare to the reference data.

4.2.1.2. Turntable setup

While the camera positioning robot was used for recording the Panel, a turntable setup was used to record the Mango Vase in the round (Figure 4-16). The turntable setup more closely resembles a setup for heritage objects and provides more practical evidence for the applications and implications of this research. The turntable allowed for the object to be rotated, while maintaining a constant camera-object distance with the camera mounted on a tripod. When working with a heritage object, this reduces the handling of the object. The turntable setup was also used for the imaging study in Section 6.2.

Figure 4-16. Imaging setup with Mango Vase test object on turntable.
The camera is mounted on a tripod and one of the two flashes with umbrellas is seen in the image. CHI scale bars are positioned on the turntable around the object.

The object was positioned on a manual turntable and images were acquired every 10° from three camera angles, referred to as 'views' (Figure 4-17). The camera-object distance was 60 cm. The Mango Vase, as a three-dimensional object, required documentation in the round facilitated by the use of a turntable. The turntable data acquisition resulted in a larger network (more than 100 camera positions)

than the seven-image convergent network for the Panel test target. The turntable acquisition is representative of how small to medium sized museum objects are recorded.

Images included reference scales and targets for processing, calibration, and scaling of the image sets. Reference images were acquired including a white field image, X-Rite ColorChecker Passport (X-Rite, Grand Rapids, MI, USA), and Spectralon Reflectance Targets (Labsphere, North Sutton, New Hampshire, USA). CHI photogrammetric scale bars (Section 2.3.2) were placed around the object during acquisition for scaling (Figure 4-16).

After images were acquired of the first view (lower ring in Figure 4-17), the camera was raised by increasing the height of the central tripod column by 20 cm to the position for view 2. The camera was not refocused, but Live View on a tethered laptop was used to ensure that the focus was still sharp, and the object was centred in the field of view. The tripod was moved to fine-tune the focus as opposed to refocusing the camera. Refocusing the camera would alter the camera calibration, so the lens focus was maintained for each dataset. The process was repeated for the second view and the camera raised by 16 cm for the third view.
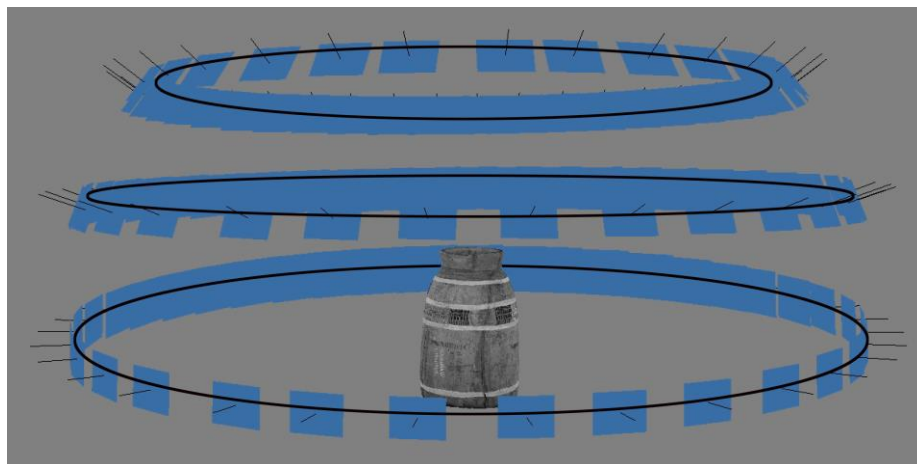
Figure 4-17. Camera positions for the 3D reconstruction of the Mango Vase. The camera positions are represented by blue rectangles.

The unmodified Canon and the 60 mm lens were used along with two Bowens Gemini GM400Rx studio strobes with umbrellas (Table 4-1). The ISO and shutter speed were the same for each image set (ISO 100 and 1/100 sec shutter speed); Table 4-4 shows the changing aperture and corresponding flash power. The flashes were positioned about 130 cm from the object centre, 97 cm from the camera, and 125 cm from the floor.

The RAW image processing and 3D reconstruction for the Mango Vase were the same as presented in Section 4.1.1 for the Panel test target using Agisoft PhotoScan and the CHI *error minimisation workflow*.

Table 4-4. Camera and flash settings for the Mango Vase image sets.

Aperture	Flash Power
f/5.6	1
f/8	2
f/11	3
f/16	4
f/32	6

There were different methods used to assess the 3D reconstruction results including visual comparisons and global and local comparisons. Visual comparisons looked at the differences between the features that could be resolved (Section 4.2.5), while the global and local comparisons were based on comparing the differences between geometries by aligning the resulting 3D reconstructions with reference data. The following more specifically describes the alignment of models and the visualisation of the surface differences.

The resulting 3D reconstructions were compared to the 3D scanned reference data using GOM Inspect. GOM Inspect was able to better handle the alignment of the reference data and the resulting 3D reconstructions, both more quickly and more smoothly than the freely available open source option CloudCompare ('CloudCompare', 2018). Similar to the Panel test target the surface deviations were visualised through colour scaled discrepancy maps that include a histogram indicating the distribution of the discrepancies. The Mango Vase test object has a rotational symmetry that made the alignment of the data more challenging, an issue that will be further discussed in the following section.

4.2.2. Alignment

Alignment proved to be an important issue with the Mango Vase due to its rotational symmetry, which was not considered when the test object was selected and developed for this research. Accuracy of the alignment is critical and can significantly impact the resulting comparison and assessment of the 3D reconstruction results. While the alignment of the Mango Vase data was focused on comparing and assessing 3D reconstruction results, the reliability and accuracy of alignment is also critical for multi-temporal data and monitoring objects over time. Discussing alignment including challenges and means of improvement are relevant for assessing 3D reconstructions and monitoring objects. It is important to first discuss the challenges related to alignment as it is the first systematic error that needs to be addressed before being able to look at other components for optimising the acquisition, processing, and assessment of image-based 3D reconstruction of the test object. The following sections look at three stages where alignment can be addressed: setup and acquisition, processing, and comparison and assessment.

Alignment issues can potentially be mitigated during the setup and acquisition by including the documentation of the base of the object and the inclusion of targets. These considerations would be for future documentation as the image data for all the experimental work had already been acquired and there was not an opportunity to reacquire additional datasets to test these considerations.

Documenting the base

The documentation of the base provides a more complete record of the object and could improve the alignment of the data by reducing the noise along the base edge and adding an additional surface for alignment. However, the base of the Mango Vase was consciously not recorded. Recording the base of an object adds handling and increased risk to the object. Generally, an object is positioned according to how it naturally "sits" and its maximised stability for a turntable acquisition. Positioning the object upside down to acquire the underside might require additional props and armatures for supporting the object without obscuring the camera view of the object. While there was less concern for the risk of the Mango Vase as a test object, the acquisition aimed to mirror the acquisition of a museum object, which was why the bottom was not documented for this experimental work. The alignment challenges with the Mango Vase for the assessment of the 3D reconstruction results encouraged the reconsideration of the documentation of the base of this object and similar objects.

Targets

Targets present another option related to setup and acquisition that could improve the alignment of 3D reconstructions (Section 2.3.3.1). While targets are widely used for photogrammetric applications outside of cultural heritage and are essential for measurement applications, they were not considered for documentation of the Mango Vase. Generally, they cannot be used on the surface of a heritage object due to potential disturbance and damage. However, studies have reported using targets around an object for alignment, scaling, and improved measurement capabilities (Robson et al., 2004; Gallo et al., 2014; MacDonald et al., 2014; Sapirstein, 2018). For the experiments run in this study, coded targets would greatly improve the ease of aligning datasets, but a challenge remains when considering the acquisition and comparison of multi-temporal data. Once the object moves in relation to the targets, the targets cannot be used to align the datasets and there is still the challenge of aligning 3D data for comparisons.
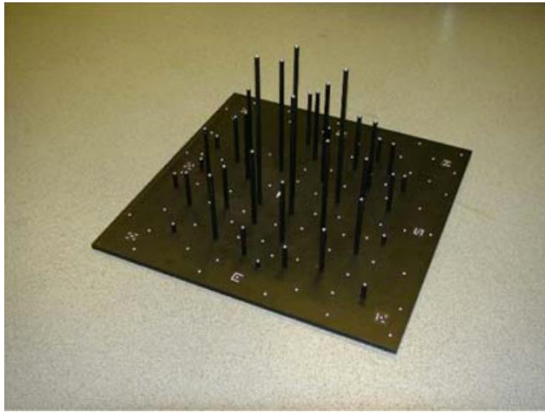
Figure 4-18. 'Manhattan' 3D test object. Image from Robson et al. (2014).
Image' from Robson et al. (2014).

While targets can help with the alignment of different datasets, they can also be useful for scaling and improved measurement capabilities, refining the camera calibration, and assessing accuracy. For future image-based 3D reconstruction, it would be worth considering the scale bar and calibration target used by Sapirstein (2018) and the potential of a control field like that used in MacDonald et al. (2014). However, the targets used by Sapirstein (2018) and MacDonald et al. (2014) were contained in a single plane at the base of the object, so there still may be limitations in the accuracy of the scaling resulting from these targets. The recording of the Mango Vase also only included scale bars in a single plane at the base of the object, which might be the source of some scaling inaccuracies. To remedy these scaling issues, the targets and scale bars need to cover the volume of the area being recorded so that references are spread through that full volume. An option may be to create a framework with posts around the object that include targets on the posts keeping in mind minimal obstruction between the camera and object. This may be constructed as an amalgamation of a 'Manhattan' 3D test object (Robson et al., 2014) (Figure 4-18), the calibration target in Sapirstein (2018) and control field in MacDonald et al. (2014).

4.2.2.2.   Processing

The previous section focused on options for addressing alignment issues in the first stages of image-based 3D reconstruction, but these cannot be used to address the challenges of aligning previously acquired datasets of the Mango Vase that did not include the base and coded targets. Processing options had to be considered to improve the alignment of already acquired data, which can be addressed in the image-based 3D reconstruction software (i.e., PhotoScan) or in the software used for assessing and comparing results (i.e., GOM Inspect).

Agisoft PhotoScan

The setup for the acquisition of the Mango Vase included the placement of four CHI scale bars around the base of the object. These scale bars include non-coded targets (cross-shaped, patterned targets) that maintained a consistent relationship with the test object through the image sets. Ideally these targets could be used as reference points, as discussed previously, for alignment during the PhotoScan processing. Using PhotoScan both coded and non-coded

targets have the potential to be automatically detected. The autodetection of coded targets provides the specific point identification for each target and the different image sets can be aligned based on these targets (a *marker-based* alignment in PhotoScan). The autodetection of non-coded targets results in different sequences of detection and a numbering of the targets based on that sequence. The sequence is not consistent and therefore the autodetection of non-coded targets in different image sets cannot be used for target-, or marker-based, alignment.

In addition to the challenges with non-coded targets and autodetection, the targets were not automatically detected in every dataset due to the oblique positioning and resulting unsharpness of the features of the scale bars. The detection of the targets both automatically and manually is impacted by DOF. As the DOF increased, the ability for the software to autodetect targets improved. With apertures of f/5.6 and f/8, three targets were detected but none of these were actually the cross-type non-coded targets on the scale bars. With apertures of f/11, f/16 and f/32, 8, 10, and 10 targets respectively were detected with four of the targets being detected on the cross-type non-coded targets. With an aperture of f/32, the ten detected targets were all on the scalebars.

A significant and recent update to the CHI image acquisition guidelines (Schroer et al., 2017b) included the acquisition of a "flat project" in addition to a full turntable acquisition of an object. If the scale bars are only placed around the object during a turntable acquisition, the coded or non-coded targets may not always be in focus, obscured by an angled view, and therefore not easily detectable by the software (Figure 4-19). A "flat project" is the acquisition of images with normal image configuration of the object surrounded by scale bars. Three passes of the scene are acquired with the camera in landscape orientation (0°), rotated 90°, and rotated 270° (Figure 4-20). This acquisition provides a clearer view of the scale bars for detecting the targets and scaling the project (Schroer et al., 2017b). The images for the "flat project" can be used for alignment and optimisation, but are disabled when building the dense cloud, mesh, and texture. Whilst this update in the CHI workflow was not implemented into the image acquisition for the Mango Vase, but it is an important consideration for the setup and acquisition of future datasets.
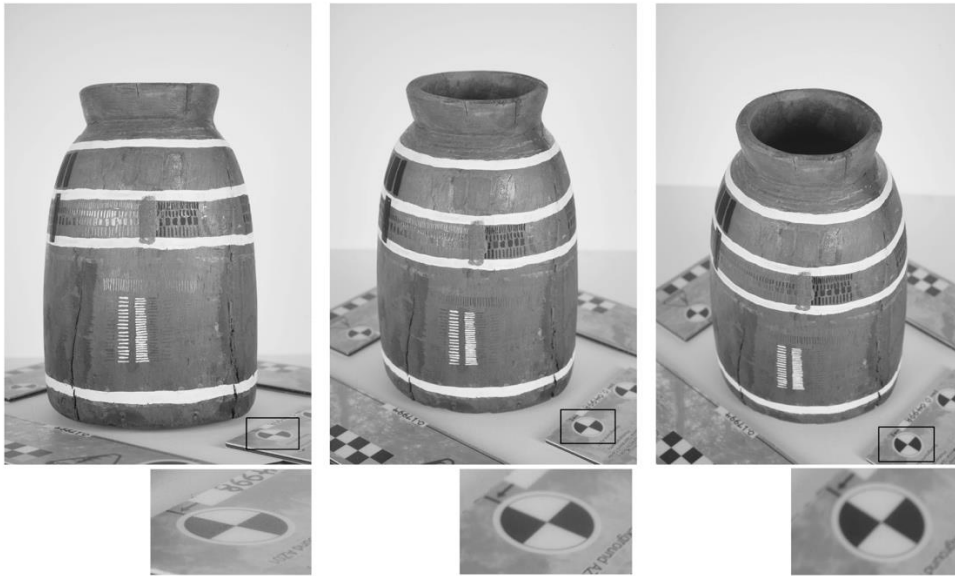
Figure 4-19. Example of targets in the image obscured by oblique positioning. Input images from the turntable workflow without "flat project" acquisition showing views of non-coded target on scale bar. From the three views, there is not always a clear view of the target for detection.
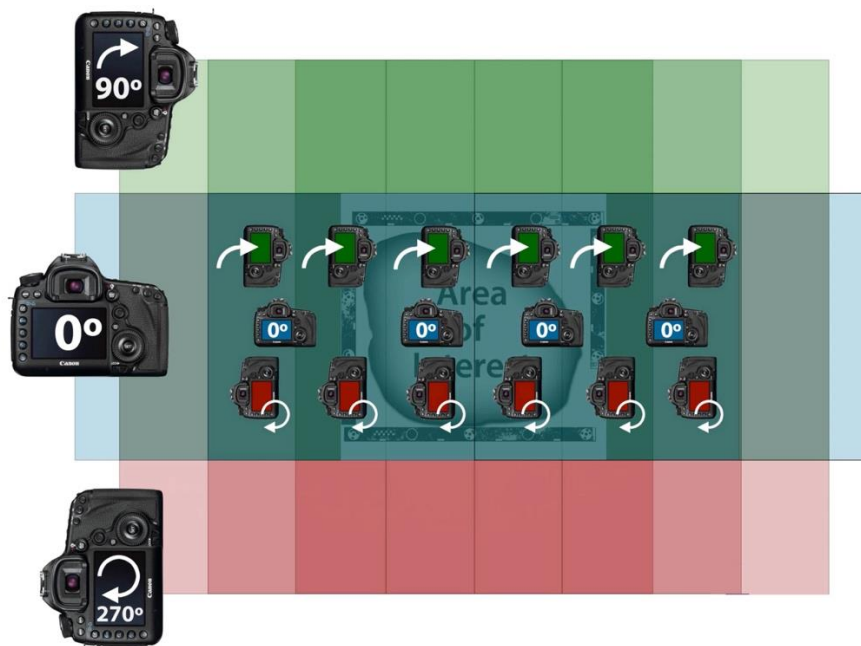
Figure 4-20. CHI illustration of "flat project" image acquisition from CHI workflow. Three passes of the scene are acquired with the camera in landscape orientation (0°), rotated 90°, and rotated 270°. Illustration is a screenshot from video tutorial (https://vimeo.com/channels/practicalphotogrammetry).

Due to the issues and limitations of autodetection of the non-coded targets on the CHI scale bars positioned at the base of the Mango Vase, the targets were manually selected. The manual process of selecting the targets has the potential to be less repeatable than automated thus introducing uncertainty. To better understand the repeatability of the manual selection of targets and the amount of uncertainty introduced by this process, the manual selection of

four targets on two scalebars was repeated three times on the same image set (the f/8 image set). The resulting 3D reconstructions (Figure 4-21) showed a difference in scaling, a small difference in standard deviation (+/-0.02 mm), and an offset from zero. This assessment of three results was not enough to fully quantify the uncertainty of manual detection of the targets for the documentation of the Mango Vase, it can be noted that there was at least an uncertainty of +/-0.15 mm from the manual detection. While this section was focusing on alignment, the manual detection of the scale bars will also impact the scaling of the model.
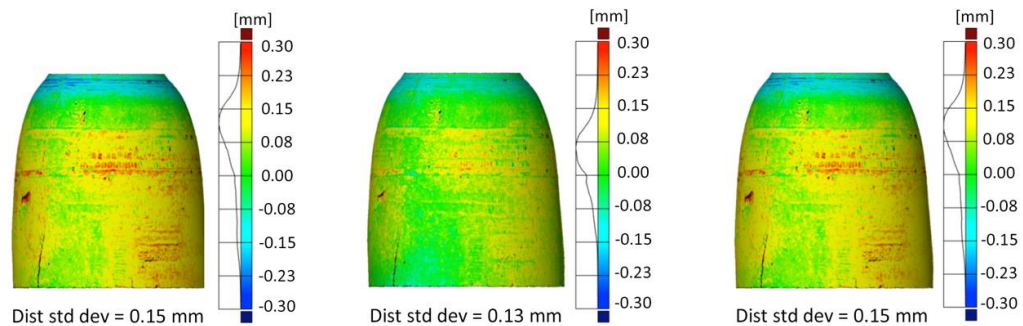
Figure 4-21. Surface discrepancy maps of the 3D reconstruction results of the Mango Vase for three iterations of manual marker selection. The figure includes surface discrepancy maps of the 3D reconstructions with the markers selected manually three times compared to the 2016 3D scanned data.

Coded targets included in the scene could have improved the accuracy of the alignment as discussed in a previous section. These would have aided in the autodetection of targets both for scaling the 3D reconstruction and also for aligning the different data sets. Autodetection of the targets is more repeatable and accurate than manually selecting the targets and also less time consuming. While coded targets would have improved the alignment for the camera characterisation and 3D reconstruction assessment, there would still be a problem with aligning the reference data and even multi-temporal data in a monitoring campaign. The reference data did not include targets, and the rotational symmetry would still challenge the alignment with the reference data and the image-based reconstructions.

4.2.2.3.   Comparison and assessment

The resulting models were compared to the 3D scanned reference data using GOM Inspect (Section 4.2.1.2) and the prealignment function, a global best-fit alignment and a subsequent local best-fit. The surface deviation was calculated and visualised through colour scaled discrepancy maps with a histogram indicating the distribution of the discrepancies. Since the base of the vase was not acquired, the bottom edges of the model were noisy and included areas with the largest deviations in the surface discrepancy maps. These larger deviations can impact the alignment of the models. When these areas were removed from the comparison, the fitting of the two models improved and the results provided a clearer

indication of the capabilities of the imaging system (Figure 4-22). The cropped versions showed a progressively improved fit of the model to the reference data (the offset from zero is reduced) and the spread of deviation is reduced (decreased standard deviation). When focusing on only a local patch (Figure 4-22, lower right), the error distribution was centred at zero with a spread of 0.09 mm showing the best fit and lowest discrepancies. The discrepancies in the patch showed more detail in the local features, the differences in the pigment patches, and line patterns was more apparent. The results from local patch do not quite reach the limitations of the system derived from the Panel test target (0.06 mm with a standard deviation of 0.01 mm), but reducing the comparison to a local patch does improve the assessment.
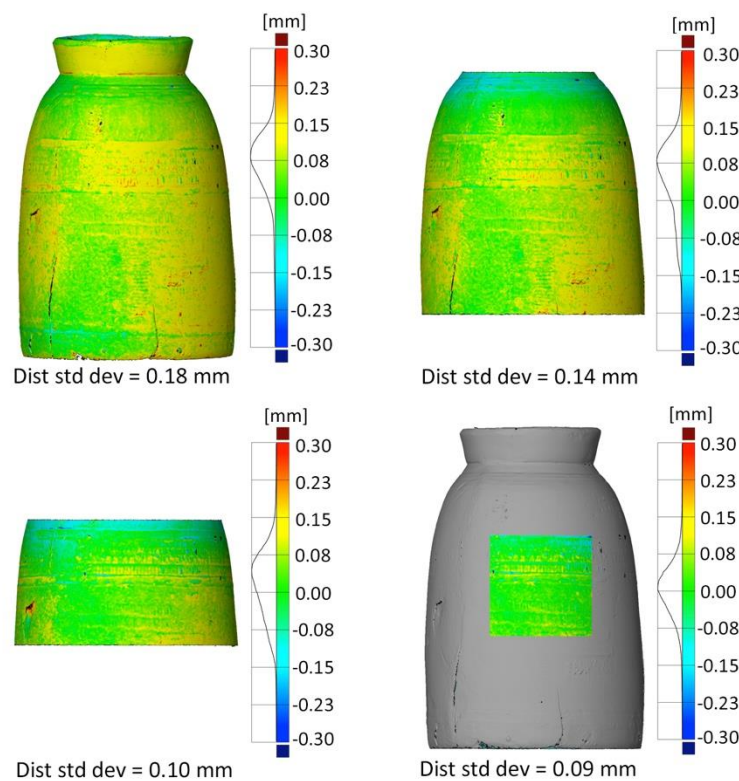
Figure 4-22. Cropping models for surface comparison to improve fit and decrease standard deviation. The figure illustrates the improvement of the fit between the reference data and the 3D reconstruction by removing the areas with larger discrepancies. Four comparisons are included: the overall model of the vase, two cropped versions, and a local patch.

The cropped versions in the round (Figure 4-22) included areas of the surface comparison that are not all visible from any given view. The surface discrepancy map can be virtually unwrapped as one option for viewing the full dataset (Figure 4-23). It is important to check all views of the surface discrepancy maps as there may be areas that reveal systematic errors important to be aware of or understand when interpreting the results (Figure 4-23, bottom example).
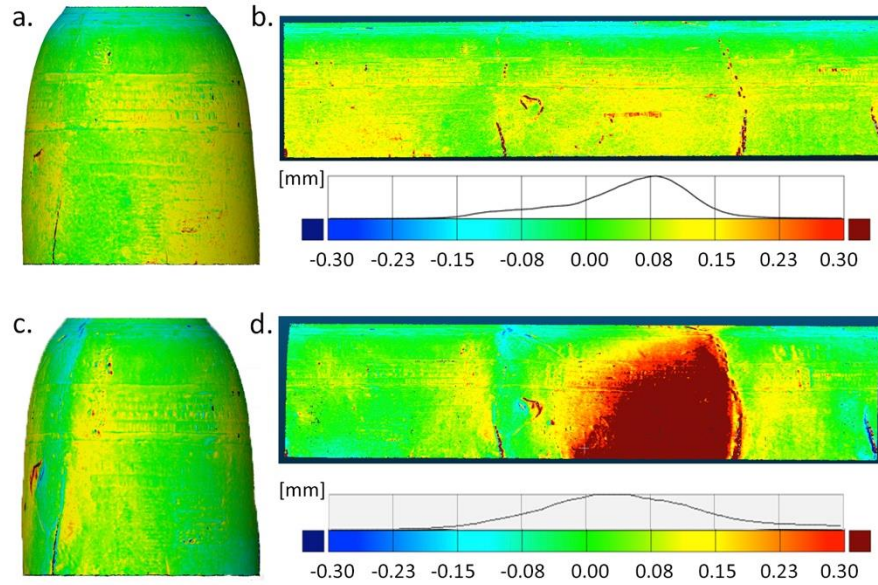
Figure 4-23. Surface discrepancy map: single view and virtually "unwrapped" view. The figure includes (a) a single view of one side of the f/11 DOF dataset compared to reference data and (b) the dataset virtually unwrapped. The bottom example (c and d) includes an example of how the same dataset can have a systematic error related to a different alignment that could be hidden on the opposite side of a surface comparison of an object in the round.

4.2.3. Camera model and parameter selection

The camera model and parameter selection were discussed in the context of the Panel test target in Section 4.1.4.2. The parameters selected for the Panel do not necessarily carry over to the Mango Vase, and the process of determining the best parameter set needed to be repeated for the Mango Vase. The parameter sets for the Mango Vase were the same as the Panel included in Table 4-3.

The results for the different camera parameter sets were assessed by comparing the 3D reconstructions with the 3D scanned reference data (Figure 4-24). The 3D reconstruction results were aligned with reference data using GOM Inspect, and the surface deviation between the models was visualised using discrepancy maps. The results showed that there is not much of a difference between B, C, E, F, and G, which would suggest that solving for only one radial distortion parameter is sufficient. No significant deformation, processing artefacts, or increased spatial variability of error were seen.

In addition to comparing the 3D reconstruction results for different parameter sets, the image sets from the DOF investigation (Section 7.2) were processed with all the parameters selected (f, cx cy, k1-4, p1-4, b1-2) and with a limited set of parameters (f, cx cy, k1) (Figure 4-25). The biggest difference between the selection of all the parameters and a

limited selection was for the f/5.6 image set and the f/11 image set. The other results had similar discrepancies between the parameter sets.

All the results in Figure 4-24 and Figure 4-25 include discrepancy distributions that are offset from zero with the offset changing between different parameter sets. The following sections will look at alignment, scaling, and reference data to better understand the inconsistent offset observed.
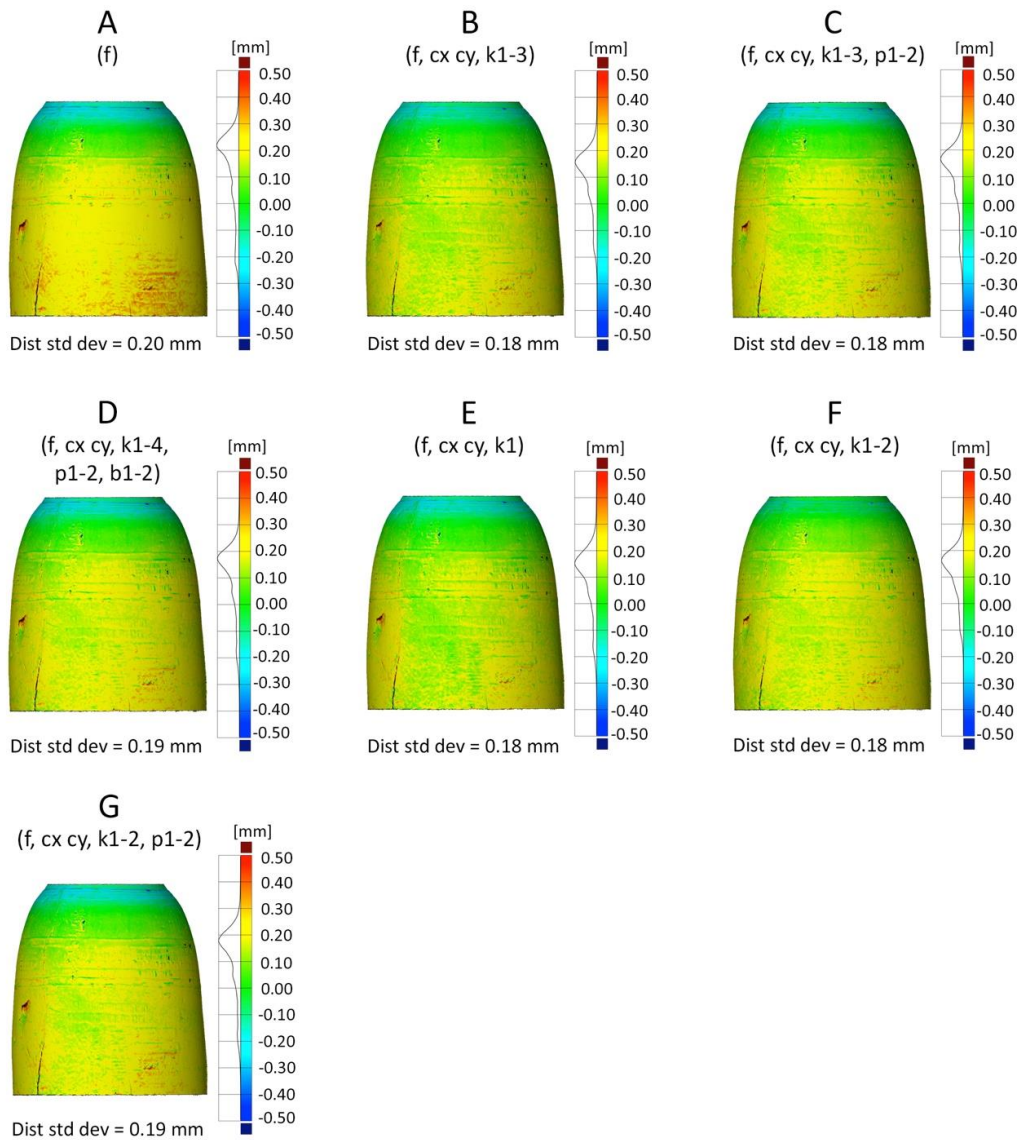
Figure 4-24. Surface discrepancy maps of the 3D reconstruction results of the Mango Vase testing different camera parameter sets. The first four sets (A-D) are from James et al. (2017) and the remaining three sets tested additional parameter set combinations.
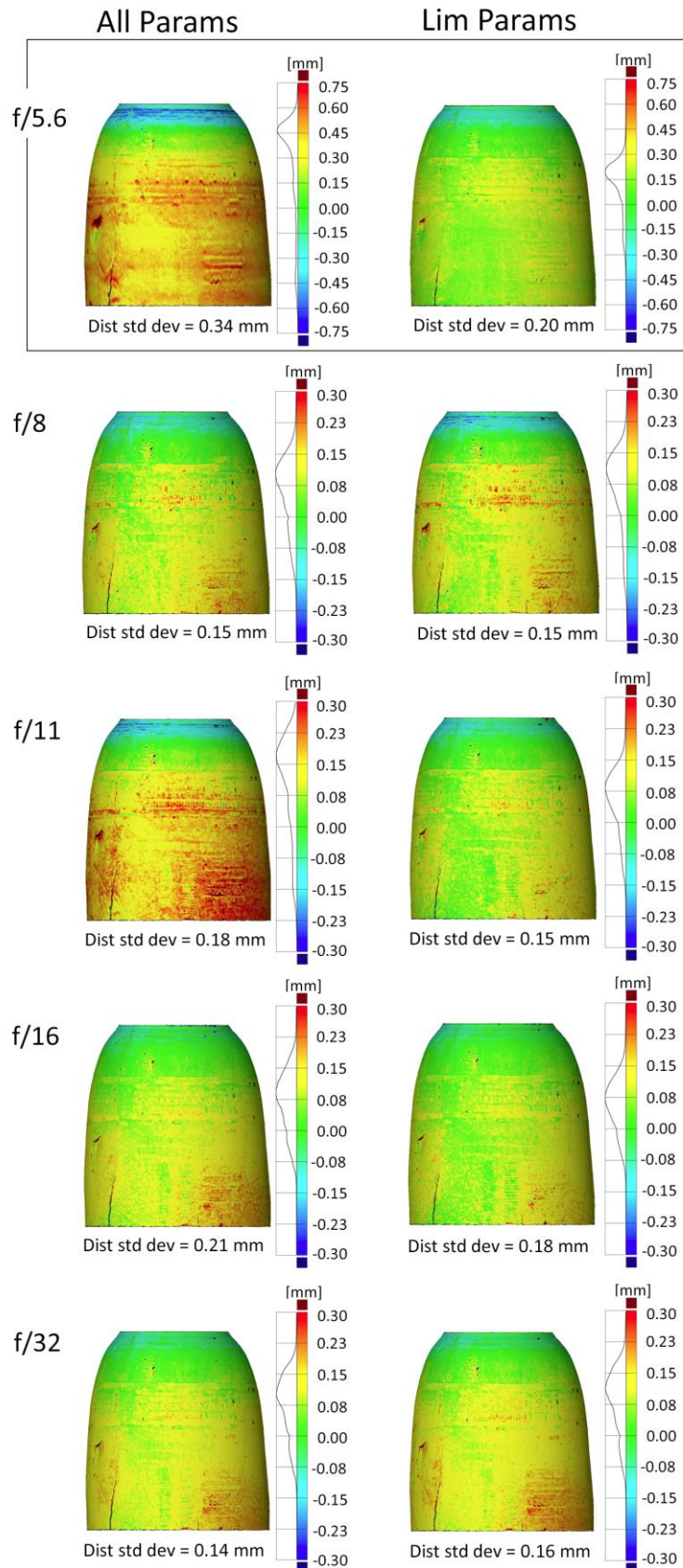
Figure 4-25. Surface discrepancy maps comparing the selection of all parameters for estimating the camera model and a limited selection of parameters (f, cx cy, k1). The figure includes surface discrepancy maps of 3D reconstructions for different apertures (f/5.6, f/8, f/11, f/16, f/32) (Section 7.2) processed with all parameters (left) and limited set of parameters (f, cx cy, k1) (right).

4.2.4. Reference data

As part of the process for identifying the error, the question arose whether the reference data was reliable. Up to this point the optimisation of the image-based 3D reconstruction and assessment had been investigated using a 3D scanned model from 2016 without questioning the accuracy of this reference data. This illustrated a point made by Toschi et al. (2014) that many studies have used 3D reference data originating from active 3D imaging systems and that the metric quality or accuracy of that 3D data was not often questioned. This final section assessed the reference data by looking at additional sources of measurement including a second 3D scanning campaign in February 2019.

Issues related to reference data were initially discussed in Section 2.4 and the challenges with the Panel test target elaborated on the discussion (Section 4.1.3). The main option for reference data for the Mango Vase was to use a more accurate 3D technique. The Mango Vase did not include a known geometric shape, and the Panel provided evidence of the limitations of the averaged reference mesh with accumulating systematic error (Section 4.1.5). The initial 3D scan of the Mango Vase in 2016 was intended as reference data, but based on the errors observed in the 3D reconstruction assessments it was necessary to assess the reliability of the 3D scanned data.

The Mango Vase was 3D scanned again in February 2019. A structured light scanner, the AICON3D smartSCAN-HE, was available from the Smithsonian Digitization Program Office (SI DPO) to scan the test object. The scanner was used with the S-150 field of view, a base length of 240 mm, and a working distance of 370 mm (Figure 4-26). The manufacturer's specifications for this configuration are included in Table 4-5. The scanner was calibrated following the AICON3D scanning procedure and using the AICON3D calibration plate (Figure 4-27). The AICON3D automated turntable was used to automate the recording of the object in the round (Figure 4-28).

Figure 4-26. AICON3D smartSCAN-HE with the S-150 mm lenses.

Table 4-5. AICON3D systems specifications for smartSCAN-HE with the S-150 lens set

Field of view size [mm]	*110 x 80*
Measuring depth [mm]	*70*
X, Y resolution [μm]	*33*
Resolution limit (Z) [μm]	*6*
Feature accuracy [μm]	*10*
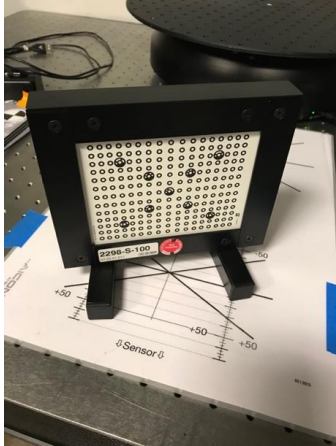
Figure 4-27. AICON3D calibration plate for the S-150 FOV.
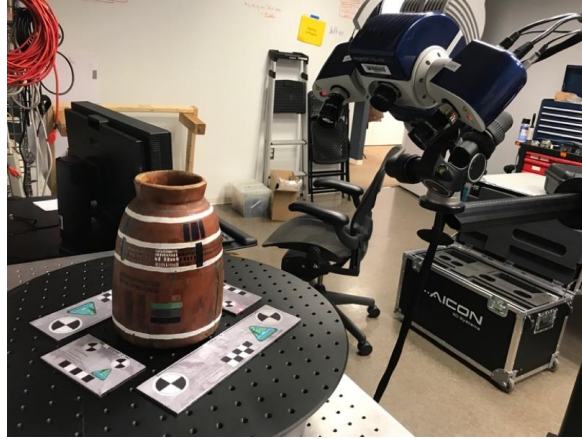
Figure 4-28. Setup for the 3D scanning of the Mango Vase in February 2019.

The re-scanning of the Mango Vase resulted in a high resolution model that was able to resolve the raised features of painted details and small scratches on the wood surface (Figure 4-29). The final model included holes in the data from areas that were problematic, mostly dark and shiny areas such as the black line patterns and the pencil line patterns. Even though the model included some holes, it could still be used to compare with the 2016 data.

Figure 4-29. Detail view of the 2019 3D scan results of the Mango Vase. This image showed the fine details that the scan resolved of the painted features including the raised paint lines of the bands going around the vase and the scratched surface of the wood. This image also showed the holes in the data represented by the black areas.

The resulting 3D data from 2019 was compared to the 2016 data using GOM Inspect (Figure 4-30). The surface discrepancy map showed a deviation of +/-0.30 mm, a difference that was larger than the minimum x, y resolution (33 μm) and the z resolution limit (10 μm), so it is worth discussing contributing factors. Similar to Figure 4-22, the different cropped selections of the comparison (Figure 4-30) showed an improved fit and reduced spread of

the deviations. The surface discrepancy maps were picking up on some of the local feature details of the drawn and painted details, which was indicating the difference between the level of detail the two scans were able to resolve.
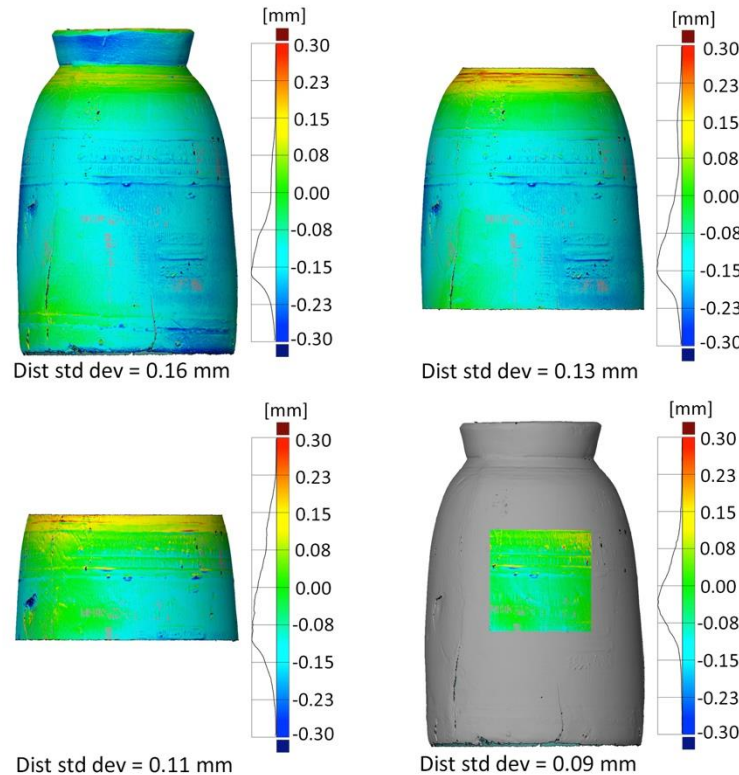
Figure 4-30. Comparison of 2019 scan data to 2016 scan data with different crop versions and a local patch. This figure (similar to Figure 4-22) illustrates the improvement of the fit between the datasets by removing areas with larger discrepancies. The figure includes a comparison with the overall model of the vase, two cropped versions, and a local patch.

With a three year difference between the acquisition of the data sets, the question arose as to whether these differences can be attributed to any physical change in the vase. While it cannot be said for certain whether the vase has physically changed or not, the nature and scale of the errors observed in the surface discrepancy maps is more likely a result from the measurement devices.

While the 3D scanners were both structured light and produced by AICON3D, the scanners were not the same and the difference between the two can be representative of changing and developing technologies. This comparison offers a useful assessment and an example of the challenges of monitoring an object with changes in technology, variations in acquisition and processing, and the limit of the scale of change that can be recorded over time. Comparing the 3D scanned data, it is difficult to say which one is "right" or "wrong". While the 2019 scan provided another source of data at a higher resolution than the 2016 scan data and

presented a surface that seemed to closely relate to the object, it is not necessarily ground truth data. Without ground truth data, the accuracy of the technique cannot be assessed.

This comparison provided an important point, in that, assessing the accuracy is only part of the evaluation. The initial 3D scan was intended to be used as reference data in order to assess the accuracy of the resulting image-based 3D reconstructions. Assessing the accuracy of the imaging system was actually accomplished by imaging the Panel test target; however, this level of detail cannot be achieved when recording the Mango Vase or a museum object. Consequently, comparison in this context becomes more about looking at the local differences and commentary about the individual techniques than about accuracy assessment.

4.2.5.   Discussion

Comparing 3D recording results

The Mango Vase was documented with a few optical imaging techniques including the two range-based and several campaigns of image-based 3D reconstruction. Visual analysis and examining the changes and differences at a global and local scale can provide insight about the techniques and technologies (Figure 4-31). The 2016 3D scanned data (Figure 4-31, left column) resulted in a very smooth surface resolving some of the cracks and the roughness of the paint patch, but the top bands around the neck of the vase were not fully recorded. The 2019 3D scanned data (Figure 4-31, middle column), representative of currently available high end 3D scanner, resolved the fine details of scratches on the surface in addition to the cracks, divots, bands around the neck and the painted details. The image-based 3D reconstruction (Figure 4-31, right column) resulted in a rough surface that was not as smooth as the 2016 data or as detailed as the 2019 data, but was what would be expected for a lower cost option. The bands around the neck of the vase are resolved, but the cracks and paint patches nearly blend in with the roughness of the surface. The resolution of the image-based documentation could be increased using more detailed images achieved by a closer camera-object distance or a different lens.

Comparing image-based 3D reconstruction results

While comparing the 3D scanned data provides information on capabilities of different instrumentation and the change of technologies, comparing the image-based 3D reconstructions over the span of this research allowed for the critical analysis of the research progression indicating whether there has been improvement in the 3D reconstruction process and where attention to detail should be applied with 3D imaging for conservation

documentation. Intercomparing data allows for one to gain insight about the techniques and technologies and also forces reflection on the advantages, limitations, and true capabilities to record and monitor cultural heritage objects.
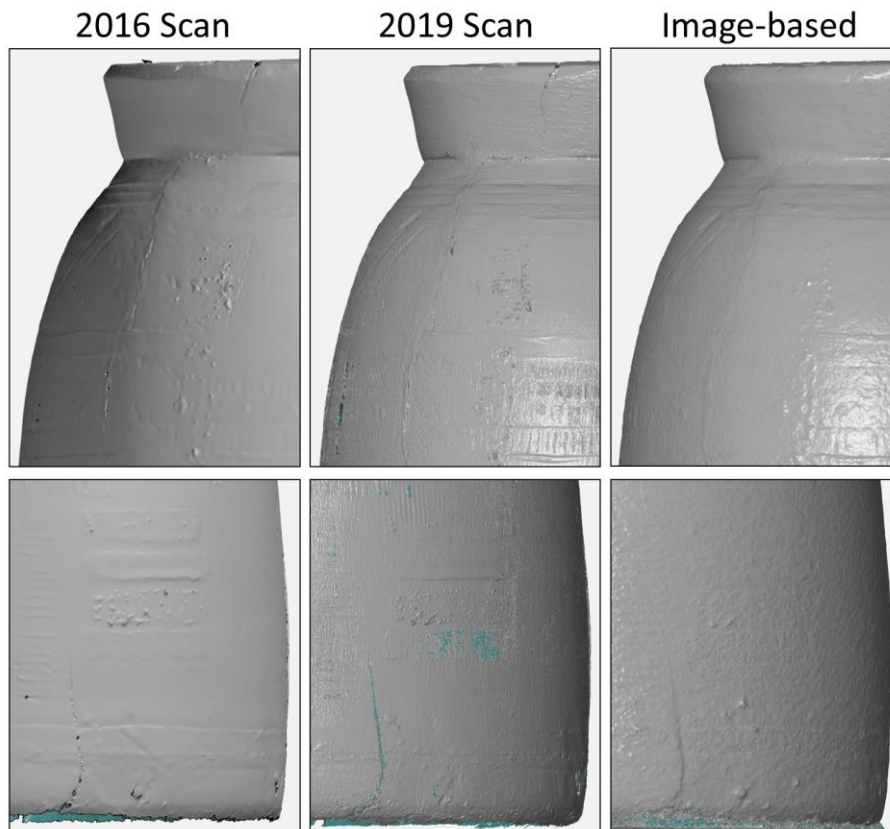
Figure 4-31. Visual analysis comparing the details of Mango Vase reconstruction results from the two scanning techniques and image-based 3D reconstruction. Two detail views compare the differences in local details resolved between the 2016 scan (left), the 2019 scan (middle) and an image-based 3D reconstruction dataset (right).

Comparing image-based 3D reconstruction results from the most recent acquisition and processing (Section 7.2) shows the consistency of the technique. The "reference" for these comparisons were 3D reconstructions from f/8 image sets (Figure 4-32) and f/11 images sets (Figure 4-33). All of the data for these 3D reconstructions (Figure 4-32 and Figure 4-33) were acquired on the same day, so it is not likely that the Mango Vase changed during this time. In addition, the setup and acquisition was the same with only the aperture and flash power changing for data sets acquired for the DOF investigation (Section 7.2). The deviations observed were random errors and mostly within a range of +/-0.10 mm for the comparisons to the f/8 and f/11 datasets. These results indicated that this imaging system and processing workflow could provide a consistent 3D reconstruction within at least +/- 0.10 mm. Even with a variation in the camera settings to optimise the photographic content (changing aperture to increase DOF), the results were still providing a consistent 3D reconstruction.
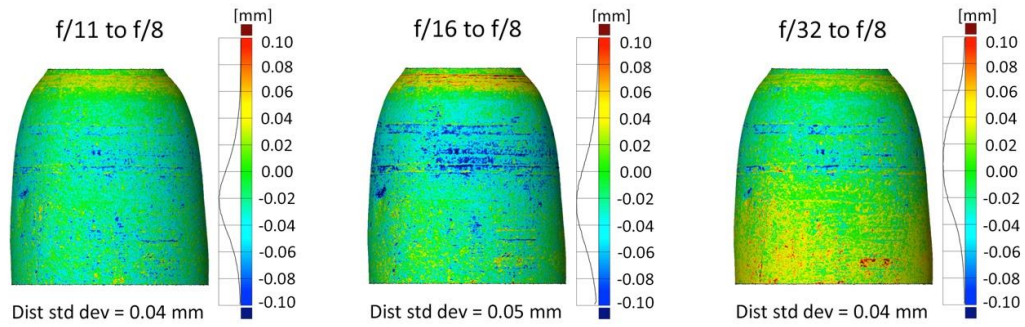
Figure 4-32. Surface discrepancy maps intercomparing image-based 3D reconstructions. The f/8 image set is used as the "reference data" for this comparison to see how consistent the image-based 3D reconstruction was at the end of the research.
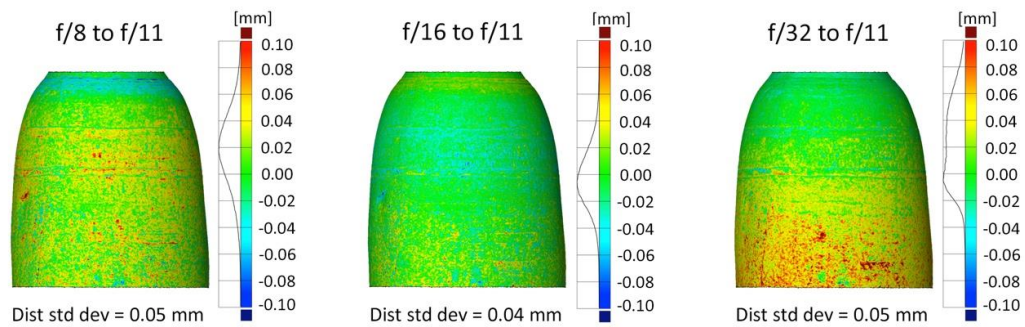
Figure 4-33. Surface discrepancy maps illustrating intercomparing image-based 3D reconstructions. The f/11 image set is used as the "reference data" for this comparison to see how consistent the image-based 3D reconstruction was at the end of the research.

Comparing image-based 3D reconstruction results from recent and older acquisition and processing showed the consistency of the technique over time (Figure 4-34). Three data sets were compared: old data with old processing, old data with new processing, and new data with new processing. The "old data" was image data that was acquired of the Mango Vase in February 2016 following a turntable setup that was very similar to the 2018 acquisition of the Mango Vase data (Section 4.2.1.2). Acquisition and processing information for the three data sets is in Table 4-6.

The comparison of the old-new data and old-new processing showed a difference of +/- 0.10 mm from the processing and a larger difference between the new and old data with new processing but still within +/- 0.20 mm (Figure 4-34). A two year time gap between the acquisition of the "new" and "old" data could have resulted in a physical change of the object. However, as discussed in the previous section, the observed differences between 3D reconstructions were likely a result of variation in the measurement devices and acquisition.

Table 4-6. Setup information for 2016 and 2018 image acquisition

	2016 Old Data Old Process	2016 Old Data New Process	2018 New Data New Process
Camera + Lens	Canon 5D Mark II Coastal Optics 60 mm	Canon 5D Mark II Coastal Optics 60 mm	Canon 5D Mark II Coastal Optics 60 mm
Camera-Object Dist (cm) Setup estimation/ Computed from PhotoScan	47 52.4	47 52	60 48.1
Camera Settings	f/16 0"5 ISO 100	f/16 0"5 ISO 100	f/8 1/100 ISO 100
Illumination Source	Continuous/ Tungsten	Continuous/ Tungsten	Studio Strobe
Image Processing and File Type	ACR RGB JPEGs	ACR Monochrome TIFF	ACR Monochrome TIFF
3D Reconstruction Camera Model	All parameters	f, cx cy, k1	f, cx cy, k1
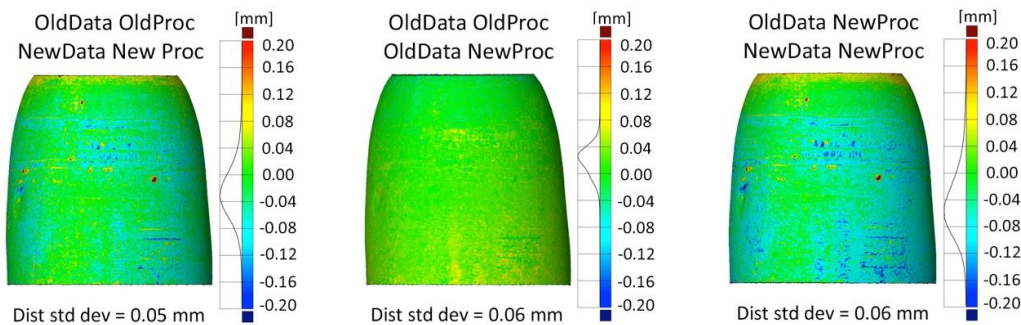
Figure 4-34. Surface discrepancy maps illustrating intercomparing image-based 3D reconstructions: old and new data and old and new processing.

While the optimisation presented in this chapter did not significantly change the resulting models of the Mango Vase, what the updated process did achieve was to increase the confidence in what can be achieved for more consistent results. The 2016 reconstructions were starting with high photographic quality, and there was not a major change observed in the resulting quality of the 3D reconstruction emphasising the importance of high photographic quality for the input images. The setup and acquisition from 2016 to 2018 did not change significantly, the main differences being illumination source (continuous vs strobe). The updated selection of the studio strobes for the 2018 acquisition was informed by the camera characterisation (Section 5.3). Most of the variation was within the workflow with the updated processing improving the quality and confidence in the data. Improving the repeatability of the setup and acquisition improves the ability to resolve change over time,

and as previously discussed improvements like acquiring the base and including coded targets would also increase the capabilities of recording change.

If an object is recorded in different campaigns over a time period, the accuracy can be impacted by a change of parameters. Several parameters influence the accuracy of the 3D imaging processes, as discussed in Section 2.2.2, and listed by Luhmann (2011, p. 2): calibration, network configuration, imaging scale, imaging measurement accuracy, the object, environmental conditions, uniqueness of object features, light conditions and contrast, and 3D calculation methods. Comparing the image-based 3D reconstruction results from old and new data and old and new processing suggests that for this imaging system and test object changes greater than 0.40 mm could be measured. This baseline of what could be recorded as change determined for the Mango Vase would be different for different objects, setups, and users.

Intercomparing 3D reconstruction results (Figure 4-34) provided an error range beyond which change in an object can be measured. However, the other side of this conversation is the discussion about the scale of the changes that might be observed in an object like the Mango Vase: global shape, cracks, divots, scratches, etc. These features would dictate the detail needed to be recorded by an imaging system and acquisition campaign. In considering the recording of fine details, MacDonald (2010) discussed the spatial resolution required for the 2D and 3D documentation of heritage objects based on the smallest detail that might be found in an object created by an artist or craftsman. While MacDonald focused on the manufacture process which were not necessarily changes in the object, understanding some of the smallest features of an object can help with informing the detail that might be required when recording the surface of an object. Identifying the grain size of substrates, the smallest brush stroke (the width of a single hair), and the limitations of the eye's ability to resolve fine detail led MacDonald to conclude that the minimum discernible feature size falls in the range of 20-75 μm (2010, p. 6).

The GSD for an image-based 3D reconstruction can be estimated from the camera distance, the focal length of the lens, and the pixel size of the camera or the camera and acquisition parameters can be determined based on a required resolution for resolving specific details (Section 2.3.1). The image-based 3D reconstruction results did not record some of the features that were resolved in the 3D scan from 2019 (Figure 4-31). Reducing the camera-object distance, increasing the focal length, and/or using a camera with an increased spatial resolution could improve the level of detail that could be resolved.

In this section, old and new data and old and new processing was compared to provide critical analysis of the research progression and ideally provide evidence of the improvement of the image-based 3D reconstruction workflow. There was not a significant change in the resulting 3D reconstructions although the confidence in the results has improved. Despite the consistency of the image-based 3D reconstruction over the course of the project, the way that the 3D reconstructions have been presented and assessed has more significantly developed over the same time period.

Assessment of 3D reconstruction results

Early outputs of this research compared image-based 3D reconstruction to 3D scanned data in Webb (2017) (Figure 4-35) or to other image-based 3D reconstructions in Webb et al. (2018) (Figure 4-36). These comparisons did not include reliable reference data, histograms illustrating the distribution of the discrepancies (to reveal systematic errors), or an assessment of the quality of the data and the spread of errors. Webb (2017) acknowledged that a "ground truth" was not available to assess the 3D reconstructions of three museum objects so the resulting models were compared to "reference data" recorded with a structured light 3D scanner (Figure 4-35). Webb et al. (2018) intercompared image-based 3D reconstruction results to assess the difference without any reference data (Figure 4-36). Webb et al. noted that the next stage was to do lab-based tests with a well understood reference surface to be able to quantify the differences of the imaging systems. These two examples are improved upon with the assessment and presentation of 3D reconstructions in this document.
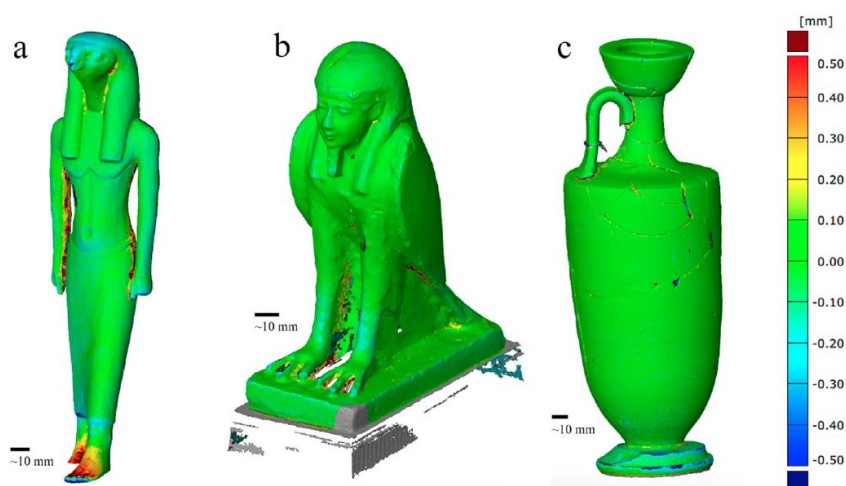
Figure 4-35. Previous assessment of image-based 3D reconstructions. Surface discrepancy maps comparing image-based 3D reconstruction of three museum objects to structured light 3D scanned data. The figure is from Webb (2017).
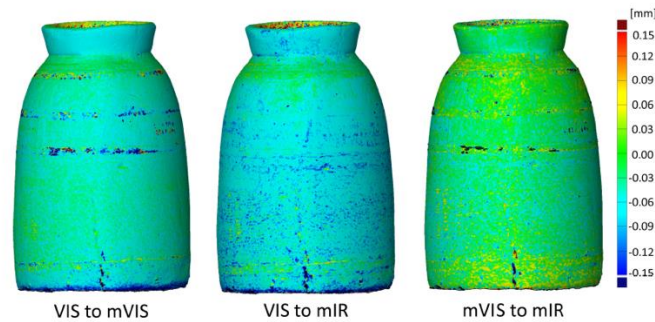
Figure 4-36. Previous assessment of image-based 3D reconstructions. Surface discrepancy maps of three resulting 3D reconstructions of Mango Vase. The figure is from Webb et al. (2018).

As part of the optimisation of the acquisition, processing, and assessment of the 3D reconstructions of the Mango Vase in Section 4.2, the assessment of the 3D reconstructions presented in Webb (2017) and Webb et al. (2018) has since been improved. The previous assessment and presentation of 3D reconstructions reflected other examples in cultural heritage literature, but it overlooked some key aspects that affect the quality and reliability of the data. This is further indication of the gap in accuracy assessment which ties directly to the analysis and presentation of 3D reconstructions of heritage objects. The way that 3D reconstructions are assessed and presented is not standardised and while there may be components of this that are built into traditional photogrammetry and metrology there is a gap between these fields and the cultural heritage applications and literature.

4.2.5.1.   Reference data and assessing 3D reconstruction

One of the reoccurring topics for both sections related to reference data and the assessment of the 3D reconstruction. The 3D reconstructions of the Panel included three different attempts for reference data for the test object (plane fitting, averaged mesh, and additional image-based 3D reconstruction), each with particular limitations. The challenges with reference data were further discussed in the section on the Mango Vase with the comparison of two models from structure light scanning and intercomparisons of image-based 3D reconstructions. The discussion about the reference data further emphasises what is found in the literature (Section 2.4) about the challenges for establishing good reference data and the complications of establishing what should be compared and evaluated (Remondino et al., 2014).

Reliable reference data and the iterative process of identifying and correcting for systematic errors, demonstrated in this chapter, allows for optimising of the 3D reconstruction and establishing limitations of the imaging system. This process of identifying and correcting

systematic errors to get at the random errors and establish the level of detail that an imaging system can resolve is an important demonstration for image-based 3D reconstruction of cultural heritage objects. While this may be a standard process for an engineer or a traditional photogrammetrist when working with 3D recording, this is not a process that is established in cultural heritage.

None of the models of the Mango Vase could be identified as the "ground truth". While the accuracy of the Mango Vase data could not be effectively assessed, the comparisons offered a useful assessment and an example of the challenges of monitoring an object with changes in technology, variations in acquisition and processing, and the limit of the scale of change that can be recorded over time. Comparing the image-based 3D reconstructions over the span of this research allowed for the critical analysis of the research progression indicating whether improvement to the 3D reconstruction process, increased confidence, and identified where attention to detail should be with 3D imaging for conservation documentation. Intercomparing data allows for us to gain insight about the techniques and technologies and also forces reflection on the advantages, limitations, and true capabilities to record and monitor cultural heritage objects.

4.3. Chapter summary

This chapter presented methods to improve image-based 3D reconstruction addressing the research question "How can consumer imaging systems be optimised to improve image-based 3D reconstruction of small to medium sized museum objects?". The optimisation presented in this chapter focused on acquisition, processing, and assessment using two test objects: the Panel test target (Section 4.1) and the Mango Vase (Section 4.2). Through an iterative process of testing and improving the methods and results the chapter established the workflow that was implemented in the following experimental chapters. The workflow and methods were building on current best practice and 3D reconstruction workflows discussed in Section 2.3. This chapter is an aspect of improving image-based 3D reconstruction using consumer imaging systems, but it is also setting the foundation with a standardised workflow that is able to achieve improved consistency allowing the investigating of wavelength and DOF in Chapters 6 and 7.

The Panel test target results showed: a convergent image configuration provided more accurate geometry than a normal image configuration and emphasised the importance of proper camera network geometry (Section 4.1.2); revealed that the Panel was not flat and explored the use of an averaged mesh as a reference for assessing accuracy (Section 4.1.3); and demonstrated the process of identifying and correcting systematic errors in order to

establish the limits of the imaging system. The final section (Section 4.1.4) focused on identifying the source of the systematic error observed as a ripple pattern. It was concluded that the limit of the imaging system with the presented parameters was the ability to resolve details larger than 0.06 mm. This accuracy achieved aligns with the state of the art for engineering and provides evidence to limitations of the available lens distortion models. To surpass the limitations of the imaging system, metrology-level instrumentation would be required. The recording of the Panel test target was an assessment of the imaging system in relation to its performance for image-based 3D reconstruction. Further characterisation of the imaging system will be conducted in Chapter 5.

The Mango Vase results pointed to the issues of rotational symmetry and critical issues of alignment leading to the discussion of methods for improving alignment and scaling (Section 4.2.2), the investigation of camera models and parameter selection (Section 4.2.3), and the assessment of reference data (Section 4.2.4). Accuracy of the alignment is critical and can significantly impact the resulting comparison and assessment of the 3D reconstructions. An approximate uncertainty +/- 0.15 mm was associated with manual selection of targets, target geometry (where the targets are located at the base of the Vase), and the resulting scaling (Section 4.2.2.2). This is a significant demonstration as it is important to take the best possible images with the imaging system based on local contrast, wavelength selection, sharpness, and focus; however, without a reliable geometric reference there cannot be certainty of the overall output geometry. This links to a fundamental principal of photogrammetry that scale is not inherent to the process and it requires external information for scaling. The scaling is only as good as what is input, and manual selection of the targets and the target geometry reduces the confidence in the resulting scaling.

Findings and recommendations:

A convergent image configuration improves the geometry as compared to a normal image configurations. The results in this chapter further support the literature discussed in Section 2.3.3.2 and the importance of proper camera network geometry which may not always be considered or emphasised in heritage projects. The results for the Panel test target, as a planar surface, can be linked to the benefit of combining normal and convergent networks to document paintings since the normal will provide a better texture and the convergent will provide a better geometry.

Part of project planning should include establishing how the accuracy and reliability of the results can be established. This chapter provided evidence and discussed challenges with accuracy assessment and available reference data, which further supports the literature

(Section 2.5.1). The workflow presented in the chapter can increase the confidence in the consistency of the results, while a test object can be used to establish the limitations of the imaging system providing insight into the accuracy and reliability of the resulting 3D reconstructions. As part of this the averaged reference mesh is not an independent reference and it accumulated the systematic errors of the 3D reconstructions used to create the mesh.

Reliable reference data and the iterative process of identifying and correcting for systematic errors, demonstrated in this chapter, allows for optimising of the 3D reconstruction and establishing limitations of the imaging system. This process of identifying and correcting systematic errors to get at the random errors and establish the level of detail that an imaging system can resolve is an important demonstration for image-based 3D reconstruction of cultural heritage objects. While this may be a standard process for an engineer or a traditional photogrammetrist when working with 3D recording, this is not a process that is established in cultural heritage. Assessment of the 3D reconstruction should go beyond a visual assessment and a review of processing statistics, if possible, in order to identify and correct for systematic errors that would influence the analysis and interpretation of the results. Surface discrepancy maps should include a histogram to assess the spread and shape of the discrepancies.

The imaging of the Panel test target provided evidence that the imaging system when used with the presented parameters has the ability to resolve details larger than 0.06 mm. This accuracy achieved aligns with the state of the art for engineering and provides evidence to limitations of the currently available lens distortion models. To surpass the limitations of the imaging system, metrology-level instrumentation would be required.

The results from the optimisation of the acquisition, processing, and assessment of the Mango Vase suggest documenting the base of an object to improve alignment and monitoring, using coded targets to improve alignment and scaling, and acquiring a "flat project" to ensure that the scale bars are in focus and to improve scaling.

Global vs local assessments will provide different information about the results and there should be a consideration of the area being compared and assessed. The global assessment may provide more information about the alignment, overall shape, and scaling, while a local assessment may be able to show the difference in recording local feature details like the drawn and painted details on the Mango Vase. Both the Panel and Mango Vase provide examples of cropped data improving the assessment. The areas of large deviations on the Panel were the square and circular photogrammetric targets that were dark and resulted in high levels of noise from the lack of signal returning. As the resulting data of the Mango

Vases was cropped and the areas of larger deviations removed, the fitting improved and the results provided a clearer indication of the capabilities of the imaging system.

Contribution to knowledge:

This chapter provides evidence of a contribution to knowledge by connecting museum imaging to the wider 3D reconstruction community. Section 2.4.4 pointed to a disconnect between automated methods of image-based 3D reconstruction and some of the photogrammetric fundamentals relating to accuracy and citing the work of James et al. (2017) in the field of geomorphology. The literature review discussed the parallels of geomorphology and cultural heritage and the disconnect from the knowledge, experience, and literature within traditional photogrammetry the field's associated accuracy and reliability. Following the lead of James et al., Chapter 4 demonstrated methods to improve processing and assessment thereby, contributing to the state of the art in museum imaging and conservation documentation. The image-based 3D reconstruction for conservation documentation can be advanced by connecting it with the wider interdisciplinary community working with 3D reconstruction as was demonstrated in this chapter by implementing methods like those presented by James et al. from geomorphology.

5. Camera characterisation

Modified cameras offer inexpensive, easy to use, portable, and high-resolution options for spectral imaging (Section 3.1.5) and could be used as accessible devices for wavelength selection to acquire images with increased local contrast to improve image-based 3D reconstruction. However, the camera requires characterisation to assess its performance, the impact of the modification, and its use as a scientific tool as part of the investigation of wavelength selection and improved 3D reconstruction (Chapter 6). The camera characterisation includes assessing the 2D image quality (Section 5.2), measuring the spectral response (Section 5.3), and evaluating the resulting 3D reconstruction (Section 5.4). Acquiring RAW data is necessary for characterising the camera, assessing the 2D image quality, and using the camera as a scientific device for measurement. The first section of this chapter (Section 5.1) will look at a proposed RAW processing workflow that takes into account the camera modification. This chapter characterises an unmodified and a modified camera to address the research question: "Can photography with a modified consumer digital camera paired with selected illumination and filtration be used as a scientific method to better benefit the 3D reconstruction of museum objects for conservation documentation?"

The modification of the camera assessed in this research is a monochrome conversion that included the removal of the IR blocking filter and anti-aliasing filter, the sensor cover glass, and about 5 μm of the microlenses and CFA, which was a service provided by MaxMax LDP LLC (Section 3.1.5). The modified camera was a Canon 5D Mark II with a full-frame CMOS sensor (36 x 24 mm), a maximum resolution of 21.1 MP (5,616 x 3,744 pixels), and a pixel pitch of 6.4 μm. To assess the results of the modified camera characterisation an unmodified camera of the same make and model (Canon 5D Mark II) was characterised using the same methods (Table 4-1).

5.1. RAW Processing

Acquiring RAW data is necessary for characterising the camera, assessing the 2D image quality, and using the camera as a scientific device for measurement (Section 3.3.1). However, a standard RAW processing workflow using Adobe Camera Raw (ACR) (Section 12) does not take into account the camera modification, so a RAW processing workflow is proposed that takes into account the camera modification.

The RAW processing workflow needed to produce 16-bit TIFF files following a linear process without demosaicing. RAW files provide the data closest to the original sensor information. A 16-bit TIFF file allows for the full recorded tonal range (14-bits for the

Canon 5D Mark II), while the recorded data maintains linearity (the input is proportional to the output) without any gamma correction. Maintaining linearity during conversion and processing is essential for scientific applications. With the CFA only a single spectral band is recorded at each photosite as a digital intensity value. Demosaicing would be used to convert these bands to a matching colour value and to interpolate values for the other spectral bands in order to construct a colour image of the scene.

5.1.1.   Modified camera RAW processing workflow (MC-RAW)

The proposed modified camera RAW processing workflow (MC-RAW) used in this study is illustrated in Figure 5-1 and Table 5-1. RAW files were processed using the DCRAW utility (Coffin, 2009) providing a 16-bit linear TIFF without demosaicing. DCRAW is open source software used to decode RAW images (Section 12). There are several processing options within DCRAW; however, the appeal of using this software was to retrieve the RAW data as close to sensor level as possible and follow a linear processing workflow. The images are processed with the command of "–D -4 –T", which indicates using the image from document mode without scaling ("–D") and processing it into a linear 16-bit ("-4") TIFF ("-T"). Figure 5-2 includes the stages of the MC-RAW processing workflow to track the linearity and compare with the ACR processing (last column).
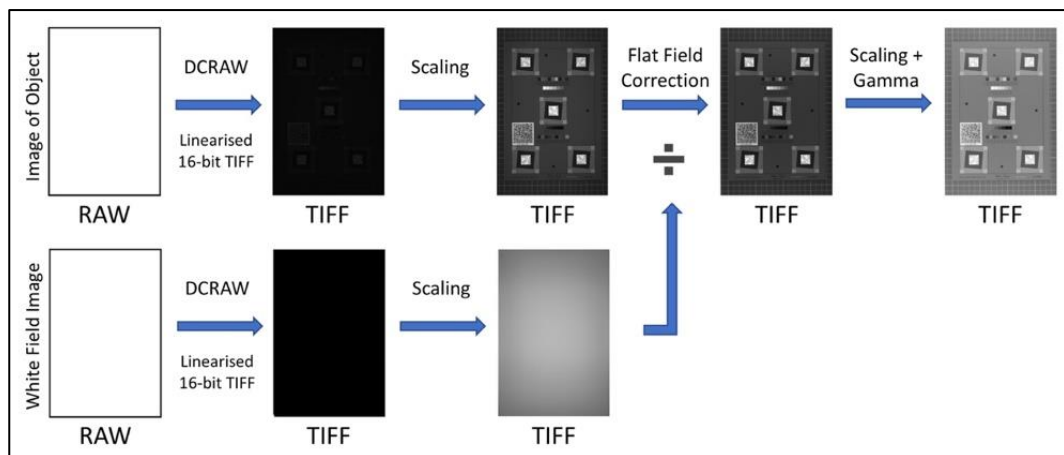
Figure 5-1. Diagram of the MC- RAW workflow.

The resulting images from DCRAW are very dark and any image detail is hard if not impossible to decipher (Figure 5-2a). The camera produces a 14-bit image and once processed by DCRAW it is being held in a 16-bit container. The TIFF images are scaled in Matlab (Section 12) using black and white reference points. For the DICE target the black and white patches are used to map to the 4% output for the blacks and 97% output for the whites. For the Spectralon diffuse reflectance standards, the black (2%) and white (99%) standards are used to map to 2% output for blacks and 99% output for whites. The scaling maintains linearity; however, displays are nonlinear so a gamma correction needs to be

applied for visualisation. A gamma correction of approximately 1/2.2 was applied providing a resulting image that is visually similar to the results from ACR processing (Figure 5-2d and e).

Table 5-1. MC-RAW workflow processing and corrections

ISSUE	CORRECTION	IMPLEMENTATION
Proprietary RAW file format	Conversion to 16-bit linear TIFF	DCRAW "-4 -D -T" '- D' document mode without scaling '- 4' 16-bit file '- T' TIFF file format
Residual pixel-level pattern	Flat field correction	Matlab Division of image by white field image
Resulting dark image	Scaling	Matlab DICE target mapping blacks to 4% output and whites to 97% Spectralon mapping black to 2% and white to 99%
Increasing contrast	Gamma correction	Matlab Gamma correction of 1/2.2
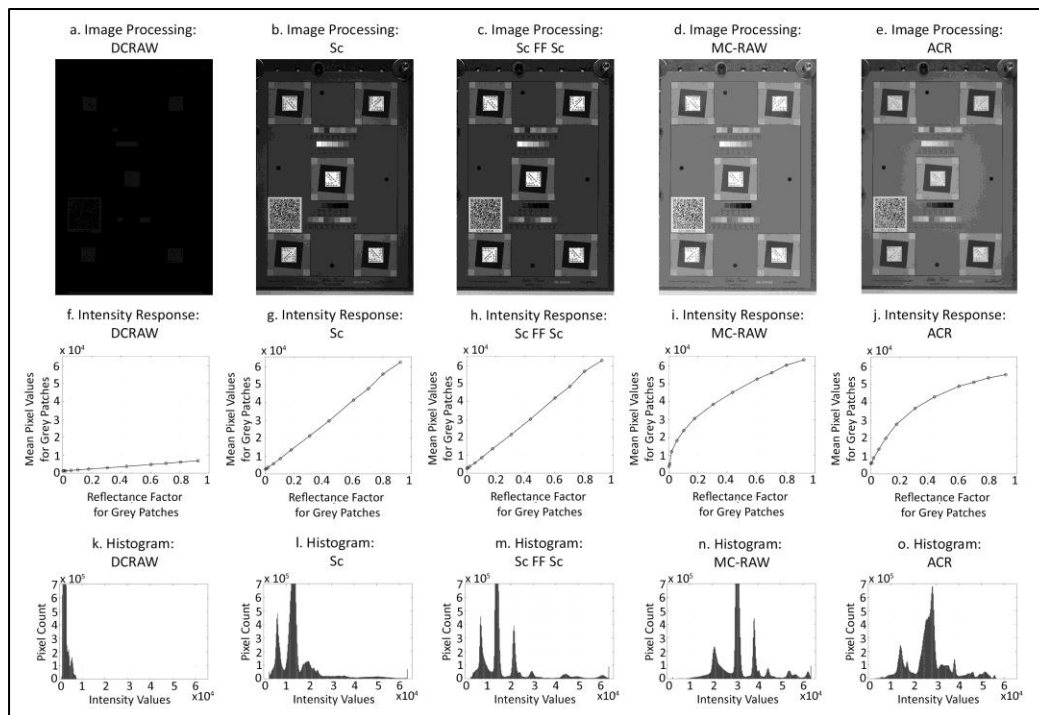
Figure 5-2. Stages of RAW processing workflow to track linearity and to compare with ACR processing. Top row: Resulting images of DICE target; Middle row: Intensity response (mean intensity value of the grey scale plotted to the reflectance factor or the Y tristimulus value); Bottom row: Histograms. Column a: DCRAW conversion ('DCRAW'); Column b: DCRAW with scaling ('Sc'); Column c: DCRAW with flat fielding and scaling ('Sc FF Sc'); Column d: DCRAW with flat fielding, scaling, and gamma correction ('MC-RAW); Column e: ACR processing ('ACR'). The figure provides evidence that the DCRAW conversion requires scaling (a); the scaling and flat field correction maintain linearity (g, h); and the flat field correction, scaling, and gamma correction resembles the ACR processing (d, e, i, j).

5.1.2. Pixel-level pattern

While DCRAW and scaling maintained a linear workflow and provided a 16-bit TIFF, viewing the images at high magnification revealed a pixel-related pattern, or fixed pattern noise (Figure 5-3). The pattern could be related to in-camera processing that differed between channels or residuals from the removal of the CFA. The pattern was consistent from image to image when a sequence of images was acquired. However, the pattern was not consistent across wavelengths and was most prominent with wavelengths shorter than 550 nm (Figure 5-4), hinting that this effect was in fact due to residual spectral selectivity at individual photosites as opposed to processing artefacts. If the images had been processed using demosaicing, this pattern would have been eliminated through averaging, but any increased effective resolution gained from the removal of the CFA would have been lost. Flat field correction acquired for each wavelength reduced this fixed pattern noise and increases the potential effective resolution. The flat field correction has been included in the MC-RAW workflow, and the acquisition of a white field image was required for each filter and illumination source and setup used. (Section 5.4 will investigate the impact of the residual pattern on 3D reconstruction results.) This pixel-level pattern may not be present with all modified cameras and would only be problematic with cameras where the CFA has been removed; however, flat field correction is part of best practices for documentation and is worthwhile to include within a workflow even if this pixel-level pattern is not observed.
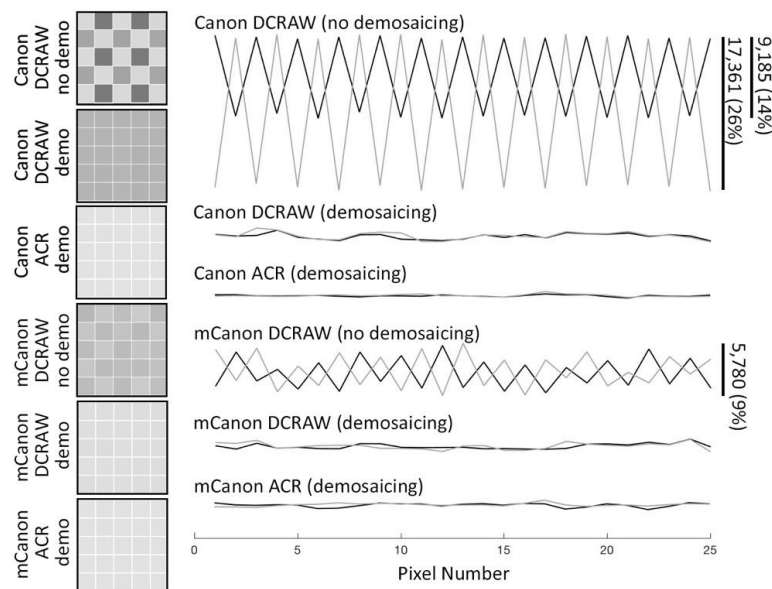
Figure 5-3. Visualisation of the pixel-level pattern and differences with the RAW processing methods. Left column: Magnified view of the pixels for the unmodified Canon and the modified mCanon cameras processed with and without demosaicing using DCRAW and ACR. Right column: Vertical profiles of pixel intensities of two rows of 25 pixels measured from a white patch in images acquired with the unmodified and modified camera and processed with DCRAW and ACR. The top profile shows what the Bayer pattern from the CFA would look like without demosaicing.
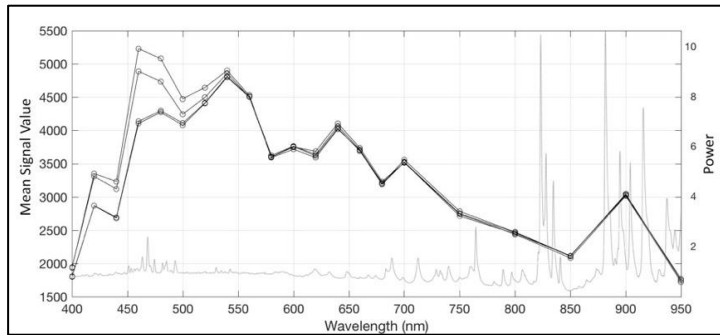
Figure 5-4. Mean signal value of 100 pixels averaged based on 2x2 pixel grid. This data has not yet been corrected for the luminous power or the filter sensitivity. The figure shows a difference in spectral response between 400 and 550 nm. The SPD of the Bowens illumination source (light grey line) has been included in the figure to indicate areas of increased output.

5.1.3. Discussion

The MC-RAW workflow provided more control over the process than the "black box" ACR option. It took into consideration the modification of the camera instead of treating the images as RGB images, and it provided an increased effective resolution (further discussed in Section 5.2.2). Despite these advantages, there were some considerations about the accessibility of the technique, and as the project progressed, there was a question of whether the pixel-level pattern was fully eliminated.

ACR provides a very easy interface to convert RAW images to TIFF or JPEG, while the MC-RAW workflow is not as accessible in both cost and complexity. ACR is already being used in conservation documentation workflows (Warda et al., 2011) (Section 3.3.1) and does not require any coding. The simple and accessible ACR interface comes at the cost of lack of control of the processing parameters. DCRAW is a freely available software, but it is based on command line and requires scripting. The scaling, gamma correction, and batch processing for the MC-RAW workflow has been done in Matlab, an expensive program that requires the ability to understand and write script.

The MC-RAW workflow has the potential to be made more accessible by creating an executable file, which could be future work for this research. However, one of the challenges with this processing workflow was the different variations of the datasets requiring either an update to the script to accommodate the variations or a more global solution that could be applied to all datasets. A global solution was not identified that worked for all datasets and instead scripts have been adapted for the variations. For example, some datasets only needed one flat field image that could be applied to all the images (Figure 5-5a), while other datasets had a flat field for each image (when the wavelength range changed or the relationship of the light or camera to the object changed) (Figure 5-5b, c). Similarly, some datasets had a black and white reference that could be applied to the whole image set (Figure 5-5a, b), while other datasets needed the black and white reference to be identified for each image (Figure 5-5c). With some datasets, the black and white reference was in the image of

the object being processed (Figure 5-5c), in other cases it was a separate reference image required for calibration (Figure 5-5a,b).
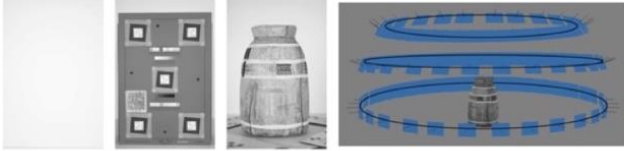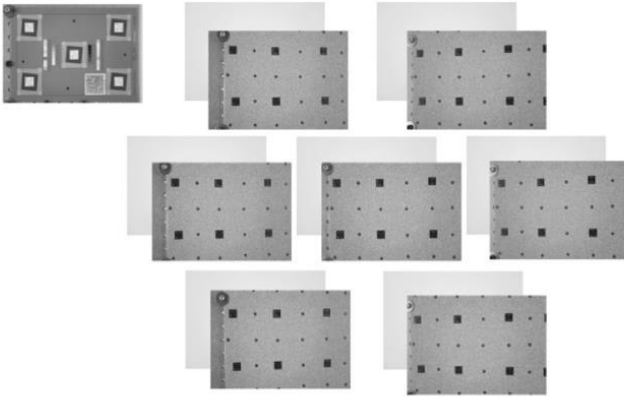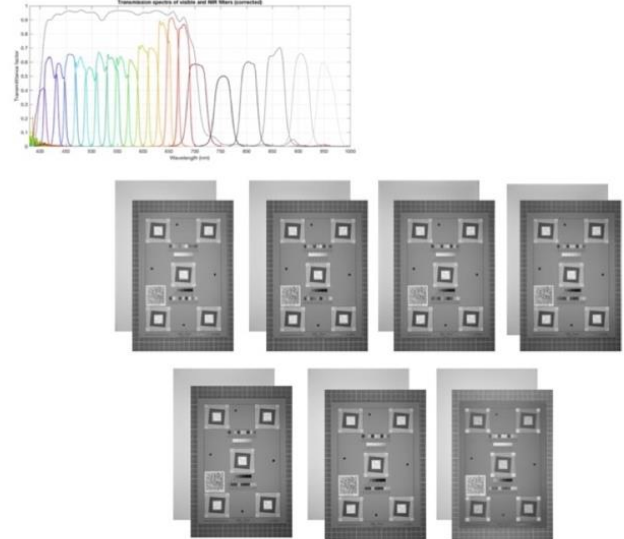
Figure 5-5. RAW processing table showing different scenarios of image sets and required flat field image(s) and black and white references.

While initial testing of the MC-RAW workflow indicated that the flat field correction was eliminating the pixel-level pattern, as the project progressed it was apparent that the processing had only reduced the effect but did not fully eliminate it. The MC-RAW processing of images of the Mango Vase resulted in some of the pixel-level pattern even after the flat field correction. Comparing images processed with and without the flat field correction, showed that the process corrected for dust specs and scratches and some areas of

the pixel-level pattern. However, the pattern was not removed across the entire image. To better visualise this and to try to map where the pattern is corrected, images with and without the flat field correction were subtracted to look at the difference between the images (Figure 5-6). The flat field correction appears to be eliminating the pattern close to the edges of the image, resembling vignetting. Vignetting can be mechanical or natural. Mechanical vignetting is related to a physical obstruction of light reaching the focal plane, while natural vignetting, following the $\cos^4$ law, results from the geometry of image formation and the natural fall-off of light. If the vignetting was natural then it would be expected to decrease as the aperture diameter decreased.

Figure 5-6. Difference image between processing with and without flat field correction.
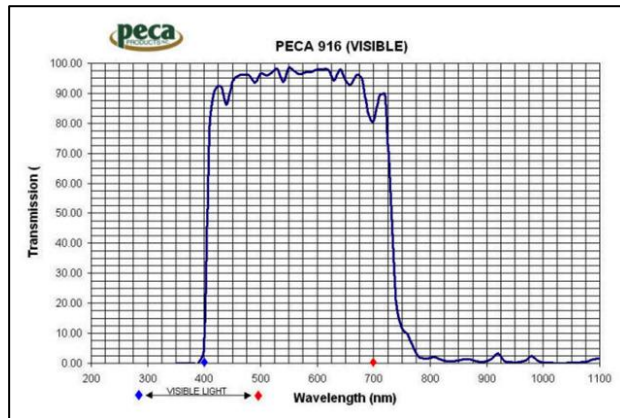
Figure 5-7. Transmission curve of Peca 916 bandpass filter ('IR-UV Filters', 2015).

To further investigate the pixel-level pattern and vignetting, images of a white field were acquired with the unmodified Canon and the modified mCanon cameras without a filter ('nf' for 'no filter') and with the Peca 916 to restrict the wavelengths to only visible light (Figure 5-7). Images were acquired with progressively smaller aperture diameters (f/4, f/5.6, f/8, f/11, and f/16) to see if the vignetting would persist even at a smaller aperture. Profiles were plotted across the white field images both horizontally and vertically to compare the vignetting (Figure 5-8). The Canon camera illustrates what would be expected as the aperture decreased: the curve of the profile reduced until the profile was close to a straight line at f/16. However, the results for the mCanon camera showed a consistent curved shape of the aperture indicating that the vignetting was not natural and was not a result from the lens design.

The modification of the camera included the removal of 5 μm of the sensor surface to remove the CFA, which in turn also removed the microlenses above the colour pixels. Microlenses are used to increase the efficiency of the pixels, or effective fill factor, by

focusing the light into the pixel. The chief ray angle of the light hitting the pixels changes based on the positioning on the sensor's surface, and the microlenses account for the variation in the chief ray angle (Allen and Triantaphillidou, 2011, p. 169). While a telecentric lens design allows light to hit the sensor's surface orthogonally at any position on the sensor, most lenses are not telecentric and the lens design needs to match the chief ray angle with the sensor design (Allen and Triantaphillidou, 2011, p. 169).
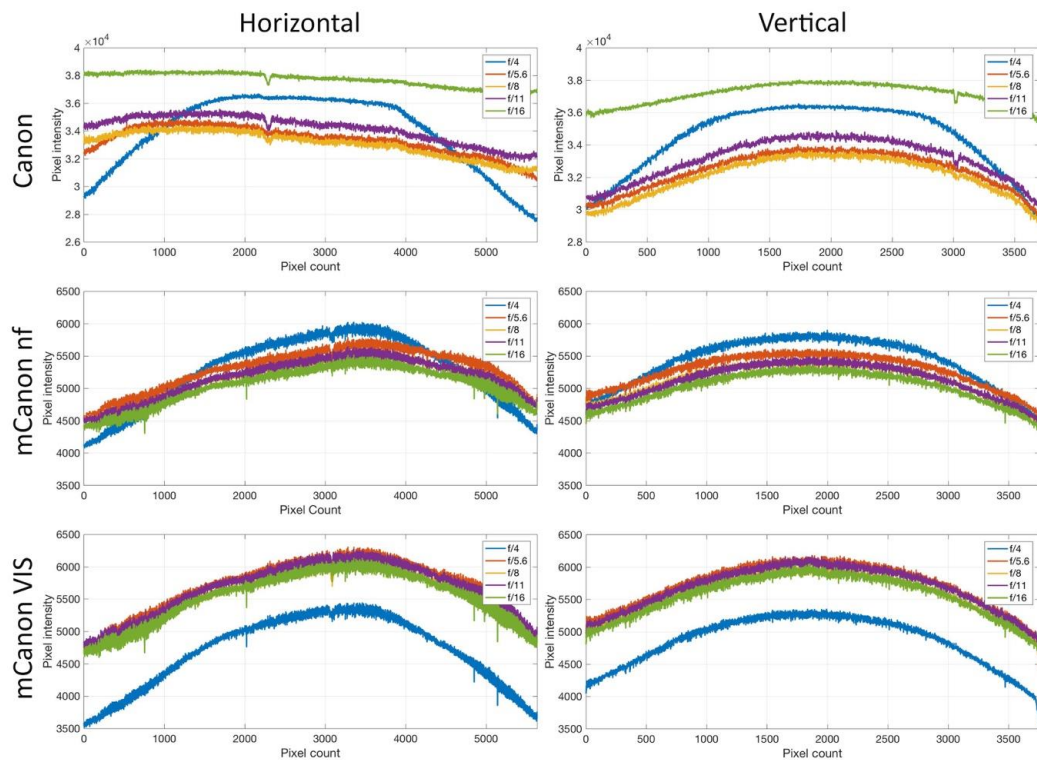
Figure 5-8. Horizontal and vertical profiles from white field images to investigate vignetting. Images were acquired with the unmodified Canon and modified mCanon cameras with progressively smaller aperture diameters (f/4, f/5.6, f/8, f/11, f/16). The mCanon images were acquired without a filter ('nf' for no filter) and with the Peca 916 filter to allow in only visible light ('VIS').

Figure 5-9 provides another way of looking at the vignetting in the images from the mCanon camera with the progressively smaller apertures. These images were processed with DCRAW. However, the ACR conversion could include processing that would factor in an amplification for the chief ray angle towards the edges of the field of view. The images were also processed using ACR, and the vignetting across the apertures was still observed (Figure 5-10). These results indicated that there may be in-camera processing for the amplification of pixels to accommodate for the chief ray angle towards the edges of the field of view.
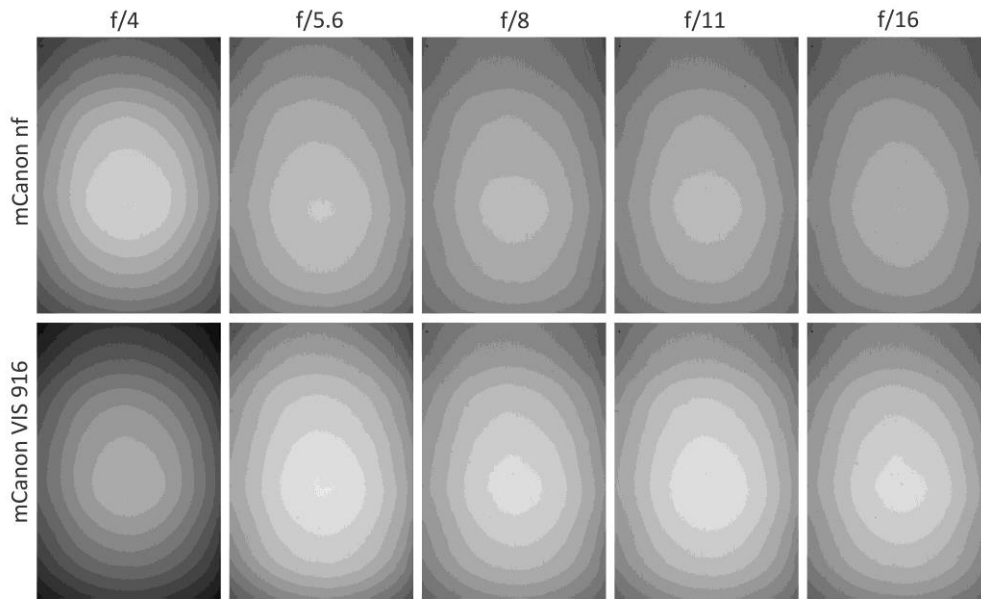
Figure 5-9. White field images acquired with the mCanon camera and progressively smaller aperture diameters. The images were acquired without a filter (top row) and with the Peca 916 filters to limit the sensitivity to visible light.
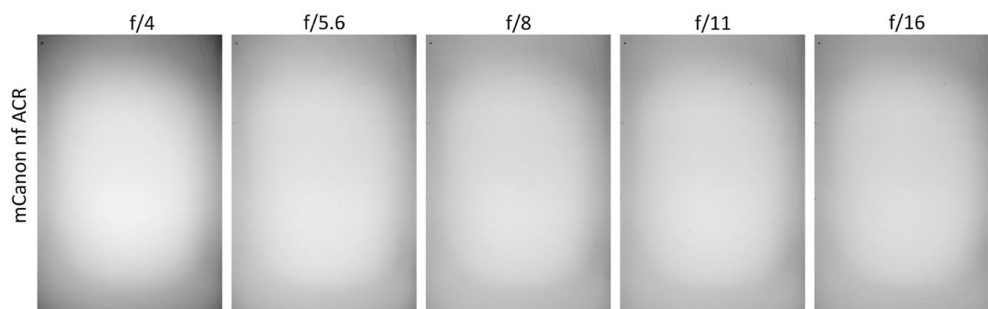
Figure 5-10. ACR processing of white field images acquired with the mCanon camera and progressively smaller aperture diameters.

When initially investigating the repeatability of the pattern, only a 4x4 pixel area at the centre of the image was assessed. The assessment for the repeatability was done by visually comparing ten, 4x4 pixel areas. This small central area was fairly similar in terms of the lighter and darker pixels. However, in an image of a white field, the pattern may not be consistent across the entire field of view, so the results from assessing only the centre would be misleading. Also, when testing the RAW processing workflow, images of the DICE target were mostly tested focusing on the centre of the image where the grey scale is positioned. When investigating the repeatability of the pattern and also the flat field correction, the assessment needs to include the full field of view and not just the centre.

To compare the relative sensitivity of the Canon and mCanon cameras, images of a white field were acquired with the same camera settings (f/8 1/40 sec; f/11 1/20 sec). The mCanon images include no filter ('nf') and images with the visible pass filter Peca 916 ('mVIS') for a comparable range to the Canon camera. The mean value of at 200 x 200 pixel area from the

RAW images were compared (Figure 5-11). The results showed an increased sensitivity with the modification both with and without the visible pass filter.
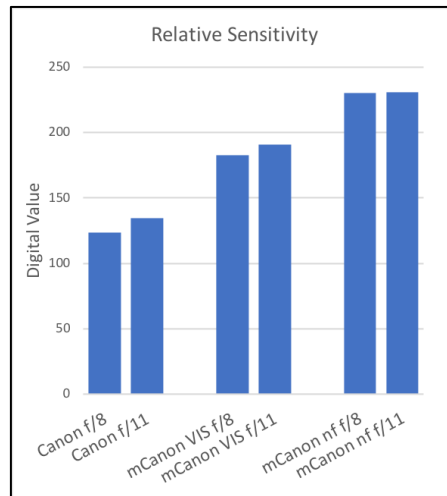
Figure 5-11. Comparison of the relative sensitivity of the Canon and mCanon cameras. The relative sensitivity for the modified camera includes with a visible pass filter ('VIS') and without any filters ('nf').

Since the microlenses increase the efficiency of the pixel, it might have been expected to see a drop in the relative sensitivity with the removal of the microlenses in the modified camera resulting in a lower relative sensitivity between the Canon camera and the mCanon camera with the visible pass filter. The transmission of the CFA is likely reducing the sensitivity even though the microlenses are increasing it. The mCanon without a filter has a wider range of sensitivity, and with a light source that has output in the NIR, more radiation will reach the sensor.

5.2. 2D Image quality

Measuring image quality was used to understand the performance of an imaging system, and in the case of characterising the modified camera, it investigated the performance and compared it to an unmodified system to better understand the impact of the modification. The first step of the camera characterisation was assessing the 2D image quality of the images acquired with the modified camera and comparing these to that of the unmodified camera. To assess the 2D image quality, the US-based FADGI guidelines and associated DICE target and software were used (Section 3.2).

5.2.1. Materials and methods

5.2.1.1. DICE Device Level Target

The DICE Device Level Target (Figure 1-4) was used for the assessment of the 2D image quality and performance. The FADGI conformance program includes best practices and guidelines that are used for collections photography and take into account advances in imaging sciences and cultural heritage documentation (Rieger, 2016) and align with Metamorfoze (van Dormolen, 2012). The target and software were selected as a turnkey solution with metrics and criteria for measuring system performance capabilities that are already being used for collections photography to assess standard digitisation setups.

While the target and software provide an assessment of a full range of image quality parameters, this research focused on assessing noise, sharpness, and resolution using measures for noise, SFR, and sampling efficiency. Noise is measured from the grey patches on the target, which is expressed as the standard deviation of the signal in the uniform area of the patch. SFR is used to measure sharpness, which measures the loss of contrast of an imaging system as a function of spatial frequency. For the DICE target and software, this is based on the slanted-edge features in five areas of the target. The SFR at the 10% modulation provides a measure for the limiting resolution of the system, and the SFR at the 50% modulation provides a threshold as a sharpness indicator (Section 3.3.2). The sampling efficiency provides a convenient measure for comparing multiple SFR results as the ratio of the limiting resolution to the Nyquist frequency (Section 3.3.2).

5.2.1.2. Image acquisition and processing

The DICE target was imaged using the Canon and mCanon cameras with a 60 mm and 50 mm lenses (Table 4-1). The target was illuminated with two Gemini GM400Rx flashes and umbrellas as diffusers. A PECA 916 filter (Figure 5-7) was used to restrict the camera sensitivity of the mCanon camera to visible light to provide a comparable sensitivity to that of the Canon camera. The images were acquired as RAW (*.CR2 Canon files) and processed following the workflows described in Section 5.1. The images were then analysed using GoldenThread Software (Section 12) focusing on noise, sharpness, and resolution using measures for noise, SFR, and sampling efficiency. The results from GoldenThread were analysed using Matlab to extract specific measurements and plot SFR, SFR50, and sampling efficiency.

5.2.2.   Results and discussion

The noise was measured in images of the DICE target acquired with the Canon and mCanon cameras and processed using three methods: RAW processing using ACR ('ACR'), DCRAW with scaling and gamma correction ('DCRAW ScGam'), and DCRAW with flat field correction, scaling, and gamma correction ('MC-RAW') (Figure 5-12). The ACR processing resulted in the lowest levels of noise, consistently falling below a standard deviation of 2 for both cameras. The ACR processing includes noise reduction, which would be why the levels remain consistent and low. The flat field correction for the mCanon image reduced the noise for the lighter patches (density less than 1.67). The noise levels in the dark patches for the mCanon image were higher than the Canon image, reaching a standard deviation over 7 in the black patch. When the density of the grey patch was about 1.67, there was a change in response to the RAW processing, and the noise in the pixel started to outweigh the processing effect. With a density less than 1.67, the RAW processing was accounting for the residual pattern, while with a density greater than 1.67, the RAW processing was not accounting for the noise.
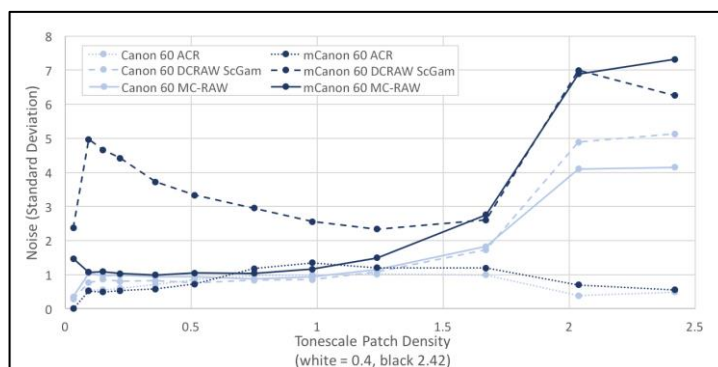
Figure 5-12. Noise measurement results from the grey patches of the DICE target. The figure plots the standard deviation of the digital values against the density of the tone scale patches from white (density = 0.4) to black (density = 2.42). The figure compares the Canon and mCanon cameras and image processing using ACR, DCRAW with scaling and gamma correction ('DCRAW ScGam'), and MC-RAW.

The DICE target and software offer one option for looking at noise from a single image. This measure links to Appendix B in ISO 15739:2017 and is referred to as "visual noise" which is designed to correlate with the visual appearance of noise in images. This is only one type of noise and one way of measuring it; it does not necessarily represent the overall performance of the modified digital camera. Future studies characterising the modified camera should include noise measurement beyond a single image measurement.

The resulting measures of the SFR from the Canon and mCanon cameras are plotted as the modulation of contrast against the spatial frequency (cycles per pixel) (Figure 5-13). The ACR processing for the images acquired with the Canon and mCanon cameras and the 60 mm lens had the lowest frequencies at 10% SFR. The DCRAW processing for the Canon camera with scaling and gamma correction ('DCRAW ScGam') and flat field correction

('MC-RAW) brought the frequencies close to the Nyquist limit, but not above it. However, the mCanon with the DCRAW processing with scaling and gamma correction ('DCRAW ScGam') and flat field correction ('MC-RAW') pushed the frequencies over the Nyquist limit. According to the sampling theorem, frequencies below the Nyquist frequency will be faithfully reproduced, but frequencies above the Nyquist frequency will be aliased (Section 3.3.2).
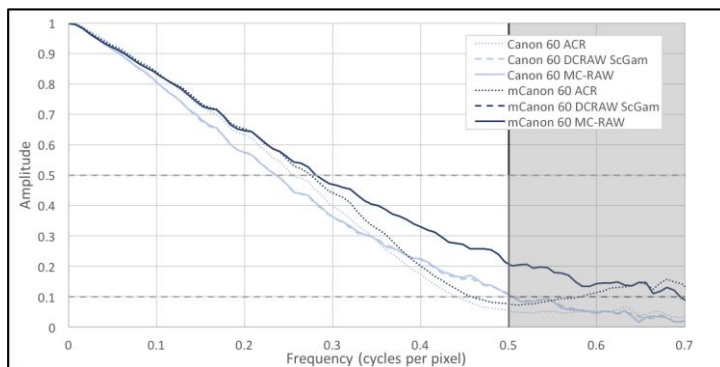
Figure 5-13. Horizontal SFR curves measured from the slanted edge features at the middle of the DICE target. These results are from the Canon and mCanon cameras with the 60 mm lens. The 10% and 50% SFR ranges are marked by dotted horizontal lines. The Nyquist frequency is marked by a vertical black line at 0.5 cycles per pixel. The grey region indicates frequencies that are at risk of aliasing.

Sampling efficiency for the Canon and mCanon cameras with the 50 mm and 60 mm lenses include two processing options, ACR and MC-RAW (Figure 5-14). The MC-RAW processing increased the resulting sampling efficiency as compared to the ACR processing. The 60 mm lens resulted in a higher sampling efficiency than the 50 mm lens for both cameras. The mCanon with the 60 mm lens resulted in a sampling efficiency over 100%, which should not be theoretically possible.
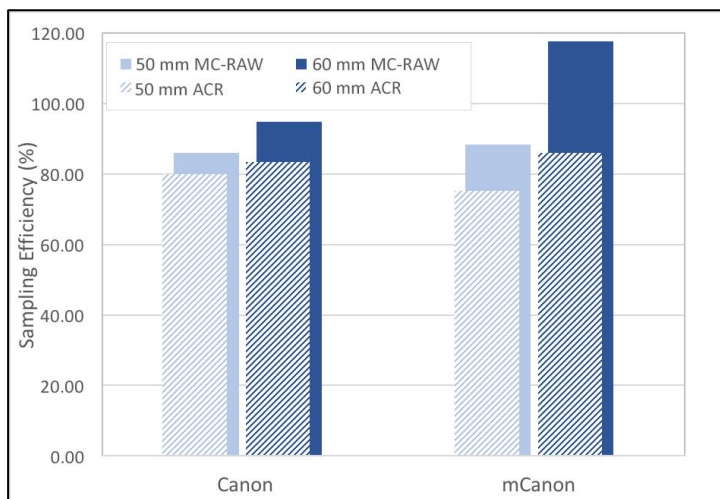
Figure 5-14. Sampling efficiency of the Canon and mCanon cameras with the 50 mm and 60 mm lenses. The image processing included ACR and MC-RAW.

Sampling efficiency and aliasing

The 60 mm lens is a high-quality lens with low aberration and distortion, so it can be expected that it performs better than the 50 mm lens. This is shown in the higher frequencies

seen in the SFR curves and the higher sampling efficiency but does not explain the SFR above the Nyquist frequency and a sampling efficiency over 100%.

The modification of this camera included the removal of the CFA and the anti-aliasing filter, an optical low pass filter, which both contribute to the increased SFR and sampling efficiency values greater than 100%. The CFA is used in consumer digital cameras to produce colour images using demosaicing to interpolate the colour information from red, green, and blue pixels. The process of averaging used for demosaicing reduces the effective resolution of a colour image. With the removal of the CFA, the image does not need to be processed using demosaicing algorithms and the effective resolution can be higher without this averaging. By incorporating a flat field correction for the residual pattern discussed in Section 5.1, the final image is able to maintain the higher effective resolution.

The anti-aliasing filter is positioned over the sensor of consumer digital cameras to reduce frequencies above the Nyquist frequency and prevent aliasing. Aliasing occurs when high frequencies are reconstructed at a lower frequency and can result in artefacts like moiré patterns. The modified camera resulted in frequencies above the Nyquist frequency and a sampling efficiency over 100%. With frequencies above the Nyquist frequency there is the risk of aliasing.

The SFR and sampling efficiency depend on the image processing and handling of the RAW files in addition to the focus of the lens when the image was acquired. The MC-RAW workflow (Section 5.1) increased the sampling efficiency as compared to ACR processing. Having sharp focus is essential for measuring and comparing SFR and sampling efficiency. However, the 60 mm lens only has manual focusing capabilities on the Canon cameras, which is a consideration for the reproducibility of the measurements.

5.3. Spectral response

The second step of the camera characterisation was the spectral response measurement. The measurement of the spectral response of the camera used a method presented by MacDonald (2015) filtering the camera with visible and NIR narrow bandpass filters (Section 3.3.3).

5.3.1. Materials and methods

A set of visible filters (400-700 nm) and NIR filters (700-950 nm) were used to acquire a sequence of images of a white target. The set of visible filters were glass dichroic transmission filters with central wavelengths at intervals of 20 nm from 400 to 680 nm inclusive with bandwidths of approximately 20 nm (Unaxis Optics, Munich, Germany)

(Figure 5-15). The transmission of the visible filters was measured with an Ocean Optics HR2000+ spectrometer by MacDonald (2015). The set of six NIR filters (Andover Corporation, Salem, NH, USA) were glass filters with central wavelengths at intervals of 50 nm from 700 to 950 nm inclusive, with bandwidths of approximately 50 nm. The transmission data for the NIR filters was provided by the manufacturer.
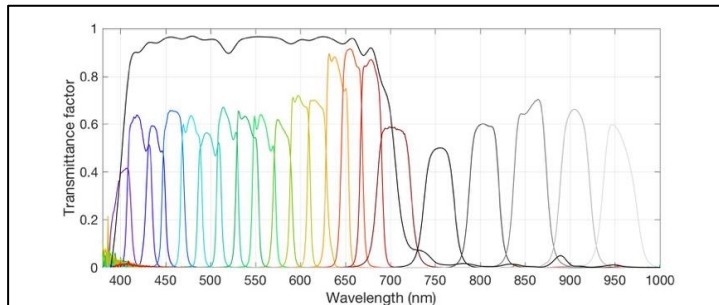
Figure 5-15. Transmission spectra of visible and NIR filters used to measure the spectral response of the cameras. The figure includes the transmission of the MidOpt UV-IR block filter (black) and the corrected spectra for the 640 nm, 660 nm, 680 nm (corrected with the transmission of the UV-IR block filter).

Lighting is a very important consideration for measuring the spectral response, and three sources were used with the different iterations of the measurement. The illumination sources will be further discussed with each iteration described and this section will conclude with a discussion about the advantages and limitations of the different illumination sources.

The Canon and mCanon cameras with the 60 mm lens and the bandpass filters were used to acquire RAW images of a white target. The images were processed using DCRAW to convert the RAW files to 16-bit linear TIFFs, but no scaling or flat fielding was used for the spectral response calculations. Images were cropped to the centre area of the white target and the mean intensity value calculated for each image. The mean intensity value was corrected for the power transmitted through each filter and normalised using the reflected illumination measurements of the white target. The reflected illumination was measured with an Ocean Optics USB2000+ spectrometer (Ocean Optics Inc., Dunedin, FL, USA). The measurements were interpolated to 1 nm intervals for the calculations and comparisons. A Matlab script, building on script used by MacDonald (2015) for the visible light characterisation of an unmodified Nikon camera, was used for the spectral response calculation.

5.3.2. Iteration #1: Tungsten lamps

The first iteration of the experiment was conducted using tungsten illumination. Tungsten illumination offers a continuous, white light source with a smooth SPD and high output in the NIR (Figure 5-16). MacDonald (2015) tested different light sources including flash, fluorescent, and tungsten lamps, and the tungsten results were the closest to the reference

data and provided the best performance. Four tungsten halogen lamps (Photolux 240V, 150W Frosted), a part of the copy stand setup (Kaiser Fototechnik, Buchen, Germany), were used to illuminate a ColorChecker white card (X-Rite, Grand Rapids, MI, USA). The camera was mounted on the copy stand above the white target and the lights were positioned at about a 30° angle to the white target. Images were acquired of the white card using the two cameras (Canon and mCanon) with each of the twenty-one visible and NIR filters. The reflected illumination of the light source from the white target was measured with an Ocean Optics USB2000+ spectrometer. Additional information about the setup for this iteration and the following ones are included in Appendix 14.4. The first iteration of this measurement was conducted with Lindsay MacDonald (UCL CEGE Honorary Professor) and Danny Garside (UCL CEGE PhD Candidate).
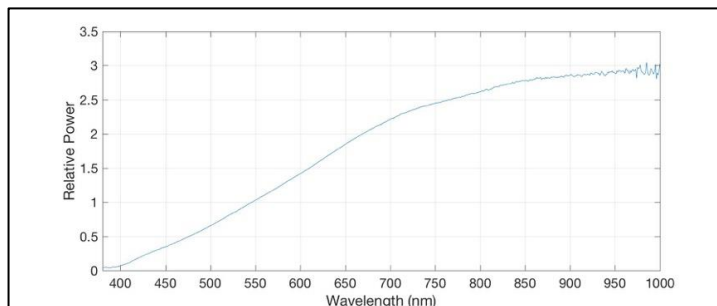
Figure 5-16. Measurement of the SPD of the tungsten halogen illumination source.

In preparing for image acquisition, MacDonald suggested using a NIR cut-off filter to suppress sidebands for the 640 nm, 660 nm, and 680 nm transmission filters (L. MacDonald, personal communication, March 6, 2017). The transmission measurements were provided for the visible light filters but the range only extended to 800 nm, which was not far enough into the NIR to document the sidebands. A MidOpt BP 550 filter (Midwest Optical Systems, Inc, Palatine, IL, USA) was used in combination with the 640 nm, 660 nm, and 680 nm filters to block UV and NIR (the transmission of the BP550 is included in Figure 5-15).

Results and discussion

The Canon results (Figure 5-17) show the three channels of the RGB camera (red, green, and blue) and a cut off in sensitivity at 700 nm, which is to be expected with the IR cut filter in the camera. There is a tail of the red channel in the blues, and while this may look unexpected it is necessary for detecting purples.

The mCanon results (Figure 5-18) show a single channel with a steep spike below 450 nm. Looking at the SPD of the tungsten lamps (Figure 5-16), there is very little output in the shorter wavelengths around 400 nm, so this spike is likely noise and not signal. The calculation of the spectral response measurement involves the multiplication of the

transmission of the filters by the SPD of the illumination, and the integration of this product results in the total power reaching the sensor. The mean sensor response (measured from the images), is divided by the total power to provide the spectral response measurement. If the total power is near or at zero, then this can skew the calculations creating the artefact seen as the spike. Figure 5-19 shows the modified camera results before correcting for the luminous power and the transmission of the filters. The spike resulted from the correction and it was expected that the measurement results would improve with an illumination source that has output in the shorter wavelengths around 400 nm.
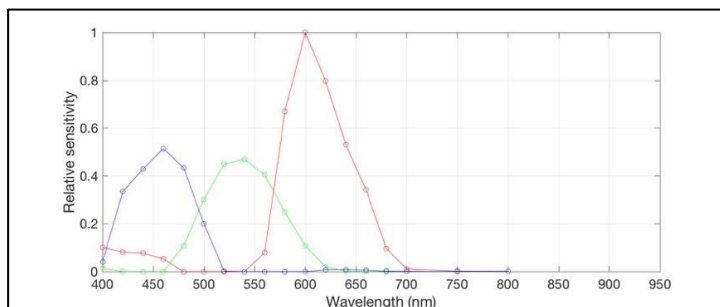
Figure 5-17. Spectral response measurement results of the Canon camera using tungsten illumination. The red, green, and blue lines are representative of the 3-channels of the RGB camera. There is a clear cut off at 700 nm from the IR cut filter in front of the sensor.
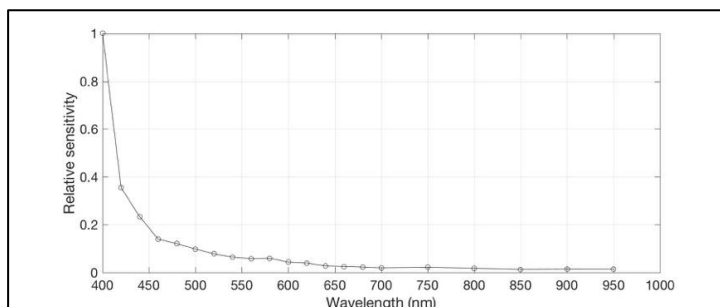
Figure 5-18. Spectral response measurements of the mCanon camera using tungsten illumination sources. The results include a steep tail below 450 nm which likely resulted from the low output of shorter wavelengths from the tungsten illumination sources.
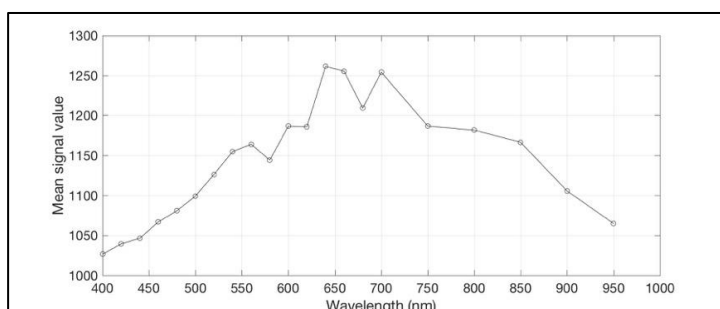
Figure 5-19. Uncorrected spectral response measurements of the mCanon camera using tungsten illumination sources.

5.3.3. Iteration #2: Off-camera flashes

The results from the first iteration of the test informed the selection of an illumination source that would have better output in the shorter wavelengths. Off-camera flashes, Canon Speedlite 580 EX II, have some output in the shorter wavelengths and also output in the NIR

(Figure 5-20). The SPD is more spiky than that of the tungsten source, but it still provides coverage in the visible and NIR regions. Instead of the ColorChecker white card, a Fluorilon-99W (Avian Technologies LLC, Sunapee, NH) diffuse reflectance standard was used as the white target. The Fluorilon has greater than 97% reflectance from 300-2200 nm providing consistent reflectance beyond visible light ('Fluorilon-99W', 2018). The standard was borrowed from the UCL Institute of Sustainable Heritage.
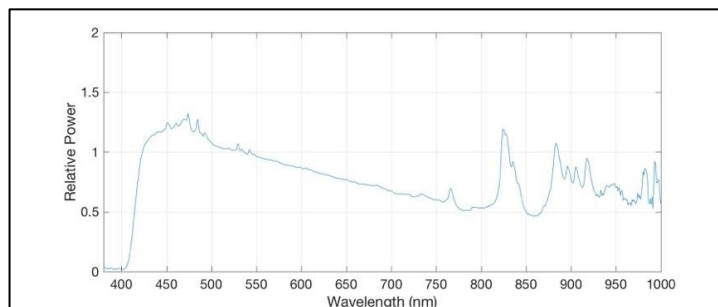
Figure 5-20. Measurement of the SPD of a Canon Speedlite 580 EX II flash unit.

The flash was measured using the Ocean Optics USB 2000+ spectrometer. An extended integration time was selected and the overhead lab lights were turned off with the Ocean Optics probe positioned above the white target to measure the reflected illumination. The flash was manually fired at regular intervals of 5-10 sec. This resulted in flash recordings interspersed with dark field recordings. The dark field recordings were used to calibrate the data against ambient noise. A Python script, building on Matlab code from Garside and MacDonald, was used to read and process the data from the Ocean View software. The code read the Ocean Optics measurements, separated the flash measurements and dark field measurements, averaged these independently, and subtracted the dark field averaged measurement from flash averaged measurement. This measurement was then corrected with the Ocean Optics correction vector to account for the sensitivity of the recording device.

Results and discussion

The Canon results (Figure 5-21) show the three channels, the cut off in sensitivity at 700 nm, and the tail of the red channel in the blues. These results were similar to the results using the tungsten source.

The mCanon results using the two Canon flashes (Figure 5-22) showed a single channel with a steep spike below 420 nm. While the Canon flashes have better output in the shorter wavelengths than the tungsten source, there is still a sharp drop off in power output around 420 nm. The spike observed in the mCanon results using the tungsten source started to climb around 460 nm whereas the spike in the results using the Canon flashes started at 420 nm.
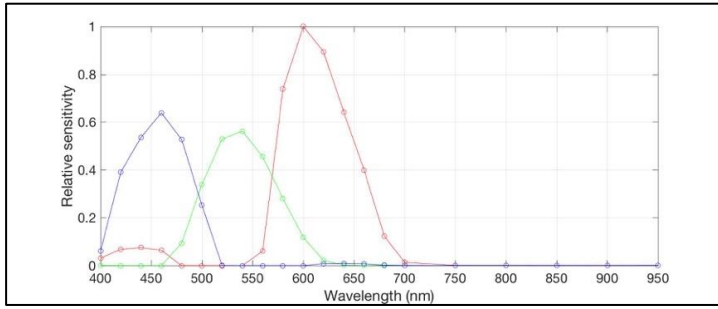
Figure 5-21. Spectral response measurement of the Canon camera using two Canon Speedlite flashes.
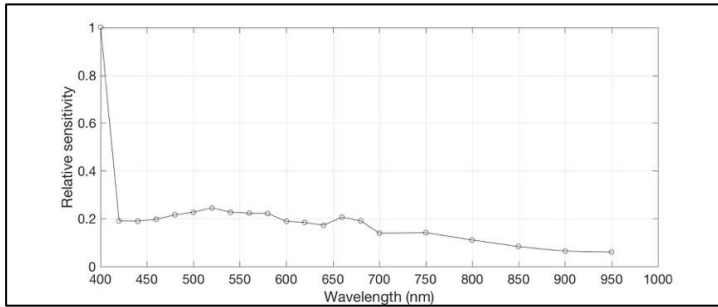
Figure 5-22. Spectral response measurement of the mCanon camera using two Canon Speedlite flashes

This indicates the increased output in the shorter wavelengths of the Canon flashes improved the results; however, this illumination source did not eliminate the spike as there was little to no output at 400 nm. A source with output at least slightly below 400 nm should resolve the spike and provide more accurate measurements for the shorter wavelengths.

The repeatability of the flashes was measured using the spectrometer and firing successive flashes. The Canon flash tests used a Spectralon 99% diffuse reflectance standard (Labsphere, North Sutton, NH, USA) to measure the reflectance and the flash was fired at a quarter power (the same power setting as the spectral response measurements). The ratio of each measurement was plotted against the mean to show the variation in the flash output. The Canon flash showed significant variation in the power output (Figure 5-23). The flash may not be recharging sufficiently between firings as suggested by the two distinct power levels. This test was also run with the flash power at $^1/_{16}$ power and full power also resulting in two distinct power levels (Appendix 14.5) suggesting that the power level may not be contributing to the variation in power output.

5.3.4. Iteration #3: Single off-camera flash

The second iteration of the experiment was run using the off-camera flashes; however, this iteration only used a single Canon 580 EX II flash. When using two flashes, if one flash fired instead of both there would still be a measurement recorded but this would result in a reduced power level. However, if using a single flash and it did not fire, there would be no

measurement providing a clear indication that the flash did not fire. The single flash was mounted onto a light stand and positioned at a high angle to reduce uneven illumination that might result from a single source. Only images were acquired using the mCanon, and three images were acquired for each filter in order to test the method's repeatability.
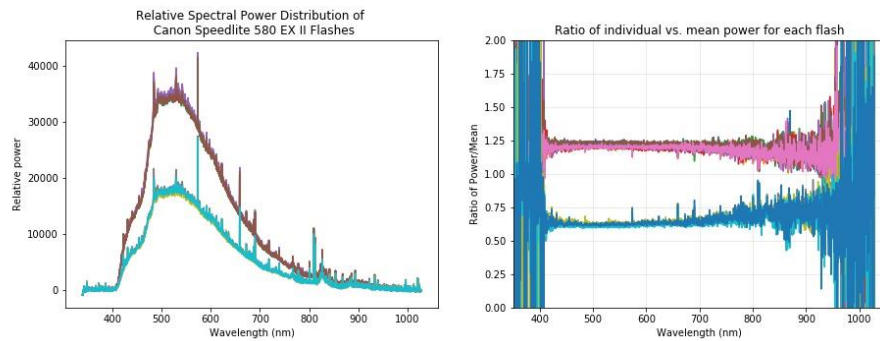
Figure 5-23. Repeatability test of Canon flash. (left) Relative SPD (uncorrected) measured using the Ocean Optics USB2000+ spectrometer for eleven successive flashes with the flash set at a quarter power. (right) Plot of the ratio of the individual vs mean power for each flash.

The Fluorilon target was not available for this iteration, so a ColorChecker Passport white card and Spectralon 99% diffuse reflectance standard were used as the white targets. The ColorChecker Passport white card would be comparable to the white card used in the first iteration and the 99% Spectralon would be comparable to the Fluorilon except with both cases the targets used for this iteration were smaller.

Results and discussion

The results for the mCanon for both Iteration #2 and #3 (three datasets for Iteration #3) are included together (Figure 5-24). The measurements at 400 nm have been removed as there was a spike for all four data sets similar to the one observed in Figure 5-22 for Iteration #2. Cropping the results to remove the spike provides a better view for comparing the shape of the spectral response results. The three sets from Iteration #3 are very similar showing good repeatability of the image data. The shape of the results from Iteration #2 corresponds to the shape of Iteration #3 but with a decrease in relative sensitivity. Iteration #2 used two flashes at ¼ power and Iteration #3 used a single flash at full power, so the different levels of illumination could explain the difference in relative sensitivity.

The results show a dip and a peak in the spectral response around 580-620 nm. This was identified as resulting from not using the UV-IR block filter. At the time of the acquisition for this iteration, there was not an UV-IR block filter available and it was not known how significant the sidebands were for the 640 nm, 660 nm, and 680 nm filters. After the datasets were acquired for this iteration, transmission measurements extending to 1000 nm for the

three filters were shared, which provided evidence of the significant impact from the sidebands (Figure 5-25). Previously the measurements available were only up to 800 nm, which did not reveal the sidebands. Figure 5-26 shows the transmission of the twenty-one visible and NIR filters and the BP550 filter before correcting the transmission of the 640 nm, 660 nm, and 680 nm filters, and Figure 5-27 shows the transmission after the correction. This provides adequate evidence that the UV-IR block filter is necessary for suppressing the sidebands with measuring the modified camera that has a sensitivity into the NIR.
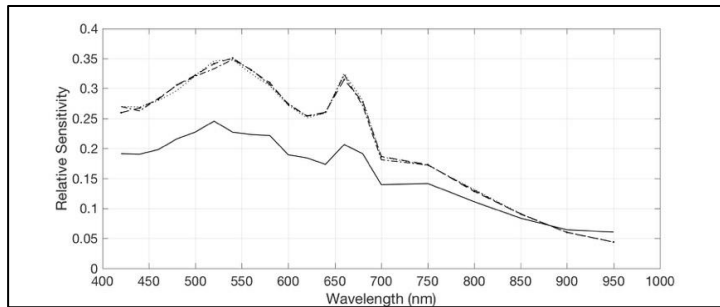
Figure 5-24. Comparison of the mCanon spectral response measurements from Iteration #3 (3 measurements) and the single measurement from Iteration #2.
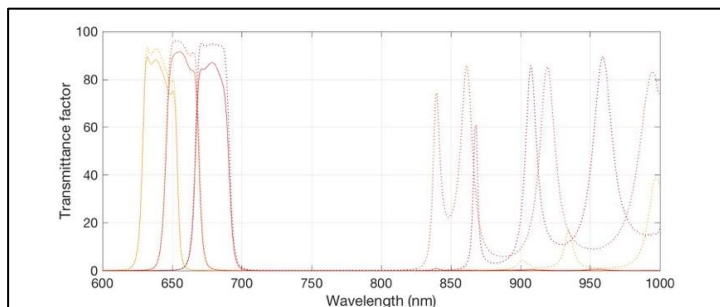
Figure 5-25. Transmission spectra of the filters 640 nm, 660 nm, and 680 nm filters. The dotted lines show the sidebands without correction and the solid lines show the transmission with the BP550 filter eliminating any transmission in the NIR.
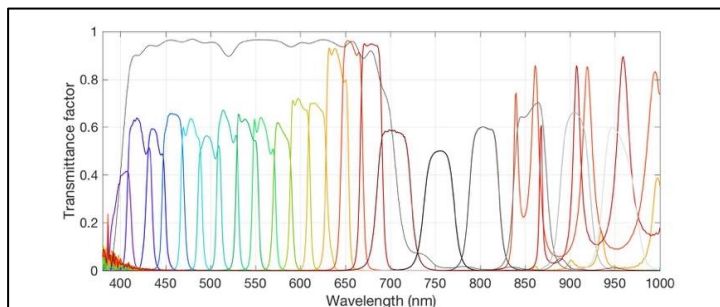
Figure 5-26. Transmission spectra of VIS and NIR filters and the BP550 filter without correcting the 640 nm, 660 nm and 680 nm filters with the transmission of the BP550 UV-IR block filter.
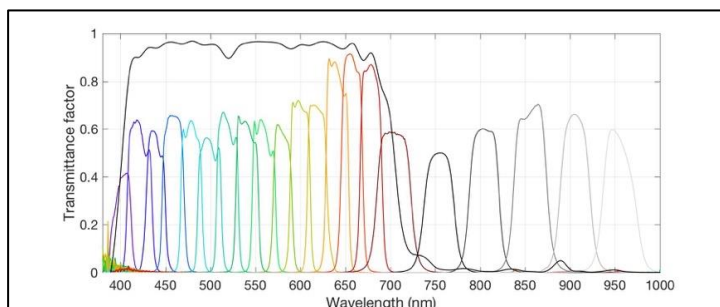
Figure 5-27. Transmission spectra of VIS and NIR filters with the correcting the 640 nm, 660 nm and 680 nm filters with the transmission of the BP550 UV-IR block filter. The sidebands in the NIR are eliminated with the UV-IR block filter.

The repeatability tests of the single flash show improved results (Figure 5-28); however, the previous repeatability tests indicated that there was a chance of variation in the output that might not be detected if one of the two flashes would still be firing and providing some illumination. The flash would need to be measured throughout the experiment to ensure whether or not the output is consistent. Using an illumination source with electric mains should eliminate this variation and uncertainty.
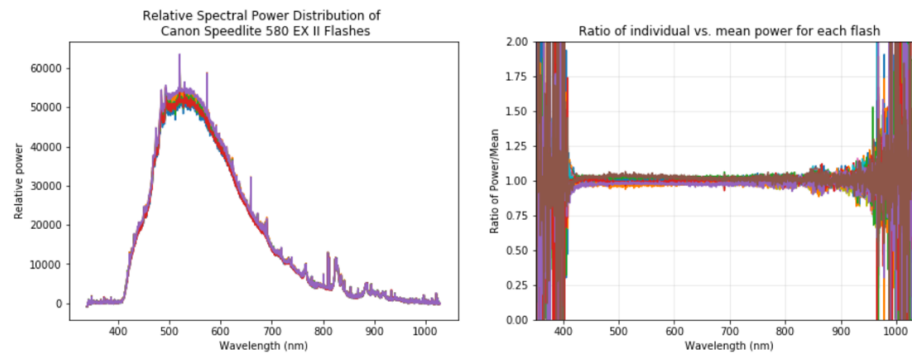
Figure 5-28. Repeatability test of Canon flash. (left) Relative SPD (uncorrected). (right) Plot of the ratio of the individual vs mean power for each flash.

5.3.5. Iteration #4: Single studio strobe

The final iteration of the experiment was informed by the previous iterations: an illumination source was required that had a repeatable output at and above 400 nm, through the visible, and into the NIR, and the use of the UV-IR block filter for the 640 nm, 660 nm, and 680 nm filters was essential. A Bowens Gemini GM400Rx studio strobe with a Lumiair Softbox was selected as the illumination source with electric mains to provide a consistent current and improved repeatability. The strobe provides output in the shorter wavelengths and NIR (Figure 5-29). Repeatability tests of the Bowens unit showed reduced variability as compared to the Canon off-camera flashes (Figure 5-30).
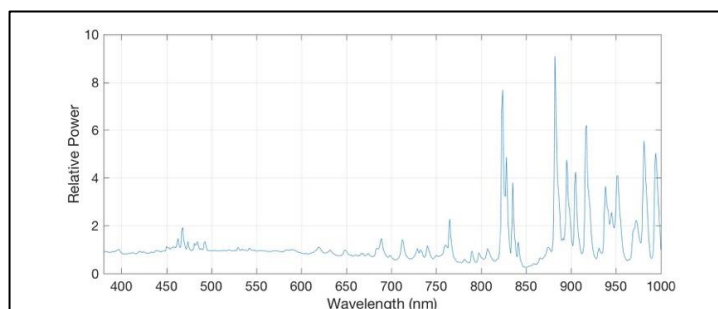
Figure 5-29. Measurement of the SPD of Bowens Gemini GM400Rx flash unit.

Results and discussion

The Canon results (Figure 5-31), similar to the previous iterations, showed the three channels, the cut off in sensitivity at 700 nm, and the tail of the red channel in the blues. The

mCanon results (Figure 5-32) showed a single channel with sensitivity from 400 to 950 nm, and the sensitivity of the device at shorter wavelengths around 400 nm was over four times the sensitivity of the longer NIR wavelengths around 950 nm. The spike in previous results (below 460 nm) has been resolved by using an illumination source with output in shorter wavelengths around 400 nm.
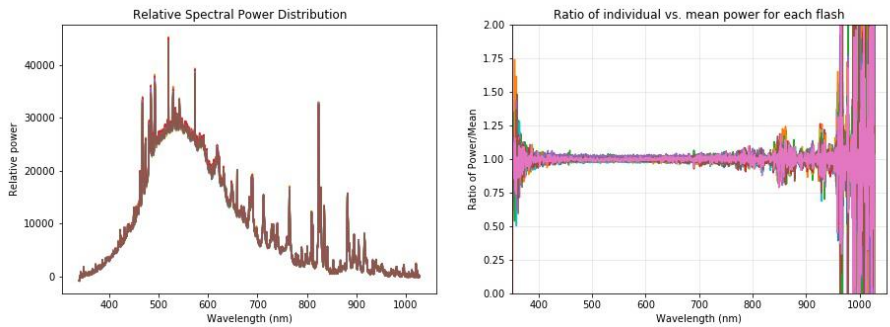
Figure 5-30. Repeatability test of Bowens flash. (left) Relative SPD (uncorrected) measured using the Ocean Optics USB2000+ spectrometer for seventeen successive flashes. (right) Plot of the ratio of the individual vs mean power for each flash.
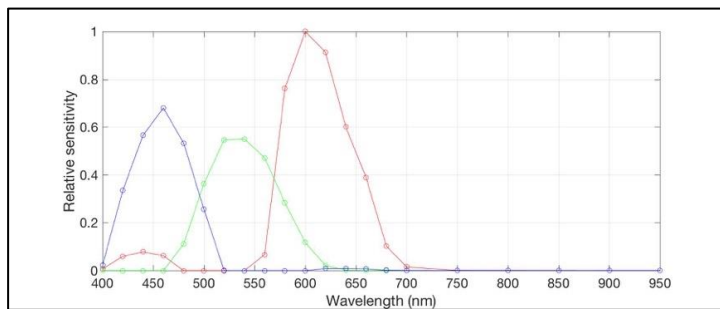
Figure 5-31. Spectral response measurement of the Canon camera using single Bowens studio strobe.
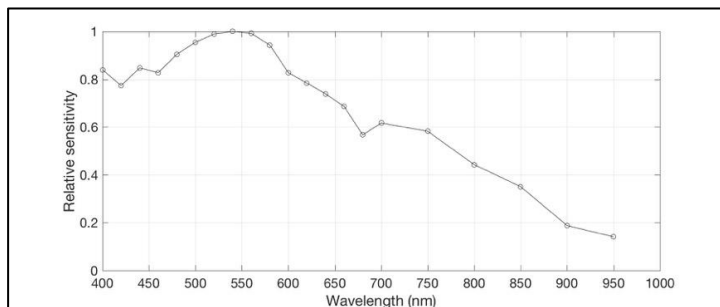
Figure 5-32. Spectral response measurement of the mCanon camera using single Bowens studio strobe.

The spectral response results for the mCanon included a dip around 660 nm. In investigating the source of the dip, higher spectral resolution measurements were requested from the manufacturer of the BP550 filter and measurements with 1 nm sampling were received. The initial transmission measurements of the UV-IR block filter from the manufacturer had a sampling of 10 nm. The 10 nm sampling measurements obscured a feature between 650 and 700 nm that was observable with the 1 nm sampling measurements (Figure 5-33). The difference in the 10 nm and 1 nm sampling changed the calculation for the transmission of

the filters (Figure 5-34 and Figure 5-35). The transmission measurements for each of the filters (including the VIS and NIR bandpass filters) was used to calibrate the image data of the reflectance standard with each filter in order to produce the spectral response measurements. While updating the processing for the spectral response measurements with increased spectral resolution measurements of the UV-IR block filter did not eliminate the peak at 650 nm (Figure 5-36), it does show that the spectral resolution of the measurement can impact the resulting calculation. However, this is not a significant impact for wavelength selection and cultural heritage documentation and would not factor into the use of this camera for these applications (Chapter 6).
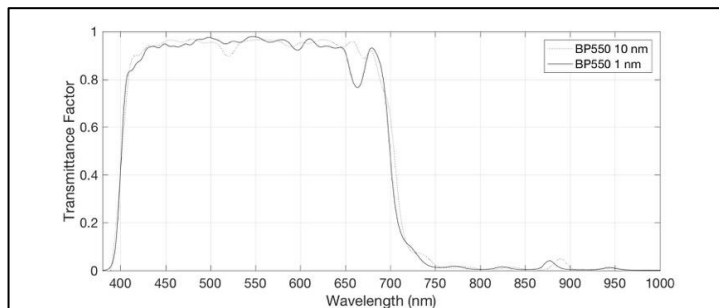
Figure 5-33. Transmission of BP550 filter measured with 10nm sampling and 1nm sampling. The absorption feature between 650 and 700 nm was not apparent with the 10nm measurement sampling.
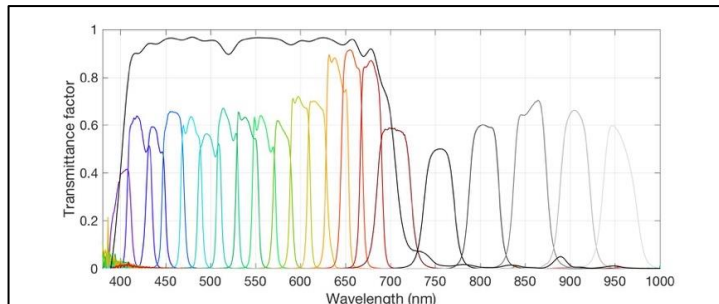
Figure 5-34. Transmission spectra of VIS and NIR filters with the corrected spectra for the 640 nm, 660 nm, 680 nm filters using the BP550 transmission measurements with a sampling of 10 nm.
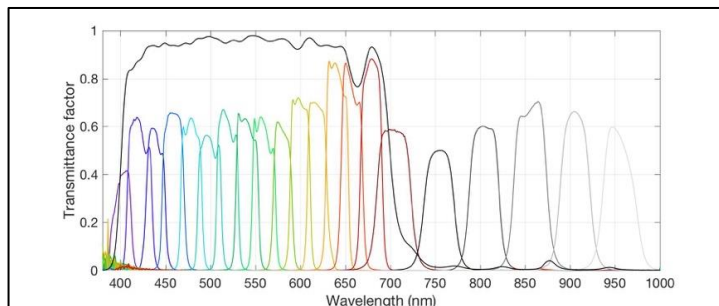
Figure 5-35. Transmission spectra of VIS and NIR filters with the corrected spectra for the 640 nm, 660 nm, 680 nm filters using the BP550 transmission measurements with a sampling of 1 nm.
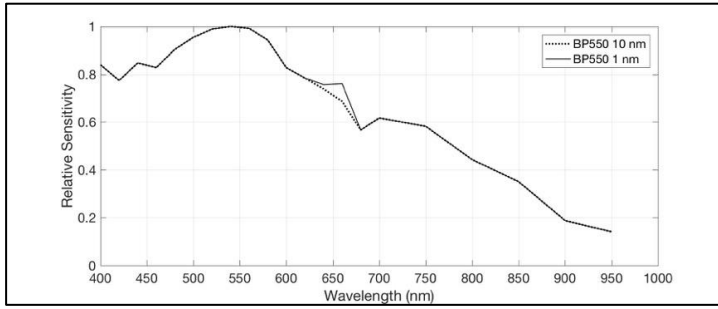
Figure 5-36. Comparison of the spectral response measurements showing the difference of results using the UV-IR block filter measurements with 1nm and 10nm sampling.

5.3.6.   Discussion

The iterations of this experiment informed its progression and development with the aim of improving the spectral sensitivity measurements. While the previous results and discussions focused on the individual results for the iterations, the following discussion and figures will look at comparing the results for the different iterations.

Figure 5-37 compares the results for the Canon camera using the tungsten lamps (dotted lines, Iteration #1 Section 5.3.2), two Canon flashes (dashed lines, Iteration #2 Section 5.3.3), and the Bowens studio strobe (solid lines, Iteration #4 Section 5.3.5). The three measurements for the unmodified camera include similar features, but the shapes showed some differences. With all three datasets the blue peaks at 460 nm, the green peaks at 520-540 nm, and the red peaks at 600 nm. The results using the tungsten lamps show differences in the relative sensitivity of the blue and green curves, and slight differences in the shape in the area of the longer wavelengths of the red curve.
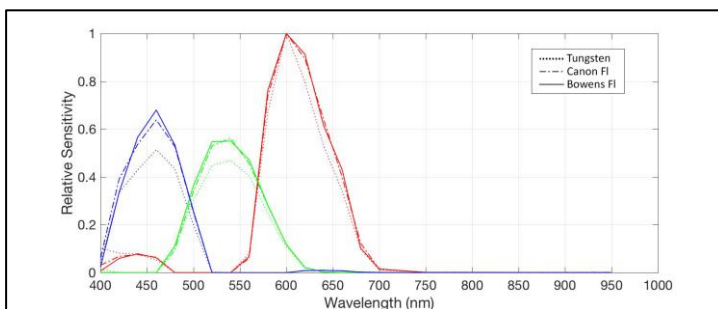
Figure 5-37. Comparison of spectral response measurement iterations of the Canon camera.

Figure 5-38 compares the results for the mCanon camera using the tungsten lamps (dotted line, Iteration #1 Section 5.3.2), two Canon flashes (bottom dashed line, Iteration #2 Section 5.3.3), one Canon flash (top dashed line, Iteration #3 Section 5.3.4), and the Bowens studio strobe (solid lines, Iteration #4 Section 5.3.5). The spikes below 460 nm for the first three iterations make it difficult to compare the results, so these were cropped to provide a better option for comparing the spectral response results (Figure 5-39). The cropped results were

normalised for comparison. The tungsten results did not resemble the flash results. There were similarities in the results for the iterations using the Canon flashes and the Bowens studio strobe with the biggest difference between 620-700 nm. The Canon flash iterations did not include the UV-IR cut filter, which could explain this region of differences. Otherwise Iterations#2, #3, and #4 showed similar results with high sensitivity in the shorter wavelengths and decreasing with longer wavelengths.
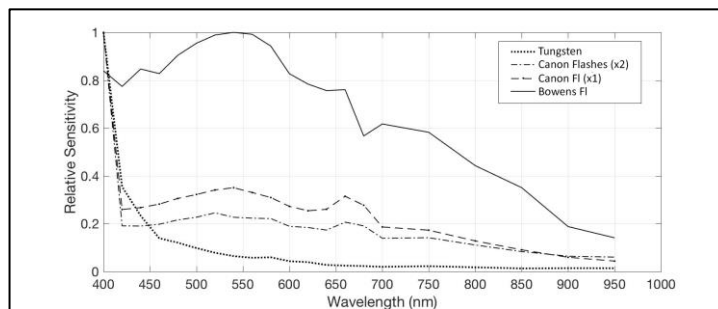
Figure 5-38. Comparison of spectral response measurement iterations of the mCanon camera. The spike below 460 nm for the tungsten lamp and Canon flash iterations make it difficult to compare the results.
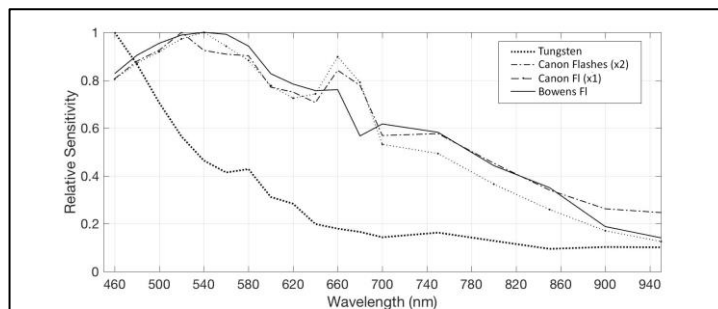
Figure 5-39. Comparison of spectral response measurement iterations of the mCanon camera with the measurements below 460 nm cropped. The Canon flash iterations and the Bowens studio strobe results showed similarities with the exception of the area between 620-700 nm.

Ideally there would be a reference dataset for verifying or comparing the resulting measurements. While there are published datasets available, the results are not consistent and there is a question of the accuracy and reliability of the available spectral characterisation data. The results of the corrected spectral sensitivity for the unmodified Canon camera were compared to Canon 5D Mark II results from Jiang et al. (2013a, 2013b) (Figure 5-40). Jiang et al. (2013a, 2013b) provided a database of 28 camera spectral sensitivities that were measured with a monochromator from wavelength 400 nm to 720 nm with an interval of 10 nm. This comparison showed significant differences in the shape and amplitude of the curves.
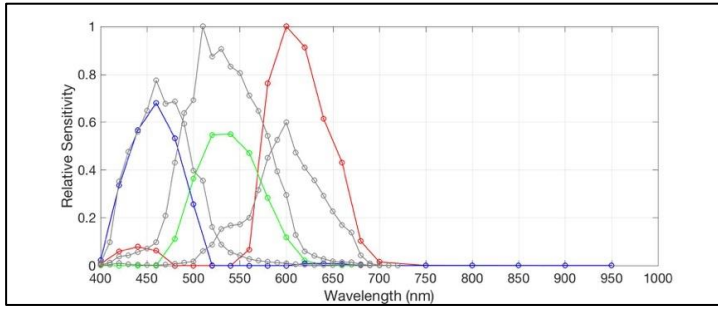
Figure 5-40. Comparison of spectral response results (red, green, and blue curves) with measurements from Jiang et al. (2013a, 2013b) (grey).

While Jiang et al. provided their datasets online, others have only included figures of their results making comparisons more challenging. The following examples show available spectral response data for the Canon 5D Mark II:

- The University of Tokyo had a database including measurements of 12 cameras using a monochromator and spectrometer with a range of 400-700 nm at a 4 nm interval ('Spectral Sensitivity Database', n.d.) (Figure 5-41).

- Results from Manakov (2016) show "ground truth" data measured with an integrating sphere, super-continuous laser for monochromatic light and acousto-optic filter and compared to measurements using an LCTF and broad-band light source (Figure 5-42).

- Measurements of the quantum efficiency are compared of the Canon 5D and Canon 5D Mark II using a spectrograph and set of narrow interference filters (Astrosurf, n.d.) (Figure 5-43).
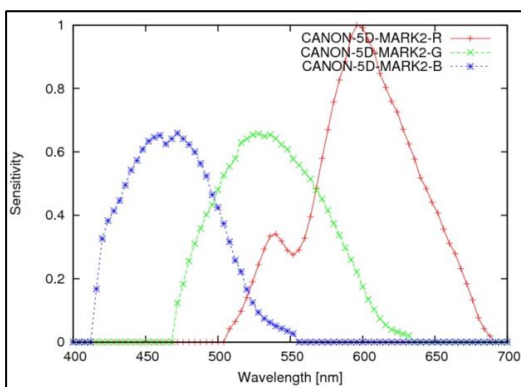
Figure 5-41. Spectral sensitivity of Canon 5D Mark II measured with a spectrometer and monochromator in the range of 400-700 with a sampling interval of 4nm ('Spectral Sensitivity Database', n.d.)
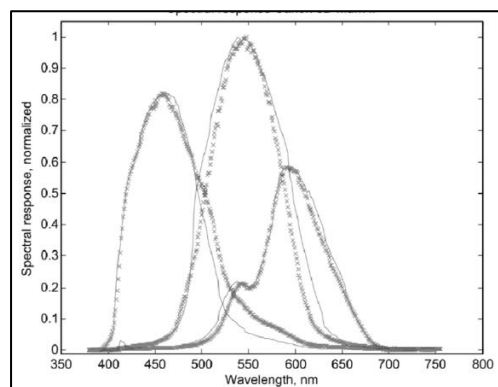
Figure 5-42. Spectral sensitivity of Canon 5D Mark II including a "ground truth" response (marked with crosses) and measurements acquired using an LCTF (Manakov, 2016).
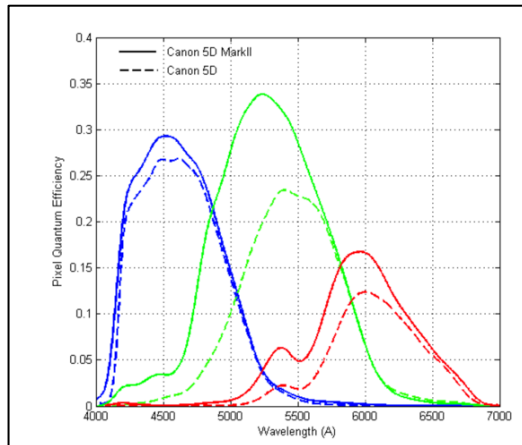
Figure 5-43. "Quantum efficiency" of Canon 5D and Canon 5D Mark II (Astrosurf, n.d.).

These three measurements for the Canon 5D Mark II share similar features: the blue sensitivity peaking at 450 nm, the green peaking at about 550 nm, the red peaking at about 600 nm, and a smaller red peak at about 550 nm. While these three have similar features the shape and features are a bit different from Jiang et al. (2013a, 2013b) and also the results from the measurements presented in this chapter.

The literature relating to measurement and estimation of spectral sensitivity has not included much about the reliability and accuracy of the results (Section 3.3.3). Darrodi et al. (2015) and Manakov (2016) are two examples that have discussed the uncertainties and accuracy of measuring and estimating spectral response. Darrodi et al (2015) is one of the few publications that discussed the uncertainty and error associated with the measurement of spectral sensitivity. Darrodi et al. provided ground truth data for two cameras (Nikon D5100 and Sigma SDMerill). However, there is a difference in the spectral sensitivity between cameras and manufacturers and this ground truth cannot be used as a reference for the Canon 5D Mark II measurements.

A weakness for the spectral response measurements presented in this chapter was that the final measurement did not include a validation process. Future spectral response measurements would benefit from acquiring measurement uncertainties during the process in addition to a validation process to provide an indication of the accuracy of the measurement. A validation could have been conducted by acquiring an image of the ColorChecker with the unmodified and modified cameras using the same illumination as the spectral response measurements. The values of the colour patches could then be used as a reference for a validation calculation. The colour patches would also need to be measured using a spectrometer. The validation could be calculated using equation 3.1 for output of an unmodified, colour sensor (ISO 17321-1:2012).

The selection of the light source for acquiring the image data for the spectral response measurement is essential. Three illumination sources, including continuous and flash, were used for the different iterations of this test (Figure 5-44). Initially data was acquired using a tungsten lamp. Tungsten halogen sources provide a continuous, white light source with a smooth SPD and high output in the NIR (dotted line in Figure 5-44). These sources have little or no output in shorter wavelength ranges near 400 nm. While these sources may be fine for many visible light and NIR imaging applications, the limitations in shorter wavelengths was problematic for the spectral response measurement and can be problematic for some spectral imaging.
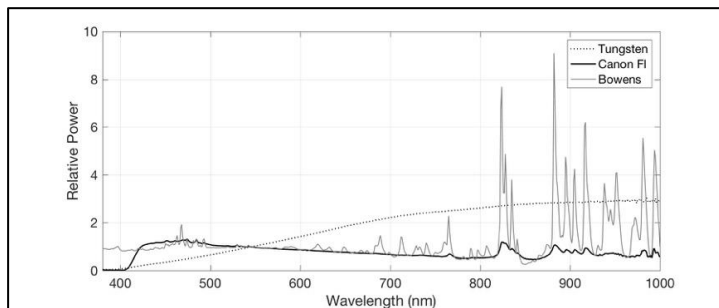
Figure 5-44. Measurements of the SPD of three illumination sources used for the spectral response measurements: tungsten lamps, Canon flash and Bowens flash.

Off-camera flashes (Canon Speedlite 580 EXII) were used for a couple iterations having improved output in the shorter wavelengths compared to the tungsten sources. However, the output was not enough to for measurements below 420 nm. In addition, repeatability tests showed variability in the power output. The Canon flashes are battery powered contributing to the varied power output, which relates to the recharge of the battery cells between firings. While off-camera flashes can offer small and portable illumination sources, the consistent current supply via electric mains is necessary for more repeatable results. The Bowens flash, used for the final dataset, had output in the shorter wavelengths and NIR, and repeatability tests showed reduced variability as compared to the Canon flashes. Various illumination sources, both continuous and flash, have advantages and disadvantages that influence why one might be selected over another. This experiment emphasised the importance of the SPD of the selection source and the reliability of the power output.

The iterations of the experiment improved the setup and results, but if it were to be run again there would be additional room for development. Ideally the setup would have stayed assembled during the duration of the experiment. Due to space constraints and a shared lab, the setup was disassembled every day or at least after each iteration of the experiment. This meant that some of the parameters of the setup changed, and the consistency of the measurement could have been improved by reducing these changes. Better practice would have also included using the same aperture throughout the project and the same white target.

Consistency across the measurements, transmission, and reflectance data, could be accomplished by using the same instrument for the different measurements. This research relied on the filter transmission measurements supplied by MacDonald and the manufacturers, which resulted in a different measurement ranges and sampling resolutions. For example, the visible light filters had measurements from 200-800 nm with a sampling interval of 0.6 nm, while the 700 nm filter was 200-2000 nm at 1 nm sampling; the 750 nm filter was 670-830 nm at 0.5 nm sampling; the BP550 filter was 350-1100 nm at 10 nm sampling. While these differences can be accommodated in the calculation process, using consistent measurements from the same device could simplify the processing and calculations. It also could provide the capability of better understanding and measuring the error and uncertainty of the calculation.

5.4. 3D Reconstruction

The third step of the camera characterisation assessed the 3D reconstruction quality from the images acquired with the mCanon camera and comparing to results from the Canon camera. The camera characterisation initially investigated the impact of the modification on the 2D image quality, which included a discussion and proposal for a RAW processing workflow. Image-based 3D reconstructions rely on 2D images for the resulting 3D model, and the 2D image quality can impact 3D quality. Investigation of the 2D image quality in Section 5.2 provided evidence that the RAW processing workflow influenced the image quality. Following on the 2D image quality investigation, this section assessed the impact of the modification and the influence of the RAW processing workflow on the resulting 3D reconstruction.

The assessment of the 3D reconstruction quality included two experiments: one using the Panel test target and the second using the Mango Vase. The first test with the Panel was used to assess the impact of the residual pattern in the modified camera images for the 3D reconstruction (Section 5.4.1). The second test with the Mango Vase test object was used to assess the 3D reconstructions from the Canon and mCanon cameras and to compare differences with RAW processing workflows (Section 5.4.2).

5.4.1. 3D Residual test with Panel test target

The first experiment assessing the 3D reconstruction for the camera characterisation used the high contrast pattern of the Panel test target to check the significance of the residual pattern and the effect on the 3D reconstruction. The exposure was reduced with each image set by one stop to decrease the contrast of the pseudo random pattern on the test object and

gradually flatten the contrast to give an indication of the level of noise related to image matching. A neutral density filter was used on the camera and the flash power was reduced by 1 stop for each image set. The reduction of the exposure provided control over the optical influence as opposed to the electronic (processing) influence.

5.4.1.1. Materials and methods

The camera positioning robot (Section 4.1.1.1) was used to reproducibly change the camera position and record the convergent image configuration (Section 4.1.2) for the 3D reconstruction of the Panel test target. The mCanon with the 60 mm lens was used to acquire the images of the target (Table 4-1). A B+W ND1.8 neutral density filter (Jos.Schneider Optische Werke GmbH Geschäftsbereich) was used with the flash to control the exposure (reducing the exposure optically as opposed to electronically). The first exposure set was acquired without a filter with a flash power setting at 2. The following exposures included the ND1.8 filter and decreasing flash power, starting at 6 and decreasing a stop for each exposure step until the minimum flash power was reached (flash power of 1). The camera settings of f/11 ISO 100 and 1/100 sec were maintained for all the image sets. A white field image was acquired after each image. Each image of an exposure set was positioned differently in relation to the target and lights and therefore a single white field could not be acquired for the entire exposure set. Images of the DICE target were acquired to provide indications of the image quality linked to the 3D reconstruction results. The images were processed following the MC-RAW workflow (Section 5.1), the 3D reconstructions were processed in PhotoScan (Section 4.1.1.2) using a limited selection of camera parameters (solving for *f, cx cy, k1, k2, p1, p2*), and the results were compared to an averaged reference dataset (Section 4.1.3).

5.4.1.2. Results and discussion

A total of seven image sets were acquired starting at exposure *a* and decreasing the exposure by 1 stop using a neutral density filter and changing the flash power. The final image set was exposure *g* acquired with the neutral density filter and a flash power of 1. The alignment for exposure *f* and *g* failed in the PhotoScan processing, and while the images aligned for exposure *e,* there was not enough detail observed to place the markers for scaling. The results for exposures *a-d* include a composite image of the DICE target (greyscale and central feature) at the four exposures; a 600 x 600 pixel detail area of the Panel at the four exposures; and surface discrepancy maps of the resulting 3D reconstructions compared to an averaged reference mesh (Figure 5-45). The four successful 3D reconstructions for

exposures *a-d* are within +/-0.06 mm of the averaged mesh showing the resilience of the pseudo random pattern for 3D reconstructions.
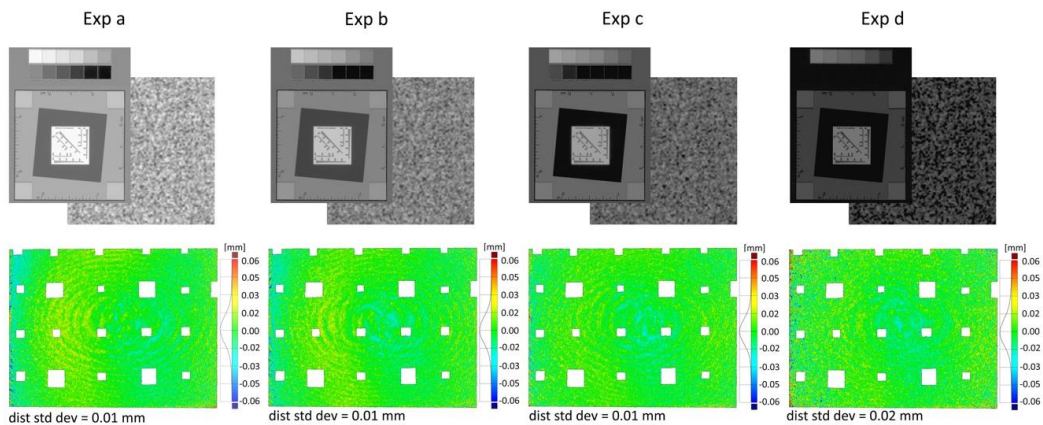
Figure 5-45. 3D Residual tests results. Top Left: Composite image of the DICE target—greyscale and central feature; Top Right: Detail of Panel (600 x 600 pixel area from centre of image); Bottom Row: Surface discrepancy maps comparing the 3D reconstruction to an averaged mesh.

The lowest contrast that produced a successful reconstruction was a pixel value difference of 18,010 between the lights and darks in the *Exp d* set of the Panel (100 x100 pixel area) (Figure 5-46, Table 5-2). When the pixel value difference was 11,116 (*Exp e* in Table 5-2), the 3D reconstruction was not successful. This would suggest that a pixel value difference greater than 11,000 would be needed for the 3D reconstruction of the Panel. Looking back at the difference of pixel values for the residual pattern (Figure 5-3), the pixel value difference was less than 6,000 which fell under the value of 11,000 needed for a 3D reconstruction. Since the amplitude of the residual pattern was less than the contrast required for the 3D reconstruction, this would suggest that the residual pattern would not impact the 3D reconstruction.
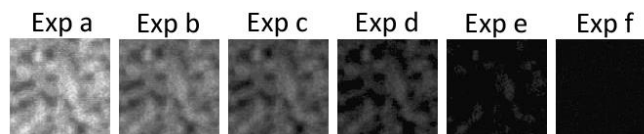
Figure 5-46. Details of decreasing contrast of Panel pattern with reduced exposure. These details from the centre of the panel image were used to calculate the minimum, maximum and difference values in Table 5-2.

The most extreme impact from the pixel-level pattern that would have the highest pixel value difference would be represented by the Bayer pattern in an image acquired with the unmodified camera and processed using DCRAW without demosaicing. The difference of pixel values was 17,361 (Figure 5-3), which would be more likely to impact the 3D reconstruction as it was greater than 11,000 and was close to the value of the contrast in the set of Exp d (18,010) which was successfully reconstructed (Figure 5-45). According to

these results the pixel level pattern observed with the modified camera should not be influencing the 3D reconstruction, but the results for the 3D reconstruction of the Panel with reduced exposure (Figure 5-45) was not representative of heritage objects and reflected more resilience for the 3D processing (based on the contrast of the pseudo random pattern) than heritage objects having a lower local contrast.

Table 5-2. Minimum, maximum, difference values for 100 x 100 pixel area of the pseudo random pattern.

	Min	Max	Diff
Exp a	20,766	60,640	39,874
Exp b	12,533	41,326	28,793
Exp c	2,621	30,433	27,812
Exp d	2,621	20,631	18,010
Exp e	2,621	13,787	11,166
Exp f	2,621	9,258	6,637

The image processing for the 3D residual test included a gamma correction to enhance the contrast for improved image matching. The gamma correction impacts the linearity of the response, and the experiment was intended to change the exposure of each set by one stop. Figure 5-47 shows the nonlinear response for the gamma corrected images (top row) and the linear response of the non-gamma corrected images (bottom row). A comparison of the 3D reconstructions of the f/11 *Exp a* image set with and without gamma correction shows a difference of +/- 0.03 mm (Figure 5-48). PhotoScan is likely implementing something like a Wallis filter, a locally adaptive filter to enhance contrast, to increase local contrast to improve image matching. If PhotoScan is implementing this processing, then not much difference in the results would be expected until the contrast is comparable to the amplitude of the noise.
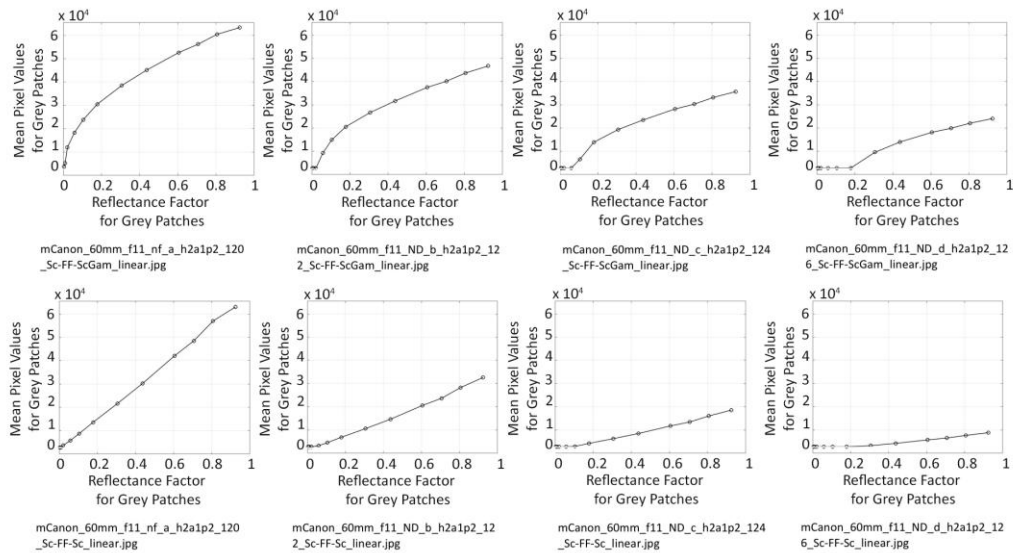
Figure 5-47. Assessing the linearity of the processing by investigating the intensity response. The top row shows nonlinear response of the images processed with gamma correction and the bottom row shows the linear response of the images processed without gamma correction.

dist std dev = 0.01 mm
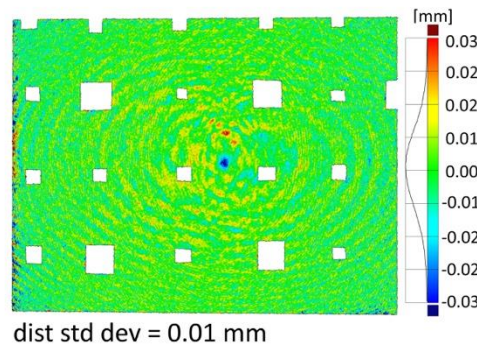
Figure 5-48. Comparison of 3D reconstructions with and without gamma correction for the f/11 Exp a image set. The 3D processing included the estimation of all the camera model parameters.

5.4.2.   3D Reconstruction of Mango Vase test object

While the Panel test target was used to look specifically at the impact of the residual pattern with the modified camera images, the Mango Vase was used to compare 3D reconstruction results from the Canon and mCanon cameras. Three image sets of a Mango Vase test object were acquired with the both cameras for the image-based 3D reconstruction of the object. These image sets included one visible light image set acquired with the Canon camera (denoted 'VIS'); one visible light image set acquired with the mCanon camera and a visible pass filter (denoted 'mVIS' for modified visible); and one reflected IR image set acquired with the mCanon camera and an IR pass filter (denoted 'IR') (Figure 5-49). These image

sets were processed using separate RAW processing workflows, totalling nine image sets. These nine image sets were processed into 3D reconstructions and the resulting models were compared to reference data of the test object to provide indications about the impact of the camera modification and the MC-RAW workflow on the resulting 3D reconstructions.
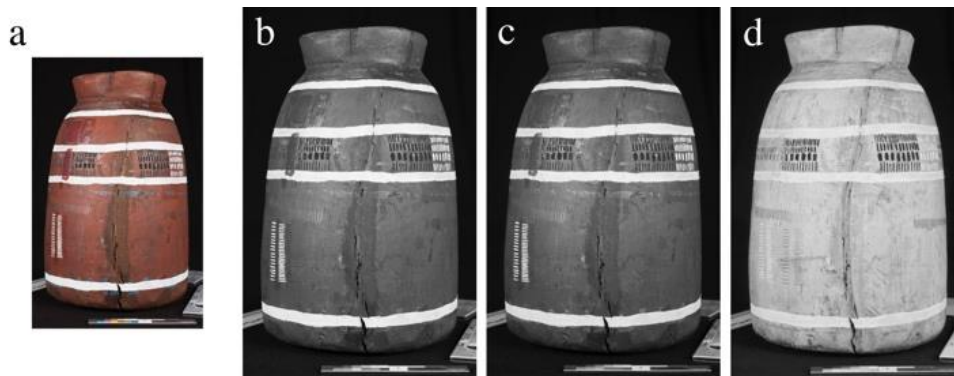
Figure 5-49. Mango Vase test object: (a) visible light image from Canon camera, (b) greyscale visible light image from Canon camera ('VIS'), (c) visible light image from mCanon camera and visible pass filter ('mVIS'); and (d) NIR image from mCanon camera and NIR pass filter ('IR').

5.4.2.1. Materials and methods

The Canon and mCanon cameras were used with the 60 mm lens (Table 4-1) to acquire images of the Mango Vase test object (Section 4.2.1.1). A UV/IR-block and VIS-pass filter, a Peca 916 filter (Figure 5-7), was used on the mCanon camera in order to simulate a similar wavelength range to the unmodified camera. A long-pass filter, a Peca 910, was used for reflected IR
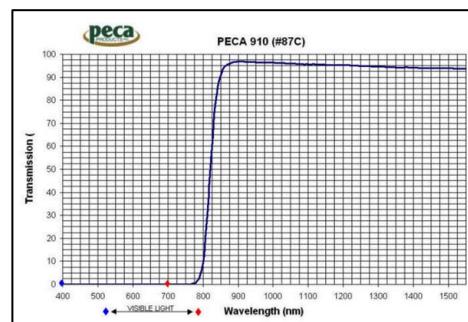
Figure 5-50. Transmission curve for Peca 910 filter cutting on at 850 nm (50% transmission) ('IR-UV Filters', 2015).

imaging, which is comparable to the Kodak Wratten 87C filter and passes wavelengths above 800 nm (Figure 5-50). Two Bowens Gemini GM400Rx studio strobes with umbrellas were used to illuminate the object for all three image sets. The setup and turntable acquisition was the same as presented in Section 4.2.1 and Figure 4-16.

The first dataset acquired was the visible light images using the Canon camera ('VIS'). All three views were acquired with the Canon camera and then the camera was switched to acquire the two datasets with the mCanon: 'mVIS' using the Peca 916 filter and 'IR' using the Peca 910 filter. The first view for the 'mVIS' dataset was acquired and then the first view for the 'IR' dataset was acquired switching the filters and changing the flash output. The camera was then raised by increasing the height of the central tripod column to the

position for view 2. The camera was not refocused, but Live View was used to ensure that the focus was still sharp and the object was centred in the field of view. The tripod was moved to fine-tune the focus as opposed to refocusing the camera. Refocusing the camera would alter the camera calibration, so the lens focus was maintained for each dataset. Images were acquired for view 2 for both the 'mVIS' and 'IR' datasets before raising the camera to the third and final view.

Table 5-3Table 5-3 provides the information about the camera and flash settings for the three image sets.

The first dataset acquired was the visible light images using the Canon camera ('VIS'). All three views were acquired with the Canon camera and then the camera was switched to acquire the two datasets with the mCanon: 'mVIS' using the Peca 916 filter and 'IR' using the Peca 910 filter. The first view for the 'mVIS' dataset was acquired and then the first view for the 'IR' dataset was acquired switching the filters and changing the flash output. The camera was then raised by increasing the height of the central tripod column to the position for view 2. The camera was not refocused, but Live View was used to ensure that the focus was still sharp and the object was centred in the field of view. The tripod was moved to fine-tune the focus as opposed to refocusing the camera. Refocusing the camera would alter the camera calibration, so the lens focus was maintained for each dataset. Images were acquired for view 2 for both the 'mVIS' and 'IR' datasets before raising the camera to the third and final view.

Table 5-3. Camera and flash settings for the Mango Vase image sets

Image Set Name	Camera	Filter	Camera Settings	Flash Power
'VIS'	Canon 5D Mark II	None	ISO 100 f/11 1/100	3
'mVIS'	Modified Canon 5D Mark II	Peca 916	ISO 100 f/11 1/100	2.6
'IR'	Modified Canon 5D Mark II	Peca 910	ISO 100 f/11 1/100	5

The image sets were each processed in three ways to compare and assess the RAW processing workflow. The standard RAW processing workflow with ACR and the MC-RAW workflow were discussed in Section 5.1. Figure 5-51 summarises the specifics about the 2D image processing for the image sets. The image-based 3D reconstruction processing used PhotoScan and followed the CHI *error minimisation workflow* (Section 4.1.1.2). For the camera model, including a single radial distortion parameter showed the best results for the Mango Vase (Section 4.2.3). The resulting 3D reconstructions were assessed by comparing each with 3D scanned data of the test object that was acquired at AICON3D

using GOM Inspect, despite limitations with this data (Section 4.2.1). Issues with the rotational symmetry and the alignment of the Mango Vase data were discussed in Section 4.2.2. The limitations of this 3D scanned data and a more complete discussion about the challenges and limitations of the reference data for the Mango Vase and cultural heritage objects were discussed in Section 4.3.

VIS	mVIS	IR
Canon Filter: None	mCanon Filter: Peca 916	mCanon Filter: Peca 910
ACR Demosaicing Converted to greyscale	**ACR** Demosaicing Converted to greyscale	**ACR** Demosaicing Converted to greyscale
DCRAW ScGam Demo DCRAW: −4 −T * Demosaicing Converted to greyscale Scaling + Gamma Cor	**MC-RAW** DCRAW : −D −4 −T No demosaicing Flat field correction Scaling + Gamma Cor	**MC-RAW** DCRAW : −D −4 −T No demosaicing Flat field correction Scaling + Gamma Cor
DCRAW ScGam no Demo DCRAW : −D −4 −T No demosaicing Flat field correction Scaling + Gamma Cor	**DCRAW ScGam** DCRAW : −D −4 −T No demosaicing Scaling + Gamma Cor	**DCRAW ScGam** DCRAW : −D −4 −T No demosaicing Scaling + Gamma Cor

Figure 5-51. Diagram summarising the image sets and 2D image processing for the three image sets. The Spectralon diffuse reflectance standards (2% and 99% standards) were used for the scaling to map the blacks to an output of 2% and the whites to an output of 99%, and a gamma correction of approximately 1/2.2 was applied were indicated.

5.4.2.2. Results and discussion

The nine resulting 3D reconstructions of the Mango Vase were aligned and compared to reference data of the test object using GOM Inspect (Figure 5-52). The third row of Figure 5-52 presents results from a second set of DCRAW processing, which looked at the impact of the residual pattern for the mCanon images. Figure 5-53 shows details from the *IR* image set with the flat field correction ('FFC') and without ('ScGam'). The pixel-level pattern (Section 5.1) is visible in the details without the flat field correction ('ScGam'). The *IR* results from the DCRAW processing without flat field correction showed better correspondence with the reference data than the *mVIS* results. This could indicate that the residual pattern was less of a problem in the IR than in the visible range; however, the *mVIS* results with ('MC-RAW') and without flatfield correction ('DCRAW ScGam') were similar which could indicate that the residual pattern was not influencing the results. A comparison of the *IR* results with and without flatfield correction (Figure 5-54) showed a difference of +/-0.05 mm. A similar comparison of the *mVIS* results with and without the flatfield correction (Figure 5-55) showed a slightly larger difference than the *IR* results of +/-0.08 mm. The change in the wavelengths and also the optical properties of the surface of the

object will impact the results and the residual pattern. The comparisons of the *IR* and *mVIS* results both had discrepancy distributions offset from zero, which could suggest that a scaling issue was preventing the observation of the true impact of the residual pattern. From these comparisons the residual pattern did not introduce an error larger than +/- 0.10 mm.
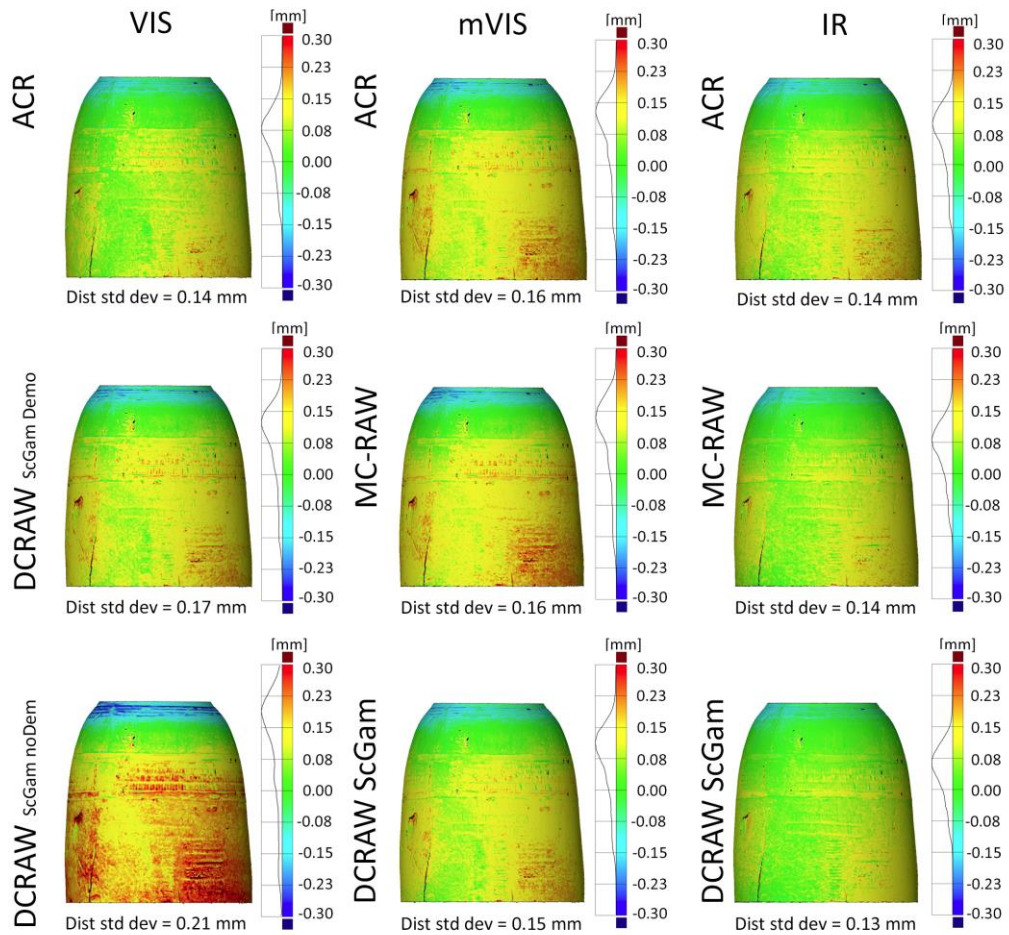
Figure 5-52. 3D Reconstruction results for testing the Canon and mCanon cameras assessed using AICON3D 2016 scanned data. The figure includes surface discrepancy maps comparing 3D reconstructions from the Canon camera ('VIS') and the mCanon camera ('mVIS' and 'IR') using different 2D image processing described in Figure 5-51.
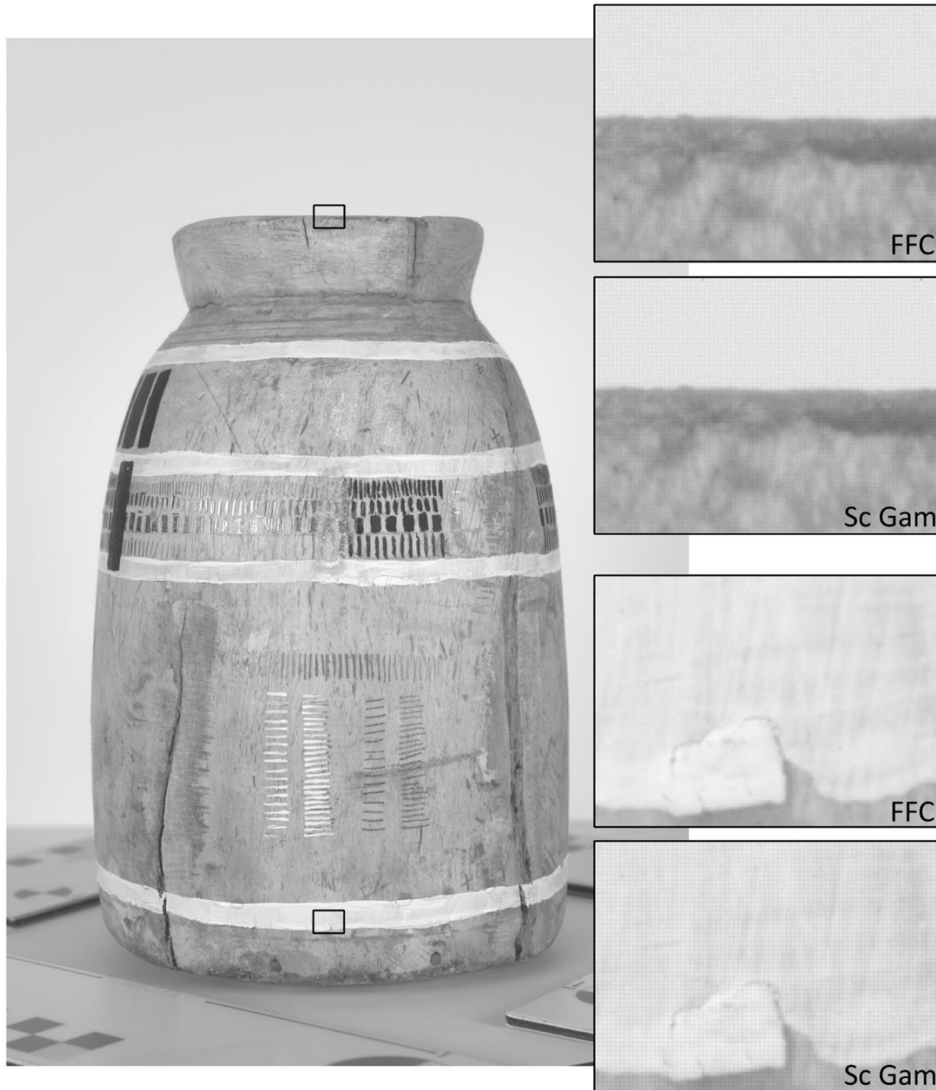
Figure 5-53. Reflected IR image of Mango Vase showing details of the image set processed with ('FFC') and without ('Sc Gam') flat fielding. The pixel-level pattern can be observed in the processing without the flat fielding.
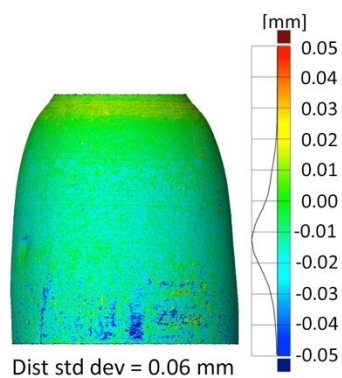
Figure 5-54. Surface discrepancy map comparing IR MC-RAW with IR DCRAW ScGam.
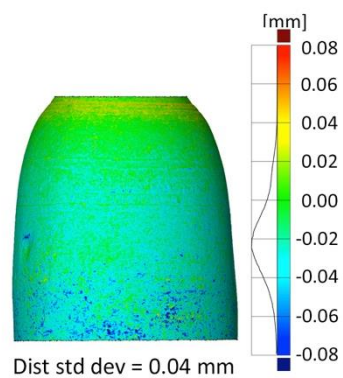
Figure 5-55. Surface discrepancy map comparing mVIS MC-RAW with mVIS DCRAW ScGam.

The largest discrepancies observed resulted from the unmodified camera ('VIS') with the DCRAW processing without demosaicing ('DCRAW ScGam noDem'). To simulate the most extreme pixel-level pattern, the *VIS* images were processed without demosaicing resulting in the Bayer pattern being present in the input images. Figure 5-56 includes a detail to show the Bayer pattern when the images are not processed with demosaicing. The images without demosaicing resulted in a 3D reconstruction that had the largest discrepancy of the nine 3D reconstructions, a discrepancy of +/- 0.30 mm. This illustrates that the pixel level pattern can impact the 3D reconstruction and at its most extreme could cause a discrepancy of +/-0.30 mm.
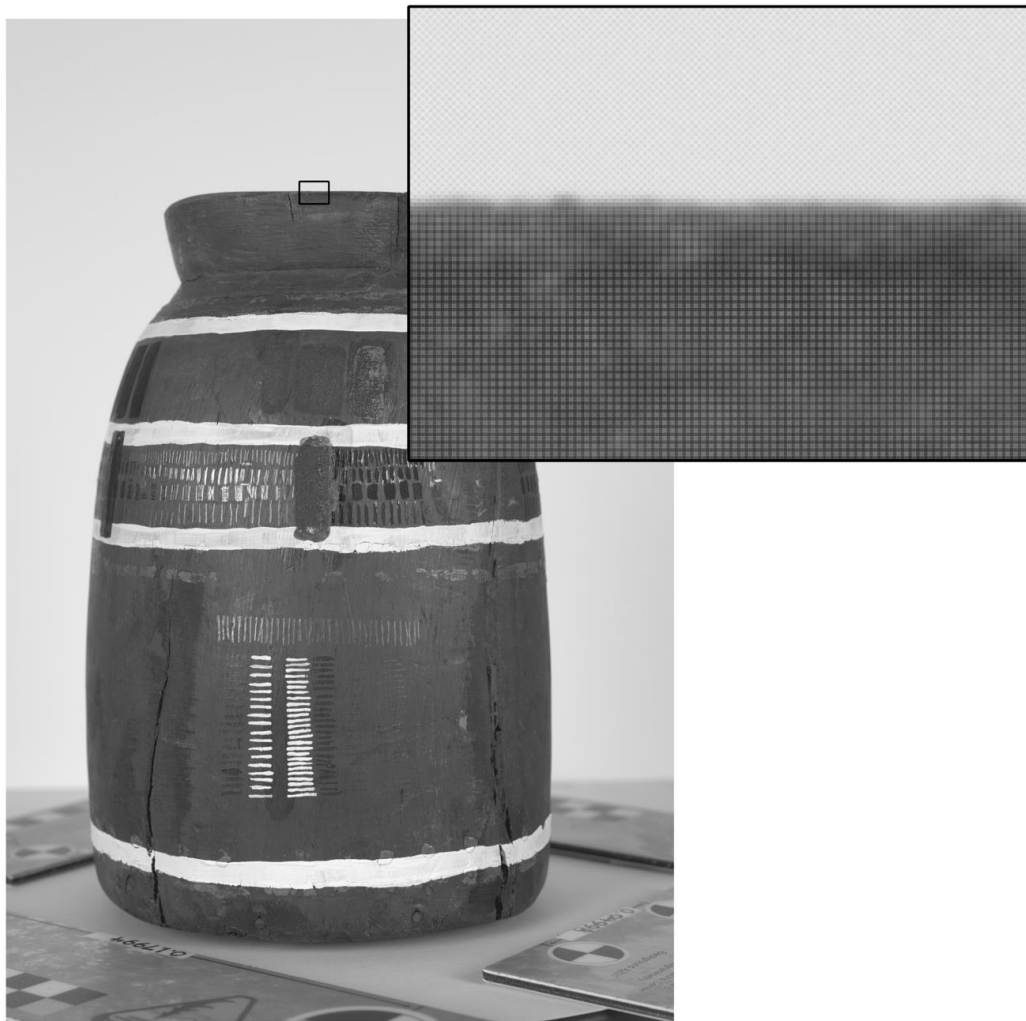
Figure 5-56. Visible light image of Mango Vase from 'VIS' image set without demosaicing showing detail of the Bayer pattern.

The other assessments of the 3D reconstructions are showing a difference of less than +/-0.30 mm from the "reference" data with standard deviations less than 0.20 mm (Figure 5-52). All of the results are showing an offset from zero, which may be representative of a scaling issue (Section 4.2). To reduce or eliminate the scaling issue, the 3D reconstructions

were compared to the "reference" data restricting the alignment (best-fit alignment with 0.20 mm tolerance) and surface comparison to two patches independently (Figure 5-57). The local surface discrepancy maps were resulting in a more normal distribution with random errors showing a difference between the models of less than +/-0.06 mm. The results of the local surface comparisons showed that there was not a significant difference between the 3D reconstructions from images acquired with the unmodified and modified cameras or with different image processing methods. The most significant error was likely resulting from a scaling issue, which might be resolved by the inclusion of targets and scale bars throughout the volume of the area being recorded and not just at the base of the object (Section 4.2.2).
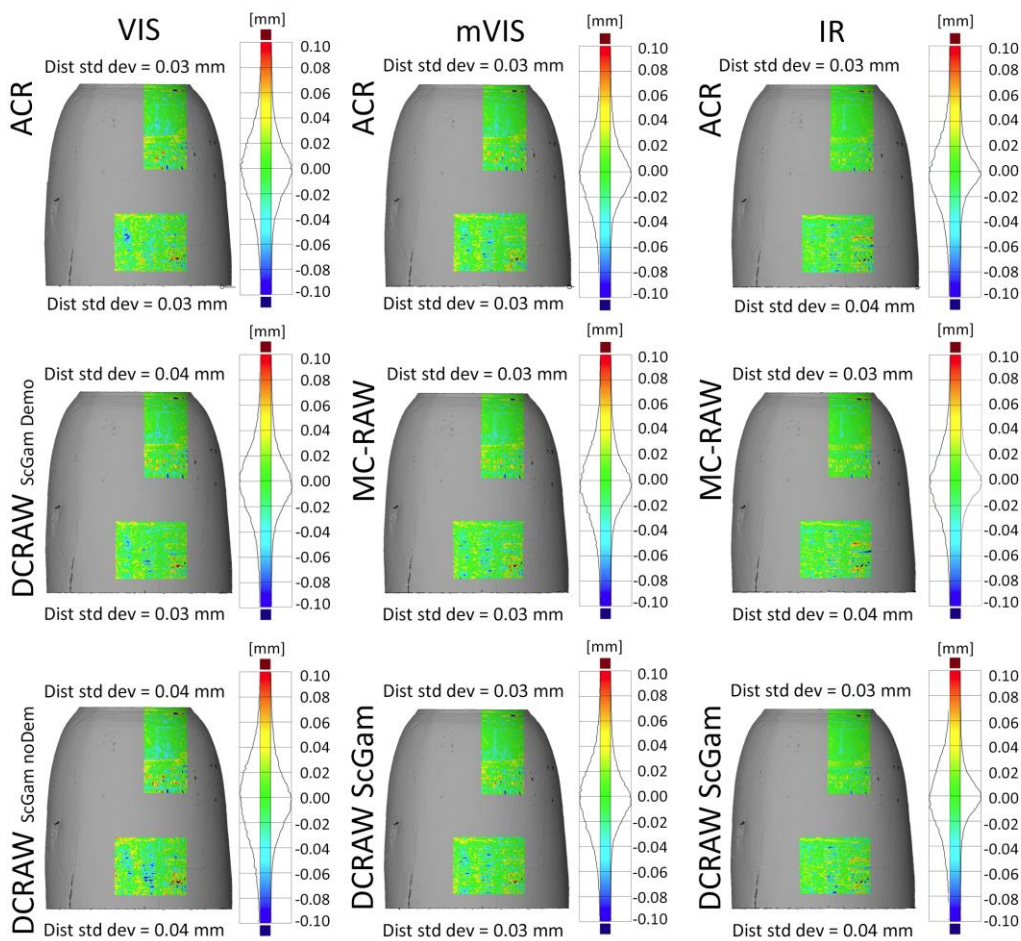
Figure 5-57. Local surface comparisons of 3D reconstruction results for testing the Canon and mCanon cameras assessed using AICON3D 2016 scanned data. The figure includes local surface discrepancy maps comparing 3D reconstructions from the Canon camera ('VIS') and the mCanon camera ('mVIS' and 'IR') using different 2D image processing described in Figure 5-51. The lower comparison is represented by the left histogram and the upper comparison is represented by the right histogram.

While there were differences observed among the 3D reconstructions from the different RAW processing, there was not a significant difference between the reconstructions results from the Canon and mCanon cameras. The MC-RAW workflow (Section 5.1) is suggested for the mCanon camera to account for the camera modification. The MC-RAW workflow

impacted the 2D image quality (Section 5.2). The pixel-level pattern did not seem to be impacting the resulting 3D reconstruction, although the *VIS* image set with DCRAW processing and no demosaicing did provide evidence that a pixel-level pattern could impact the reconstruction and at its extreme the discrepancy was 0.30 mm.

5.5. Chapter summary

This chapter presented the camera characterisation of the modified camera addressing an aspect of the research question "Can photography with a modified consumer digital camera paired with selected illumination and filtration be used as a scientific method to better benefit the 3D reconstruction of museum objects for conservation documentation?" The research question is focused on the use of the modified camera as a scientific tool and as part of the wavelength selection process to improve image-based 3D reconstruction. In order to assess or use the device as a scientific tool and as a part of the wavelength selection process, characterisation is required to define the nature of the system. As discussed in Section 3.3, characterisation is necessary to assess the modified camera's performance and to understand the impact of the modification. The modified camera was characterised by assessing the 2D image quality (Section 5.2), measuring the spectral response (Section 5.3), and evaluating the resulting 3D reconstruction (Section 5.4).

A RAW processing workflow is essential for the recording of scientific information, but the standard workflow does not take into account the camera modification. The MC-RAW workflow was proposed (Section 5.1) that included a flat field correction to reduce the effect of a fixed pattern noise. The MC-RAW workflow provided more control over the processing and took into consideration the camera modification. While the workflow reduced the fixed pattern noise, it did not eliminate it, and the implementation of the workflow is limited as it is not yet an accessible solution. Future research will include investigating and testing a better correction for the fixed pattern noise and increasing the usability of the processing.

The 2D image quality assessment (Section 5.2) included evaluating the noise, sharpness, and resolution using the DICE target and software. The Canon and mCanon cameras were compared in addition to the 60 mm and 50 mm lenses. The results for the noise assessment showed low noise for the ACR processing, but increased noise levels for the MC-RAW processing. The ACR processing includes noise reduction that keeps the noise levels below 2σ, while the MC-RAW processing does not include noise reduction and noise levels reached as high as 7σ. The mCanon camera paired with the high quality 60 mm lens and the MC-RAW workflow resulted in a higher effective resolution but at the risk of aliasing (SFR10 results above the Nyquist limit and a sampling efficiency over 100%). The 2D

image quality assessment indicated that the RAW processing workflow is an important consideration for the resulting 2D image quality. While the MC-RAW workflow corrected for the fixed pattern noise and allowed for an increased effective spatial resolution, the resulting SFR assessment and sampling efficiencies indicate the risk of aliasing.

The spectral response measurements (Section 5.3) included four iterations showing the experimental progression and development with the aim of improving the final measurements. The four iterations included three illumination sources (tungsten lamps, off-camera flashes, and studio strobes), testing the repeatability of the flash sources, and providing evidence for the critical use of the UV-IR block filter for the 640 nm, 660 nm, and 680 nm filters. The final setup and acquisition included a studio strobe with electric mains that provided repeatable output from the near UV through visible and into the NIR. The camera modification increased the spectral sensitivity range, as can be expected with the removal of the IR blocking filter and the CFA. The spectral response results showed an increased sensitivity in shorter wavelengths around 400 nm, which is over four times the sensitivity of the camera to the longer NIR wavelengths around 950 nm.

The 3D reconstruction quality assessment (Section 5.4) included tests with the Panel test target and Mango Vase. The Panel and the contrast of the pseudo random pattern was used to check the significance of the residual pattern and the effect on the 3D reconstruction. The amplitude of the residual pattern is less than the pixel value difference required for the 3D reconstruction suggesting that the residual pattern should not be impacting the 3D reconstruction. While there is a difference observed with the 3D reconstructions of the Mango Vase from different RAW processing, there does not seem to be a significant difference between the reconstructions results from the unmodified and modified cameras. The MC-RAW processing workflow (Section 5.1) is suggested for the modified camera to account for the camera modification, but the workflow impacted the 2D image quality (Section 5.2). However, the pixel-level pattern does not seem to be impacting the resulting 3D reconstruction.

Findings and recommendations:

A RAW processing workflow is essential for recording of scientific information. The standard workflow does not take into account the camera modification, so this research presented the MC-RAW workflow. While the workflow takes into account the camera modification and reduced the fixed pattern noise, it did not eliminate it, and the implementation of the workflow was limited as it is not yet an accessible solution. Future

research will include investigating and testing a better correction for the pattern and increasing the usability of the processing.

Understanding the characteristics of the different parts of the imaging system is important for broadband and narrowband spectral imaging (SPD of illumination/radiation source, transmission of the filters, spectral sensitivity of the camera, and the image quality of imaging system). This helps to better understand what is being recorded which can inform the interpretation and analysis of the results.

2D image quality assessment provides a method that can be used for comparing results with other systems. In Chapter 4, there was a discussion about monitoring objects over time and the change of technology and instrumentation. 2D image quality assessment could provide a baseline to show how the technology and instrumentation may be changing over time and provide an indication of the scale of change that could be recorded.

Camera characterisation is necessary to use the device as a scientific tool. The research demonstrated methods for camera characterisation for conservation documentation using known methods from collections photography and scientific imaging. A better understanding of the device, through characterisation, can provide improved results and a better understanding of these results in addition to the capabilities to measure and quantify the outcomes.

Measuring the spectral response quantifies the modified camera as a scientific device for more accurate measurements and provides indications of wavelengths that could improve documentation based on sensitivity. The spectral response measurements help with understanding where the camera performs with the highest sensitivity. A consideration in using this data is pairing it with the appropriate light source and filters looking at the SPD of the light source and the transmission measures for potential filters. Areas of lower camera sensitivity, lower output of the light source, and/or lower transmission of the filter can result in image data with increased noise. The spectral response measurements can be paired with laboratory tests investigating the impact of wavelength on image quality and local image geometry in order to select wavelengths that minimised the surface discrepancy for 3D reconstruction (Chapter 6).

Contribution to knowledge:

This chapter provides evidence of a contribution to knowledge by ensuring consistent imaging quality and capabilities through the processes of camera characterisation presented including the MC-RAW processing workflow. Camera characterisation is not common for

conservation documentation, and spectral response measurements are generally not reported as part of cultural heritage documentation. There are early examples of camera characterisation for MSI that establish the limitations of the imaging system like Casini et al. (1999), but these studies have not been linked to current uses of modified cameras for conservation documentation. This research demonstrated methods for camera characterisation for conservation documentation borrowing known methods from collections photography and scientific imaging through the use of the DICE target, FADGI guidelines and underlying ISO standards, and the spectral response measurements followed a method with links to scientific imaging and colour science.

The results provide an understanding of the limitations of a modified consumer digital camera as a scientific tool for cultural heritage documentation, which has not previously been available. A better understanding of the device, through characterisation, can provide improved results and a better understanding of these results in addition to the capabilities to measure and quantify the outcomes. While the characterisation is demonstrated by assessing a modified consumer camera that has benefits for museum imaging, these methods can be used for assessing other imaging sensors that are not necessarily modified or low cost. The characterisation method is beneficial to ensuring quality and consistency across a wide range of imaging sensors and museum recording applications.

6. Improved 3D reconstruction: Wavelength

Imaging using selected wavelengths rather than full spectra within or beyond visible light can increase the image contrast of materials or features to provide an enhanced view. In turn, improved local detail and contrast through wavelength selection can be expected to improve image-based 3D reconstruction for conservation documentation. Consequently, this chapter explores improvements in image quality through the use of wavelength selection (Section 6.1) and its effect on image-based 3D reconstruction of a museum object (Section 6.2). The work contributes to the research question: "Can photography with a modified consumer digital camera paired with selected illumination and filtration be used as a scientific method to better benefit the 3D reconstruction of museum objects for conservation documentation?"

6.1. Wavelength and image quality

The work builds on the modified camera characterisation (Chapter 5) and the filter set transmission to select narrow wavelength bands informed by the spectral response measurements and filter combination to confer the system's highest sensitivity. While sensitivity information could be used to select wavelength ranges for image acquisition, further quantification of image quality and performance at the selected waveband is needed coupled with an understanding of the spectral characteristics of the museum object under investigation. Quantification of imaging performance in relation to wavelength was explored as described in this section by imaging the DICE target with the modified camera and the visible and NIR filter set.

6.1.1. Materials and method

A set of visible filters (400-700 nm) and NIR filters (700-950 nm) (Section 5.3.1 and Figure 5-15) were used to acquire a sequence of images of the DICE target. Studio strobes, Bowens Gemini GM400Rx flash units, were used to illuminate the target. Using a strobe for illumination introduced limitations in balancing the exposure for this test. With a continuous tungsten lamp source, the aperture and ISO could remain constant while the shutter speed could be adjusted (within the limits of image noise) to balance the illumination reaching the sensor with a given filter set. However, with the strobe the shutter speed is limited to the flash sync speed of the camera. In practice, shutter speeds between 1/60th and 1/200th of a second did not change the exposure of the image as the same amount of light reaches the sensor and depends instead on the output of the flash. For all strobe imaging the shutter was standardised at 1/100th of a second and the aperture was held constant. Changing the aperture will impact the image quality, so the aperture needed to remain constant. Balancing of the

exposure with different filter transmissions was achieved by adjusting the strobe output power and the effective ISO setting on the camera. When possible the ISO was kept at 100 to minimise the introduction of noise, but in some cases the output of the flash was maximised and there was still not enough light reaching the sensor for a proper exposure. In this case the ISO was increased to balance the exposure.

The unmodified and modified cameras were paired with the 50 mm and 60 mm lenses (Table 4-1) and bandpass filters. RAW images of the DICE target with the series of bandpass filters were acquired. The images were processed using ACR and the MC-RAW workflow (Section 5.1). The images were analysed using GoldenThread software focusing on noise, sharpness, and resolution using measures for noise, spectral frequency response, and sampling efficiency (Section 5.2). Results were analysed using Matlab to extract specific measurements and plot SFR, SFR50, and sampling efficiency.

6.1.2. Filtered camera approach

The first iteration of this test involved filtering the camera following a similar method to that used for the spectral response measurement (Section 5.3). The visible and NIR bandpass filters were mounted onto the lens of the camera and the target was illuminated using the studio strobes with umbrellas for even diffuse illumination. The camera was mounted on the copy stand above the target and the lights were positioned at a 45° angle (Figure 6-1 and Figure 6-2). The camera-object distance (measured from the plane mark on the DSLR body) for the 60 mm lens was 65 cm, and for the 50 mm lens 54 cm.
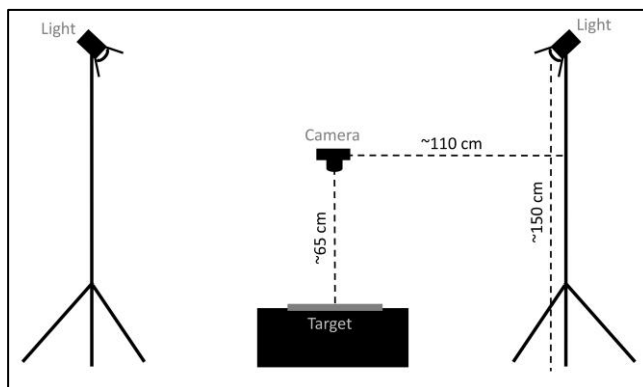
Figure 6-1. Diagram of imaging setup for filtered camera approach.

Figure 6-2. Image of setup for filtered camera acquisition.

Mounting and removing filters from the camera could influence and shift the focus, so magnetic camera lens adapters (XUME, Manfrotto) were used to reduce handling of the lens. The magnetic adapters permitted the filters to be "placed" on the lens as opposed to threading, which the rotating motion increases the handling time and risk of shifting the focus.

The initial focus was using Live View looking at a high contrast central feature of the target at 200% magnification on a laptop screen and manually adjusting the focus. The first dataset was acquired without actively refocusing or checking the focus for the mCanon camera images. Without refocusing the camera, there is the potential to see the effects of focus shift as the imaging wavelength changes provided that focus is not influenced by mounting and removing the filters. A preliminary visual assessment of the resulting images from the first acquisition indicated that the NIR images were not sharp. However, it could not be determined whether this was from a focus shift relating to the lens design and wavelength change or the physical handling of the filters and lens.

The second dataset was acquired using the 60 mm lens with the lens focused using Live View at 200% before mounting the filter and then the focus was checked after the image was acquired ensuring the image was sharp. The 50 mm lens has the capability of autofocus, which could be used through the filters. Since these datasets were being focused with each filter, the final results would not be able to reflect a focal shift from the construction of the lens even if there was one.

6.1.2.1. Results and discussion

The wavelength and image quality tests include a comparison of sampling efficiency because the analysis involved twenty-one images per dataset and over four datasets and sampling efficiency provides a more convenient comparison than SFR curves. As the ratio of the limiting resolution and the sampling resolution, the comparison of the sampling efficiency values will still provide an indication of the increase and decrease of sharpness with different filters and sampling efficiencies over 100% will indicate a risk of aliasing.

Calculated sampling efficiency for the mCanon and 60 mm lens image sets processed with ACR and the MC-RAW showed a seemingly random increase and decrease of sharpness that does not necessarily correlate to wavelength (Figure 6-3). The images were acquired without actively refocusing or checking the focus, and the mounting and removal of the filters may have changed the focus which is reflected in these inconsistent results. In addition to the images acquired for the mCanon and filter set, an image of the DICE target

was acquired with the unmodified Canon camera with the 60 mm lens as a reference. The sampling efficiency when processed with ACR was 79% and when processed with the MC-RAW workflow was 86%.
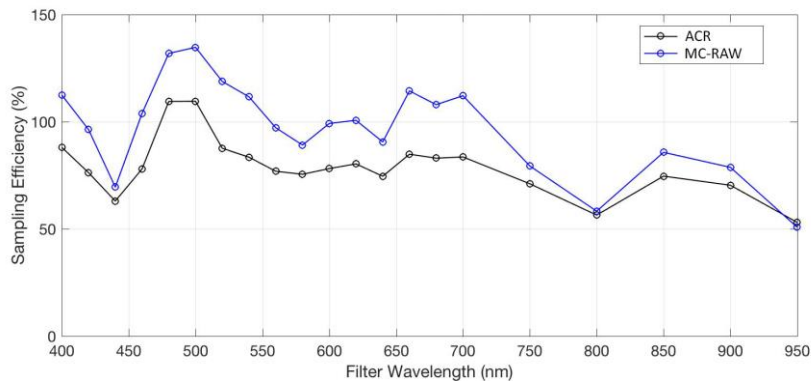
Figure 6-3. Sampling efficiency results from the first iteration of the filtered camera approach using the modified camera and 60 mm lens. The sampling efficiency results are plotted for each filter (marked on the x-axis by wavelength nm) for ACR and the MC-RAW workflow. The sampling efficiency for the unmodified camera with the 60 mm lens when processed with ACR was 79% and when processed with the MC-RAW workflow was 86%.

To improve the reliability of the results, the focus was adjusted and checked with each filter for the second iteration of the filtered camera approach. The resulting sampling efficiency shows a decrease at 620 nm, 660 nm, and 680 nm but otherwise follows a similar trend with a higher sampling efficiency at 700 nm and a decrease in the NIR as the wavelengths get longer (Figure 6-4). An image of the DICE target was also acquired with the Canon camera with the 60 mm lens as a reference resulting in a sampling efficiency of 84% when processed with ACR and 95% when processed with the MC-RAW workflow.
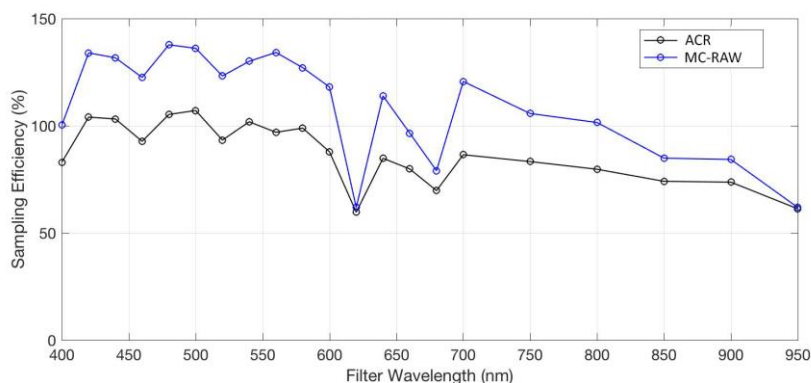
Figure 6-4. Sampling efficiency results from the second iteration of the filtered camera approach using the modified camera and 60 mm lens. The sampling efficiency results are plotted for each filter (marked on the x-axis by wavelength nm) for ACR and the MC-RAW processing. The sampling efficiency for the unmodified camera with the 60 mm lens when processed with ACR was 84% and when processed with the MC-RAW workflow was 95%.

The 640 nm, 660 nm, and 680 nm filters required the additional IR blocking filter (Section 5.3.4), which could be an explanation for decreased sampling efficiency for 660 nm and 680 nm. However, this is not consistent with the results with the sampling efficiency decreasing at 620 nm and increasing at 640 nm. Despite adjusting and checking the focus for each image, inconsistencies in focus could be influencing the results. Focus is critical to these results, and it was important to understand how consistent the lens could be focused with the manual focus of 60 mm lens.

The sampling efficiency results included values over 100%, which should not be theoretically possible. The impact of the camera modification and the RAW processing on the SFR analysis and sampling efficiency results was discussed in Section 5.2.2. Results above the Nyquist frequency and a sampling efficiency over 100% have a risk of aliasing despite having an increased effective resolution.

Focus Test

A focus test was conducted to better understand how consistently the 60 mm lens could be focused and whether an inconsistency was impacting the results. A set of ten images were acquired for both the 50 mm and the 60 mm lenses using the mCanon camera. In between each image acquisition, the filter was removed, the camera refocused manually, and the filter re-mounted on the lens. The filter used for this test was the UV/IR-block and VIS-pass filter, the Peca 916 (Figure 5-7, Section 5.1.3). Each image was manually focused using Live View looking at a high contrast central feature of the target at 200% magnification on a laptop screen. These images were processed with the MC-RAW workflow and assessed using GoldenThread.

Sampling efficiency results over ten image samples from the focus test (Figure 6-5) demonstrated a standard deviation of 9% for the 50 mm lens and 11% for the 60 mm lens (Table 6-1). Results show differences linked to filter changes but cannot be separated from manual focus inconsistencies.

Options to improve this variation included a different approach to filtering the camera or filtering the illumination. A filter wheel could be an option for reducing the handling of the lens during acquisition; however, the number of wavelengths tested would be limited by the number of slots in the filter wheel. Most filter wheels do not hold twenty-one filters, the number of filters used in this experiment. There are other considerations in using a filter wheel, but as there was not a filter wheel available for this test it was not further considered. Another option would be filtering the illumination instead of filtering the camera. The same filter set could be used to filter a single illumination source, which would eliminate any

handling of the lens and therefore eliminate the impact of this handling on the resulting focus.
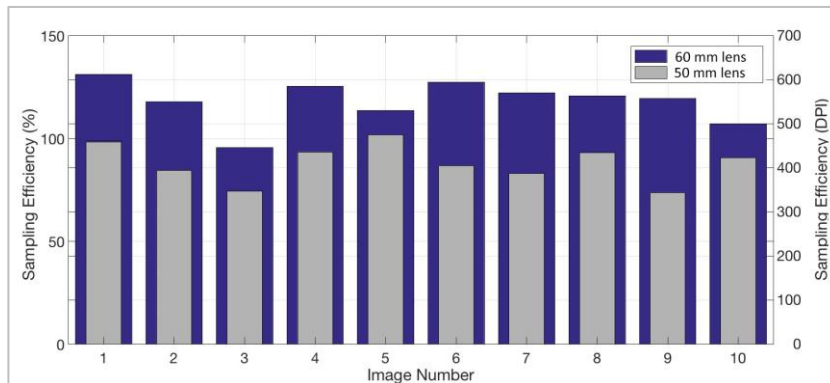
Figure 6-5. Focus test comparing sampling efficiency results.

Table 6-1. *Focus test and the variation in sampling efficiency (% and DPI)*

	Sampling Efficiency (%)	Sampling Efficiency (DPI)
mCanon 50	Mean = 88	Mean = 410
	Std Dev = 9	Std Dev = 44
mCanon 60	Mean = 118	Mean = 551
	Std Dev = 11	Std Dev = 49

Noise

Noise was also assessed to better understand wavelength and image quality. RAW processing impacts the resulting image quality (Section 5.2.2), so images were processed with both ACR and the MC-RAW workflow (Section 5.1). Since the ACR processing includes noise reduction (Section 3.3.1), the ACR results have lower levels of noise than the MC-RAW workflow. Furthermore, the noise levels are consistent from white to black. There are no trends in the data that can be associated with wavelength (Figure 6-6).

Lens performance and wavelength

The results of the filtered camera approach provided some indication of the lens performance related to wavelength by plotting the ISO setting and the flash power against wavelength (Figure 6-7). The 50 mm lens was not as efficient at transmitting light above 800 nm as seen by the increasing IS0 with the flash output maximised at a power of 6. There was a peak of increased transmission for the 60 mm lens at 540-560 nm where the flash output was at its lowest power for the image set and the ISO is set at 100.

Figure 6-6. Noise measurements for filtered camera approach. The figure includes measures for the 50 mm lens (top row) and 60 mm lens (bottom row) with the images processed using ACR (left column) and the MC-RAW workflow (right column). The noise is measured from the grey patches of the DICE target and the standard deviation of the digital values is plotted against the density of the tone scale patches from white (density = 0.04) to black (density = 2.42). The results are colour coded with filter wavelength in Figure 5-15.

Figure 6-7. The ISO setting and flash power plotted against the filter wavelength for both the 50 mm and 60 mm lenses for the filtered camera acquisition. This figure provides an indication of the performance of the lens related to wavelength (or transmission of the filters).

Vignetting and ghosting

The filtered camera method resulted in both vignetting and ghosting in some images. The images acquired with the 640 nm, 660 nm, and 680 nm filters have vignetting, which is observed with the darkened corners of the images (Figure 6-8). The vignetting was likely resulting from the thick filter stack for these three filters. These filters had to be used with an additional blocking filter (Section 5.3), and these filters are the largest filter stacks of the set measuring about 2 cm in thickness.
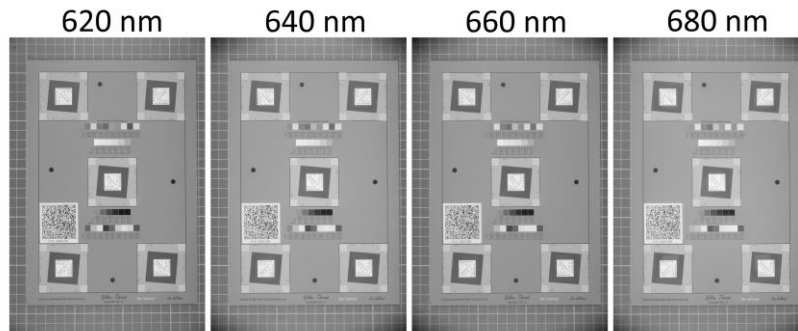
Figure 6-8. Vignetting observed in the images using the 640 nm, 660 nm, and 680 nm filters. The image using the 620 nm filter was included to show an image without the vignetting.

In addition to vignetting, some of the images resulted in ghosting. The images acquired with the 640 nm, 660 nm, 680 nm, 750 nm, 800 nm, 850 nm, and 900 nm filters with both the 50 mm and 60 mm lenses included ghosting that was most visible around the white features of the DICE target (Figure 6-9). When physically rotating the filter on the camera lens, the ghosting rotates around the white DICE feature suggesting that it was related to internal reflections between the filters and lens. Filtering the illumination instead of filtering the camera would eliminate the vignetting and the ghosting if it were related to internal reflections between the filters and lens.

Filtering the camera allowed for even illumination of the target using two flash sources, but by mounting the filters on the camera for each exposure, there was a potential to influence the focus. The process of taking the filter on and off the camera increased the variability of the results, and the process of manually focusing the camera decreased the repeatability of the acquisition. In addition to these issues with the focus, the filtered camera approach resulted in some images with vignetting and ghosting. Filtering the illumination, as opposed to filtering the camera, has the potential to reduce the issues with focus and eliminate the vignetting and ghosting.

6.1.3. Filtered illumination approach

The second approach of this test involved filtering the illumination source instead of filtering the camera. This had the potential of improving the repeatability of the acquisition and accuracy of the results by removing any handling of the lens. A metal conical snoot was mounted on a single Bowens Gemini GM400Rx flash unit in order to filter the illumination with the same set of visible and NIR filters used for the filtered camera approach. The setup is illustrated by the diagram in Figure 6-10 and the image in Figure 6-11.
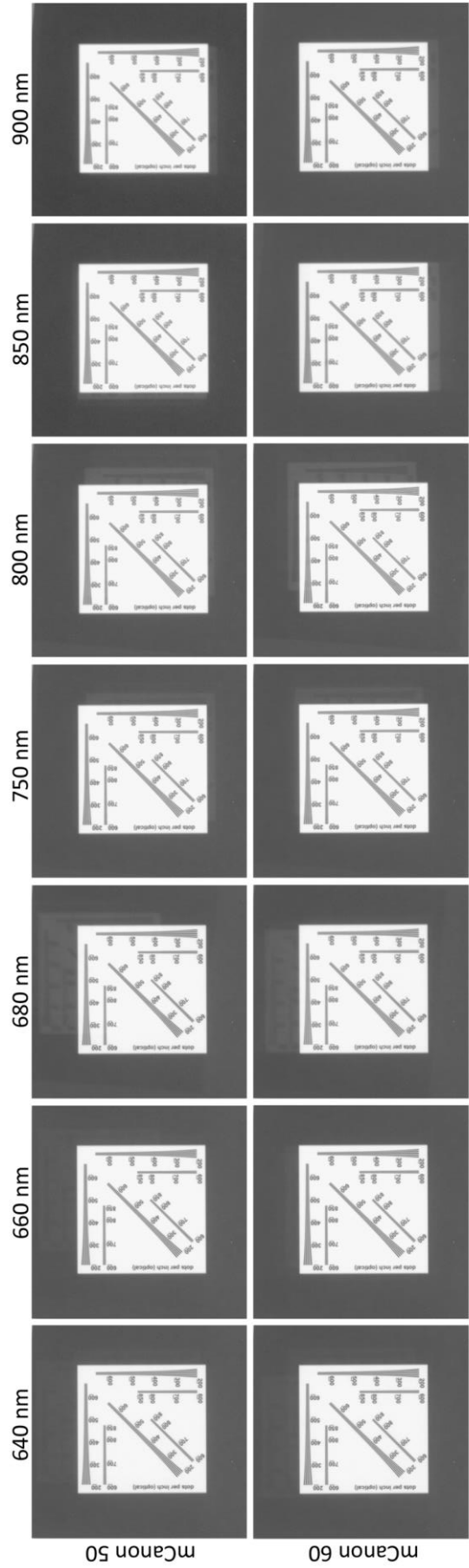
Figure 6-9. Details of bottom left feature of DICE target to illustrate the ghosting observed with certain filters. (The ghosting is faint and may not be reproduced well depending on how this document is reproduced.)
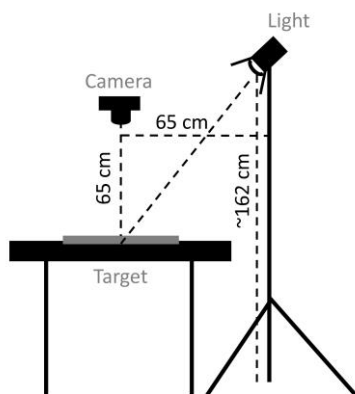
Figure 6-10. Filtered illumination setup diagram for the 60 mm lens.

Figure 6-11. Image of setup for the filtered illumination acquisition.

A disadvantage of filtering the illumination and this particular setup was that there was only one set of filters and therefore only one illumination source could be used. A single illumination source results in uneven illumination. However, the flat field correction, as part of the MC-RAW workflow (Section 5.1), was intended to reduce the fixed pattern noise of the residual pattern, but also serves to correct uneven illumination. The focus was set at the beginning of the acquisition and the camera was not handled at all during the acquisition. The changing of the filters involved mounting and removing each filter from the snoot on the illumination source, so while the light source was handled, the camera remained untouched. For the 50 mm lens, the autofocus was used for the initial focus and the lens was switched to manual focus to prevent refocusing during the acquisition. For the 60 mm lens, the lens was focused manually using Live View and focusing on the central feature of the DICE target at 200% magnification.

The shutter speed was kept at 1/100 sec and the aperture also remained constant. While the flash output could be adjusted for the filtered camera approach, the full power was required for the entire image set for the filtered illumination approach. The use of a single flash reduced the amount of light available; however, the bigger impact was the reduction in transmission of radiation caused by the filters, which greatly limited the amount of light illuminating the target and returning to the sensor. Even with the flash at full power, there was not enough light reaching the sensor, so the ISO was increased with the knowledge that this would also increase image noise with the increased gain.

Results and discussion

The filtered illumination approach intended to eliminate issues related to focus and changing the filters on the lens for the filtered camera approach. By eliminating this variable, the results should provide insight about the influence of wavelength on image quality. The sampling efficiency results for the filtered illumination approach were compared to the results for the filtered camera approach using the mCanon camera with the 50 mm and 60 mm lenses (Figure 6-12). The 50 mm lens results for both filtered approaches were similar in the NIR (700-900 nm) with a consistent decrease in sampling efficiency as the wavelengths get longer. The 60 mm lens results for the filtered illumination showed improved consistency over the filtered camera results with smoother transitions and less drastic increases and decreases in sharpness. While the sampling efficiency for the 50 mm lens steadily decreased in the NIR with longer wavelengths, the 60 mm lens sampling efficiency remained fairly consistent with less of a decrease. This can be explained by the corrections of the 60 mm lens for wavelengths beyond visible that categorise this lens as apochromatic.
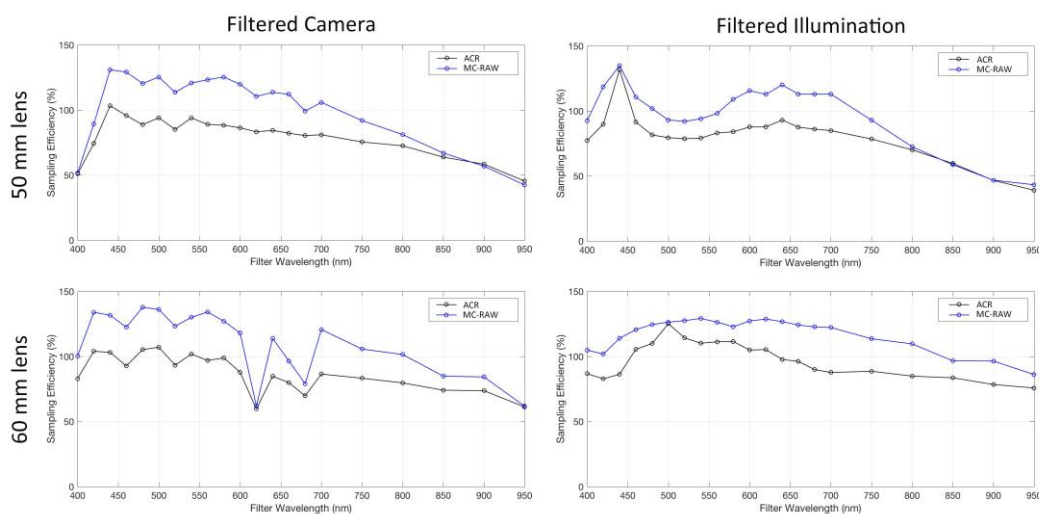
Figure 6-12. Sampling efficiency results comparing the filtered camera and filter illumination approaches. The figure includes results from the second iteration of the filtered camera approach (left column) and the filter illumination approach (right column) for both the 50 mm lens (top row) and the 60 mm lens (bottom row). The sampling efficiency (%) results are plotted for each filter (marked on the x-axis by wavelength nm) for ACR and the MC-RAW workflow.

Focus shift

The filtered illumination approach allowed for the tracking of the focus shift from visible into the NIR, which was not as possible with the filtered camera approach and adjusting the focus with each exposure. A visualisation of this focus shift was seen by tracking a visual resolution feature from the centre of the DICE target through the visible and into the NIR for both the 50 mm and the 60 mm lenses (Figure 6-13). Since the focus was constant for the

acquisition of the full image sets and the camera was not handled or adjusted, the change in sharpness and difference between the 50 mm lens and the 60 mm lens was the result of a focus shift. The 60 mm lens is an apochromatic lens with chromatic correction. The performance of this lens from visible to NIR is possible through a combination of lens coating layers and lens elements made of calcium fluoride. The visualisation in Figure 6-13 can be linked back to the sampling efficiency plots in Figure 6-12. The plot for the 50 mm lens with filtered illumination showed a decrease in sampling efficiency from 700 nm to 900 nm, whereas the 60 mm lens maintained a fairly consistent sampling efficiency even as the wavelengths get longer.
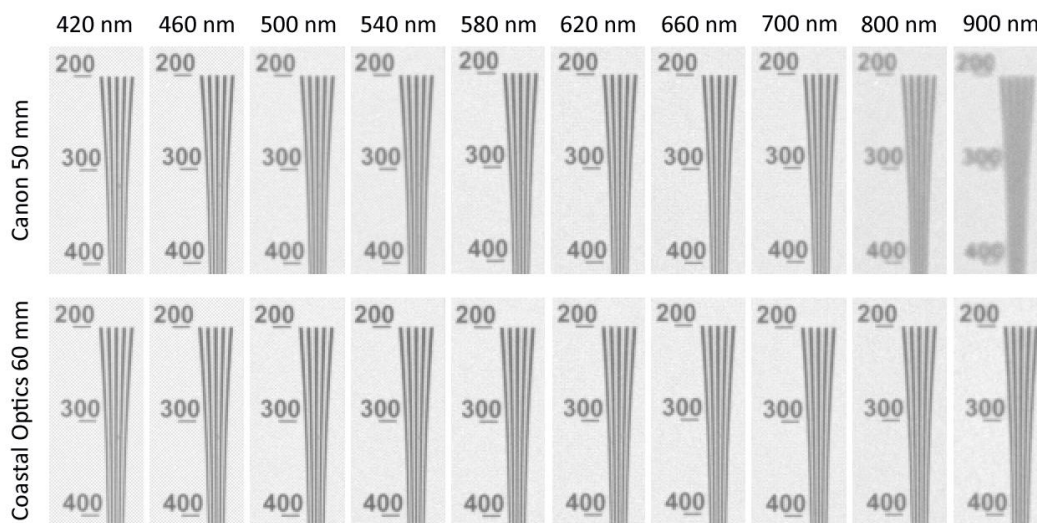
Figure 6-13. Visualisation of the focus shift comparing the 50 mm and 60 mm lenses. Details of the visual resolution feature from the centre of the DICE target are shown through the visible and into the NIR. For the 50 mm lens, starting at 700 nm the sharpness of the resolution feature starts to degrade, which is not the case for the 60 mm lens.

As a follow up to the focus test in Section 6.1.2, images were acquired at the start and finish to test whether there was any drift or change in the focus through the acquisition despite no handling of the camera or lens. Table 6-2 provides the sampling efficiency (% and DPI) for the images acquired at the start and finish of the acquisition. These indicate slight 4% change for the 60 mm lens acquisition and less than 1% change for the 50 mm lens acquisition.

Table 6-2. Sampling efficiency for images acquired at the beginning and end of the filtered illumination acquisition.

	Start	Finish
mCanon 50	83 %	83%
	410 DPI	386 DPI
mCanon 60	120 %	116 %
	557 DPI	540 DPI

Noise

As discussed in Section 6.1.2, the results for the ACR processing showed lower levels of noise that are consistent from white to black, while the MC-RAW workflow increased levels of noise with no trend that can be associated with wavelength (Figure 6-14). When comparing these results to the noise levels in the filtered camera results (Figure 6-6), there was an increase in noise level in the filtered illumination results. This was attributed to the higher ISO settings required for the filtered illumination acquisition. Most of the images for the filtered camera approach were acquired with an ISO of 100 (the exceptions being the shortest and longest wavelengths), whereas all of the images acquired for the filtered illumination approach were greater than an ISO of 100. The increase in ISO absolutely influenced the level of noise.
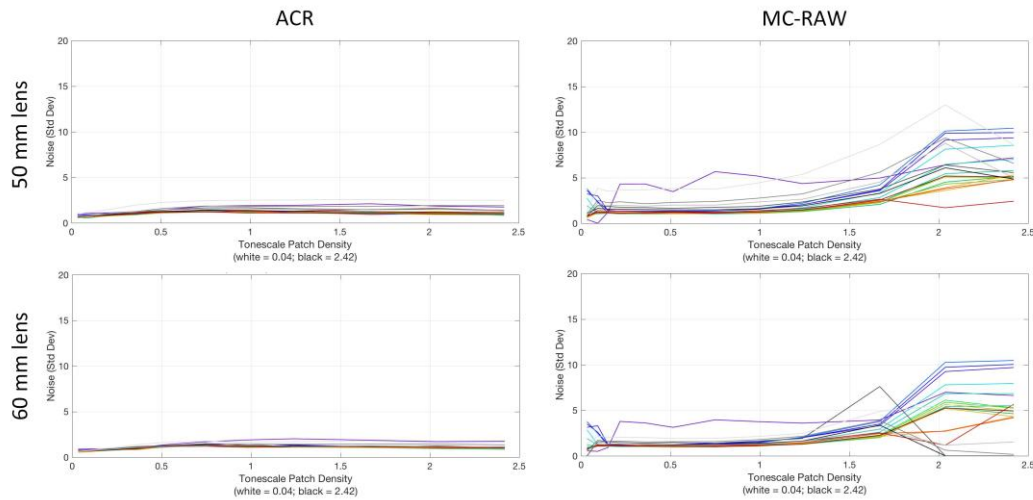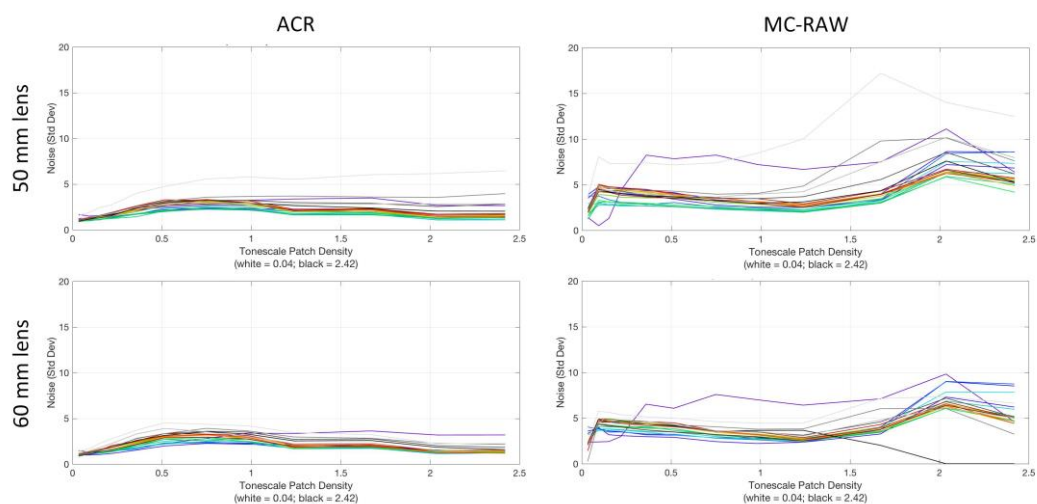

Figure 6-14. Noise measurements for filtered illumination approach. The figure includes measures for the 50 mm lens (top row) and 60 mm lens (bottom row) with the images processed using ACR (left column) and the RAW processing workflow (right column). The noise is measured from the grey patches of the DICE target and the standard deviation of the digital values is plotted against the density of the tone scale patches from white (density = 0.04) to black (density = 2.42). The results are colour coded with filter wavelength in Figure 5-15.
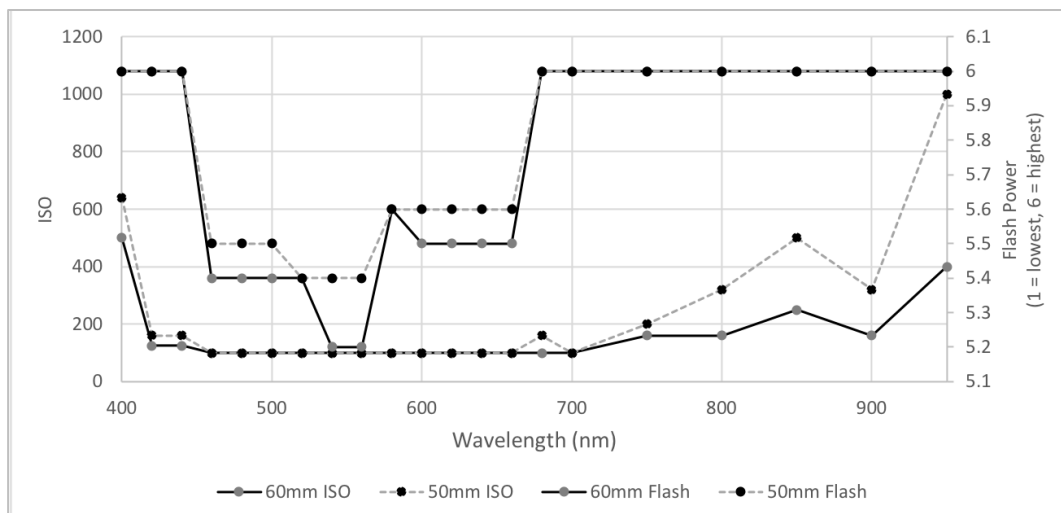
Lens performance and wavelength

The filtered illumination approach results (Figure 6-15) provided less insight about the lens performance related to wavelength than the filtered camera approach (Figure 6-7). However, the results have been included to show the increased ISO levels needed for their acquisition. The flash power remained at the highest power level for the acquisition for both the 50 mm and 60 mm lenses, and the ISO levels were quite high in comparison to the filtered camera approach. The y-axis in Figure 6-15 includes an ISO range of 0-6000 while Figure 6-7 includes an ISO range of 0-1200. Higher ISO settings were required for the filtered illumination approach due to the reduced illumination reaching the sensor (a combination of

the single illumination source and the transmission of the filters) despite using the full power of the flash. Similar to the filtered camera approach, the results from the filtered illumination approach showed a reduced transmission for NIR by the 50 mm lens. It would be expected that the 60 mm lens has a higher transmission in the NIR based on its coatings and corrections to perform beyond visible light.
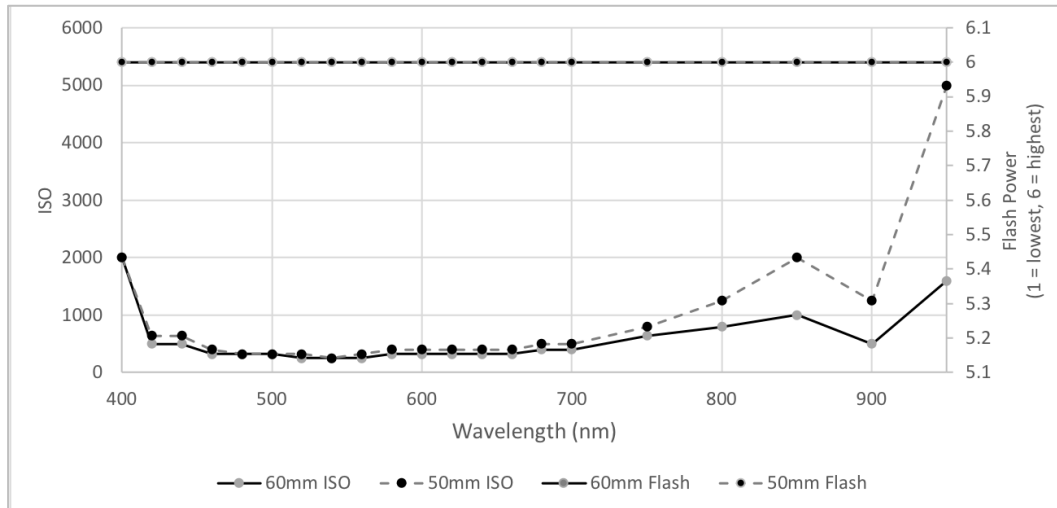
Figure 6-15. The ISO setting and flash power plotted against the filter wavelength for both the 50 mm and 60 mm lenses for the filtered illumination acquisition. In the case of the filtered illumination, there is less light available (as compared to the filtered camera acquisition) with only a single source. The flash output is maximised for all the images and with the longer wavelengths especially at 950 nm a very high ISO is required.

Vignetting and ghosting

The filtered illumination approach offered an option for eliminating vignetting and ghosting, which both had been issues with images acquired with the filtered camera approach. Without the filter stacks mounted on the camera lens, vignetting was not a problem, and the filtered illumination approach eliminated the ghosting. Details from the images acquired with the 680 nm filter show the elimination of the ghosting for both lenses (Figure 6-16).

6.1.4. Discussion

Two approaches were tested to investigate the influence of wavelength on image quality: filtering the camera and filtering the illumination. Challenges with the filtered camera approach led to the test of filtering the illumination; however, there were still some limitations with the filtered illumination approach. The filtered camera approach allowed for the use of two illumination sources providing even, diffuse illumination, but mounting the filters on the lens impacted the repeatability, increased the variability of the results, and resulted in vignetting and ghosting in some images. The filtered illumination approach addressed the issues of focus and repeatability and eliminated vignetting and ghosting. This

approach recorded the focus shift from 400-900 nm because the focus was not changed during the acquisition.
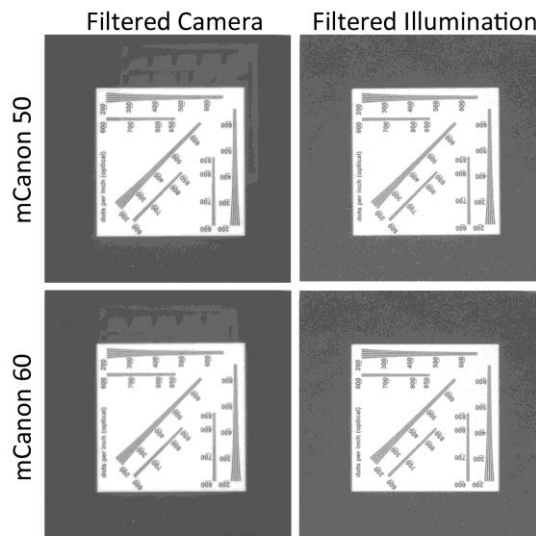
Figure 6-16. Detail images of the DICE target providing evidence that the filtered illumination approach eliminated the ghosting. This example is using the 680 nm filter with the left column details from the filtered camera acquisition and the right camera from the filtered illumination acquisition.

Lens selection

The selection of the lens and the quality of the optics are important when considering and assessing the resulting image quality. The lens will impact the resulting image quality even if the acquisition is within the range of visible light. As the acquisition moves beyond visible, consumer lenses are likely to decrease performance. This was seen by lower transmission of IR radiation observed using the 50 mm lens in addition to a shift in focus and decrease in sampling efficiency in the NIR with longer wavelengths. The 60 mm lens is an expensive, specialised lens that performs well beyond visible light; however, the price may be prohibitive and the manual focus negatively influences the repeatability of the results.

Focus

Sharpness and focus significantly influence 2D image quality assessment, specifically SFR analysis and sampling efficiency. The 60 mm lens requires manual focus making it important to understand how repeatable the manual focusing could be. The focus test investigated the impact of changing filters on the camera lens and the results led to a chance in the setup to eliminate the focus variability.

Illumination

The setup for the filtered illumination approach was limited to a single illumination source because there was only one filter set. The single source reduced the amount of available illumination, which the transmission of the filters reduced even further. To compensate for the reduced illumination, higher ISO was required, which in turn increased the image noise. At least two illumination sources should be used to document an object to provide sufficient and even illumination. While the filtered illumination approach presented advantages for testing wavelength and image quality, this setup would not be an optimal option for improved imaging of a museum object. A second set of filters for a second illumination source would drastically increase the cost of the setup. Instead of optical filters tunable light sources could be used (Section 3.1.6).

The results showed that the imaging wavelength is not the largest factor impacting the resulting image quality. However, to increase confidence in the results, the acquisition could include multiple images that are averaged to improve the reliability of the results. The experiment pointed out other factors that significantly impact the image quality including lens selection, focus, and illumination.

6.2. Imaging study

Imaging using selected wavelengths can increase image contrast and the previous section established that variables other than wavelength have a more significant impact on image quality. The effect of wavelength selection for the improvement in image quality is explored through the surface recording of a museum object. An imaging study of a museum object demonstrates the application of wavelength selection for image-based 3D reconstruction, provides examples of the setup and workflow, and includes critical assessment for the improvement of the technique.

A wooden sculpture of a coyote and turtle, *Untitled* (1986.65.339), from the Smithsonian American Art Museum (SAAM) has cracking running along the carved back and side of the coyote (Figure 6-17). Conservators were concerned that fluctuating environmental parameters (relative humidity and temperature) in the gallery would contribute to increased cracking (Figure 6-18). The object has been placed in a vitrine with conditioned silica gel to minimise fluctuations in humidity and provide a more stable environment while on exhibition. Conservators have documented the cracking by using a piece of Mylar to trace the crack as a baseline for comparison to monitor dimensional movement over time.
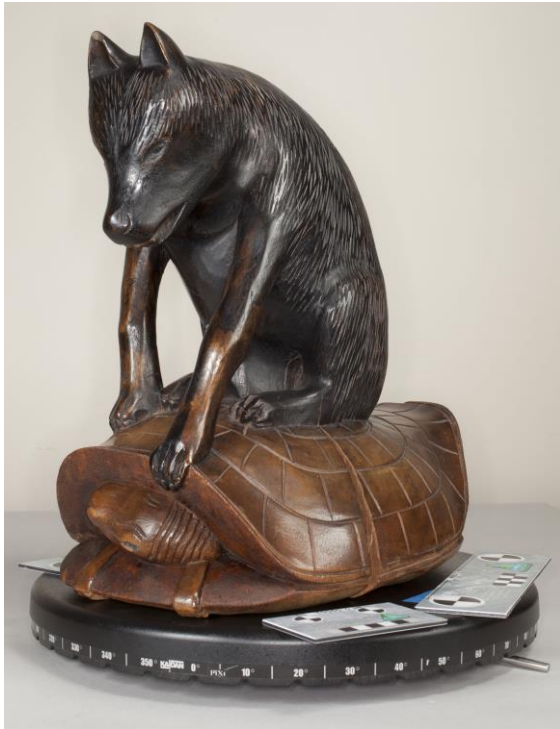
Figure 6-17. Wooden sculpture of a coyote and turtle, Untitled (1986.65.339), 39.2 x 24.5 x 35.5 cm , part of the SAAM collections.
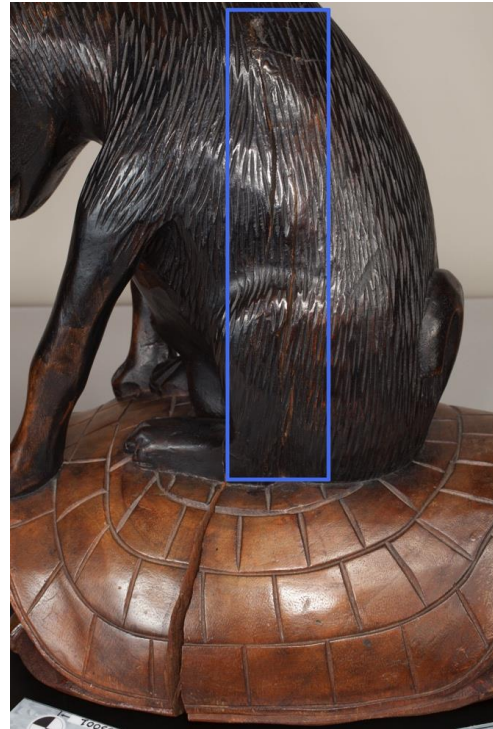
Figure 6-18. Detail image of cracking with blue box indicating the area of interest for monitoring the dimensional change.

The object is a carved, varnished, and painted walnut sculpture of a coyote sitting on a turtle. It measures 39.2 x 24.5 x 35.5 cm and dates after 1930. The sculpture is thought to portray a Hopi, or Native American, tale about a turtle tricking the coyote into helping him get back home after the turtle had left the river (SAAM Collections database record for 1986.65.339, accessed November 8, 2017). There were thought to be at least two coatings on the object including a dark stain on the coyote and a second coating on the turtle (H. Ingalls, personal communication, February 15, 2017).

3D imaging has the potential to improve the monitoring of the cracking and any dimensional change over time. However, the dark and shiny finish presents challenges for visible light recording. The objectives of the imaging study were to establish a detailed baseline imagery for monitoring dimensional change, to investigate the use of spectral and 3D imaging techniques for documenting museum collections, and to establish a workflow for wavelength selection and spectral-3D recording. The imaging study demonstrated the practical applications of this research within museum imaging and addressed specific needs of museum professionals. Imaging was conducted twice (January and September 2017) with image sets acquired for both visible light and reflected IR image-based 3D reconstruction. The imaging campaigns will be described with the results and assessment of the capabilities of spectral-3D to improve the 3D output.

6.2.1. Initial image acquisition (January 2017)

The goals of the initial image acquisition, conducted on 13 January 2017, included creating baseline imagery for measuring dimensional change and investigating spectral-3D imaging for improved monitoring of the object. The imaging took place at SAAM in a multipurpose room off of the gallery with the SAAM objects conservator. The object was on exhibition at the time of the imaging. Object handlers removed the sculpture from view in the morning and returned it to its vitrine the same evening.

6.2.1.1.   *Materials and method*

The image-based 3D reconstruction included a turntable setup (Section 4.2.1.2). Visible light images were acquired using the unmodified Canon camera with the 50 mm lens (Table 4-1). The object was illuminated using a Canon Macro Ring Lite MR-14EX and 3 Canon Speedlite 580 EX II with umbrellas (Figure 6-19). (The imaging was completed before the camera characterisation reported in Chapter 5, and therefore, the repeatability testing of the Canon flashes had not been conducted.) The acquisition included seven camera views with rotations of the object at each position. Additional images were acquired using the 50 mm lens and the Canon 100 mm f/2.8 macro lens (serial no. 19503840) for increased resolution of the crack details (Figure 6-20). Information about the setup for both the visible light and reflected IR acquisition including camera and flash parameters is in Table 6-3. Figure 6-21 includes the camera positions for the visible light and reflected IR image acquisition.

Table 6-3. Camera and flash settings for January 2017 acquisition

Image Set	Camera + lens	Filter	Camera Settings	Camera-Obj. Dist. (cm)	Flash Settings*	Images
Visible (overall)	Canon 5D Mark II + Canon 50 mm f/2.5	None	ISO 200 f/16 1/100	95	Fl 1: ½ Fl 2: ½ Fl 3: ½ Fl 4: 1	250
Visible (detail)	Canon 5D Mark II + Canon 50 mm f/2.5	None	ISO 200 f/16 1/100	50	Fl 1: ¼ Fl 2: ½ Fl 3: ½ Fl 4: 1	28
Visible (detail)	Canon 5D Mark II + Canon 100 mm f/2.8	None	ISO 200 f/16 1/100	65	Fl 1: ¼ Fl 2: ½ Fl 3: ½ Fl 4: 1	55
IR (overall)	Mod. Canon 5D Mark II + Coastal Optics 60 mm	Peca 910	ISO 250 f/16 1/100	119	Fl 1: 1 Fl 2: 1 Fl 3: 1 Fl 4: 1	72
IR (detail)	Mod. Canon 5D Mark II + Coastal Optics 60 mm	Peca 910	ISO 250 f/16 1/100	60	Fl 1: 1 Fl 2: 1 Fl 3: 1 Fl 4: 1	58

'Fl 1' = ring light on camera; 'Fl 2' and 'Fl 3' are Canon flashes at object level; 'Fl 4' is high Canon flash. Two Canon Speedlite flashes with umbrellas were positioned close to object height (~110 cm height from floor to base of flash) with the third flash positioned above the object (~205 cm height from floor to base of flash) (Figure 6-19).

Figure 6-19. Imaging setup with positions of three Canon Speedlite flashes and object on turntable.
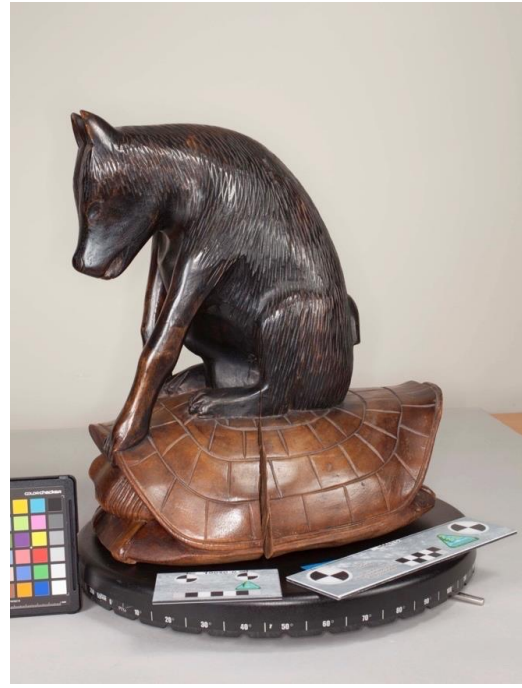
Figure 6-20. Setup of coyote and turtle sculpture with references and targets. Targets include X-Rite ColorChecker (bottom left) used for white balance and CHI scale bars (around object placed on turntable) used for scaling the 3D model.
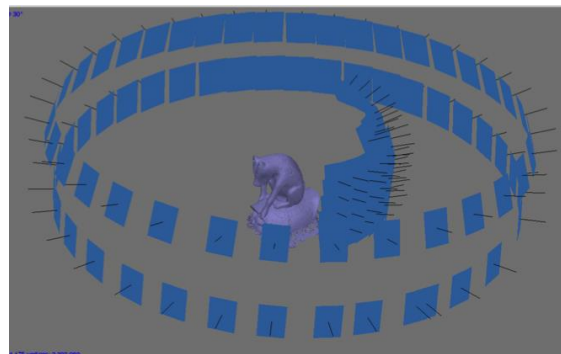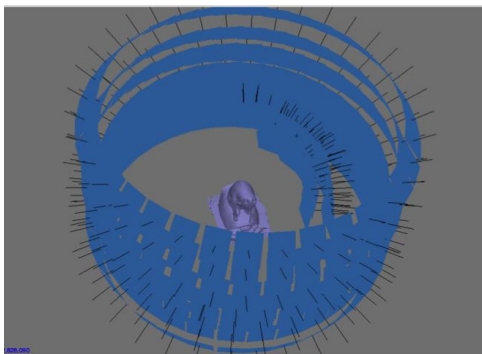
Figure 6-21. Camera positions for 3D reconstruction. Left image: Visible light image acquisition, screenshot from PhotoScan. Right image: Reflected IR image acquisition, screenshot from PhotoScan.

Reflected IR images were acquired using the modified Canon 5D Mark II with the 60 mm lens (Table 4-1). A Peca 910 filter was used on the lens to restrict the recorded radiation to the near IR region, cutting off wavelengths below about 800 nm (Figure 5-50). Similar illumination as the visible light imaging was used. However, the ring flash was not able to mount onto the 60 mm lens with the IR filter and was handheld in front of the lens for each exposure. A Spectralon 99% Diffuse Reflectance Standard was included in an initial image as a reference for exposure. The acquisition included two camera views with rotations of the object at each position. Detail images were acquired using the 60 mm lens at a shorter camera-object distance.

Images included reference scales and targets for the processing, calibration, and scaling (Section 4.2.1). CHI photogrammetric scale bars (Section 2.3.2) were placed around the object during acquisition for scaling (Figure 6-20). An X-rite ColorChecker Passport was used for processing the white balance of the images. Images were acquired as RAW files (*.CR2 Canon files) and converted to JPEGs with ACR. The image-based 3D reconstruction processing used PhotoScan and followed the CHI-BLM *error minimisation workflow* (Section 4.1.1.2). The imaging study was conducted prior to some of the investigations presented in the thesis specifically the RAW processing workflow (Section 5.1) and the camera model and parameter selection (Section 4.1.4.2). For the imaging study, JPEGs were used to process the image-based 3D reconstruction; however, there is a risk of losing information in low frequency areas due to compression and other experimental work was conducted with TIFFs. In addition, all parameters were used for the camera model.

6.2.1.2.   *Results and discussion*

The resulting visible light and reflected IR point clouds and meshes (Figure 6-22 and Figure 6-23) have holes in the data in areas that were self-occluded on the object including the back of the front legs, underneath the chin, and the tip of the nose. These areas are not easily recorded because parts of the sculpture blocked the line of sight for the camera, and since these areas are not recorded the resulting point clouds and meshes include holes and areas of increased noise. While holes in the datasets are not ideal for overall documentation of the object, the holes in the coyote and turtle datasets are not problematic for this study since the area of the interest is the cracking along the side of coyote.
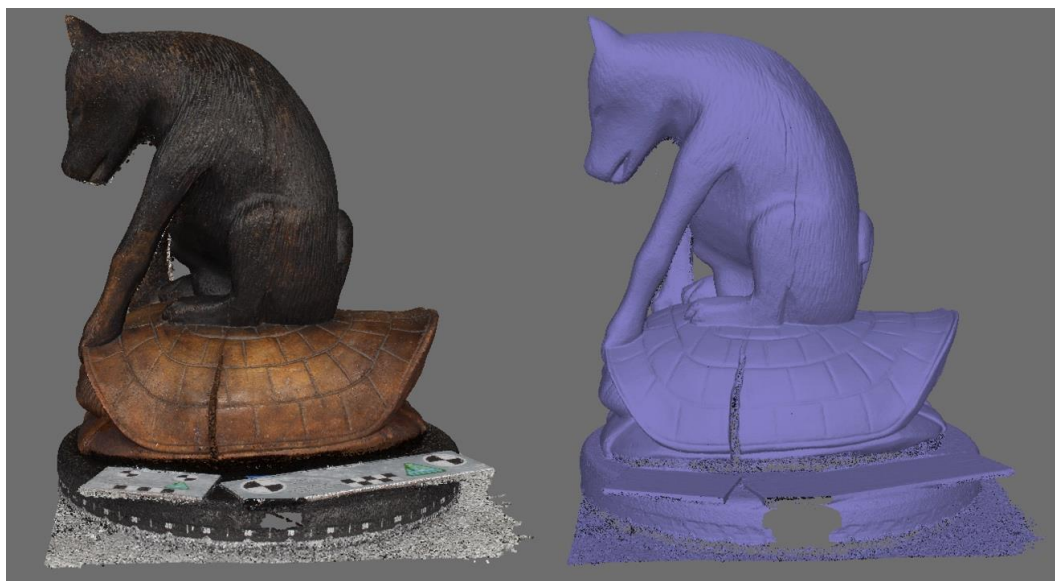
Figure 6-22. Visible light 3D reconstruction results of coyote and turtle sculpture. Visible light dense point cloud (left) and mesh (right).
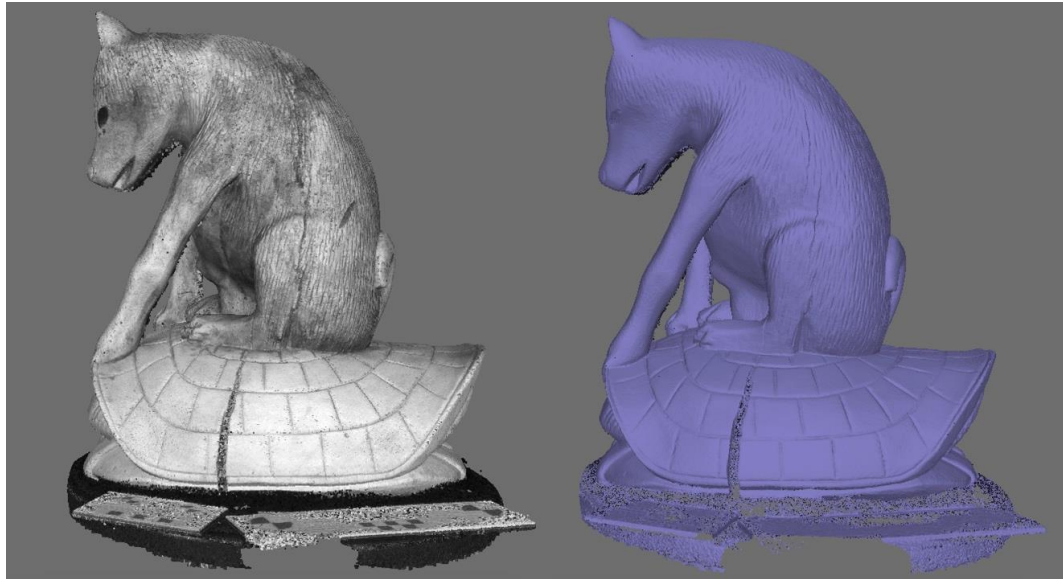
Figure 6-23. Reflected IR 3D reconstruction results of coyote and turtle sculpture. Visible light dense point cloud (left) and mesh (right).

Visible light input images of the object included specular highlights from the gloss in the coating of the coyote that changed position as the object was rotated and the angle of the lights with respect of the features changed (Figure 6-24, left). Specular highlights can be problematic for 3D reconstruction and can result in models with holes and inaccuracies in the geometry. In addition to the specular highlights, the dark varnish used for the coyote increased the difficulty to record the cracking details running from the coyote's back to its proper left back foot (Figure 6-24). The IR images provided increased contrast and enhanced visibility of the features of the crack resulting from the different interaction of the IR radiation with the varnish coat and the reduced effect of specular highlights (Figure 6-24, right). Since the reflected IR images provide an enhanced view of the features of interest, these could be used to improve the resulting 3D reconstruction for monitoring the dimensional change of the object.

As an initial comparison of visible light and reflected IR image-based 3D reconstructions, the resulting models were aligned and compared using GOM Inspect. Visually comparing the resulting models (Figure 6-25), the reflected IR reconstruction shows increased levels of detail resolved of the carved features despite the camera network including significantly less images than the visible light network. This comparison of the difference of the two models did not include reference data, and therefore, was not an assessment of the accuracy of the technique. The resulting models and the comparison of the models (Figure 6-25) provided evidence that the geometries had enough of a difference to pursue the hypothesis that imaging with different spectral bands might improve 3D reconstruction as compared to visible light 3D reconstructions. A visual comparison indicates that the reflected IR

reconstruction has resolved the incision marks for the fur with more definition than the visible light reconstruction, and the surface deviation maps show areas that have a difference between 0.3-0.6 mm surrounding the cracking features and the fur details.

Figure 6-24. Visible light and reflected IR detail images of cracking on coyote and turtle sculpture: visible light (left) and reflected IR (right).
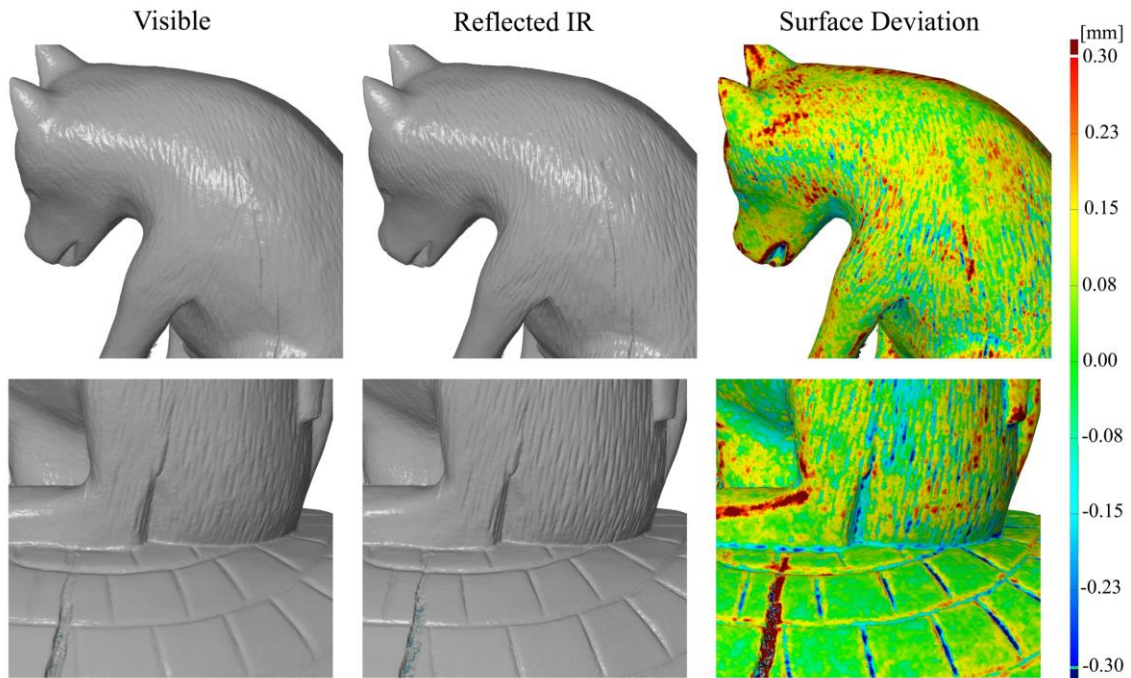
Figure 6-25. Details of 3D models created from visible light images and reflected IR images and surface discrepancy map comparing the two models.

The initial comparison showed differences between the models; however, the setup and acquisition between the two datasets varied enough that the comparison could not isolate the differences to a function of wavelength. The image sets were acquired with different lenses, lighting, and camera networks, all factors that would impact the resulting 3D reconstruction (Table 6-3). The 50 mm lens was used for the visible light image set with the ring flash mounted on the lens, while the 60 mm lens was used for the IR image set and the ring flash was handheld. To improve the comparability of the setups, either an adapter needed to be used to mount the ring flash onto the 60 mm lens or the 50 mm lens needed to be used for both visible and reflected IR imaging. The camera networks, including the number of input images, needed to be the same to more accurately compare the results.

While it is possible and necessary to improve the consistency of the setup and acquisition, it may not be feasible to record datasets with the same equipment, setup or camera network when considering monitoring an object over time. Nor will unlimited access to museum objects be assured. There are real life limitations when studying exhibition objects. If datasets are acquired to measure change over time, but using different equipment, setups or camera networks, it is important to understand how different the recording technique is. It would be worth future investigations into reference objects that could be used to understand the accuracy of a technique and then be able to assess whether the object is changing over time.

The imaging conducted in January 2017 was the initial acquisition data set for monitoring the coyote and turtle sculpture. The data provided detailed baseline imagery and the visual difference and the deviation maps suggested that the reflected IR images could provide a better imaged-based 3D reconstruction, which in turn could improve the monitoring of the crack. However, the acquisition of the visible light and reflected IR images was not consistent and this comparison cannot confirm that the difference between visible light and reflected IR was the only factor contributing to an improved 3D reconstruction. Additional imaging needed to be done to investigate whether reflected IR images could improve the image-based 3D reconstruction when surface details are obscured in the visible range by dark features and specular highlights. In order to increase the comparability of the data, the next imaging campaign needed to be more consistent with the equipment, lighting setup, and camera networks for the visible light and reflected IR imaging.

6.2.2. Secondary image acquisition (September 2017)

A second round of image acquisition of the sculpture was conducted 19 September 2017 within the Lunder Conservation Center of SAAM. The goals of this imaging included

acquiring image sets with increased comparability and creating reference data for assessing the accuracy of the image-based 3D reconstructions. Since the overall objective of the imaging was to monitor the cracking on the coyote, only the area of interest around the cracking was imaged and not the entire object. A structured light scanner was used to create a reference and to assess the resulting visible light and reflected IR reconstructions.

6.2.2.1.   *Materials and method*

The image-based 3D reconstructions included a turntable setup (Section 4.2.1.2). Visible light images were acquired using the unmodified Canon camera with the 60 mm lens (Table 4-1). The object was illuminated using a Canon Macro Ring Lite MR-14EX and 3 Canon Speedlite 580 EX II with diffusers and umbrellas (Figure 6-26). The ring light was mounted onto the lens of the camera (using an adapter that was not available for the initial January acquisition). The camera was positioned approximately 111 cm from the object and the acquisition included 4 camera positions with partial rotations of the object (only 100° rotation) at each position (Figure 6-27). Information about the setup for both the visible light and reflected IR acquisition including camera and flash parameters is in Table 6-4.

Figure 6-26. Imaging setup in the Lunder Conservation Center that shows the position of the lights to the right of the camera.
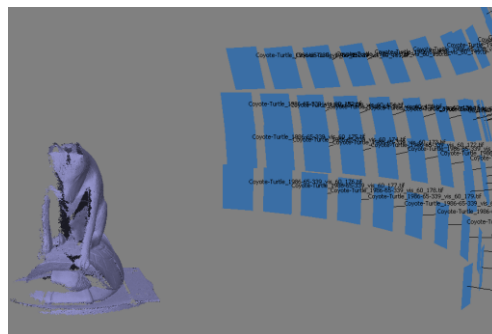
Figure 6-27. Camera positions for visible light image acquisition. Screenshot from PhotoScan.
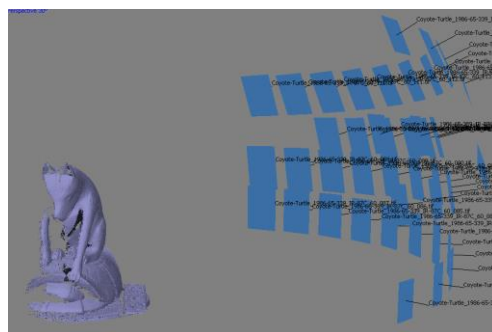
Figure 6-28. Camera positions for reflected IR image acquisition. Screenshot from PhotoScan.

Reflected IR images were acquired using the mCanon camera with the 60 mm lens and the Peca 910 filter (Figure 5-50) to restrict the recorded radiation to the near IR region. Similar illumination was used for visible light imaging and reflected IR imaging (Table 6-4). The same camera network was used for the reflected IR images as the visible light images using the camera height and degree markings on the turntable to replicate the positions (Figure 6-28). Images were acquired and processed as described in Section 6.2.1.1.

Table 6-4. Camera and flash settings for September 2017 acquisition

Image Set	Camera + lens	Filter	Camera Settings	Camera-Obj. Dist. (cm)	Flash Settings*	Images
Visible (overall)	Canon 5D Mark II + Coastal Optics 60 mm	None	ISO 160 f/11 1/100	111	Fl 1:A: ¼ B: 1 C: 1 Fl 2, 3, 4: $^1/_1$ -0.7	44
IR (overall)	Mod. Canon 5D Mark II + Coastal Optics 60 mm	Peca 910	ISO 160 f/11 1/100	111	Fl 1:A: ½ B: 1 C: 1 Fl 2, 3, 4: $^1/_1$ -0.7	44

*'Fl 1' = ring light on camera; 'Fl 2' and 'Fl 3' are Canon flashes at object level; 'Fl 4' is high Canon flash. Two Speedlite flashes with umbrellas were positioned close to object height (~112 cm height from floor to base of flash) with the third flash positioned above the object (~164 cm height from floor to base of flash) (Figure 6-26).

A "flat run" was acquired for both the VIS and IR image sets (Section 4.2.2.2). The camera was handheld (but not refocused) and images were acquired that were overlapping and planar to the scale bars. These images were used to improve the focus and documentation of the scale bars. This is an additional step that has been introduced to the CHI workflow to improve scaling.

Options for assessing the accuracy of image-based 3D reconstruction were discussed in Section 2.4. Acquiring reference data using another higher accuracy technique was the best option for the coyote and turtle sculpture without having known geometric shapes or enough data to process an averaged reference mesh. An AICON3D smartSCAN-HE structured light scanner (Figure 4-26) was available from the Smithsonian Digitization Program Office (SI DPO) to scan the object at SAAM. Information about the scanner was included in Section 4.2.4 and Table 4-5.

A detailed area of the cracking was 3D scanned to provide a reference dataset to assess the image-based 3D reconstructions. Jon Blundell (SI DPO) assisted with setup and calibration of the device. The scanner was calibrated following the AICON3D scanning procedure and using the AICON3D calibration plate (Figure 6-30). A total of 58 scans were acquired, and the scans included between 1 and 3 exposures to acquire more complete data of the dark surface. A manual turntable was used to rotate the object. Many of the scans were automatically aligned in the software; however, some required picking points between

model and scans. The 3D scanning took about 3 hours and only focused on the detail of the cracks along the side and back of the coyote.

Figure 6-29. Setup for acquiring the 3D scanned data of the sculpture.
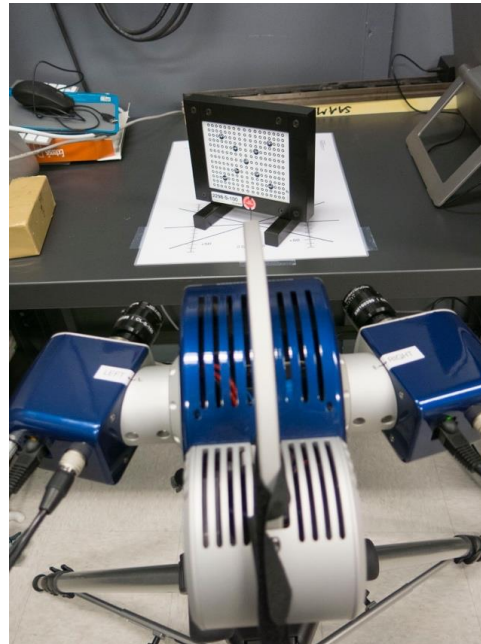
Figure 6-30. Calibration process with the scanner recording the calibration plate at different angles and distances.

A final aspect of this imaging campaign was the acquisition of single images using bandpass filters to investigate the wavelength selection process for the documentation of a heritage object. Single images were acquired using the mCanon camera with bandpass filters on the lens to restrict the recorded radiation to discrete bands of wavelengths from visible to NIR. Similar lighting for the reflected IR imaging was used for the filtered set of images. The Unaxis-Andover filter sets used for Section 5.3 and 6.1 were not available for the research conducted at the Smithsonian in Washington, DC. Instead, a set of broad bandpass machine vision filters (MidOpt BK100, Midwest Optical Systems, Inc. Palatine, IL, USA) was used. The transmission data was provided by the manufacturer (Figure 6-31). There is not a regular wavelength interval between these filters, but the machine vision filters offer a higher transmission and lower cost when compared to conventional interference filters.

The Unaxis-Andover filter set and MidOpt filter kit are not comparable filter sets. The MidOpt filters are broad bandpass (60-80 nm) while the Unaxis filters are narrow bandpass. Advantages of the MidOpt filters include less angle sensitivity and higher transmission. The increased transmission can be beneficial since the amount of light reaching the sensor is already limited. The Unaxis-Andover set has more and better coverage in the NIR range with six filters, while the MidOpt kit had two broadband NIR filters and one long-pass IR filter. This research did not include an assessment to compare the performance of the filters;

however, the narrow bandpass filters and larger number of the Unaxis-Andover filters was beneficial for the spectral response measurements as the narrow bands can provide a more reliable result with a higher spectral sampling.
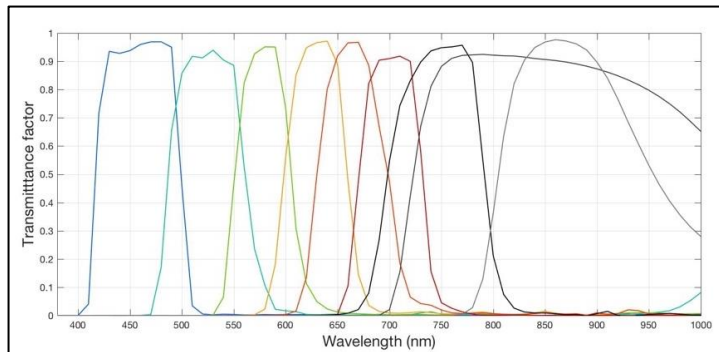
Figure 6-31. Transmission spectra of VIS and NIR MidOpt filters. Information from MidOpt Website (midopt.com)

6.2.2.2.   Results and discussion

The dark, shiny surface of the object proved to be problematic for the 3D scanning and the final data resulted in a model with holes (Figure 6-32 and Figure 6-33). Dark and reflective surfaces will be difficult for most optical imaging techniques working in the visible light region. Despite the scanner having a higher resolution and accuracy than the image-based 3D reconstruction, this model does not provide a good reference for the image-based 3D reconstructions to assess the accuracy or precision of the presented image-based 3D reconstruction. The 3D scanned data was used for comparison despite limitations with the data. These limitations are additional evidence of the challenges of reference data for heritage projects as discussed in Section 2.4 and 4.2.5.1.

Visually comparing detail views of the resulting models from the 3D scanning and the image-based 3D reconstruction (Figure 6-34*)*, the effect of the specular reflections is observed in the visible light reconstruction as a more rough surface than the reflected IR reconstruction. The reduced effect of the specular reflections in the IR input images has improved the recording of the surface. The carved detail of the fur is smoothed in the image-based 3D reconstructions (both VIS and IR) as compared to the 3D scan. The recording of the detail could be improved by decreasing the camera-object distance and/or changing the focal length. While the 3D scanning is suffering from the same surface properties that the visible light image-based 3D reconstruction (dark and shiny), it is not doing the same averaging of the image-based 3D reconstruction and there is no information recorded from the cracks resulting in holes in the model.

Figure 6-32. Screenshot of 3D scanned results viewed in Meshlab (Cignoni et al., 2008).
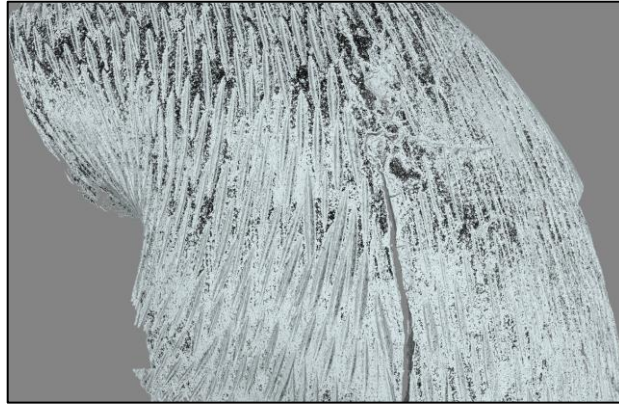
Figure 6-33. Screenshot of 3D scanned results in Meshlab.
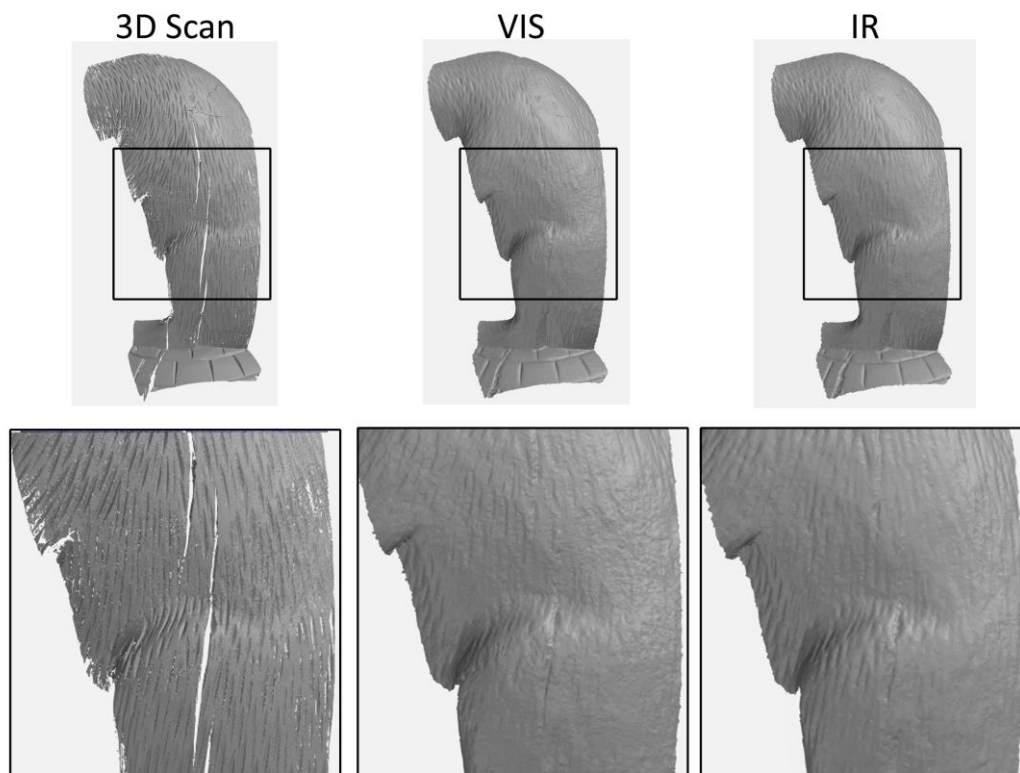
Figure 6-34. Secondary acquisition results of coyote and turtle: 3D scanned mesh (left), visible light image-based 3D reconstruction (centre), and reflected IR image-based 3D reconstruction (right). Top row includes overall views of the results and the bottom row includes detail views of the results with the detail location indicated by the box on the overall views. The visible light and reflected IR reconstructions were cropped to the 3D scanned mesh for the comparison.

The visible light and the reflected IR reconstructions were compared with the 3D scanned reference data using GOM Inspect (Figure 6-35). The datasets were aligned using the prealignment function, a global best-fit alignment and a subsequent local best-fit. The

surface deviation was calculated and visualised through colour scaled discrepancy maps with a histogram indicating the distribution of the discrepancies. The comparison of the visible light and reflected IR reconstructions show good correspondence of the image-based techniques (+/- 0.30 mm) with the largest discrepancies above the hip (yellow area) (Figure 6-35, right). These areas are likely a result of the specular highlights in the visible light input images and the difference with the IR input images that have a reduced effect from specular reflectance.
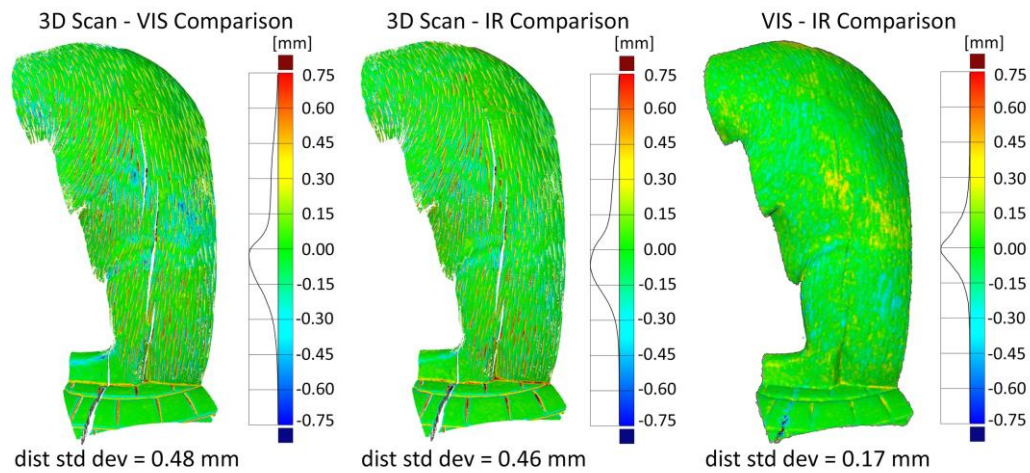
Figure 6-35. Surface discrepancy map comparisons: 3D scan to visible light mesh (left), 3D scan to IR mesh (centre), and visible light mesh to IR mesh (right).

The holes in the 3D scanned data could be contributing to the higher discrepancy of +/-0.75 mm and the standard deviation values approaching 0.5 mm. However, a local comparison in GOM Inspect (Figure 6-36) only shows minimal improvements with the reduction of the discrepancies and the standard deviation value. Both the local comparison and a comparison of the surface profiles (Figure 6-37) show the 3D scan resolving deeper incisions for the fur. The image-based 3D reconstruction allude to a more "complete" model (no holes in the data), but with this configuration the image-based 3D reconstruction are not able to resolve the depth of the incision marks if the 3D scan data is considered to more closely resemble the object's surface.
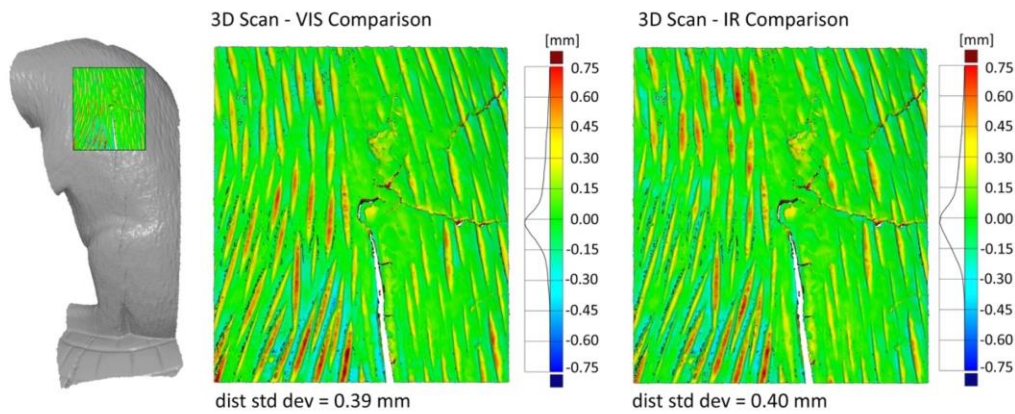
Figure 6-36. Local surface discrepancy maps comparison: 3D scan to visible light mesh (left) and 3D scan to IR mesh (right). Image on left provides location of the local surface comparison.
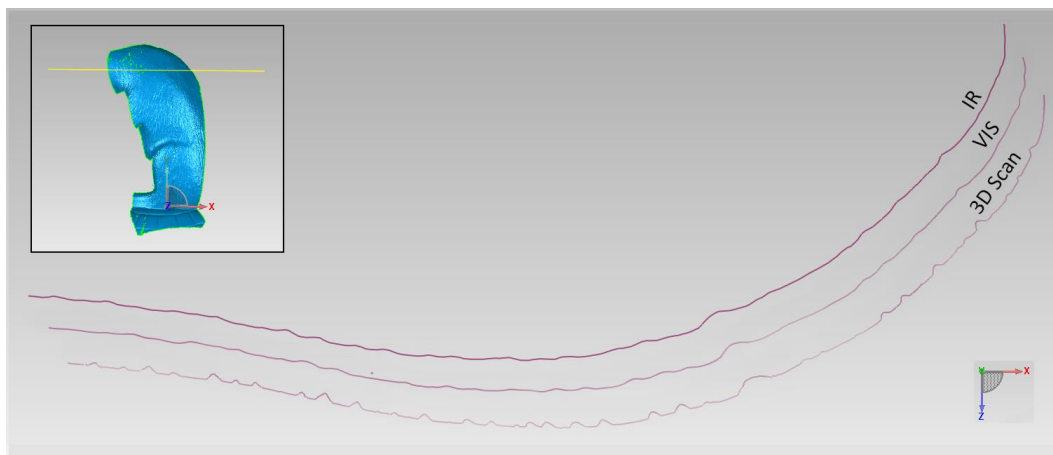
Figure 6-37. Profiles showing local results of the image-based models (IR and VIS) and the 3D scanned model. Image at top left of figure includes a horizontal line indicating the location of the surface profile.

A visual comparison shows that the details of the crack and the carved details of the fur for both the visible light and reflected IR reconstructions are not as well resolved as the initial datasets acquired in January (Figure 6-38). There are several differences between the initial January acquisition and the secondary September acquisition (lens, lighting setup, and camera network), so the comparison of the resulting data needs to be done with caution. The inclusion of detail images in the input image set increased the resolution, and a visual comparison shows that more detail of the crack and the carved fur could improve the reconstruction (Figure 6-38). This is not surprising, but it provides indications on how the imaging study could be improved with the acquisition of future datasets. It also shows the difficulty in acquiring scientifically valid 3D data for comparison. The level of detail for the September acquisition is not enough for monitoring the cracking, but it provides evidence of improved 3D reconstruction by using reflected IR images. The visible light results for both January and September show increased surface noise when visually compared to the reflected IR results. Despite the difference in the number of input images, the January

reflected IR model shows improved results compared to the visible light reconstructions. With the same camera networks for the September data, the reflected IR reconstruction also shows improved results compared to the visible light results.
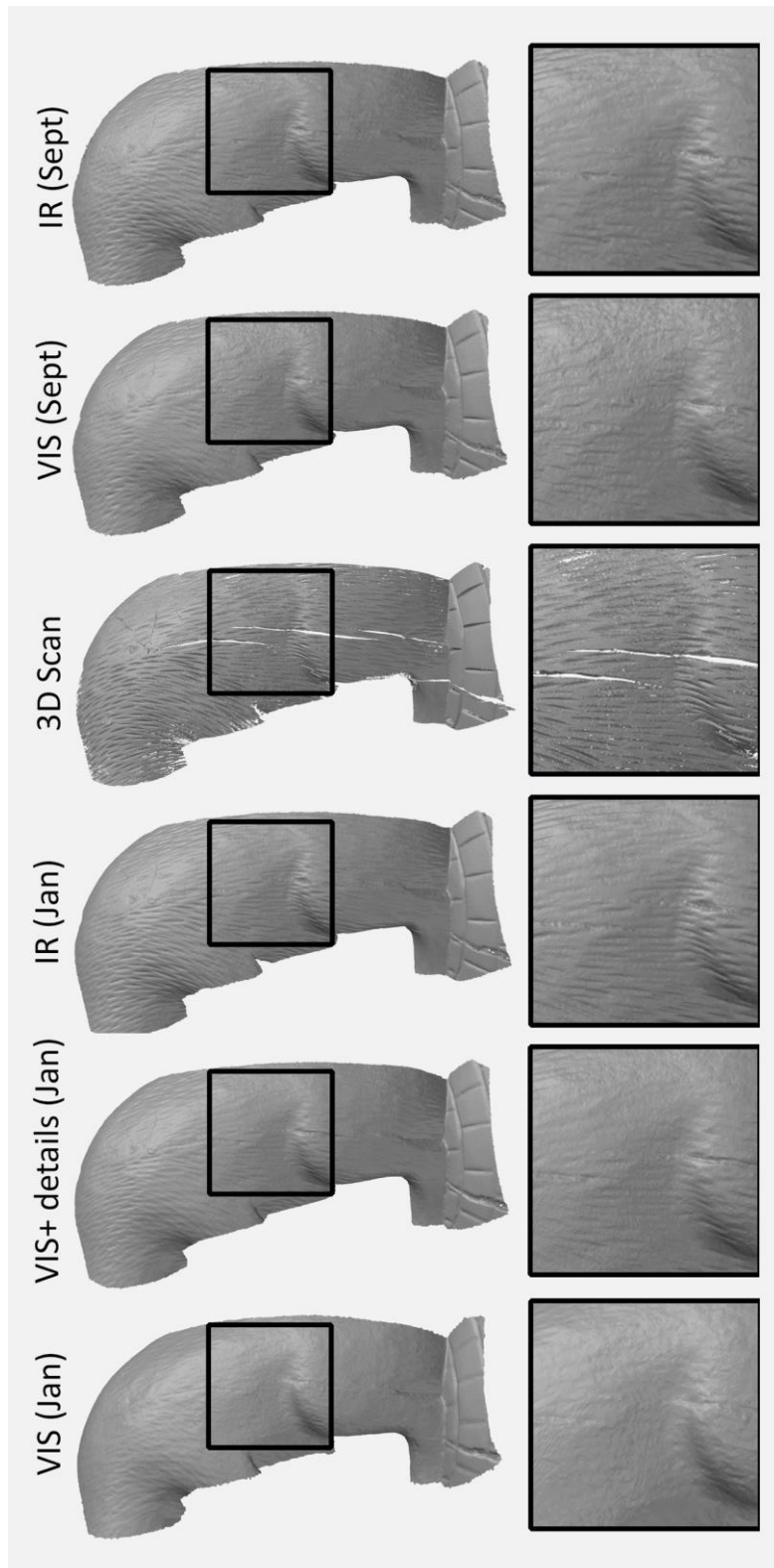
Figure 6-38. Visual comparison of the initial January acquisition and the secondary September acquisition.

The initial comparison of the January and September image-based 3D reconstruction results using GOM Inspect (Figure 6-39, *top*) included parts of the turtle shell at the foot of the coyote and edges of the coyote's leg and belly that had large discrepancies. The turtle shell includes a fairly deep crack that is not well recorded by either technique and had high levels of noise. The edges of the models also have increased levels of noise with less data redundancy and overlap and the areas that are challenging to document like the coyote's belly also have increased levels of noise. By limiting the region of comparison and removing these areas of larger discrepancy, the comparison is better able to assess the difference of the techniques (Section 4.2.2.2) (Figure 6-39, *bottom*).
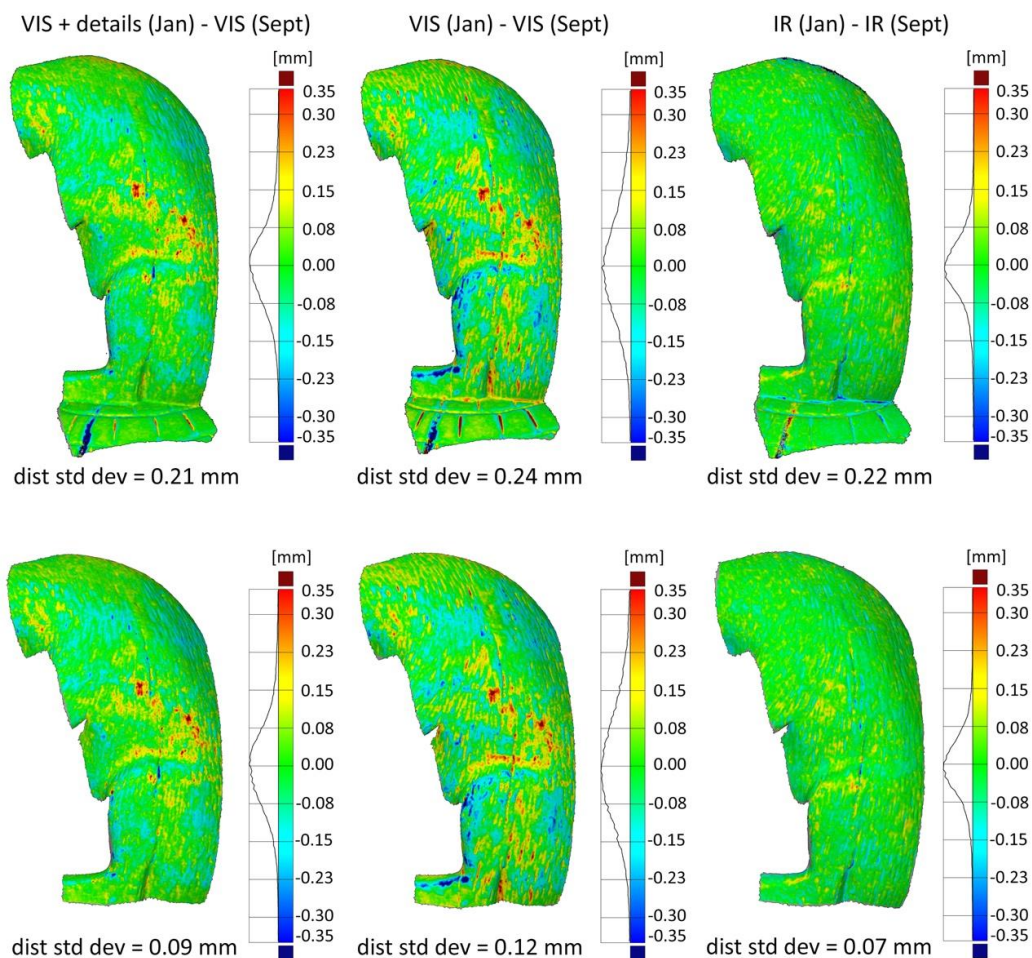
Figure 6-39. Surface discrepancy maps comparing the initial January acquisition with the secondary September acquisition. Bottom row: the models are cropped removing the larger discrepancies around the shoulder/back of the coyote and the crack on the turtle shell. Removing these discrepancies reduced the standard deviation by at least half.

The comparison of the visible light results shows increased deviations likely resulting from specular reflections. Reducing the impact of the specular reflections by using IR input images, the geometry is improving and the variability in the results is reduced specifically

relating to the camera network. The comparison of the IR results shows improved consistency of the results despite the differences in the image networks between January and September. Since the IR data shows more tolerance of the differences in the image network than the visible light data, this suggests a more forgiving and flexible option for recording data over time.

6.2.3. Discussion

The imaging study of a wooden sculpture of a coyote and turtle presented the use of wavelength selection to optimise the input images and improve the 3D reconstruction for the documentation and monitoring of a museum object. Two campaigns of imaging were presented providing examples of the setup and workflow for documenting the museum object and also critical assessment that resulted in the improvement of the comparability of the resulting data. The imaging study showed that reflected IR images provided increased visibility of the crack features when compared to visible light images. This increased visibility resulted from the dark varnish becoming transparent with IR radiation and the reduced effect of the specular highlights with the IR radiation. While the first iteration suggested that the reflected IR images could improve the 3D reconstruction, the inconsistencies between the visible light and reflected IR image sets needed to be addressed to improve the comparability.

The two campaigns provided important improvements for the setup and acquisition of a heritage object to increase the comparability both for assessing visible light and reflected IR image-based 3D reconstruction and also for monitoring an object over time. The improvements included more consistency between the image sets using the same lens, lighting, and camera network. While the comparability of the setup was improved, detail images were not acquired in the second iteration of the imaging study reducing the resulting resolution of the model suggesting continued improvement for future setups and acquisition. Inclusion of targets around the object would aid in the alignment of the two datasets, improve the scaling, and also provide means of assessing the accuracy and precision of the 3D reconstruction (Section 4.2.2).

The imaging study reiterated the challenge of acquiring reference data for cultural heritage documentation that was cited in the literature (Remondino and Menna, 2008; Remondino et al., 2014; Sapirstein, 2016). As discussed in Section 2.4, reference data is important for assessing the metric quality of 3D reconstructions, but it can be difficult to acquire reference data especially for heritage objects. Image-based 3D reconstruction is often selected for heritage documentation because it is low-cost, accessible, and portable, so acquiring

reference data with a range-based scanning method may not be an option due to cost, complexity, and portability. Other options for reference data include the use of known geometric shapes and averaged data to create a reference mesh. In the case of the coyote and turtle sculpture, a higher accuracy technique was available and used to document the object, but the challenges presented for visible light image-based 3D reconstruction were also challenges for structure light scanning. The shiny and dark surface of the object with fine carved details resulted in a reference data set with holes and incomplete surface coverage. While this reference was still used for comparison, the incomplete data set is limited in its ability to assess the accuracy of the 3D reconstructions.

The need to assess the metric quality of 3D reconstructions and the challenges with the acquisition of reference data could inform future research on the use of a test object with reference data that is representative of a collection or object. There are challenges with the creation of a test object that is representative of a heritage object and includes accurate reference data. The Mango Vase being a good example of the challenges (Section 4.2.4). In addition to being able to assess the metric quality of the 3D reconstruction, a test object could be beneficial for assessing monitoring data over time especially as equipment, setup, and camera networks change with the changing technologies.

6.3. Wavelength selection workflow

The initial objectives of the imaging study included establishing a workflow for wavelength selection and spectral-3D imaging, which will be presented in this section using the coyote and turtle sculpture example to illustrate the process. This workflow (Figure 6-40) is building on image-based 3D reconstruction pipelines and workflows discussed in Section 2.3. The following sections will discuss the project planning and wavelength selection.

6.3.1. Project planning

The first stage of the project is the design or planning phase, which involves examining the object and establishing the object characteristics: dimensions, materials, surface characteristics, features of interest and dimensions of those, etc. This information will help to guide the planning, set the project requirements, and establish the technology and parameters required. The project requirements for resolution and quality need to be identified in order to inform the selection of the best technology and parameters including camera, lens, illumination, and camera parameters. The GSD can be used to understand the parameters required for recording the smallest detail that needs to be resolved. As with other image-based 3D reconstruction projects, there needs to be planning for the camera

positioning and configuration design. The defined project requirements and selection of equipment during the planning phase (selected based on the object size and the size of the features of interest) will inform the positioning (camera-object distance). A strong camera network is important and can impact the resulting geometry as observed in Section 4.1.2.
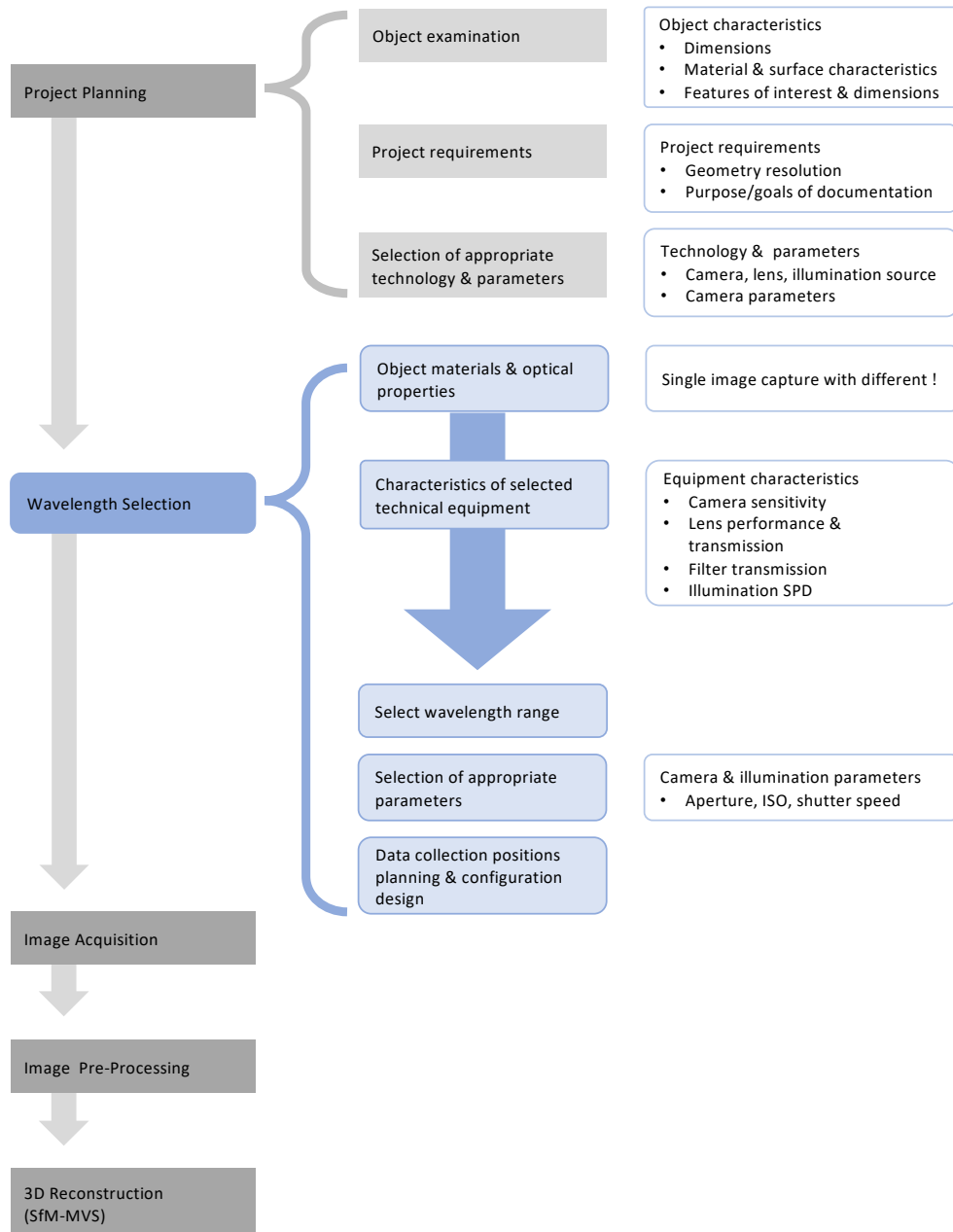
Figure 6-40. Wavelength selection workflow incorporated into established pipelines/workflows for image-based 3D reconstruction. The elements of the established pipeline for image-based 3D reconstruction are grey elements: project planning, image acquisition, and 3D reconstruction. The wavelength selection is presented as the blue elements and it is informed by aspects of the project planning component and is also part of the project design.

6.3.2. Wavelength selection

Wavelength selection involves considering both the object (object materials and surface characteristics) and the characteristics of components of the imaging system to determine wavelengths that would be used to optimise the recording of the object's geometry. Acquiring images of an object using a set of visible and NIR filters can provide an indication of how the materials respond to different ranges of wavelengths and present an option for selecting the best range for recording images for 3D reconstructions. The features that are of interest for the recording of the object need to be included in these single images (i.e., the crack detail of the coyote and turtle object) to best inform the wavelength selection.

An example is provided using the coyote and turtle sculpture (Figure 6-41). Single images recording the cracked feature along the side of the coyote were acquired using the MidOpt filter kit (Figure 6-31), resulting in a total of nine images recording wavelength ranges from 470 nm to 880 nm. This series of single images show how the materials that make up the object respond differently to different wavelengths presenting an option for wavelength selection. In the image acquired with the 470 nm filter, the coyote and turtle both appear dark absorbing radiation in this range. The object includes specular highlights from the shiny varnish and the features of the crack are visible, but with low local surface contrast. As the wavelengths get longer, the varnish on the turtle becomes transparent as seen with the images using the 635 nm and 660 nm filter, and the varnish for the coyote becomes transparent in the NIR as seen with the images using the 800 nm and 880 nm filters. The images recording NIR radiation (800 nm and 880 nm filters) show the crack feature with the most local surface contrast and clarity indicating that these ranges provide improved image data for the image-based 3D reconstruction. Once a wavelength range is selected an additional image should be acquired with a different view to see if there is a change in specularity and to ensure that the resulting imagery is consistent across the area of interest, which is important for the 3D reconstruction.

Combining information about the object materials from the initial investigative images with the information about the equipment characteristics can inform the selection of the wavelength range that provides the best view of the features of interest with an enhanced local contrast. Information about the equipment can be provided through characterisation as was presented in Chapter 5. This characterisation included the spectral response measurement (Section 5.3), and the process of measuring the sensitivity provided information about the illumination output and the filter transmission. The spectral response measurement provided evidence of where the camera would perform the best based on where it has the highest sensitivity. At areas of lower sensitivity, the images may have

higher levels of noise. The output of the illumination and the transmission of the filter will also impact the performance of the camera. Lower filter transmission or lower output in the illumination source will reduce the amount of light reaching the camera sensor, which can result in higher levels of noise.

As an example of how to look at both the camera sensitivity and filter transmission, Figure 6-42 provides an example from the coyote and turtle study of looking at the equipment characteristics to select wavelengths. Figure 6-41 shows that the NIR images are providing the best contrast for viewing the crack details. However, the sensitivity of the modified camera decreases significantly in the NIR, so it would be best to use the range of the shortest wavelengths that still provide good image contrast of the feature of interests. While the 880 nm filter provides better contrast of the coyote's fur and the crack features, the camera has about 50% increased sensitivity in the 735 nm range over the 880 nm range. Another consideration could be the difference in transmission between these two filters both considering the amplitude and width. Both filters have high transmission and are not very narrow. Even though the Unaxis-Andover filter set were not used for the documentation of the coyote and turtle sculpture, it is worth looking at the transmission of those filters as an example for the wavelength selection (Figure 6-43). The Unaxis-Andover filters are narrower than the MidOpt filters and therefore reduce the available radiation that could reach the camera sensor. The impact of the decreasing sensitivity of the modified camera sensor as the wavelengths get longer (moving further into the NIR from the visible) will be greater for the narrow bandpass filter.

While this discussion has been focused on bandpass filters with a defined bandwidth and the selection between different wavelengths, the reflected IR acquisition of the coyote and turtle object presented in Section 5.2 was with the Peca 910, a long-pass filter that cuts on at about 850 nm (50% transmission) (Figure 5-50). Long-pass filters transmit wavelengths shorter or longer than the provided cut on point (Warda et al., 2017, p. 137). The Peca 910 is similar to the Kodak Wratten 87C filters, one of the long-pass filters recommended by Warda et al. (2017). While bandpass filters are mentioned by Warda et al., long-pass filters are referenced as the primary filters for IR applications and most of the tables and examples reference the series of Kodak Wratten IR long-pass filters.
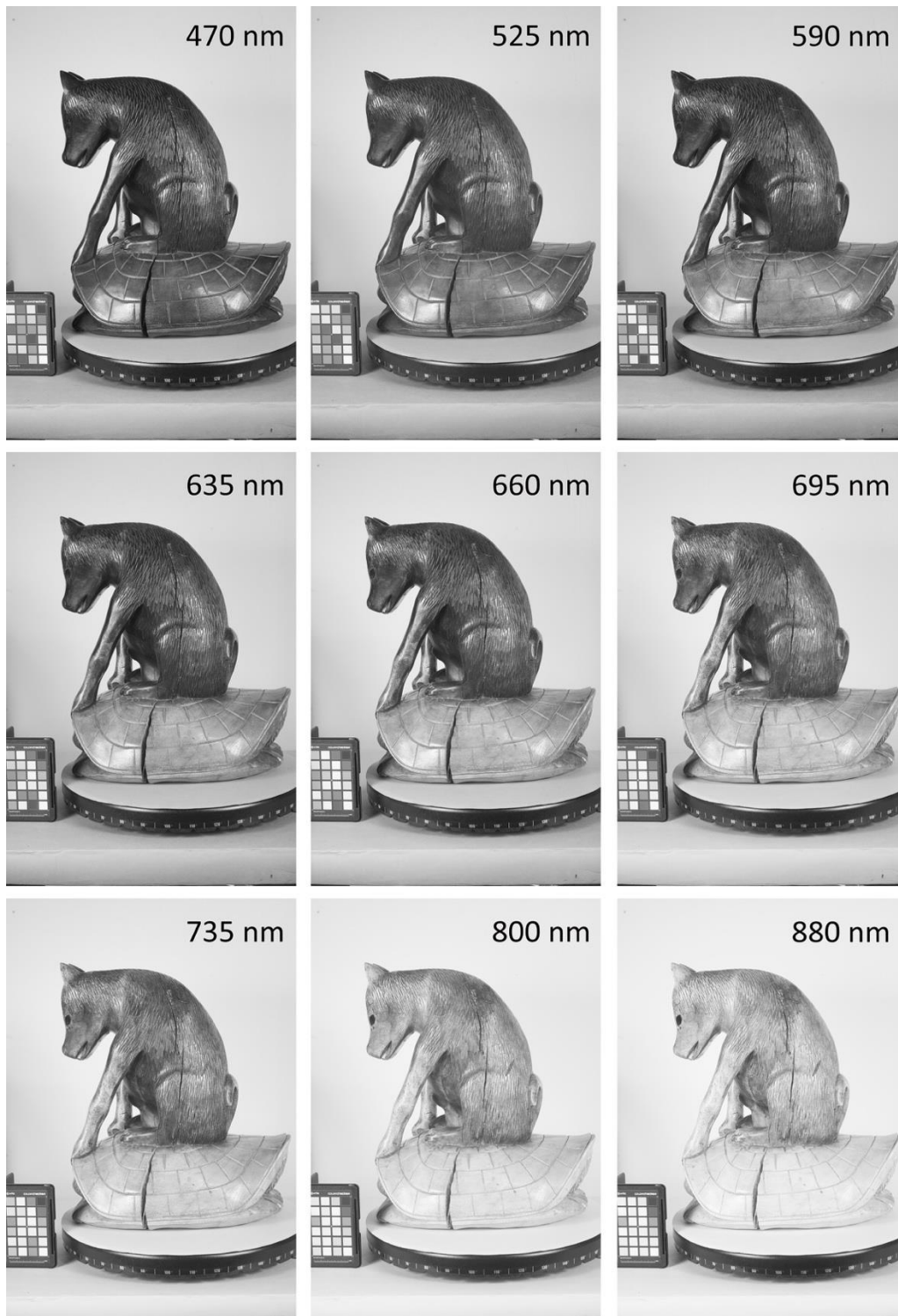
Figure 6-41. Wavelength selection image set of coyote and turtle sculpture using modified camera and MidOpt bandpass filters. This image set provides information about the object materials and surface characteristics to inform the selection of imaging wavelengths.
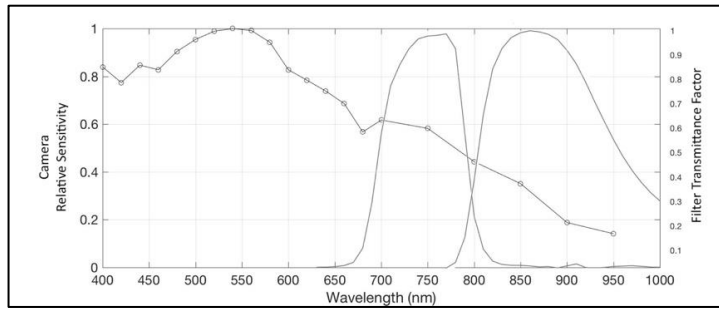
Figure 6-42. The transmission of the MidOpt 735 nm and 880 nm filters compared to the relative sensitivity of the modified camera.
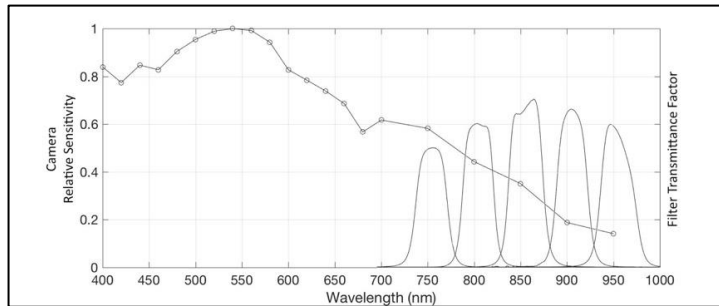
Figure 6-43. The transmission of the Andover NIR filters compared to the relative sensitivity of the modified camera.

In addition to the camera sensitivity and filter transmission, the output of the illumination source is an important consideration. This was emphasised in Section 5.3 with the iterations of the spectral response measurement and the use of three different illumination sources (Figure 5-44). The challenges presented with the spectral response measurement and the illumination sources were focused in the shorter wavelengths and output around 400 nm, while the coyote and turtle imaging study is focused on longer wavelengths and the NIR range. The three illumination sources used in Section 5.3 all have output in the NIR, so for the coyote and turtle imaging study these sources all could be used. However, if the desired wavelength range was around 400 nm, then the tungsten lamps and the Canon Speedlite flashes should not be considered for the illumination source as was concluded with the spectral response measurements.

Once the wavelength range is selected based on the materials of the object and the characteristics of the imaging system, camera parameters and light settings will need to be adjusted for this range. The next steps for the image-based 3D reconstruction would be image acquisition and processing, and the wavelength selection process does not necessarily add or alter these steps.

6.3.3. Discussion

As the final objective for the imaging study, this section presented a workflow for wavelength selection and spectral-3D imaging of museum objects. The workflow builds on established image-based 3D reconstruction pipelines and workflows (Section 2.3), and it

takes into consideration the requirements of museum imaging providing an approachable way for spectral-3D imaging to improve the image-based 3D reconstruction of museum objects.

The presented workflow involves multiple steps and takes time, but wavelength selection can be valuable and solve some otherwise tough 3D reconstruction problems. With an example like the coyote and turtle, wavelength selection changes the surface properties and makes a dramatic difference for the 3D reconstruction. The workflow is only useful if the surface properties change dramatically with different wavelengths and is increasingly valuable if there is a collection of objects with similar surface properties that have proven to be worthwhile with specific wavelengths. The example of the coyote and turtle imaging study is only one example using NIR wavelengths, and these results cannot be generalised to all objects or different wavelengths. While the workflow presents steps for establishing the best wavelengths for an object, the research has not defined specific wavelengths for specific materials or types of objects. Future work would be required to investigate the potential of different wavelengths for other materials and objects.

The wavelength selection workflow presented here includes bandpass filters and acquiring images to understand the object materials and surface properties. Another option could include the use of fibre optic reflectance spectroscopy (FORS) or NIR spectroscopy and the use of a spectrometer to measure the reflectance spectra. A spectrometer would provide information about the optical properties of the materials. By looking at the reflectance spectra, wavelength ranges could be selected based on absorption or reflectance features. Multiple points would need to be measured to understand the combination of materials and how these materials would respond for a wavelength range and if the use of a wavelength selection would provide areas of higher contrast between materials.

6.4. Chapter summary

This chapter focused on wavelength and improved 3D reconstruction addressing the research question "Can photography with a modified consumer digital camera paired with selected illumination and filtration be used as a scientific method to better benefit the 3D reconstruction of museum objects for conservation documentation?" Chapter 5 started to address this research question through the camera characterisation to assess the modified camera's performance and to understand the impact of modification, and characterisation was necessary to assess the imaging system as a scientific tool as part of the wavelength selection process. To further answer the research question this chapter included the assessment of the influence of wavelength on 2D image quality (Section 6.1), the use of

wavelength selection to improve image-based 3D reconstruction (Section 6.2), and the presentation of a wavelength selection workflow that can be adopted by heritage users (Section 6.3).

In answering the research question, the imaging study of the coyote and turtle sculpture (Section 6.2) provided evidence that selected illumination and filtration can be used to improve the 3D reconstruction of museum objects for conservation documentation. The imaging study shows that wavelength selection, specifically the use of NIR radiation for this object, could increase the local contrast and reduce specular reflections which improved the consistency of the method despite differences in image networks. By improving the consistency and using a camera that has been characterised, the workflow presented can be used as a scientific method that benefits the 3D reconstruction of objects for conservation documentation, especially the monitoring of objects over time. A comparison of the IR results from two campaigns for the imaging study showed improved consistency between datasets despite differences in the image networks suggesting a more forgiving and flexible option for recording data over time. To add applicability to this finding, Section 6.3 presented the workflow for wavelength selection and spectral-3D imaging of museum objects in order to be used by heritage professionals.

Imaging using selected wavelengths rather than full spectra within or beyond visible light can increase the image contrast of materials or features to provide an enhanced view. The quantification of imaging performance in relation to wavelengths was investigated to understand whether or not wavelength impacted image quality as part of the wavelength selection process. The wavelength and image quality assessment (Section 6.1) included two approaches: filtering the camera and filtering the illumination. Challenges with the filtered camera approach led to an updated approach of filtering the illumination; however, there were still some limitations with the filtered illumination approach. While the filtered illumination approach presented advantages for testing wavelength and image quality, this setup would not be an optimal option for improved imaging of a museum object. The results showed that the wavelength is not the largest factor impacting the resulting image quality, but instead other significant factors were the lens selection, focus, and illumination. While these two approaches were focusing on assessing wavelength and 2D image quality, the presented advantages and limitations carry over to MSI documentation of objects and the consideration of how wavelengths can be selected.

The imaging study of a wooden sculpture of a coyote and turtle (Section 6.2) presented the use of wavelength selection to optimise the input images and improve the 3D reconstruction for the documentation and monitoring of a museum object. The study aimed to establish

detailed baseline imagery for monitoring dimensional change, to investigate the use of spectral and 3D imaging techniques for documenting museum collections, and to establish a workflow for wavelength selection and spectral-3D recording. The imaging study demonstrated the practical applications of this research within museum imaging and addressed specific needs of museum professionals. The imaging study demonstrated the realistic time constraints and logistics for accessing museum collections and presented challenges with monitoring an object over time. Two campaigns of imaging were presented providing examples of the setup and workflow for documenting the museum object and also critical assessment that resulted in the improvement of the comparability of the resulting data. The study showed that reflected IR images increased the local contrast and reduced specular reflections to provide improved images for the 3D reconstruction.

The final section (Section 6.3) presented a workflow for wavelength selection and spectral-3D imaging of museum objects using the coyote and turtle sculpture as an example. Wavelength selection is informed by the characteristics of the object (object materials and surface characterisation) and the characteristics of the imaging system and components of the setup (camera sensitivity, filter transmission, and illumination output). Acquiring images of the object using a modified camera and optical bandpass filters provides information about the object materials to inform the selection of the wavelength range that provides the best view of the features of interest with enhanced local contrast. Information about the equipment can be provided through characterisation as was presented in Chapter 5.

Findings and recommendations:

Lens selection, focus, and illumination impact the resulting image quality more than wavelength. The lens will impact the resulting image quality even if the acquisition is within the range of visible light. Sharpness and focus significantly influence 2D image quality assessment, specifically SFR analysis and sampling efficiency. Even illumination is important for the resulting image quality, but the methods for selecting or filtering wavelengths may be a limitation.

The imaging study provided evidence that the use of a modified camera and wavelength selection can improve image-based 3D reconstruction. This study showed that reflected IR images increased the local contrast and reduced specular reflections that improved the consistency of the resulting 3D reconstruction.

Wavelength selection workflow provides recommendations for how to select wavelengths in order to implement spectral-3D imaging to improve image-based 3D reconstruction.

Wavelength selection can be valuable and can solve otherwise tough 3D reconstruction problems, but it is only useful if the surface properties change dramatically which can be tested by looking at the object with different wavelengths. The wavelength selection workflow for spectral-3D imaging and improved 3D reconstruction is increasingly valuable if there is a collection of objects with similar surface properties that have proven to response the recording with selected wavelengths to increase the local contrast and/or reduce specular reflections.

Combining information about the object materials from initial investigative images with the information about the equipment characteristics can inform the selection of the wavelength range that provides the best view of the features of interest with an enhanced local contrast. Understanding the characteristics of the different parts of the imaging system (spectral response of the camera, transmission of filters, spectral power distribution of illumination source) is important as part of the wavelength selection workflow.

Contribution to knowledge:

This chapter provides evidence of a contribution to knowledge through the use of a modified camera and selected wavelengths to improve the recording of fine detail for image-based 3D reconstruction. Increasing the local surface contrast and reducing specular reflection through wavelength selection can improve image-based 3D reconstruction as demonstrated by the imaging study of the coyote and turtle. While modified cameras are being used for broadband spectral imaging and MSI for conservation documentation, to the knowledge of the author, these devices have not been used for optimising image-based 3D reconstruction, so this chapter presents a novel workflow and application for conservation documentation. Other fields, like astrophysics and machine vision, have used selected wavelengths for improved recording; however, this has not been done for conservation documentation for the increase of local contrast for improved surface recording using a modified camera and optical filters.

7. Improved 3D reconstruction: Depth of field

Limited DOF is an issue with close-up 2D and 3D imaging of small to medium sized objects (Section 2.5.1). While DOF is well understood in the context of 2D imaging and it is considered with the acquisition of image-based 3D reconstruction, "acceptable" sharpness has not yet been quantified for image-based 3D reconstruction in the photogrammetric and computer vision communities (Section 2.5). Consequently, this chapter investigates the influence of DOF and sharpness on 3D reconstructions to better understand the parameters (specifically aperture, angle, distance) and provide evidence of the limitations of DOF relating to 3D using the Panel test target (Section 7.1) and the Mango Vase (Section 7.2). Assessment of 2D image quality using the DICE target links to the 3D reconstruction results to quantify and connect the 2D DOF calculations with the range of acceptable sharpness for 3D and resulting 3D reconstruction quality. This work contributes to the research question: "How can the limitations of DOF be mitigated using consumer imaging systems for image-based 3D reconstruction of small to medium sized museum objects?"

7.1. Panel test target

The Panel test target was used to investigate the parameters and provide evidence for the limitations of DOF relating to 3D reconstruction of a plane focusing on aperture, angle, and camera-object distance. The parameters influencing DOF were isolated and investigated using the Panel and the camera positioning robot (Section 4.1.1.1). Two tests were conducted using the Panel: 'DOF-3D-Plane' and 'DOF-Sharp-SFR'. The DOF-3D-Plane test investigated the impact of aperture and angle on DOF with incremental changes in the camera-object angle, while the DOF-Sharp-SFR test investigated the impact of aperture and distance on DOF with incremental changes in the camera-object distance.

The camera positioning robot was used to reproducibly change the camera position and record the camera networks required for the 3D reconstruction of the Panel in addition to maintaining the same relationship between the target and illumination. Changing the diameter of the aperture influences the image quality in terms of DOF, the range of "acceptable" sharpness, and diffraction. Using a range of apertures will provide evidence for the selection of DOF and the balance of image quality and the range of acceptable sharpness, so datasets were acquired with three apertures (f/5.6, f/11, f/32).

Both of the tests included image acquisition of the DICE target at each camera-object angle and distance to assess the image quality. The DICE target was recorded at the middle camera position (h2p2) at each of the camera-object angles and distances to link 2D image quality to

the 3D reconstruction. The FADGI star rating system was used as a point of reference for the image quality relating to the 3D reconstruction. While the FADGI star rating system is based on a combination of several image quality parameters, this test only focused on sampling efficiency and SFR. There are other image quality parameters within the FADGI criteria that could improve or diminish the star rating for these image sets, but for these tests were limited to sampling efficiency and SFR.

The unmodified Canon camera with the 60 mm lens (Figure 4-1) was used to record images of the two test objects with the two Bowens Gemini 400Rx flash units and umbrellas. Images were acquired at ISO 100 with a 1/100 shutter speed. To maintain consistent illumination on the sensor surface as the aperture diameter decreased and the amount of light was reduced, the flash power needed to be increased: at f/5.6 the flash power was 1, f/11 the flash power was 3, and f/32 the flash power was 6. The camera was focused at the same position for each aperture using Live View at 200% magnification, viewing the central feature of the DICE target or the pattern at the centre of the Panel test target.

The acquisition, processing, and assessment for this experimental work built upon the methods of optimisation and assessment presented in Section 4.1. This included using a convergent image configuration for improved geometry (Section 4.1.2), using an averaged mesh for comparison (Section 4.1.3), and selecting a limited parameter set for the camera model to avoid over-parameterisation (Section 4.1.4.2).

RAW images were acquired and processed using a standard RAW processing workflow with ACR (Section 5.1). These tests were run with the unmodified camera and standard RGB images, so the MC-RAW workflow was not necessary. The image sets were batch-processed for a greyscale conversion using an Adobe Photoshop Action script. The GoldenThread Software was unable to detect the features and therefore analyse a majority of the images, so *sfrmat3* (Section 12) was used for the SFR analysis. See Appendix 14.6 for information about SFR analysis process using *sfrmat3* and a comparison of the results with GoldenThread. The results from *sfrmat3* were visualised and analysed using Matlab.

7.1.1. DOF-3D-Plane

The DOF-3D-Plane test investigated the parameters and provided evidence for the limitations of DOF relating to 3D reconstruction of a plane. The camera-object angle was incrementally changed by 10° starting from 0° and rotating to 30°. The data was acquired using convergent image configurations for three apertures (f/5.6, f/11, f/32) at four angles (0°, 10°, 20°, 30°) and the resulting 3D reconstructions were assessed by comparing the

results with the averaged reference mesh (Section 4.1.3). In addition to acquiring images of the Panel test target for 3D reconstruction, images of the DICE target were acquired with the three apertures at the middle camera position (h2p2) for each of these angles to link image quality to the resulting 3D reconstruction.

The theoretical impact of changing the camera-object angle on image quality, specifically sharpness, was estimated by considering the DOF calculations for the three apertures (Table 7-1) and the relationship of the target to these different ranges of acceptable sharpness as the angle increases (Figure 7-1). With the largest aperture diameter of this experiment, f/5.6 had the smallest DOF, while f/32 with the smallest aperture diameter had the largest DOF. Generally, the optimum aperture, balancing DOF and diffraction, is closing down three stops from the maximum aperture. For the 60 mm lens, the maximum aperture is f/4 and the optimum aperture would be around f/11 providing a good balance between the DOF and diffraction. It was assumed that the f/11 datasets were going to provide the highest image quality and f/32 would provide consistent results as the camera-object angle changed because the smaller aperture diameter provided the largest DOF and the target remained in this range for the four angles tested.

Table 7-1. DOF calculations using standard circle of confusion diameter (C = 0.03 mm)

	f/5.6	f/11	f/32
Near limit (mm)	583.66	568.72	517.24
Far limit (mm)	617.28	634.92	714.29
DOF (mm)	33.63	66.20	197.04

This estimated theoretical impact of the changing camera-object angle in relation to the DOF for f/5.6 and f/11 (Figure 7-1) aided in estimating the 2D and 3D impact of DOF. At a1 (0°), the full target was within both the DOF for f/5.6 and f/11. At a2 (10°) the features on one side of the target were within and the other side outside of the f/5.6 DOF (85% of the target within this range), while the entire target remained within the f/11 DOF (Figure 7-1a). As the angle changed to a3 (20°) (Figure 7-1b), both sides of the target were outside of the f/5.6 DOF with only 43% of the target within this range, while one side was partially outside and the other side was within the f/11 DOF or 85% of the target within this range. At a4 (30°) both sides were outside of the f/5.6 and f/11 DOF with 29% of the target was within the f/5.6 DOF and 58% of the target was within the f/11 DOF (Figure 7-1c).
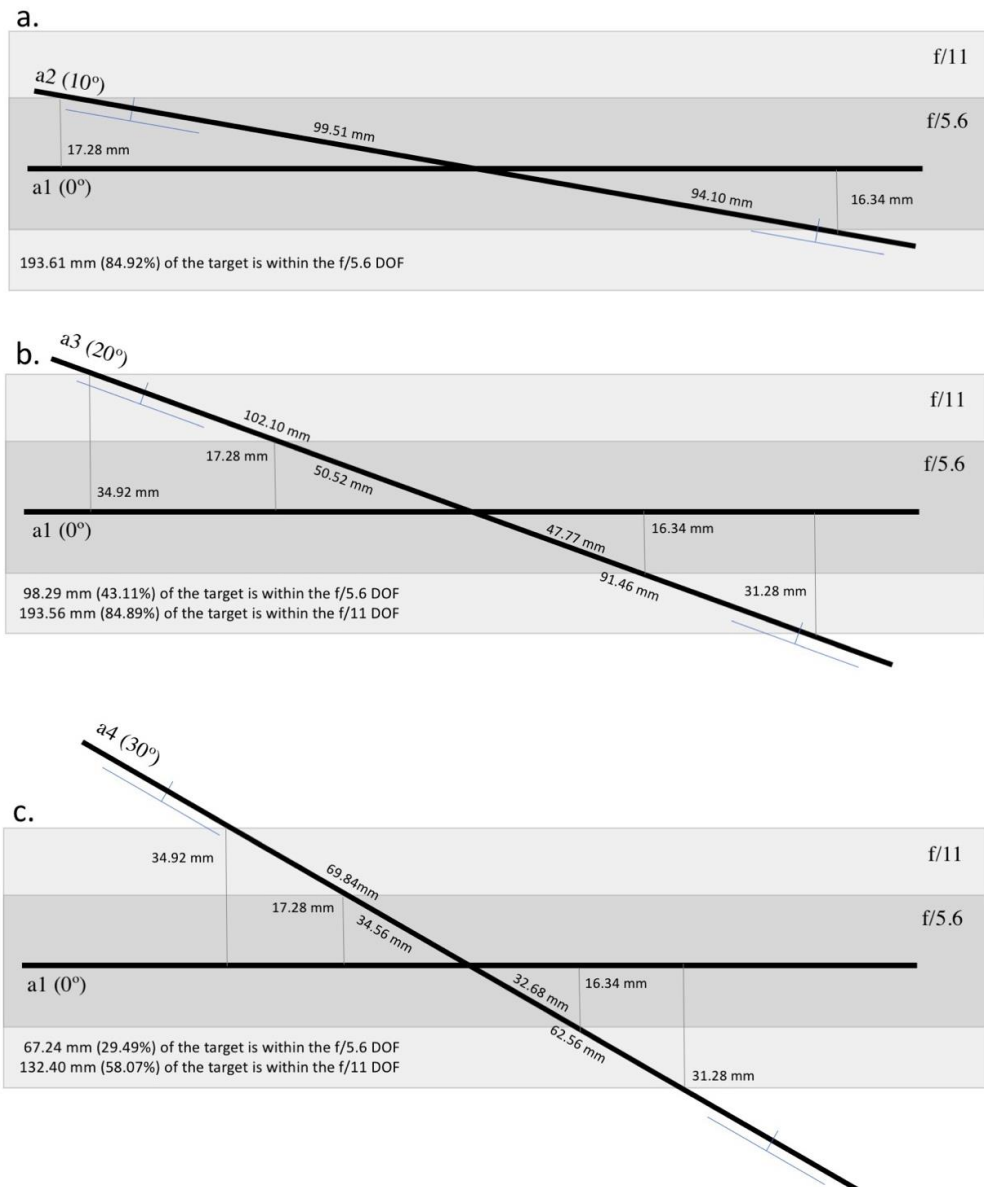
Figure 7-1. Theoretical impact of changing camera-object angle based on calculated DOF. The calculated DOF for f/5.6 and f/11 using C=0.03 mm (Table 7-1) are represented by grey boxes to illustrate the impact of the changing angle. The slanted-edge features that are measured for the SFR analysis and sampling efficiency calculations are located in the four corners and centre of the DICE target. The DOF for f/32 is not included in the figure because the target remains within this DOF at all four angles. The features at the four corners of the target are represented by the blue lines parallel to the black lines representing the target angle with the blue perpendicular line representing the centre of the features. The area of the target represented by this illustration is 22.8 x 15.3 cm and does not include the margin around the edges of the target. The centre of the corner features are ~ 2.5 cm from the edge of the target. At a1 (0°), represented as the horizontal line in all of the illustrations, the full target is within both the DOF for f/5.6 and f/11. (a) At a2 (10°), the one side of the target is within the DOF for f/5.6 and both sides are fully in the DOF for f/11. (b) At a3 (20°), the slanted-edge features on the four corners of the target are outside of the DOF for f/5.6 and one side is partially outside the DOF for f/11. (c) At a4 (30°), the four features at the corners are the target are outside of the DOF for both f/5.6 and f/11.

Relating the theoretical impact of the changing camera-object angle to 2D image quality it was hypothesised that the centre for both f/5.6 and f/11 would remain sharp for all four angles but it was expected to see the image quality decrease at the four corners as the angle increased. At a2 (10°) a decrease in image quality was expected for the f/5.6 datasets, but

not for the f/11 since the entire target was still within the range of acceptable sharpness for the f/11 DOF. At a3 (20°), there should be a noticeable decrease in image quality for the f/5.6 dataset with only 43% within the acceptable sharpness range. It was expected to start to see a decrease in image quality in the f/11 dataset at a3 (20°), although a more significant decrease should be observed at a4 (30°) when only 58% of the target was within the DOF.

Relating the theoretical impact of the changing camera-object angle to 3D reconstruction it was hypothesised that the centre of the reconstruction would have less noise because the image data will remain sharp. However, as the edges started to fall outside of the DOF the surface noise along the edges would have increased. At a2 (10°) a decrease in the quality of the 3D reconstruction would have been expected for the f/5.6 datasets, but not for the f/11 since the entire target was still within the range of acceptable sharpness for the f/11 DOF. At a3 (20°), there should be a noticeable decrease in quality for the f/5.6 dataset. Similar to the 2D image quality discussed above, it was expected to see a decrease in quality with the f/11 dataset at a3 (20°), although a more significant decrease would be observed at a4 (30°).

The DOF-3D-Plane analysis required *sfrmat3* for the SFR measures because images beyond the first angle (0°) were not readable in GoldenThread due to the unsharpness of the image data. The slanted edge features in the DICE target were extracted as 330 x150 pixel areas (or 150 x 330 pixel areas depending on horizontal or vertical orientation) from the twelve images (three apertures and four angles) before analysing each of these features with *sfrmat3* (Appendix 14.6). The resulting *.xls files were converted to *.xlsx and analysed using Matlab. The horizontal and vertical values for the five features on the DICE target were kept separate, as opposed to averaging the values, in order to compare the results of the two sides and centre of the target as the angle changed.

FADGI defines a four-star rating system as a quality indicator of acceptability for the documentation of cultural heritage materials with one-star being the lowest rating and four-star being the highest rating and representing the state of the art in image capture (Section 3.3.2). A higher star rating indicates a more consistent image quality and also a greater technical performance from the operator and imaging system (Rieger, 2016, p. 10). While the FADGI star rating system is based on a combination of several image quality parameters measured from the DICE target, this test was only focusing on sampling efficiency and SFR. These parameters were used as a point of reference for the 2D image quality of these image sets to link with 3D reconstruction, but it was recognised that there are other image quality parameters within the FADGI criteria that could improve or diminish the final star rating for these image sets if the full Digital Image Conformance Evaluation (DICE) process were followed.

7.1.1.1. Results and discussion

As estimated by the theoretical impact (Figure 7-1), the SFR analysis showed that the centre features maintained a fairly consistent quality for each aperture as observed from the sampling efficiency results (Table 7-2) and the SFR curves (Figure 7-3) even as the camera-object angle changed. The rotation was at the centre of the target so this area would fall within the DOF for the three apertures as the angle increased. For the f/11 datasets the sampling efficiency for the centre feature was mostly within the 3-star rating from a1-a4, whereas the f/5.6 and f/32 datasets were below the FADGI 1-star rating but the centre measures were fairly consistent. At a2 (10°) there was a decrease in image quality for the f/5.6 datasets, but not as much for the f/11 datasets since the entire target was still within the range of acceptable sharpness for the f/11 DOF. At a3 (20°), the f/11 datasets decreased in image quality with both sides below the FADGI 1-star rating.

Table 7-2. DOF-3D-Plane sampling efficiency (%) and colour coded FADGI star rating. The sampling efficiency results of the target are designated by three areas (left, centre, right) outlined in Figure 7-2.

f/5.6 — Horizontal

	Left	Centre	Right
a1	68	65	61
a2	25	58	66
a3	14	54	27
a4	12	52	16

f/5.6 — Vertical

	Left	Centre	Right
a1	60	59	51
a2	21	58	74
a3	13	50	26
a4	11	44	15

f/11 — Horizontal

	Left	Centre	Right
a1	79	84	79
a2	51	84	79
a3	29	81	53
a4	22	76	33

f/11 — Vertical

	Left	Centre	Right
a1	80	84	77
a2	49	83	80
a3	27	83	48
a4	21	81	30

f/32 — Horizontal

	Left	Centre	Right
a1	51	55	52
a2	52	55	52
a3	50	54	51
a4	48	52	50

f/32 — Vertical

	Left	Centre	Right
a1	51	53	50
a2	53	54	52
a3	52	53	51
a4	49	54	51

FADGI star rating
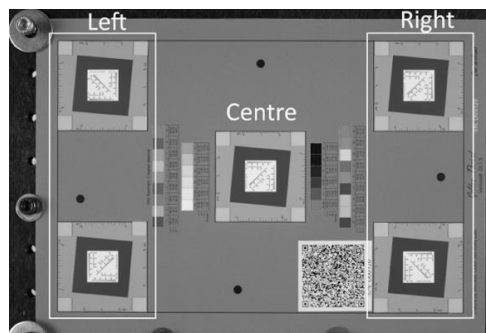
Rating	
★★★	
★★	
★	
below 1 star	

Figure 7-2. Image of the DICE target indicating the three areas represented in the sampling efficiency percentage results.

The target remained in the f/32 DOF for all of the angles; however, with the smaller aperture diameter, the image quality resulted in degradation from diffraction. The f/32 datasets were very consistent as seen with the sampling efficiency values clustered around 50% (Table 7-2) and very similar SFR curves in (Figure 7-3). While a smaller aperture diameter increased the DOF showing little to no impact as the camera-object angle changed,

diffraction reduced the image quality below the FADGI 1 star rating. The f/5.6 datasets had the lowest sampling efficiency rates of the three apertures, and the greatest impact was observed with these datasets as the camera-object angle changed due to the small DOF. According to the sampling efficiency percentages, only the initial dataset acquired at 0° (a1) fell within the FADGI star rating system. The f/11 datasets maintained the highest image quality especially at the centre of the target. The f/11 datasets showed the effect of the DOF as the camera-object angle increase, but also the balance of image quality and DOF in the selection of apertures.

The challenges with the reference data for the Panel test target were discussed in Section 4.1.4 concluding that there were limitations with the averaged reference mesh and the Nikon data. Despite falling short of true reference data, both datasets were used to assess the 3D reconstruction results for the DOF-3D-Plane test in order to understand the impact of different "reference" datasets. The averaged reference mesh (Figure 7-4) resulted in a consistently smaller spread than the Nikon data and the ripple pattern was apparent in the surface discrepancy maps especially with a range smaller than +/- 0.15 mm. The Nikon data comparisons (Figure 7-5) showed some "doming" effect (Section 4.1.2), but ultimately both comparison sets showed similar trends.

The f/5.6 3D reconstructions showed the most discrepancy as the camera-object angle increases and f/32 showed the least discrepancy, which was to be expected with the difference in DOF between f/5.6 and f/32 (Figure 7-4 and Figure 7-5). The f/5.6 reconstructions clearly showed the impact of DOF with increased surface noise from the smaller aperture diameter and limited DOF. The f/11 a3 and a4 reconstructions also showed effects of DOF, while the f/32 reconstructions tolerated the reduced image quality from diffraction that was observed (Table 7-2).

In addition to assessing the surface discrepancy maps, the PhotoScan processing results (Table 7-3) provide insight into the 3D reconstruction quality. For the f/5.6 datasets as the camera-object angle increases, the number of tie points and projections decreased, and the RMS reprojection error increased. This trend and impact from DOF was not as clearly observed with the f/11 datasets, but the f/11 a1 and a2, which are both within the calculated DOF, had the highest tie point and projections count (with the exception of the f/32 a4 dataset) and the lowest RMS reprojection error.
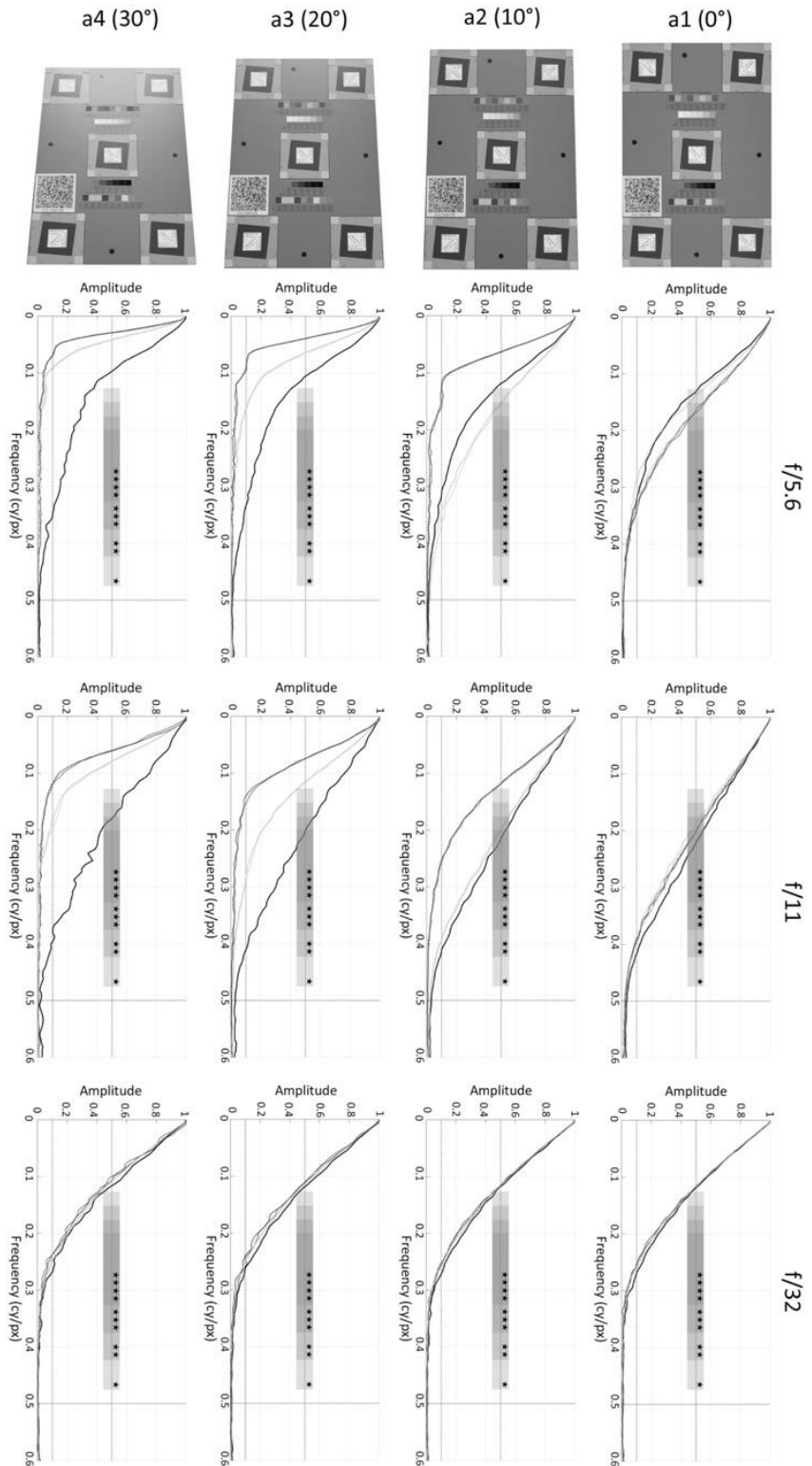
Figure 7-3. SFR analysis results for horizontal measures at f/5.6, f/11, and f/32 from four angles (a1, a2, a3, a4). The SFR curves include measures from the five features on the target and are represented by different line types. The thick black line is for the centre feature, the grey lines are the right features, the solid lines (with the exception of the thick black line) are the bottom features. The images included in the left column were acquired at f/11 and are intended to provide a view of what the target looks like at each angle. As specified by ISO 12233:2017, horizontal and vertical results for the SFR analysis should be presented together; however, due to space limitations only the horizontal results have been included in this figure without the vertical results. Appendix 14.7 includes figures with both the vertical and horizontal results for each of the datasets.
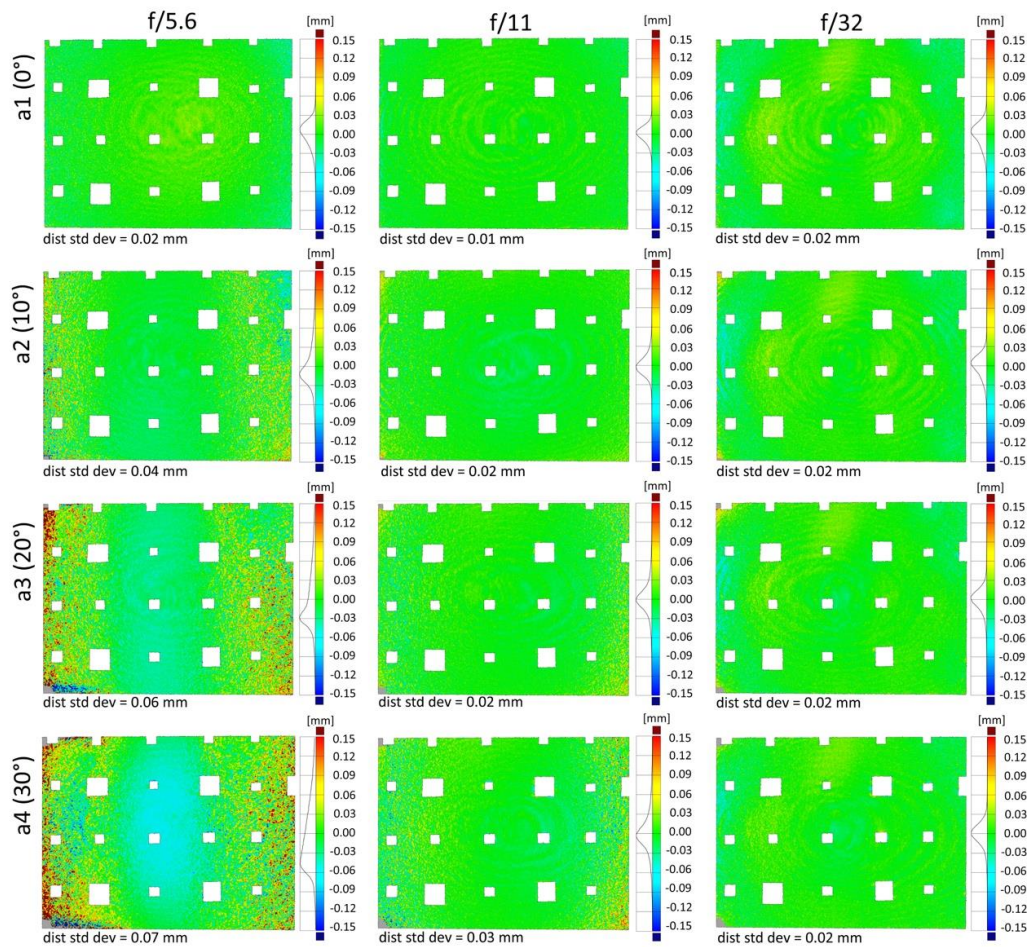
Figure 7-4. The 3D reconstruction results for 3D-DOF-Plane assessed using the averaged reference mesh. The figure includes surface discrepancy maps comparing three apertures (f/5.6, f/11, f/32) and four angles (a1, a2, a3, a4) of the 3D reconstructions to the averaged reference mesh.

The surface discrepancy maps of the 3D reconstructions (Figure 7-4) can be linked back to the theoretical estimation of image quality (Figure 7-1) and the 2D image quality results (Table 7-2 and Figure 7-3). The f/32 datasets with the smallest aperture and the largest DOF produced 3D reconstructions at all four angles that had the lowest discrepancy. The Panel test target was within the calculated f/32 DOF at all four angles, so the image data would have been within the acceptable range of sharpness. However, the image quality of the input images is well below the FADGI 1 star rating due to diffraction. The 3D processing tolerated the lower quality image data and, in this case, produced consistent reconstructions. The diffraction limit reduced the ability of resolving and recording high frequency features at a small aperture.

The f/5.6 datasets with the largest aperture and the smallest DOF showed the greatest impact of DOF on the 3D reconstructions starting at a2 (10°). The image quality of the input images (sampling efficiency and SFR) was mostly below the FADGI 1 star rating, even at a2 (10°). These results indicated that a large aperture is not going to optimise image-based 3D reconstruction for either DOF or image quality.
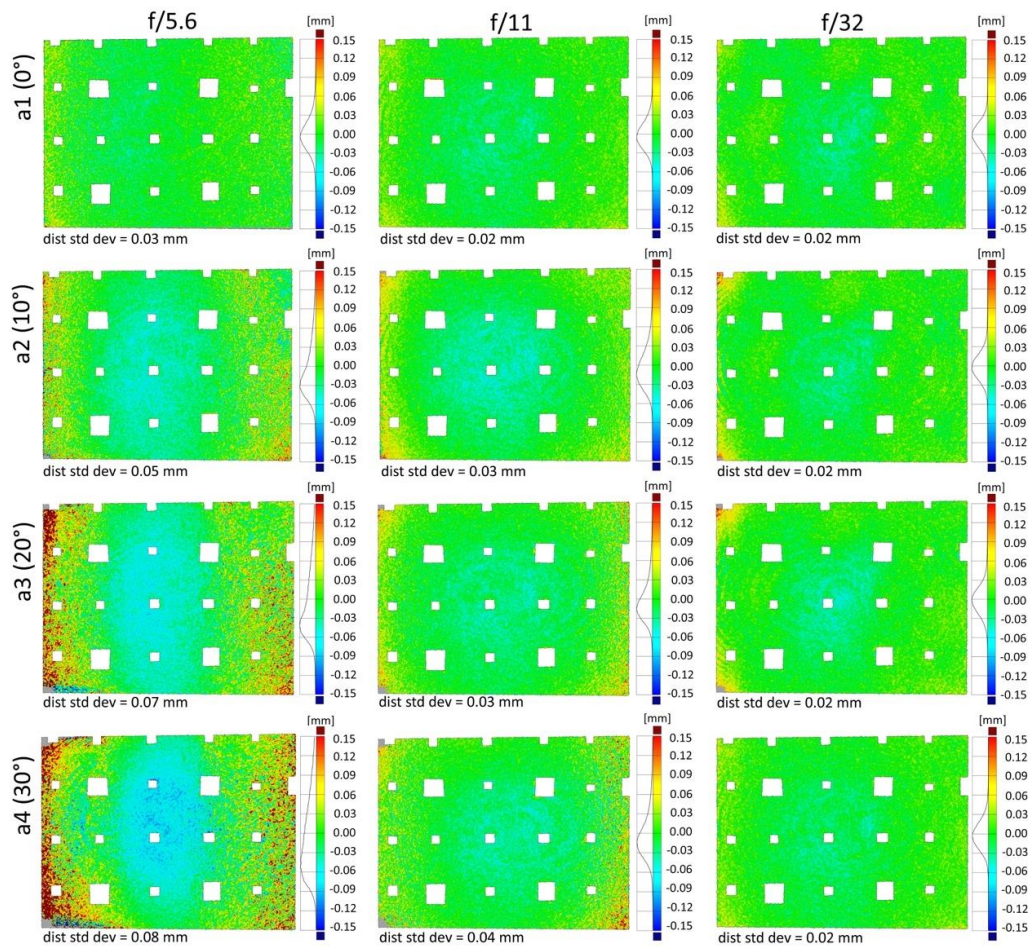
Figure 7-5. The 3D reconstruction results for 3D-DOF-Plane assessed using the Nikon dataset. The figure includes surface discrepancy maps comparing three apertures (f/5.6, f/11, f/32) and four angles (a1, a2, a3, a4) of the 3D reconstructions to the averaged reference mesh.

The f/11 datasets balanced DOF and image quality the best, maintaining mostly a FADGI 3 star rating for the centre of the target. The effects of DOF were observed with the f/11 datasets as was projected with Figure 7-1 with the features falling outside of the DOF at a3 (20°). However, there is more possibility that high frequency features can be resolved using f/11 as compared to f/32 and the impact of diffraction.

The results of the DOF-3D-Plane experiment showed that the larger aperture diameter (represented by f/5.6) should be avoided due to the overall reduction of image quality and the impact of the small DOF on 3D reconstructions. An optimal aperture (e.g., f/11) showed a balance of DOF and image quality. The smaller aperture diameter (represented by f/32) showed the lowest discrepancies when compared with the reference mesh providing evidence that the 3D reconstruction process tolerated the reduced image quality from diffraction. Even though the diffraction is tolerated by the process, high spatial frequency features may not be resolved because of the effect of diffraction on the 2D image quality.

Table 7-3. PhotoScan processing results for DOF-3D-Plane

f/5.6

	a1 (0°)	a2 (10°)	a3 (20°)	a4 (30°)
tie points	23,150	22,417	19,402	18,456
projections	84,099	81,918	70,147	67,742
RMS reprojection error (pix)	0.103	0.114	0.152	0.189

f/11

	a1 (0°)	a2 (10°)	a3 (20°)	a4 (30°)
tie points	25,813	26,150	25,357	25,975
projections	109,064	107,049	99,499	102,627
RMS reprojection error (pix)	0.172	0.0825	0.103	0.139

f/32

	a1 (0°)	a2 (10°)	a3 (20°)	a4 (30°)
tie points	24,452	24,230	19,243	27,054
projections	104,879	101,440	72,460	105,581
RMS reprojection error (pix)	0.0714	0.0761	0.11	0.0936

These results were not necessarily new information as much is known about aperture diameter, DOF, and diffraction, yet the experiment provided specific evidence for these assumptions and also provided a method for linking 2D image quality with 3D reconstruction.

7.1.1.2. *Focus test*

A major component of this research involved 2D image quality assessment, specifically SFR and sampling efficiency, which is directly influenced by sharpness and the focus of the camera. The 60 mm lens requires manual focus making it important to understand the repeatability of the manual focus. Section 6.1.2 included a focus test that assessed manual focus comparing the 60 mm lens and the 50 mm compact macro lens using the modified camera for effect of wavelength on 2D image quality. The results showed a large variation in the focus, a standard deviation of 11% for ten images acquired using the 60 mm lens and the modified camera. This data informed an updated setup for the wavelength and 2D image quality test. Instead of filtering the camera which required refocusing the camera and touching the lens as the filters were taken on and off, the illumination was filtered.

A second focus test conducted for the DOF experiments assessed the 60 mm lens on the unmodified camera by looking at image-based 3D reconstruction and using the camera

positioning robot (Figure 7-6). Ten images were acquired with each image being defocused and refocused between each acquisition (Image Set 1). A second set of ten images were also acquired without any changes in focus to see if there was any internal variation that may be a factor (Image Set 2). This focus test resulted in a mean sampling efficiency of 81% and a standard deviation of 2% for the ten images acquired refocusing the 60 mm lens. The ten images without the focus changed resulted in a mean sampling efficiency of 81% and a standard deviation of less than 1%. It was concluded that internal factors were not impacting the results of the focus test.
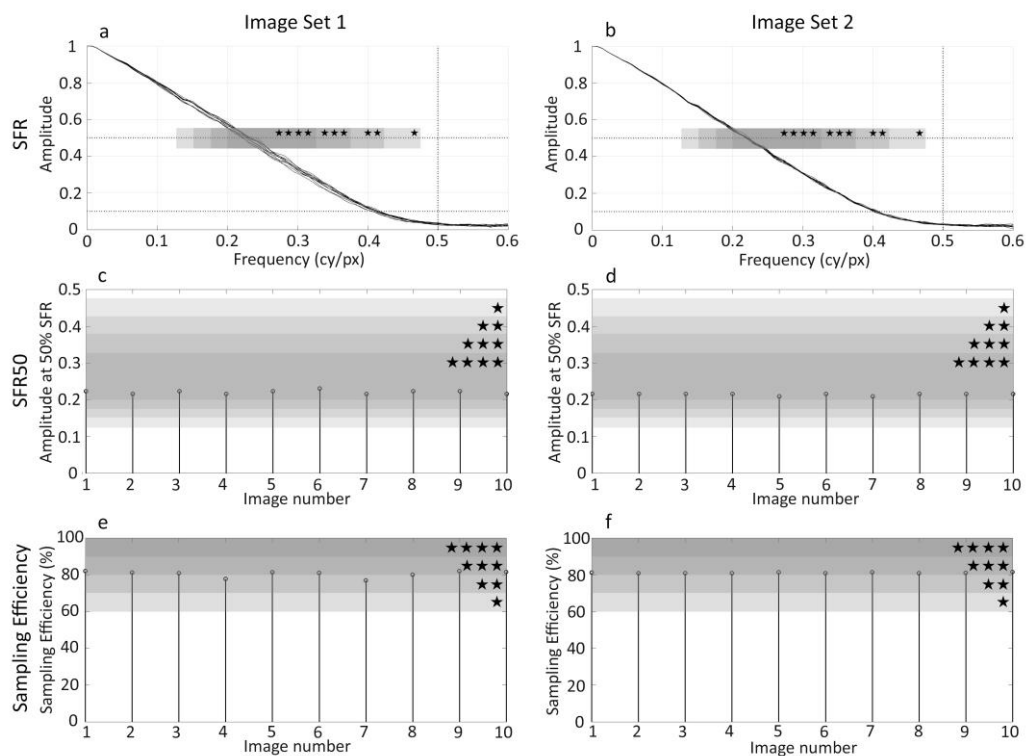
Figure 7-6. Focus test results and SFR analysis of a set of 10 images defocused and refocused (Image Set 1, left column) and a set of 10 images without any changes between images (Image Set 2, right column). (a, b) Horizontal SFR curves measured from the slanted edge features at the middle of the DICE target imaged at different camera-object distances. The 10% and 50% SFR ranges are marked by dotted horizontal lines and the Nyquist frequency is marked by a vertical black line at 0.5 cycles per pixel. (c, d) The SFR50 frequency values have been extracted from the horizontal SFR curves for each of the camera-object distances. (e, f) The sampling efficiency was calculated for each of the camera-object distances. The SFR, SFR50 and sampling efficiency plots include indications of the FADGI star rating ranges relating to those parameters using grey gradients and corresponding number of stars.

The two focus tests provided very different results, which could be explained by the variation in setup between the two tests. The first test was set up using the copy stand with the camera pointing down. With the effect of gravity there could be some drift in the lens, which might explain the change observed between the start and finish of the acquisition with the filtered illumination. The second test was set up using the camera positioning robot and a vertical setup, which would not have any drift contributing to a change in focus during acquisition. In addition to different orientations of the camera, the tests were conducted with

different cameras. The first focus test was using the modified camera and involved mounting and unmounting filters, while the second test used the unmodified camera without filters. With the modified camera the sampling efficiency was over 100%, so the range being assessed is not the same for both tests.

Due to the manual focus of the 60 mm lens, it was important to understand how much variation may be introduced into the experiment from manually focusing. For the wavelength and 2D image quality experiment, this variation was eliminated by running a version of the test where the illumination was filtered instead of the camera. For the image-based 3D reconstruction, the focus test indicated that the variation was minimal (below 2%) and would not introduce a significant error.

7.1.2. DOF-Sharpness-SFR

The DOF-Sharpness-SFR test quantitatively related DOF and camera-object distance to sharpness, SFR, and the resulting 3D reconstruction. The camera-object distance was incrementally changed by 5 mm moving through and beyond the range of acceptable sharpness, or DOF, to assess sharpness and resulting 3D reconstructions. Both the DICE target and Panel test target were recorded with these different camera-object distances.

The camera positioning robot (Section 4.1.1.1) was used to reproducibly change the camera-object distance by 5 mm increments and to record the convergent image configurations required for 3D reconstruction. The initial acquisition included three aperture settings to record the DICE target (f/5.6, f/11, f/32); however, the f/32 showed a very consistent but low image quality in comparison to f/5.6 and f/11 and the extended range for the DOF (197.04 mm for $C = 0.03$ mm) would be difficult if not impossible to fully assess with the configuration of the camera positioning robot (Table 7-4). Only two aperture settings (f/5.6, f/11) were used for the second acquisition of the DICE target and 3D reconstructions of the Panel test target. The initial acquisition of this test included a range from -30 mm to +70 mm and only included images of the DICE target using three apertures. The camera positioning robot had an initial setup that allowed for the additional distance behind the focus position. However, the setup was rotated on the optical table allowing for the use of the larger illumination setup with studio strobes, but also limiting the distance behind the focus position. The final acquisition for this test included a range of -15 mm to +50 mm with images of the DICE target for assessing the image quality and image sets of the Panel for 3D reconstruction using two apertures.

Table 7-4. *DOF calculations based on standard C values*

		$C = 0.0216$ mm	$C = 0.03$ mm
f/5.6	Near limit (mm)	588.14	583.66
	Far limit (mm)	612.34	617.28
	DOF (mm)	24.19	33.63
f/11	Near limit (mm)	577.15	568.72
	Far limit (mm)	624.74	634.92
	DOF (mm)	47.59	66.20
f/32	Near limit (mm)	538.02	517.24
	Far limit (mm)	678.12	714.29
	DOF (mm)	140.10	197.04

The camera was focused at the same position for each aperture using Live View at 200% magnification, viewing the central feature of the DICE target or the pattern at the centre of the Panel test target. Once the focus was set at the 'focus position' for one aperture, it was not changed for the full acquisition of that image set. The camera was then positioned at -15 mm from the focus position and images were acquired at 5 mm increments until the position reached +50 mm from the focus position (Figure 7-7). The DICE target was imaged from the middle position of the convergent image configuration at each camera-object distance, and the Panel was imaged using the convergent image configuration to acquire seven images from three positions at three heights (Section 4.1.2).
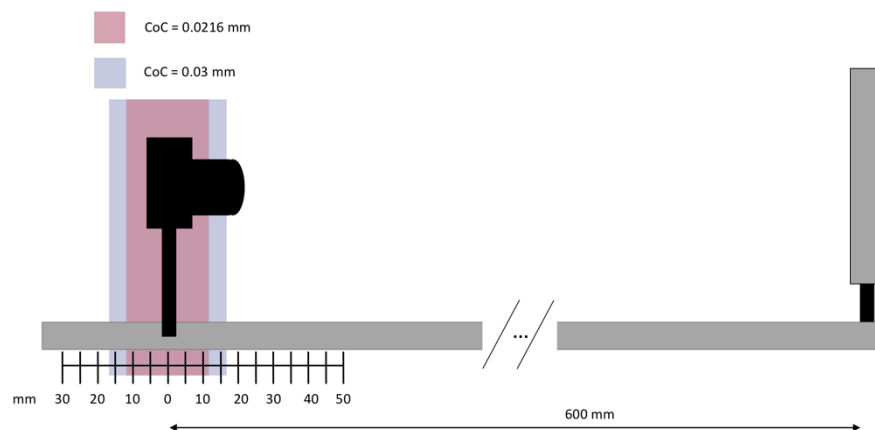
Figure 7-7. *Illustration of DOF-Sharp-SFR setup. The DOF for f/5.6 is shown with a pink area (calculated from C = 0.0216 mm) and blue area (calculated from C = 0.03 mm). The tick marks at the bottom indicate the 5 mm intervals for the different camera-object distances.*

Initial assessment focused on 2D image quality using SFR analysis. The SFR was calculated from the central feature of the DICE target averaging the two horizontal slanted edge features. With 14 images represented in a stationary SFR plot, it is difficult to differentiate or even label the camera-object positions represented by the curves (Figure 7-8a and b). When assessing the results using Matlab, dynamic plotting can be used which provides a better understanding of the SFR results relating to the camera position with each curve being plotted one at a time starting -15 mm beyond the focus position and moving to 50 mm in front of the focus position. As would be expected, the images that were acquired closer to the point of focus are represented by the curves that are furthest to the right in the plot and those images acquired further from the point of focus fall closer to the y-axis. The FADGI star rating based only on the SFR50 values indicates that only four curves for the f/5.6 images fall within the star rating range with the rest falling below the 1 star rating, while six of the f/11 images fall within the star rating range, four images within the 3-4 star range.

Plotting SFR50 values for each camera position is potentially an easier way to look at some of the information from the SFR curves and to achieve a better understanding of how it relates to the camera-object distance (Figure 7-8e and f). While the highest SFR50 frequency and sampling efficiency for the f/5.6 image sets is for the focus position, this is not the case for the f/11 image sets and it appears that the best focus was 10 mm behind the focus position. The 60 mm lens is a manual lens and it is likely that the focus was slightly behind the panel for this image set. Section 7.1.1.2 discussed challenges with manual focus and provided results on manual focus repeatability. The standard deviation of the focus test from 10 images was 2%. For the f/11 image set, the sampling efficiency at -10 mm is 84% which is 4% greater than the sampling efficiency 0 mm (81%). This is nearly within 2σ of the focus test and suggests that it falls within the error of manual focus.

The SFR50 plot for both f/5.6 and f/11 (Figure 7-8c and d) indicate that the image quality falls below FADGI 1 star rating before reaching the near or far limit of the DOF for either a diameter of circle of confusion of 0.0216 mm or 0.03 mm. The sampling efficiency plots (Figure 7-8e and f) provide similar results as the SFR50 for both f/5.6 and f/11. The sampling efficiency falls below FADGI 1 star rating before reaching the near or far limit of the DOF for both values of the circle of confusion. This suggests that a smaller diameter for the circle of confusion is necessary for achieving results within the FADGI star rating system.
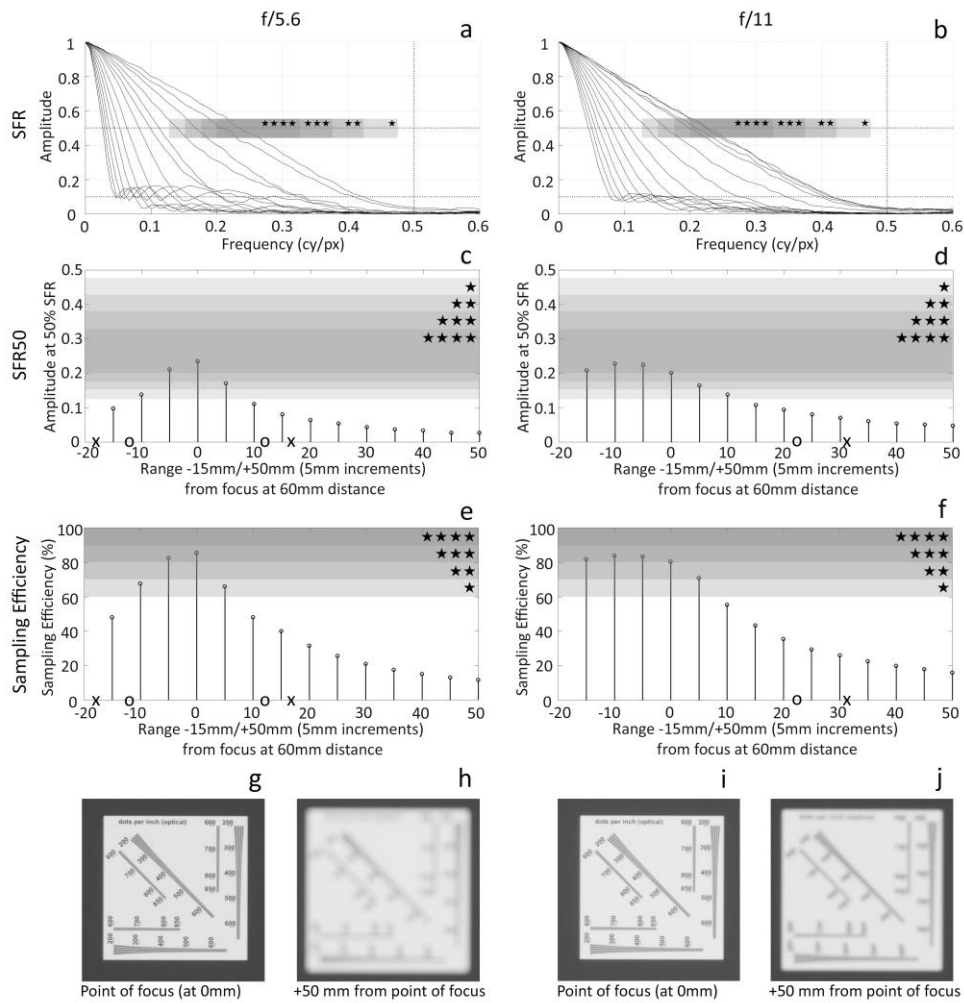
Figure 7-8. SFR analysis for DOF-Sharp-SFR test with FADGI star rating ranges. SFR analysis of f/5.6 (left column) and f/11(right column) image sets with plots for overall SFR curves (a and b), SFR50 values at each position (c and d), and sampling efficiency at each position (e and f), and image details of the central feature of the DICE target to provide a visualisation of the degradation of image quality moving to and from the point of focus (g-j). The grey gradients and stars indicate the quality ranges based on the FADGI star ratings for paintings and other two-dimension art (other than prints) (Rieger, 2016, p. 47). The DOF field is marked on the x-axis using "o" for a C = 0.0216 mm and "x" for C = 0.03 mm. (a, b) Horizontal SFR curves measured from the slanted edge features at the middle of the DICE target imaged at the different camera-object distances. The 10% and 50% SFR ranges are marked by dotted horizontal lines and the Nyquist frequency is marked by a vertical black line at 0.5 cycles per pixel. (c, d) The SFR50 frequency values have been extracted from the horizontal SFR curves for each of the camera-object distances. (e, f) The sampling efficiency was calculated for each of the camera-object distances. (g-j) The image details are from the point of focus (0 mm) (Figure 7-8g and i) and the smallest camera-object distance (50 mm from the point of focus) (Figure 7-8h and j) for both f/5.6 and f/11.

A visual example of the image data at different camera-object distances may be easier to interpret than the SFR and SFR50 plots. The central feature of the DICE target acquired at the point of focus (Figure 7-8g and i) provides a point of reference for the sharpness of the visual resolution wedges. When acquired from the more extreme position of 50 mm from the point of focus, the image quality is degraded to the point that the visual resolution wedges are not legible for either the f/5.6 and f/11 image sets (Figure 7-8h and j). The blur for the f/5.6 image is more significant than the f/11 due to the smaller DOF.

The FADGI star rating provides an indication of the acceptable level of sharpness for image content relating to cultural heritage documentation; however, this does not provide an indication of the quality of the 3D reconstruction at each of the camera-object distances. The resulting 3D reconstructions were assessed with comparisons to the averaged reference mesh. There are limitations with this data as "reference" data which is more fully discussed in Section 4.1.5. The f/5.6 results (Figure 7-9) overall showed an increase in noise as the camera-object distance moves further from the focus position. Beyond the DOF calculated from $C = 0.03$ mm (indicated by the white box and starting at 20 mm), more random noise is observed. The random noise is still within approximately +/- 0.05 mm.
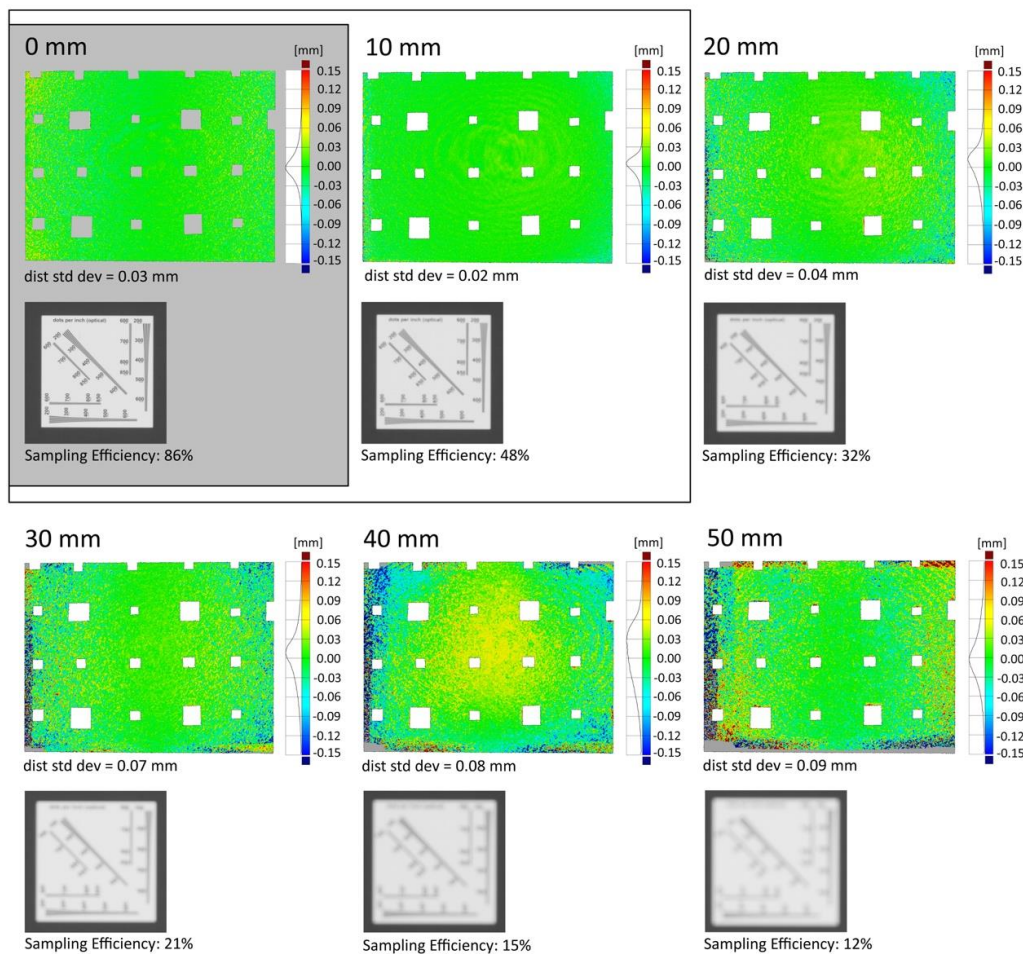
Figure 7-9. 3D reconstruction results for DOF-Sharp-SFR f/5.6 image sets. The 3D reconstructions are compared to the averaged reference mesh and image details of the central feature of the DICE target are included below the surface discrepancy maps. The grey box that encloses the focus position (0 mm) indicating the results within the FADGI star rating based on SFR and Sampling Efficiency results, and the white box encloses the positions that fall within the DOF field based on a C diameter of 0.03 mm.

The 3D reconstruction for the focus position, 0 mm, has larger errors than the 3D reconstruction from +10 mm from the focus position despite the SFR analysis indicating the point of focus having a higher sampling efficiency and SFR 50. This could be attributed to the manual focus of the lens. The lens has a different focus for the images of the DICE target

and the image sets of the Panel because the depth of the targets is different. Since the lens has to be manually focused, there is a chance that the focus is slightly in front of or behind the Panel meaning that 0 mm for the f/5.6 datasets may not be the exact focus position.

Even at the maximum distance (50 mm) with a low image quality (sampling efficiency of 11.5%), the Panel is still reconstructed within +/- 0.15 mm with the largest discrepancies along the edges of the model. The visual example of the central feature of the DICE target provides evidence of how bad the image quality is for the input images. Even though these images are able to be used to produce a 3D reconstruction of the panel, the images would not be useful as records of a heritage object surface and fall well below any FADGI star rating. The high contrast of the Panel proves to be resilient even when the image data is not sharp.

The f/11 results (Figure 7-10), similar to the f/5.6 results, overall show an increase in noise as the camera-object distance moves further from the focus position, but more gradually than the f/5.6 results due to the increased DOF. Similar to the f/5.6 results beyond the DOF calculated from $C = 0.03$ mm starting at 40 mm, more random noise is observed which is within +/- 0.05 mm.

The findings of this experiment can be compared to Verhoeven (2018), who focused on masking for DOF, but in presenting the background for his study discussed the foundations and assumptions associated with DOF and sharpness. Image-based 3D reconstruction assumes that the object is "acceptably" sharp in each image of the set, but Verhoeven pointed out that the fields of computer vision and photogrammetry have not quantified the range of acceptable sharpness for this application. He noted that it is more or less standard practice to mask areas that are "not sharp enough". While it is believed that if the object's surface falls within the DOF, and it is within the range of acceptable sharpness, then the object will be adequately reconstructed while areas beyond the DOF may only be partially reconstructed or not as accurate. Verhoeven stated that there are issues with this assumption because DOF is "a perceptual quantity without a direct relation to IBM" (IBM referencing 'image based modelling' which is referenced as image-based 3D reconstruction in this research) and that there is no agreed upon value for the circle of confusion when calculating the DOF for 3D reconstruction or how the value of the circle of confusion impacts the accuracy and precision of the 3D reconstruction (2018, p. 1152).
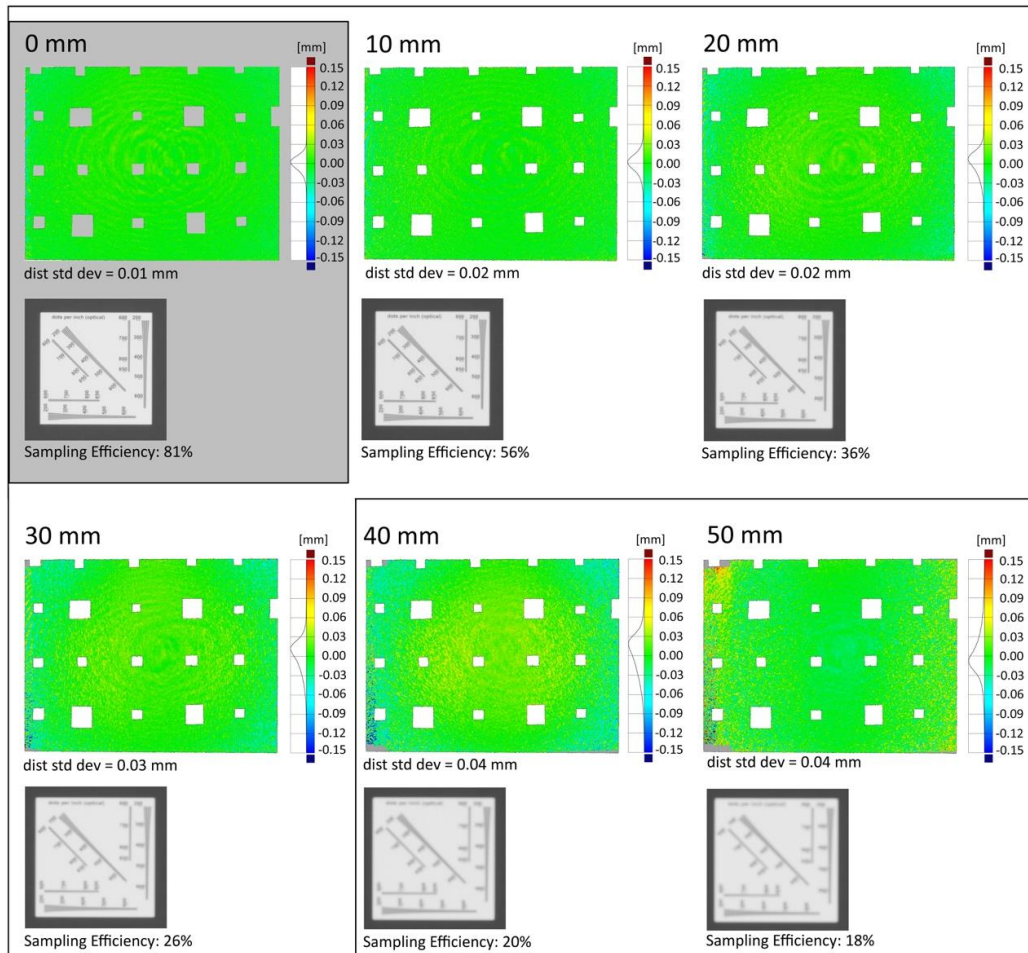
Figure 7-10. 3D reconstruction results for DOF-Sharp-SFR f/11 image sets. The 3D reconstructions are compared to the averaged reference mesh and image details of the central feature of the DICE target are included below the surface discrepancy maps. The grey box that encloses the focus position (0 mm) indicating the results within the FADGI star rating based on SFR and Sampling Efficiency results, and the white box encloses the positions that fall within the DOF field based on a C diameter of 0.03 mm.

If the 2D input images were to fall into the FADGI star rating for both f/5.6 and f/11 with the same parameters as the DOF-Sharp-SFR test (u = 600 mm, f = 60 mm), the diameter of the circle of confusion would need to be around 0.01 mm which would result in a DOF of 11.20 mm for f/5.6 and 22.01 mm for f/11. This small diameter of the circle of confusion, one-third of the standard 0.03 mm and under the size of 2 pixels for the Canon 5D Mark II, would only prove beneficial for 2D image quality and following some of the measurement parameters for the FADGI star rating.

Focusing on the 3D reconstruction results of the Panel for the DOF-Sharp-SFR test (Figure 7-9 and Figure 7-10) provides more flexibility for an increased diameter for the circle of confusion and DOF. Within the parameters of this test, the 3D reconstruction never fails to reconstruct the panel. At all distances for both f/5.6 and f/11, the image orientation and dense matching are successful and resulting models have less than +/-0.15 mm deviation from the reference mesh.

If the DOF is calculated using the standard $C = 0.03$ mm, the near limit for f/5.6 is 583.66 mm, or about 12 mm from the point of focus, and for f/11 is 568.77 mm, or about 31 mm from the point of focus (Table 7-4). When setting the parameters for the test, it was at first assumed that going to 50 mm would be far enough beyond the DOF to see a significant impact on the resulting 3D reconstruction. If the test had resulted in a distance where the reconstructions were no longer successful or there was a noticeable impact to the results, then this distance could be selected to calculate the largest circle of confusion possible to reconstruct this particular object. If the maximum distance for the test (50 mm) was used as the extreme near limit (not knowing how much further the camera-object distance could be reduced before significantly influencing the 3D reconstruction), the circle of confusion could be calculated using the near limit equation 2.3 to derive the equation for C :

$$C = \frac{f^2(u - R)}{RNu}$$

(7.1)

The diameter of the circle of confusion would be about 0.1 mm for f/5.6 and about 0.05 mm for f/11 or about 15 pixels for f/5.6 and just under 8 pixels for f/11 for the Canon 5D Mark II.

An important consideration with image-based 3D reconstruction is the reuse of the images, which would require the image to be "acceptably sharp" for other applications and not just 3D reconstruction. Figure 7-9 and Figure 7-10 show details of the central feature of the DICE target at each of the distances at 10 mm increments for f/5.6 and f/11. As would be expected, the features are sharp at 0 mm and illegible at 50 mm.

This discussion provides extreme options for the diameter of the circle of confusion: one that takes into consideration the required image quality for the FADGI star rating providing a very small circle of confusion and narrow DOF and the other takes into consideration the 3D reconstruction results with a larger circle of confusion and an extended DOF. These circle of confusion values calculated based on the 3D reconstruction of the Panel are biased by the high local contrast of the pseudo-random pattern optimised for image matching. The panel proved to be quite resilient for 3D reconstructions with image data degraded from unsharpness or decreased contrast. As previously discussed, this pattern was matched with the method and can provide results in less than ideal circumstances. The resilience of the Panel will likely not correspond with most actual heritage objects. Many heritage objects

would likely have surfaces with lower local contrast, lower spatial frequency and may not be as resilient when it comes to image-based 3D reconstruction and unsharp image data that may be acquired outside of the DOF.

7.2. Mango Vase

The Mango Vase test object was used to investigate the parameters and provide evidence for the limitations of DOF with considerations of the direct applicability to museum objects. Chapter 4 presented a similar transition from the Panel test target to the Mango Vase. The Panel was used to investigate the parameters and provide evidence for the limitations of DOF, specifically angle and distance. Using the camera positioning robot to document the Panel, the parameters influencing DOF (specifically angle and distance) could be isolated and investigated. However, the panel is not representative of cultural heritage collections. The Panel is an engineering test object that has been optimised for image matching that can provide insight for imaging science, while the Mango Vase is a reference object to better relate the research to heritage objects providing insight for practical applications in museum imaging.

7.2.1. DOF-3D-MangoVase

A turntable setup was used to acquire image sets with five apertures (f/5.6, f/8, f/11, f/16 and f/32). More than 100 images were acquired of the object in the round with three views. As discussed in Section 4.2.1.2 the turntable setup contrasted the seven-image convergent networks used to record the Panel, but it is more representative of the recording of small to medium sized museum objects. The turntable acquisition did not allow for the controlled investigation of angle and distance related to DOF that is presented in Section 7.1. The first view for each of the apertures was acquired before raising the height of the camera for the second view, and this was repeated for the second and third view. A total of 111 images were acquired for each of the image sets for the five apertures.

The DOF-3D-MangoVase datasets were acquired at the same time as the 3D reconstruction camera characterisation datasets (Section 5.4.2). By maintaining a consistent setup and camera network, the 3D quality assessment for the unmodified and modified cameras could be linked with the DOF and 3D reconstruction tests. Initially only the extreme apertures were considered for the DOF tests (f/5.6 and f/32) providing the smallest and largest DOF. The more useful comparison after illustrating the extremes was to look at f/8, f/11, and f/16. Images of the DICE target were acquired with each image set to link the 3D reconstruction results with the image quality assessment.

The unmodified Canon camera and the 60 mm lens (Figure 4-1) were used to acquire images of the Mango Vase test object illuminated by two Bowens Gemini GM400Rx studio strobes with umbrellas. The ISO and shutter speed were consistent for each image set, and to maintain consistent illumination on the sensor surface as the aperture diameter decreased and the amount of light was reduced, the flash power needed to be adjusted (Table 4-4). The flashes were positioned about 130 cm from the object centre, 97 cm from the camera, and 125 cm from the floor. (The imaging setup was the same as described in Section 4.2.1 and Figure 4-16)

The acquisition, processing, and assessment for this experimental work has been informed by the methods of optimisation and assessment presented in Section 4.2. This includes considerations for improving alignment and components increasing uncertainty (Section 4.2.2), limited parameter selection for the camera model to avoid over-parameterisation (Section 4.2.3), and considerations with the challenges with reference data and assessing 3D reconstructions (Section 4.2.4).

RAW images were acquired and processed using a standard RAW processing workflow with Adobe ACR (Section 5.1). This test was run with the unmodified camera and standard RGB images, so the RAW processing workflow presented for the modified camera images was not necessary. The image sets were batched processed for a greyscale conversion using an Adobe Photoshop Action script. The GoldenThread software was used for the analysis of the DICE target images. The image-based 3D reconstruction processing used PhotoScan and followed the CHI *error minimisation workflow* described in Section 4.1.1.2. For the camera model, including a single radial distortion parameter showed the best results for the Mango Vase (Section 4.2.3). The resulting 3D reconstructions were assessed by comparing each with 3D scanned data of the test object that was acquired at AICON3D using GOM Inspect despite limitations with this data (Section 4.2.1). The limitations of this 3D scanned data and more complete discussion about the challenges and limitations of the reference data for the Mango Vase and cultural heritage objects is included in Section 4.3.

7.2.1.1.   *Results and discussion*

The results for the DOF investigation using the Mango Vase included the assessment of the 2D image quality and the 3D reconstructions. The 2D image quality analysis focused on the assessment and comparison of the SFR curves, SFR50, and sampling efficiency (Figure 7-11). Based on these metrics the imaging system performed best around f/11 with f/8 and f/16 showed comparable performance. The apertures of f/8, f/11, and f/16 showed the highest performance based on the SFR curves, SFR50 and sampling efficiency mostly

within the FADGI 3 and 4 star ratings. This aligned with what would be expected with the optimal aperture being a few stops closed down from the largest aperture (f/4 for the 60 mm lens). This also aligned (at least with the general FADGI star ratings) for the DOF-3D-Plane (Section 7.1.1) and DOF-Sharp results (Section 7.1.2). The f/16 results did not show the effect of diffraction, but the f/32 definitely did, falling to a FADGI 1-star rating and below.

While the Mango Vase test object was easy to position with the turntable setup (the object sits upright on its own), the DICE target was difficult to position and required a support to keep it planar with the camera sensor. The DICE target may not have been perfectly planar with the turntable setup, which is why the centre feature was the area used for the image quality assessment and linking with the 3D reconstruction results. The DICE target was imaged at view 1 for all of the apertures when the camera sensor would have been parallel to the target surface. The image quality assessment for these tests did not investigate different angles as the DOF-3D-Plane test did (Section 7.1.1).
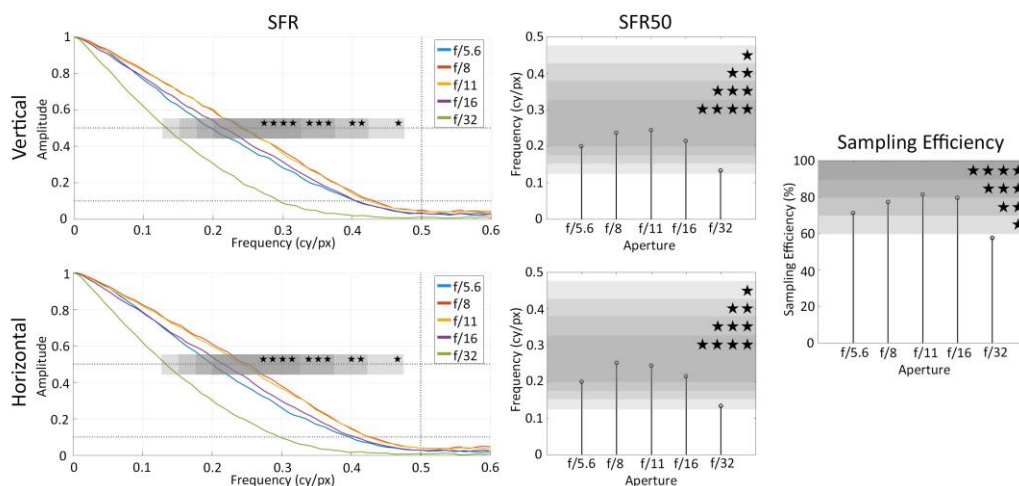
Figure 7-11. SFR analysis and sampling efficiency results for DOF-3D-MangVase image sets. The figure includes SFR curves (left column), SFR50 results (centre column), and sampling efficiency results (right figure) with associated FADGI star rating with the vertical results presented on the top row and the horizontal results on the bottom row. The plots include grey gradients and stars to indicate the quality ranges based on the FADGI star ratings for paintings and other two-dimension art (other than prints) (Rieger, 2016, p. 47). The SFR plots and SFR50 were calculated from the central feature of the DICE target. The modulation of contrast is plotted against the spatial frequency (cycles per pixel) for each aperture (left column). The plot indicates the limiting resolution at 10% SFR and the sharpness indicator at 50% SFR with horizontal lines, and the Nyquist frequency is denoted with a vertical line at 0.5 cycles per pixel.

Visualisations and plots from the 3D reconstruction process provide evidence of the impact of aperture and DOF on the image matching and tie point identification (Figure 7-12). This impact was most notable from the highest view (View 3) of the camera network where the increased camera-object angle revealed the effect of DOF. PhotoScan provides a view of the tie points overlaid onto the input images showing the results of the identification of the tie points. The blue points shown in the screenshots indicate used matches and correspond to

points of the sparse point cloud, while the white points are unused matches. The results for the identification of tie points for the DOF-3D-MangoVase image sets showed the increased number of tie points and larger coverage area on the object as the DOF increases. Table 7-5 provides the calculated DOF for the five apertures using a C = 0.03 mm. The height of the vase is 19 cm, so the largest DOF with an aperture of f/32 is 197.04 and would include the full height of the object. An aperture of f/5.6 provided the smallest DOF for this experiment, and the screenshot of the tie points for an f/5.6 image showed points clustered around the top and shoulder of the vase where the image data is in focus, but where the image fell out of focus outside of the DOF there are not many tie points (Figure 7-12). An aperture of f/32 provided the largest DOF for this experiment, and the screenshot of the tie points for an f/32 image showed points in the background and covering the full vase (Figure 7-12). The apertures in the middle showed an increase in tie points covering the body of the vase and points picked up in the background as the aperture diameter decreased and the DOF increased. These results were expected and provided evidence that the detection of tie points corresponds with our expectations of DOF and related sharpness of the image data.

Table 7-5. DOF calculations using standard circle of confusion diameter (C = 0.03 mm)

	f/5.6	f/8	f/11	f/16	f/32
Near limit (mm)	583.66	576.92	568.72	555.56	517.24
Far limit (mm)	617.28	625	634.92	652.17	714.29
DOF (mm)	33.63	48.08	66.20	96.62	197.04

In addition to viewing the results for the tie point identification, the histograms for the projections per image (Figure 7-12, middle row) and for the error for each image (Figure 7-12, bottom row) show additional evidence of the effect of aperture and DOF. The histogram of projections (Figure 7-12, middle row) illustrated how the increase in DOF increased the number of projections per image and this increased number in more images (the histogram is moving towards the right as the aperture diameter decreases and the DOF increases). The histogram of errors (bottom row) illustrated how the increase of DOF reduces the spread of error.

The resulting 3D models also show the impact of aperture and DOF (Figure 7-13). The two models with the smallest DOF (f/5.6 and f/8) include artefacts reconstructed around the rim of the vase, whereas these artefacts are not present in the models with the larger DOF (f/11, f/16, f/32). The larger DOF means that the rim and the interior of the rim are better resolved in the input images and the model results in a more reliable reconstruction of the feature.
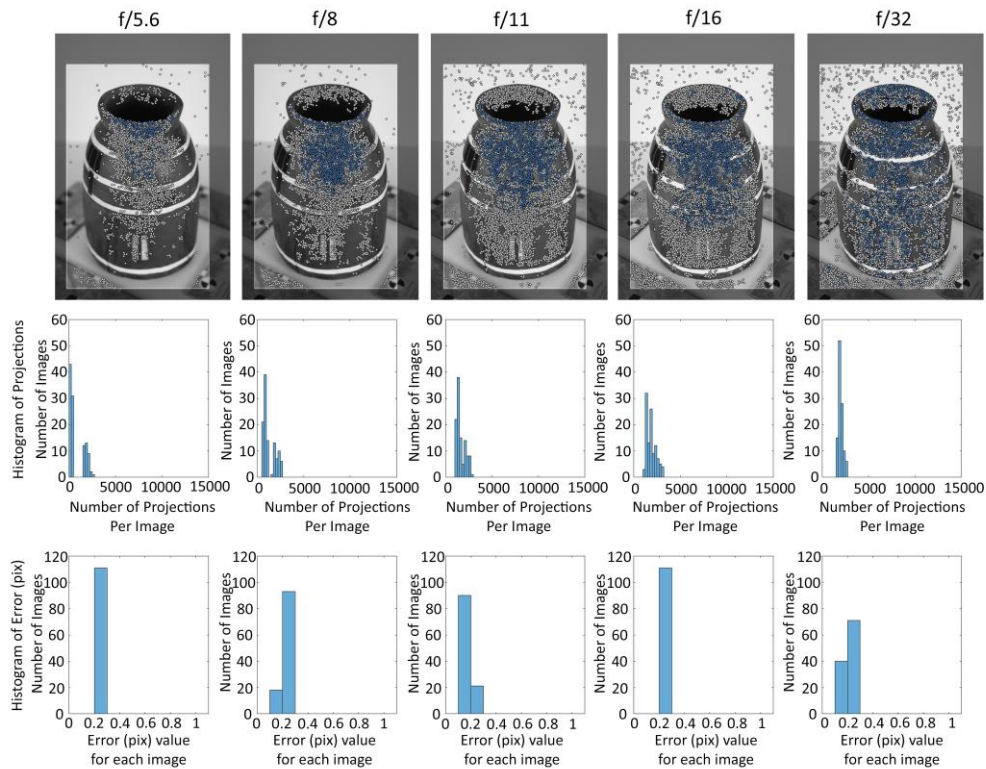
Figure 7-12. Visualisations and plots from the PhotoScan 3D reconstruction process to illustrate effect of aperture and DOF. These results are after optimisation using the error minimisation workflow. Top Row: Screenshots from PhotoScan of the matching points (i.e., tie points) from the highest view (view 3). The blue points are used matches and correspond to points of the sparse point cloud, while white points are unused matches. Middle Row: Histogram of projections with the number of images plotted against the number of projections per image. Bottom Row: Histogram of error (pix) with the number of images plotted against error (pix) value for each image.

Figure 7-13. Detailed views of resulting models from the DOF-3D-MangoVase test. The datasets acquired with the smallest DOF (f/5.6 and f/8) resulted in artefacts around the rim of the vase while the datasets acquired with a larger DOF were able to better record the rim and interior of the rim of the vase.

The resulting 3D reconstructions were compared to the AICON3D scan from 2016 despite the issues of this model as reference data (Figure 7-14). Due to the lack of true reference data and the limitations of the available comparative data (Section 4.2.4), the interpretations of the comparisons should be handled with care and caution. The comparison was conducted using GOM Inspect and the prealignment function, a global best-fit alignment and a subsequent local best-fit. The surface deviation was calculated and visualised through colour scaled discrepancy maps with a histogram indicating the distribution of the discrepancies. The results for f/8, f/11, f/16 were consistent. The f/16 data had a slightly increased standard deviation but the mean of the deviation is slightly closer to zero when compared with the f/8 and f/11 results.
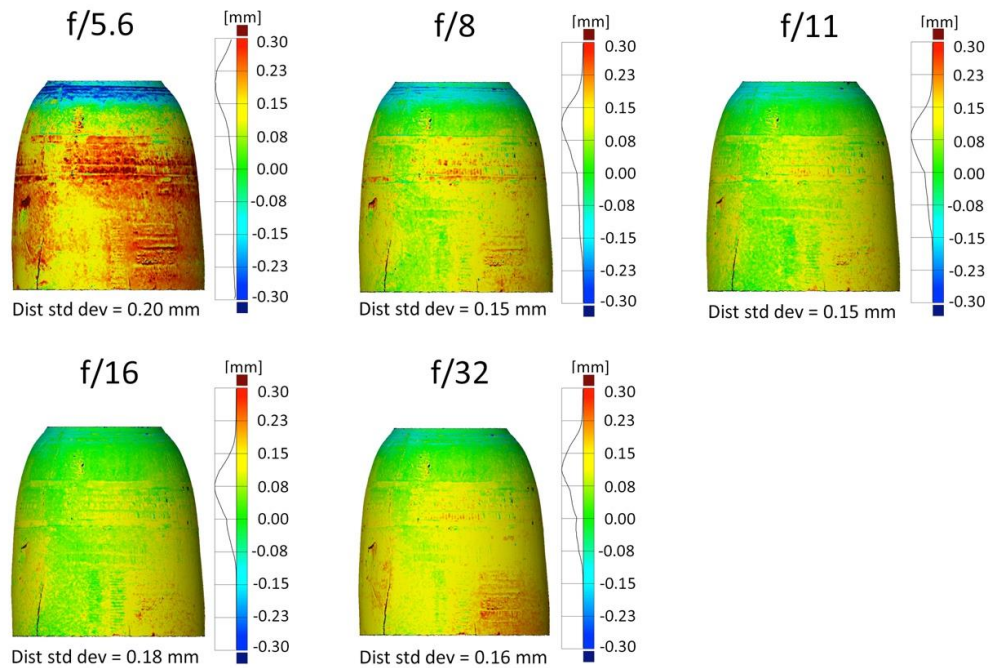
Figure 7-14. 3D reconstruction results for DOF-3D-MangoVase assessed using AICON3D 2016 scanned data.The figure includes surface discrepancy maps comparing 3D reconstructions from five apertures (f/5.6, f/8, f/11, f/16, f/32).

The impact from diffraction on image quality observed with the f/32 image set (Figure 7-11) did not seem to impact the resulting 3D reconstruction, specifically the global shape. The smaller DOF for the f/5.6 image set had a larger impact on the 3D reconstruction than diffraction for the f/32 image set. Even though the 2D image quality of the f/5.6 images (when the target was parallel to the image sensor) was higher than that of the f/32 images, the f/5.6 reconstruction was a lower quality than the f/32 image set.

Local surface comparisons were calculated for an area on the lower part of the vase and an area on the upper part of the vase (Figure 7-15). The models were aligned for the comparison using local best-fit with a tolerance of +/- 0.20 mm restricting the alignment to just the area of the surface comparison (i.e., two independent alignments for the two different comparisons). The local surface comparisons showed a difference between the models that is less than +/-0.10 mm with a standard deviation of 0.05 mm or less. The alignment also showed a better fit than the more global surface comparisons with a normal discrepancy distribution centred at zero (Figure 7-14). The slightly non-normal discrepancy distribution that was offset from zero in the more global surface comparisons (Figure 7-14) was resolved with the local comparisons suggesting that there may be a scaling issue. This could easily be attributed to the scaling of the model based off of scale bars positioned at the base of the object and manual target selection. This scaling issue could be resolved by using

coded targets, creating a framework with targets in full volume of the object space (Section 4.2.2.1), and using the "flat project" for CHI's updated workflow (Section 4.2.2.2).
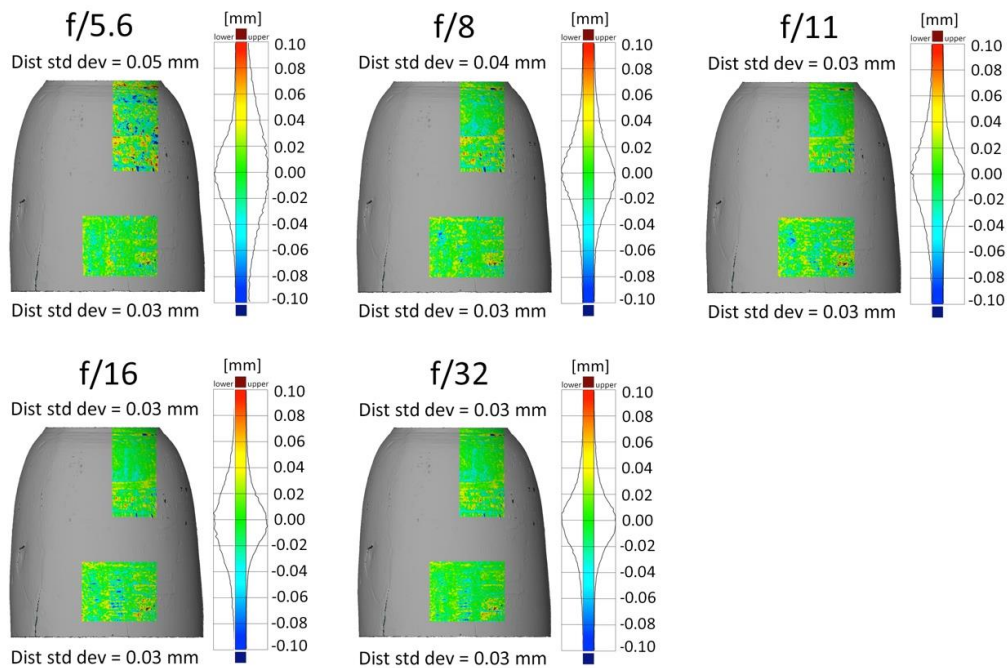
Figure 7-15. Local surface comparisons from 3D reconstruction results of DOF-3D-MangoVase tests assessed using AICON3D 2016 scanned data. Each 3D reconstruction includes two independent local surface comparisons with the histogram of the lower comparison discrepancies on the left of the colour range and the histogram of the upper comparison discrepancies on the right.

In addition to assessing the surface discrepancy maps, the PhotoScan processing results (Table 7-6) can provide insight into the 3D reconstruction quality. As the aperture size decreases and the DOF increases, the tie points and projections increase. There is not a clear trend with the error (both RMS reprojection and max reprojection), but the RMS reprojection error is below about 0.2 pix for all the datasets.

Table 7-6. PhotoScan processing results for DOF-3D-MangoVase

	f/5.6	f/8	f/11	f/16	f/32
camera-object dist (cm)	47.7	48.1	48.1	48.3	48.9
ground resolution (mm/pix)	0.046	0.0459	0.0466	0.0471	0.0478
coverage area (cm^2)	237	236	235	236	237
tie points	33,601	54,430	61,193	59,937	57,359
projections	97,445	163,307	187,229	191,567	200,177
reprojection error (pix)	0.236	0.238	0.216	0.214	0.225

The results of the DOF-3D-Mango experiment aligned with the results from the DOF-3D-Plane and showed that the larger aperture diameter (represented by f/5.6) should be avoided due to the overall reduced image quality and the impact of the small DOF on the resulting 3D reconstruction. An optimal aperture (represented by f/11) had a balance of DOF and image quality with the effects of DOF still be observed at the greater camera-object angles. The smaller aperture diameter (represented by f/32) showed similar performance to f/8, f/11 and f/16, but the SFR analysis showed a significant decrease in image quality from diffraction providing evidence that the 3D reconstruction process tolerates the reduced image quality from diffraction. Even though the diffraction is tolerated by the process, high spatial frequency features may not be resolved because of the effect of diffraction on the 2D image quality.

7.3. DOF-Sharpness-Masking

Image pre-processing can optimise image microcontrast and increase the processing performance for 3D reconstruction with most efforts focused on masking out irrelevant background image content (Section 2.5.3). Similarly, image pre-processing based on sharpness masking might be expected to improve image-based 3D reconstruction. Methods of masking input images for 3D reconstruction based on areas of sharp focus and DOF were investigated to optimise the processing in the SfM-MVS workflow. Two methods of masking were tested: a method to create masks from image content and a method to create masks from depth maps.

The aim of the masking as part of image pre-processing was to improve the image-based 3D reconstruction focusing on decreasing the processing time. As discussed in Section 2.5, image pre-processing methods have been implemented into the image-based 3D reconstruction workflows to optimise images and increase the processing performance (Section 2.5.3). These included methods to mask the background or non-essential features with studies reporting on the improvement of the alignment quality (Abate et al., 2016) and the decrease in the reconstruction processing time (Gallo et al., 2012; Koutsoudis et al., 2013; Troisi et al., 2015) with Gallo et al. (2014) reporting that the use of background masks could reduce the computational time by up to 75%.

Despite studies showing improvements from image pre-processing and background masking, these initial investigations into two masking approaches added steps and additional software to the 3D reconstruction process and did not necessarily reduce the processing time. With a sharpness-based masking method that reduces the image area input into the 3D reconstruction processing, the question arises if and how much the masking impacts the

camera calibration. This could be more problematic for an object like the Panel test target that fills the field of view. Future research should look into the impact of the masking on the estimation of the camera model.

With initial testing the masking methods consistently increased the tie points and projections for two test objects and the two museum objects, which was unexpected with less image information being available for the processing. The input data for the masking methods is known to be good quality (i.e. sharp), but the unmasked method also has this good quality data in addition to the unsharp information that has not been masked out. The increased resulting tie points and projections could be an indication of an improvement from the masking methods; however, it is possible that PhotoScan has an inbuilt process that is filtering the data in a similar way. PhotoScan, as a black box software, has unknown underlying processes, so future work could investigate these results to better understand the impact of the masking methods.

The masking approaches and initial tests were not showing improvements to justify the investment of time to follow these masking approaches. Masking has proven beneficial for the 3D reconstruction process as evidenced by the internal masking tools in PhotoScan and the pre-processing workflows to mask out the background or non-essential features cited in Section 2.5.3. Masking has been used to improve the quality of the alignment and decrease the reconstruction processing time, so by streamlining methods masking from sharpness would be beneficial. There is still potential for sharpness-based masking to improve the image-based 3D reconstruction, but the methods tested would need to be further tested and streamlined. Future research could include testing with image stacking to improve the reliability of the camera calibration with the stacking workflow (Section 2.5.2), investigating focus measure operators from Shape From Focus (SFF) as a means for masking based on sharpness (Section 2.5.3), and even testing the Matlab toolbox presented by Verhoeven (2018) despite stated challenges and limitations (Section 2.5.3).

7.4. Chapter summary

This chapter investigated the influence of DOF on 3D reconstructions as part of addressing the research question "How can the limitations of optical depth of field be mitigated using consumer imaging systems for the 3D reconstruction of small to medium sized museum objects?" The first part of answering this question is being able to define DOF as it relates to 3D reconstruction. The Panel test target (Section 7.1) and Mango Vase (Section 7.2) were used to better understand the parameters (aperture, angle, and distance) and provide evidence of the limitations of DOF relating to 3D reconstruction. The chapter presented the

novel use of the DICE target to link 2D image quality to the 3D reconstruction results to quantify and connect the 2D DOF calculations with the range of acceptable sharpness for 3D and resulting 3D reconstruction quality. While DOF is well understood in the context of 2D imaging and it is considered with the acquisition of image-based 3D reconstruction, this chapter worked to define "acceptable" sharpness for image-based 3D reconstruction.

This chapter aimed to answer the research question first by better defining DOF and acceptable sharpness for 3D reconstruction and then by initial tests implementing sharpness-based masking for improved 3D reconstruction as a method for mitigating the limitations of DOF. While masking was expected to improve what an imaging system could achieve, the 3D reconstruction process proved to be more robust than expected in relation to DOF and unsharp images. The Panel and Mango Vase have less of an issue with DOF, so further work is needed for smaller objects and macro photography. As the magnification increases, DOF becomes a bigger issue with a larger impact on the resulting quality.

The Panel was used to investigate some of the parameters that influence DOF (aperture, angle, and distance) in two tests: DOF-3D-Plane (Section 7.1.1) and DOF-Sharp-SFR (Section 7.1.2). The camera positioning robot was used to reproducibly change the camera position and record the camera networks required for the 3D reconstruction of the Panel in addition to isolating and investigating the DOF parameters. The DOF-3D-Plane test investigated the impact of aperture and angle on DOF with incremental changes in the camera-object angle, while the DOF-Sharp-SFR test investigated the impact of aperture and distance on DOF with incremental changes in the camera-object distance. Images of the DICE target were acquired with each image set to link the 3D reconstruction results with the 2D image quality assessment.

The Mango Vase test object was used to investigate the parameters and provide evidence for the limitations of DOF with considerations of the direct applicability to museum objects. While the tests with the Panel and the camera positioning robot were able to isolate aperture, angle, and distance, the DOF-3D-MangoVase implemented a turntable workflow that mirrors the recording of museum objects. The turntable workflow, recording in the round with three views, combines the effect of many angles and distances. The Mango Vase was recorded using five aperture diameters. Initially only the extreme apertures were considered for the DOF tests (f/5.6 and f/32) providing the smallest and largest DOF. The more useful comparison after illustrating the extremes was to look at f/8, f/11, and f/16. Images of the DICE target were acquired with each image set to link the 3D reconstruction results with the image quality assessment.

The results from Section 7.1 and 7.2 can provide a foundation for continued investigation of DOF and 3D reconstruction and feed into future studies of sharpness-based masking, and they informed initial investigations into sharpness-based masking (Section 7.3). Masking as part of image pre-processing aimed to improve the image-based 3D reconstruction focusing on decreasing the processing time; however, the initial tests did not show improvements to justify the investment of time with the two masking approaches tested. Masking has been used to improve the quality of the alignment and decrease the reconstruction processing time, so there is still a potential for sharpness-based masking to improve image-based 3D reconstruction but additional research is required. Future research could include testing with image stacking to improve the reliability of the camera calibration with the stacking workflow (Section 2.5.2), investigating focus measure operators from Shape From Focus (SFF) as a means for masking based on sharpness (Section 2.5.2), and even testing the Matlab toolbox presented by Verhoeven (2018) despite stated challenges and limitations (Section 2.5.3).

Findings and recommendations:

The results of the DOF-3D-Plane and DOF-3D-MangoVase tests showed that the larger aperture diameter (represented by f/5.6) should be avoided due to the overall reduced image quality and the impact of the small DOF on the resulting 3D reconstruction. An optimal aperture (represented by f/11) shows a balance of DOF and image quality with the effects of DOF still observed at the greater camera-object angles. (The performance for f/8, f/11, f/16 were similar.) The smaller aperture diameter (represented by f/32) showed low discrepancies when compared with the reference data and the 3D reconstructions seemed to tolerate the reduced image quality from diffraction. Even though the diffraction was tolerated by the process, high spatial frequency features may not be resolved because of the effect of diffraction on the 2D image quality.

The results of the DOF-Sharp-SFR tests provided evidence that the circle of confusion diameter, taking into consideration 3D reconstruction, would fall between the extremes of what would be required to achieve the FADGI star rating and what is needed for the 3D reconstruction of the Panel. If the 2D input images were to fall into the FADGI star rating, the diameter of the circle of confusion would need to be around 0.01 mm, which is one-third of the standard 0.03 mm and under the size of 2 pixels for the Canon 5D Mark II. This would only prove beneficial for 2D image quality and following some of the measurement parameters for the FADGI star rating. On the other extreme, if the test had resulted in a distance where the reconstructions were no longer successful or there was a noticeable impact to the results, then this distance could be selected to calculate the largest circle of

confusion possible to reconstruct this particular object. If the maximum distance for the test (50 mm) was used as the extreme near limit (not knowing how much further the camera-object distance could be reduced before significantly influencing the 3D reconstruction), the diameter of the circle of confusion would be about 0.1 mm for f/5.6 and about 0.05 mm for f/11 or about 15 pixels for f/5.6 and just under 8 pixels for f/11 for the Canon 5D Mark II.

These results indicated that the 3D reconstruction was less sensitive than initially thought due to expectations from visual observation. A limited DOF impacts the resulting image quality which can easily be observed visually; however, the 3D reconstruction can tolerate more blur than a 2D image acting as an object record. This increases the "acceptable" range of sharpness from 2D imaging to 3D imaging; however, the surface properties will still influence the results. The success of the 3D reconstruction of an object is dependent on the surface properties, and the Panel test target is more resilient (because of the high local contrast) than most heritage objects. Smaller objects are going to be more challenging than the size of objects looked at in this research. Aperture is an important consideration for the resulting quality of 3D reconstruction even if DOF was not as limiting for some of the objects presented in the thesis.

Focus is a critical component for assessing 2D image quality, specifically SFR analysis and sampling efficiency. Due to the manual focus of the 60 mm lens, it was important to understand the repeatability of the focus. The study has reported on two focus tests, one associated with the wavelength and image quality assessment (Section 6.1.2) and one as part of the DOF investigations (Section 7.1.1.2). The two focus tests provided very different results, which could be explained by the variation in the equipment and setup. The variation resulting from the wavelength and 2D image quality focus test was eliminated by changing the setup of the experiment to filter the illumination instead of the camera. For the image-based 3D reconstruction, the focus test indicated that the variation was minimal and it was not necessary to make changes in the setup or acquisition.

Contribution to knowledge:

This research contributed to the understanding and quantification of DOF and image-based 3D reconstruction by providing evidence of the influence and limitations of DOF and sharpness on the 3D reconstruction. DOF is well understood in the context of 2D imaging and it is considered with the acquisition of image-based 3D reconstruction, but DOF and the calculations for 2D imaging are not well connected with the required range of acceptable sharpness for 3D and resulting 3D reconstruction quality. A better understanding of the

parameters relating to 3D ensures optimal sharpness and DOF as input for 3D reconstruction.

An important part of the DOF investigation was linking established components of 2D DOF and image quality assessment with the 3D reconstruction results. By imaging and assessing the DICE target, the SFR analysis and sampling efficiency results could be connected with the assessment of the 3D reconstructions linking the 2D image quality to the 3D reconstruction results. Currently there are no established methods for accomplishing this. There are best practices, guidelines, and standards for 2D image quality assessment provided by collections photography (FADGI guidelines) and imaging science (ISO standards), and there are ways that the quality of 3D reconstructions can be assessed, although these are not yet standardised. The FADGI guidelines cover only the visible light range for 2D image quality assessment, and the ISO standards referenced for 2D image quality assessment also only cover 2D and not 3D documentation. Aspects of the FADGI guidelines, the DICE target, and analysis software were used to assess 2D image quality using different wavelengths within and beyond visible light and also to link 2D image quality with 3D reconstruction. This assessment focused on sharpness and resolution using SFR and sampling efficiency to evaluate and compare results. The FADGI star rating was used as a point of reference for the quality of the image sets to link 2D image quality with 3D reconstruction results.

8. Discussion

Cultural heritage objects can be recorded by a variety of 3D techniques, and accessible consumer imaging systems make it relatively easy to capture image sets that can be processed to produce 3D reconstructions. In turn, heritage objects are being recorded in 3D by an increasing number of heritage users who do not necessarily need to be skilled in the process. The availability, flexibility, and automation that make image-based 3D reconstruction an accessible process also increase the challenges of maintaining consistent, fit for purpose, 3D output. With the wider use is also the increased variability in the 3D output; however, conservation applications for image-based 3D reconstruction require scientific rigour to establish reliable and accurate models for monitoring and measuring change overtime. Widening access requires better investigative methods to improve image-based 3D reconstruction and thereby ensure consistent high-quality outputs. This research investigated the optimisation of image-based 3D reconstruction as accurate and reliable scientific records for conservation documentation. The output of the reconstruction is dependent on the quality and geometry of the input images, so this research focused on the local contrast, modified cameras and wavelength selection, sharpness, and focus to improve image-based 3D reconstruction.

This discussion chapter brings together the experimental chapters by reviewing how the research questions were addressed, critiquing the methodology used, and providing recommendations for heritage professionals. The research sits at the intersection of the three museum imaging categories (collections photography, conservation documentation, and scientific imaging), and this chapter will present the research in the context of the state of the art for each category to connect the research outcomes with the needs of heritage professionals seeking to either use or benefit from image-based 3D reconstruction.

8.1. Optimisation to improve image-based 3D reconstruction

The overarching research question of this thesis was "How can consumer imaging systems be optimised to improve image-based 3D reconstruction of small to medium sized museum objects?" This question can be approached many ways, but this research was focused on the optimisation of the input photographic quality to improve the 3D reconstruction. All of the experimental chapters addressed this first research question, which approached the improvement of image-based 3D reconstruction through three methods:

1. Establishing best practices and workflow for the research by testing and refining aspects of acquisition, processing, and assessment (Chapter 4),

2. Increasing local contrast and reducing specular reflectance using a modified camera and wavelength selection (Chapter 6) informed by the results from the characterisation of the modified camera (Chapter 5), and

3. Quantifying DOF for 3D reconstruction and using sharpness to mask input images as an image pre-processing method (Chapter 7).

The second and third methods are linked directly to the second and third research questions and will be discussed in Section 8.2 and 8.3.

The first method of establishing best practices and the workflow for this research through testing and refining aspects of acquisition, processing, and assessment (Chapter 4) built on available best practices (Section 2.3) and demonstrated methods that may be more widely applied outside of cultural heritage. Two purpose developed test objects were used to support quantitative assessment: the Panel test target and the Mango Vase. The specific improvements included the use of a convergent image configuration instead of a normal configuration, the identification and correction of systematic errors, and the assessment of resulting 3D reconstructions using different reference data and reviewing histograms of deviation distribution. Included in the discussion of Chapter 4, additional improvements could result from documenting the base of an object, using coded targets, and acquiring a "flat project". Some of these methods are related to issues that are well established in the field photogrammetry but are not necessarily addressed in the cultural heritage literature, so demonstration of these methods in Chapter 4 is beneficial to heritage professionals. The combined presentation of the processes and results provide useful tools and evidence for heritage professionals.

Reoccurring topics in this thesis related to reference data and the assessment of the 3D reconstruction, which are critical aspects of understanding the accuracy and reliability of the results. Three different attempts were made for reference data of the Panel (plane fitting, averaged mesh, and additional image-based 3D reconstruction), each with limitations (Section 4.1). The challenges with reference data were further discussed in the section on the Mango Vase with the comparison of two models from structure light scanning and intercomparisons of image-based 3D reconstructions. The discussion about the reference data further emphasises what is found in the literature (Section 2.4) about the challenges for establishing good reference data and the complications of establishing what should be compared and evaluated (Remondino et al., 2014).

Reference data and the iterative process of identifying and correcting for systematic errors, demonstrated in Chapter 4, allowed for the optimisation of the 3D reconstruction and

establishing the limitations of the imaging system. This process of identifying and correcting systematic errors to get at the random errors and establish the level of detail that an imaging system can resolve is an important demonstration for image-based 3D reconstruction of cultural heritage objects. While this may be a standard process for an engineer or a traditional photogrammetrist when working with 3D recording, this is not a process that is established in cultural heritage.

Comparing the image-based 3D reconstructions of the Mango Vase over the span of this research allowed for the critical analysis of the research progression indicating improvement to the 3D reconstruction process and increased confidence (Section 4.2.5). Intercomparing data allows insight to be gained about the techniques and technologies and also forces reflection on the advantages, limitations, and true capabilities to record and monitor cultural heritage objects. While the optimisation presented in Chapter 4 did not significantly change the resulting models of the Mango Vase, the updated process did increase the confidence in what can be achieved for more consistent results.

A comparison of the assessment of 3D reconstruction during the project with examples of early outputs in Figure 4-35 from Webb (2017) and in Figure 4-36 from Webb et al. (2018) provided evidence of how the assessment and visualisation of 3D reconstructions has improved over the research progression (Section 4.2.5.1). While these earlier assessments and presentations of 3D reconstructions reflected examples in cultural heritage literature, they overlooked key aspects that affect the quality and reliability of the data. The early assessments did not include reliable reference data, histograms illustrating the distribution of the discrepancies (to reveal systematic errors), or an assessment of the quality of the data and the spread of errors. This is further indication of the gap in accuracy assessment which ties directly to the analysis and presentation of 3D reconstructions of heritage objects. The way that 3D reconstructions are assessed and presented is not standardised, and while there may be components of this that are built into traditional photogrammetry and metrology, there is a gap between these fields and the cultural heritage applications and literature.

8.2. Modified cameras as scientific devices and wavelength selection

The second method of optimisation addressing the first research question included using a modified camera and selecting wavelengths to increase local contrast and reduce specular reflection (Chapter 6), which builds on the characterisation of a modified camera (Chapter 5). This method of optimisation directly links to the research question "Can photography with a modified consumer digital camera paired with selected illumination and filtration be

used as a scientific method to better benefit the 3D reconstruction of museum objects for conservation documentation?"

Imaging using a modified camera and selected wavelengths and the imaging study of a museum object, the coyote and turtle sculpture, showed improved consistency of the 3D reconstruction (Section 6.2). Even though there were limitations with the reference data to assess improved geometry of one technique over another, the increased local contrast and decreased specularity in the reflected IR images reduced the variation in the resulting model even with differences in the image configuration and acquisition. The imaging study was building on the characterisation of the modified camera (Chapter 5) and assessing the impact of wavelength on image quality (Section 6.1) to inform the selection of wavelengths based on the sensitivity of the camera paired with the response of the optical properties of the object (Section 6.3).

This second research question was addressed by the camera characterisation in Chapter 5 and the investigation of wavelength and improved 3D reconstruction in Chapter 6. The camera characterisation was necessary to understand the imaging system for the investigation of wavelength and improved 3D reconstruction in addition to understanding the limitations of the device and its use as a scientific tool.

8.2.1. Camera characterisation

The camera characterisation presented in Chapter 5 provided insight about the impact of the camera modification on the resulting 2D image quality, spectral response, and 3D reconstruction quality including the significance of the RAW processing workflow. The advantages of the modification include the extended spectral recording sensitivity (to include near UV and NIR) and the increased effective resolution. The characterisation indicated an increased sensitivity in shorter wavelengths around 400 nm over four times the sensitivity of the camera to the longer NIR wavelengths (Section 5.3) and an increased effective resolution that is only achieved with a RAW processing workflow that does not include demosaicing (Section 5.2.2). The extended spectral resolution allows the camera to be paired with selected illumination and filtration for spectral imaging (reflected IR, VIL, and MSI, Section 3.1) and for the wavelength selection process (Chapter 6). The increased effective resolution can increase the spatial resolution and recording capabilities of the imaging system; however, this comes at the risk of aliasing when recording high frequencies (Section 5.2.2).

A RAW processing workflow is essential for recording of scientific information, but the standard workflow does not take into account the camera modification. The MC-RAW workflow was proposed (Section 5.1), which provided more control over the processing, took into consideration the camera modification, and reduced the fixed pattern noise (but did not eliminate it). However, the implementation of the workflow is limited as it is not yet an accessible solution. Future research will include investigating and testing a better correction for the pattern and increasing the usability of the processing.

The disadvantages of the modification include the increased risk of aliasing, the increased noise levels (Section 5.2.2), and the introduction of a fixed pattern noise (Section 5.1.2). These disadvantages are observed and are a result of a RAW processing workflow that does not include demosaicing, noise reduction, or some form of averaging as seen with the fixed pattern noise (Section 5.1.2). The MC-RAW workflow both revealed the fixed pattern noise resulting from the monochrome conversion and attempted to correct for it. While the fixed pattern noise is an issue for 2D image quality, the 3D reconstruction quality assessment suggested that the residual pattern would not significantly impact the 3D reconstruction (Section 5.4).

The fixed pattern noise will not be an issue with all modified cameras. One of the less invasive camera modifications includes only the removal of the IR blocking filter with the CFA left intact. This type of modification, both single wavelength and full-spectrum conversions (Section 3.1.5), will not result in a fixed pattern noise. Since the CFA is still in place for those two conversions, the demosaicing may need to be a part of the RAW processing workflow; however, the spectral response of the camera is then impacted by the transmission of the red, green, and blue filters that make up the CFA.

Measuring the spectral response quantifies the modified camera as a scientific device for more accurate measurements and provides indications of wavelengths that could improve recording based on sensitivity. The spectral response measurements help with understanding where the camera performs with the highest sensitivity. A consideration in using this data is pairing it with the appropriate light source and filters looking at the SPD of the light source and the transmission measures for potential filters. Areas of lower camera sensitivity, lower output of the light source, and/or lower transmission of the filter can result in image data with increased noise.

This thesis only presents the characterisation of a single manufacture and model of camera. The spectral response cannot be generalised to other cameras because the spectral response can vary between cameras (Section 3.3.3). While this chapter demonstrated the methods for

camera characterisation as a resource for heritage professionals, it is unreasonable to assume that every heritage professional working with modified cameras would be able to measure the spectral response of their device due to the cost and complexity of these measurements. It would be beneficial for these heritage professionals to have access to spectral response measurements of different modified cameras to understand what the range of sensitivity of their camera might be specifically when working with the wavelength selection process. Jiang et al. (2013a, 2013b) provided measurements of the spectral response of several manufacturers and models of unmodified cameras, and a similar data set of modified cameras would be a useful resource for heritage professionals who are using modified cameras for spectral imaging and wavelength selection. If a data set like this were to be assembled, it would be important to consider the uncertainties and accuracy of the measurement methods discussed in Section 3.3.3 and by Darrodi et al. (2015) and Manakov (2016).

8.2.2. Modified cameras as scientific devices

The modified camera can be used as a scientific tool only if it has been characterised. The characterisation, by better defining the relationship of the inputs and outputs and understanding the limitations of the device, allow the use of the modified camera as a scientific tool when paired with best practices and standards. The discussion about the use of a modified camera as a scientific tool for conservation documentation benefits from the categorisation of museum imaging (Section 1.1) and a consideration for the balancing of accuracy and accessibility.

Unlike a modified consumer camera, a monochrome scientific camera would provide a device with known inputs and outputs, and the camera would be used for its intended purpose. There are two directions forward: (1) encouraging the purchase of scientific cameras (which could be cheaper than the modified cameras) and focus on training heritage users on these devices; or (2) acknowledging that modified cameras will continue to be purchased and used and focus on the limitations of the device and the best applications for these (which is not all applications). While cameras specifically manufactured for scientific applications are optimised for measurements and may be better suited for some spectral imaging applications, modified consumer digital cameras will continue to be used by conservators and heritage users because they are relatively inexpensive and they retain the same user-friendly properties and interfaces to a wide range of photographic accessories and software. In some cases, modified cameras will be used for broadband spectral imaging that demands a general understanding of the camera modification and performance, but other applications with more narrow band imaging and more quantitative results require a specific

understanding of the device as a scientific tool (spectral sensitivity and image quality). Conservators and other heritage professionals will use these modified cameras for qualitative assessments, which may not need the same scientific rigour that measurements would require.

Applications like broadband spectral imaging, intended for visualisation and qualitative assessment, may be the best use of a modified camera by a non-expert user differentiating this from scientific imaging applications and acknowledging that a specialist would be required for MSI to ensure proper calibration and processing. This reiterates the conclusion from George et al. (2017) and the importance of heritage users understanding calibration, accuracy, precision, and the limits of imaging systems in order to address the high variability of more quantitative spectral imaging results.

Scientific imaging requires metadata that fully describes the setup and acquisition parameters, as much of this information will not be recorded in the camera's metadata and it is necessary in understanding and interpreting the results. This information is essential for understanding the image as a scientific record as emphasised by Schroer et al. (2017a). The metadata needs to include information about the camera modification, lighting, filters, setup, and processing for both qualitative visualisations and intended scientific records. One of the benefits of image-based 3D reconstruction is the ability to revisit and reprocess archived images especially when the input images have a high photographic quality as emphasised in this thesis. The reuse and reprocessing make the metadata all the more important, and without this information, the data will not be useful in the future.

The aspects that make a technique more flexible and accessible also impact the accuracy and reliability. There is a balance between the accessibility of a technique and its accuracy. As was emphasised by Falco (2009), an accessible technique can mean that more objects can be documented and investigated that otherwise would not. An accessible tool can help conservators in the work that they are doing as long as the limitations are understood and care is taken in the interpretation and analysis of the results. The balance of accessibility and reliability is further discussed in Section 8.5.

8.2.3. Wavelength selection

The imaging study of a wooden sculpture of a coyote and turtle provided evidence of the benefit of using a modified camera and wavelength selection to improve the image-based 3D reconstruction of a museum object (Section 6.2). Two campaigns of imaging were presented providing examples of the setup and workflow for documenting the museum object and also

critical assessment that resulted in the improvement of the comparability of the resulting data. Reducing the impact of the specular reflections by using IR input images improved the geometry and reduced the variability in the results specifically relating to the camera network. The comparison of the IR results shows improved consistency of the resulting reconstructions despite the differences in the image networks between the two campaigns (Section 6.2.2.2). Since the IR data shows more tolerance of the differences in the image network than the visible light data, this suggests a more forgiving and flexible option for recording data over time.

Wavelength selection can be valuable and can solve some otherwise tough 3D reconstruction problems but it is only useful if the surface properties change dramatically with different wavelengths as was the case with the coyote and turtle. Looking at the object with different wavelengths can help to test whether the effect will be dramatic and the process worthwhile. The presented workflow (Section 6.3) can be a lot of work, but it makes a dramatic difference with something like the coyote and turtle where the use of the reflected IR input images reduces the specular highlights and increases the consistency of the results. This workflow is increasingly valuable if there is a collection of objects with similar surface properties that have proven to be worthwhile using the wavelength selection to improve 3D reconstruction.

The research has focused on accessible, consumer imaging systems, specifically SfM-MVS for image-based 3D reconstruction and a consumer camera modified for spectral imaging, with the intention of heritage users being able to implement the workflow. The camera characterisation (Chapter 5) and the assessment of the influence of wavelength on 2D image quality (Section 6.1) show the potential of using a modified camera, as an accessible device, as part of the wavelength selection process for spectral-3D and improved 3D reconstruction. The research and imaging study only provide one example using NIR wavelengths and it is acknowledged that this object is not representative of all heritage objects. The success of this workflow on other objects is dependent on their surface properties. The workflow in Section 6.3 presented the steps for selecting the best wavelengths, but this research has not defined what wavelengths should be selected for different purposes or specific materials and objects. Additional imaging studies will provide more examples of materials and wavelengths that may or may not work providing resources and references to heritage professionals interested in this workflow and technique. Heritage objects include a wide variety of materials and combination of materials, so there is not an easy way to categorise what may or may not work depending on the object or material.

A future project will be partnering with the Smithsonian's Freer|Sackler Galleries to investigate spectral-3D imaging of a collection of cylinder seals. The image-based 3D reconstruction of these objects is not straight forward with the size and material of the seals presenting challenges. The seals are very small (as small as 2 x 1cm) with fine details depicting daily life activities, religious and royal figures, and inscriptions often bearing the name of the owner of the seals. The surface properties of some of the seals present challenges for any optical documentation technique (i.e., reflective, translucent, and transparent). This project would investigate whether wavelength selection and spectral-3D imaging could aid in the documentation of the more problematic seals, specifically looking at blue light and UV radiation. This project would investigate different materials and objects in addition to different wavelengths from the coyote and turtle imaging study presented in this thesis. In addition to wavelength, the project would also be working with DOF as objects this size will present a more limited DOF than the objects in this thesis. This future project would provide additional examples, findings, and resources for spectral-3D and improved 3D reconstruction of heritage objects building on the research presented in this thesis.

8.3.   Defining and mitigating DOF limitations

The third method of optimisation addressing the first research question included quantifying DOF for 3D reconstruction and initial tests using sharpness to mask input images as a pre-processing step (Chapter 7). This method of optimisation directly links to the research question "How can limitations of optical depth of field be mitigated using consumer imaging systems for the 3D reconstruction of small to medium sized museum objects?".

DOF is challenging for 2D and 3D documentation of small to medium sized heritage objects as discussed in Section 2.5.1. Some studies published have opted to decrease the aperture diameter to increase DOF sometimes to avoid focus stacking (Sapirstein 2018, Marziali and Dionisio 2017, Verhoeven and Missinne 2017) and other times just to reduce the number of images acquired (Clini et al. 2016). These authors acknowledged the selection of the smaller aperture diameter as a compromise of increased DOF and decreased sharpness from diffraction.

The research presented in Chapter 7 provided extreme options for the value of the circle of confusion diameter: one that takes into consideration the required image quality for the FADGI star rating providing a very small circle of confusion (0.01 mm) and narrow DOF and the other takes into consideration the 3D reconstruction results with a larger circle of confusion and an extended DOF. Calculations for 2D DOF are generally based on the circle

of confusion diameter of $C = 0.03$ mm. The DOF-Sharp-SFR tests (Section 7.1.2) provided evidence that this value falls between the extremes of what would be required to achieve the FADGI star rating and what is needed for the 3D reconstruction of the Panel.

These results for the DOF and improved 3D reconstruction investigation indicated that the 3D reconstruction was less sensitive than initially thought due to expectations from visual observation. A limited DOF impacts the resulting image quality which can easily be observed visually; however, the 3D reconstruction can tolerate more blur than a 2D image acting as an object record. This increases the "acceptable" range of sharpness from 2D imaging to 3D imaging although the surface properties will still influence the results. The success of the 3D reconstruction of an object is dependent on the surface properties, and the Panel test target is more resilient (because of the high local contrast) than most heritage objects. Aperture is an important consideration for the resulting quality of 3D reconstruction even if DOF was not as limiting for some of the objects presented in the thesis. Smaller objects are going to be more challenging than the size of objects looked at in this research.

The experimental setup for the DOF-3D-Plane (Section 7.1.1) and DOF-Sharp-SFR (Section 7.1.2) with the camera positioning robot was not able to achieve angles and distances that were extreme enough for the 3D reconstruction of the Panel to fail. The DOF-3D-Plane (Section 7.1.1) results showed that the most impact from angle was observed with the f/5.6 datasets with the lowest DOF. The impact from distance (DOF-SFR-Sharp, Section 7.1.2) was observed beyond the DOF calculated with a circle of confusion diameter $C = 0.03$ mm. If the tests were to be revisited, the setup would need to be able to achieve more extreme angles and distances.

8.4.   Test objects and targets

The methodology for the thesis was an experimental approach based on scientific principles that included lab-based experiments and practical experiments. As part of the methodology, test objects were essential for providing reliable and significant results for the 2D and 3D quality assessment and for providing evidence of improved image-based 3D reconstruction. The research incorporated three test objects: the Panel test target, the Mango Vase, and the DICE target. Each was selected or designed for 2D image and 3D reconstruction assessment based on specific requirements of the research. If aspects of the research were to be revisited, it is worth discussing the advantages of these test objects, how they could be improved, and the potential of creating of a test object based on the advantages and limitations observed with the objects used in this research.

The Panel test target is an engineering target and associated with scientific imaging, the Mango Vase is representative of a conservation documentation target with the materials being closely linked to a heritage object, and the DICE target is a collections photography target. The three targets have served different purposes in how a technique or result is assessed; however, the use of the three targets in this research support the claim that the research is working at the intersection of the three museum imaging categories and further illustrate the interdisciplinary nature and needs of museum imaging.

The imaging of the Panel provided an assessment of the imaging system in relation to its performance for image-based 3D reconstruction, a further component of the camera characterisation presented in Chapter 5. The Panel is an engineering test target that has been optimised for Digital Image Correlation (DIC) and the detection of local deformation. However, this test target does not represent museum collections and the results of these tests are harder to relate to heritage collections because of the shape, material, and overall nature of the object. The panel is resilient and the optimisation of the pattern allows for the limits of the system to be reached. The use of the target is beneficial for establishing the sensitivity of a system, but these results will not be representative of the performance when documenting a museum object, and the target did not provide capabilities for 2D image quality or spectral imaging assessment.

Section 3.3.2 discussed the usefulness of custom built targets to better represent the materials in museum collections and testing the usability of an imaging system for specific materials or collections (Cucci et al., 2019). The idea of the custom built target informed the creation of the Mango Vase test object; however, the Mango Vase does not represent the surface properties of all heritage objects. A significant aspect of 3D recording is the surface properties of the object. Surface properties of the object can be a limitation of the surface recording of an object, which links directly to the wavelength filtering process and the demonstration of improved output presented in Chapter 6. Replicating the surface properties of an object can be challenging and this might only be representative of a single object, so the use and implementation of test objects that can provide an understanding of the base level of accuracy present a good compromise because realistically test objects are limited. While the assessment of the resulting 3D reconstruction of the Mango Vase does not provide the performance and limitations of an imaging system, the documentation of the Mango Vase illustrated the influence of the object on the resulting 3D reconstruction quality and provided a reference for the documentation of museum objects.

The DICE target and GoldenThread software (Section 12) provided a turnkey solution with metrics and criteria for measuring system performance capabilities that are already being

used in museum imaging by collection photographers. While the target and software provide an assessment of a full range of image quality parameters, this research focused on assessing noise, sharpness, and resolution using measures for noise, SFR, and sampling efficiency. The software does not require any coding experience or a background in imaging science, and it also provided several metrics to initially explore for the 2D image quality assessment. However, the FADGI guidelines and DICE target only cover the visible light range for 2D image quality assessment, and they do not address spectral or 3D imaging.

The 2D image analysis focused mostly on SFR analysis. Other targets and software could be used for the 2D image quality assessment including *sfrmat3* and OpenDICE. The *sfrmat3* is a freely available option for SFR analysis that was used in Chapter 7 when GoldenThread was unable to detect features. Appendix 14.6 provides a comparison of *sfrmat3* and GoldenThread results. OpenDICE is open source and an official FADGI conformance measurement and analysis tool ('Tools: OpenDICE and AutoSFR', 2018). OpenDICE follows the FADGI guidelines and DICE testing and is consistent with the results obtained with GoldenThread, and it can be used with three targets the DICE target, the XRite ColorChecker SG, and the Universal Test Target (UTT).

These test objects do not cover all aspects of the 3D recording process, but they provide a good start to understanding the performance of the imaging system. While the Panel is an engineering object and could not easily be documented in a standard photographic or conservation studio, recording a flat plane can provide valuable information about the maximum capabilities of an imaging system. While the Mango Vase has limitations related to its rotational symmetry and its ability to measure the sensitivity of an imaging system, it does take into account materials and shape that are related to heritage objects.

Reviewing the advantages and limitations of these test objects offers criteria and features for the creation of a new target that could provide museum professionals with a target or targets that could deliver information about the performance of their imaging system. The combined use of the Panel and Mango Vase provided an example of how surface recording and assessment could be accomplished in a museum setting. Recording a flat plane can provide valuable information about the maximum capabilities of an imaging system. The flat plane should include a pseudo-random pattern with high local contrast and medium frequency (like the Panel), slanted-edge features in different areas of the field of view (like the DICE target), and coded targets for alignment, scaling, and quantification of the accuracy and precision (discussed in Section 4.2.2.1). This would provide a test object that could be used to evaluate the performance of an imaging system for image-based 3D reconstruction. A final consideration would be the creation of a framework with posts and targets around the

object that filled the full volume improving the target network (Section 4.2.2.1). This could incorporate a combination of features or designs from the Manhattan object (Robson et al., 2014), the calibration target in Sapirstein (2018), and control field in MacDonald et al. (2014). This framework could be implemented for improved alignment, scaling, and measurement capabilities and would be beneficial to address some of the scaling and shape issues (Section 4.2.2.2 and 4.3).

8.5.   Museum imaging

As introduced in Section 1.1, imaging within museums and heritage institutions can be categorised into three main areas: collections photography, conservation documentation, and scientific imaging. These areas are defined by different techniques, workflows, and applications, yet they are interrelated and overlap (Figure 1-1). Defining the categories provided a context for the research at the intersection of the categories, identified best practices and standards to inform the research methods, and provided examples of the different uses of 3D output to understand the requirements of the results. The focus of the research was producing scientific records for conservation documentation, and methods were borrowed from scientific imaging and collections photography to achieve improved image-based 3D reconstruction.

Assessment of 2D image quality (Section 5.2) was used throughout the research, and this was borrowing methods from collections photography and scientific imaging. The 2D image quality assessment was mostly using the FADGI guidelines with the DICE target and GoldenThread software borrowed from the collections photography and closely relate to ISO standards that would be categorised as scientific imaging. The 2D image quality assessment is found in most of the experimental chapters (Chapter 5-7) focusing on SFR analysis and sampling efficiency although Chapter 5 and 6 include some noise measurements. When the GoldenThread software could not be used for analysis in Chapter 7, *sfrmat3* was used which links to ISO standards and scientific imaging, specifically ISO 12233:2017. The 2D image quality assessment was used to link to the 3D reconstruction to quantify DOF (Chapter 7).

Spectral response measurement (Section 5.3) as part of the camera characterisation was borrowing methods from scientific imaging and colour science. The approach used was a filter-based method presented by MacDonald (2015).

Spectral imaging can be considered in both categories of conservation documentation and scientific imaging; however, image-based 3D reconstruction, specifically traditional

photogrammetry, is metrology, or the scientific study of measurement, falling into the category of scientific imaging. While it is a scientific imaging technique, it is not necessarily established as scientific imaging within museum imaging, but instead has been introduced as an automated and accessible technique for collections photography and conservation documentation. The available workflows and best practices for image-based 3D reconstruction within museum imaging would not be categorised as scientific imaging. The assessment of 3D reconstructions presented in this research can be considered scientific imaging and is situated at the intersection of conservation documentation and scientific imaging. The 3D reconstruction assessment is found in all of the experimental chapters.

The thesis focused on conservation documentation, and this category of museum imaging realised the largest contributions of the thesis. Consumer imaging systems are important for conservation documentation as these systems provide accessible solutions for conservation documentation to record the condition, inform the care, and increase the understanding of objects. Conservators are specialised in the care and treatment of objects and have a general understanding of imaging to aid in their work but they may not necessarily have expert knowledge in imaging. The flexibility and automation that make these solutions accessible also increase the challenges of maintaining consistent output. Improved consistency is essential for conservation applications of 3D imaging in order to monitor an object and measure change over time. The methods presented in this thesis addressed the requirements of improved consistency of image-based 3D reconstruction for conservation documentation focusing on acquisition, processing, and assessment workflows (Chapter 4), camera characterisation (Chapter 5), wavelength selection (Chapter 6), and defining DOF in relation to 3D reconstruction (Chapter 7). The previous paragraphs described the methods borrowed from collections photography and scientific imaging to improve the image-based 3D reconstruction for the recording of scientific records for conservation documentation.

In addition to providing context for the positioning of the research, the categorisation of museum imaging recognises the connections and synergy between areas enabling the discussion for the development of techniques and technologies, workflows, best practices, and standards. As more techniques become accessible for conservation documentation, it is important to discuss these topics. The AIC Annual Meeting in May 2019 in Uncasville, Connecticut, USA included a panel discussion, organised and moderated by the author, focusing on this topic and accessible techniques for conservation documentation. The panellists provided examples of institutional structure of the museum imaging categories discussing the support of imaging within different institutions. The panellists also discussed case studies of accessible techniques in practice and perspectives on the assessment of

available imaging tools and techniques to better understand possibilities and limitations. This panel discussion illustrated the relevancy of the topic to the field of conservation in addition to providing a foundation for the discussion of the development and direction of conservation documentation.

The museum imaging categories also aid in discussing the accessibility and accuracy of the available techniques. A focus of this research and a priority of the work at the MCI Imaging Studio has been on accessible imaging techniques for conservation documentation. Accessible techniques allow for implementation by the non-expert user with the benefit of these techniques being used by more people to document more objects. However, some of the aspects that make the techniques more flexible and accessible also impact the accuracy and reliability emphasising the importance of understanding the limitations of the technique specifically looking at reproducibility and comparability. Steps that increase the reproducibility and comparability can represent a shift towards more scientific imaging, which can increase the costs and complexity making the technique less affordable and accessible. Does the question become accessibility vs accuracy, a question of one or the other?

While accessibility has the benefit of the documentation of more things, there is a risk of increased confidence in the results and insufficient knowledge of the processing. This links back to Remondino et al. (2017, p. 591), "Without sufficient knowledge of the processes and the software being used, non-expert users can potentially invest greater confidence in the results of their work than may be warranted." There then becomes a gap in the critical analysis of the results and a true understanding of the strengths and weaknesses of the systems and techniques. In recognising this balance between accessibility and accuracy, looking at the museum imaging categories and the relationship between conservation and scientific imaging can provide a better understanding of this dynamic. This can include weighing the balance between the limitations of the technique, its accessibility, and the need of standardisation.

The discussion does not offer the final word on the balance of accessibility and accuracy but encourages the continued investigation and increased awareness of the limitations of accessible techniques staying focused on the overarching goal of the stewardship of our cultural heritage.

8.6. Recommendations for heritage professionals

The process and findings from this research to improve image-based 3D reconstruction result in recommendations for heritage professionals seeking to either use or benefit from image-based 3D reconstruction. This section includes the resulting recommendations.

8.6.1. Optimisation to improve image-based 3D reconstruction

- The camera network geometry is an important consideration for consistent and accurate results. A convergent image configuration improves the geometry as compared to a normal image configurations. The recording of a painting would benefit from combining normal and convergent networks to provide the best results for texture and geometry.
- When planning a project, there should be a consideration for how the results will be assessed.
    - Assessment of the 3D reconstruction should go beyond a visual assessment and a review of processing statistics, if possible, in order to identify and correct for systematic errors that would influence the analysis and interpretation of the results.
    - Reliable reference data and the iterative process of identifying and correcting for systematic errors allows for optimising of the 3D reconstruction and establishing limitations of the imaging system.
    - Global vs local assessments will provide different information about the results and there should be a consideration of the area being compared and assessed. The global assessment may provide more information about the alignment, overall shape, and scaling, while a local assessment may be able to show the difference in recording local feature details
    - Surface discrepancy maps should include a histogram to assess the spread and shape of the discrepancies.
- Documenting the base of an object, including coded targets, recording a "flat project", and selecting parameters for the camera model should be considered to improve scaling and alignment for the recording of heritage objects.

8.6.2. Modified cameras as scientific devices and wavelength selection

- A RAW processing workflow is essential for recording of scientific information.
- Understanding the characteristics of the different parts of the imaging system (SPD of illumination/radiation source, transmission of the filters, spectral sensitivity of the

camera, and the image quality of imaging system) is important for broadband and narrowband spectral imaging. This helps to better understand what is being recorded which can inform the interpretation and analysis of the results.

- 2D image quality assessment can be used for comparing results with other systems by providing a baseline to show how the technology and instrumentation may be changing over time and an indication of the scale of change that could be recorded.

- Camera characterisation is necessary to use the device as a scientific tool. Chapter 5 demonstrates methods for characterising both unmodified and modified cameras.

- Lens selection, focus, and illumination impact the resulting image quality more than wavelength and should be considered for high quality photographic input for image-based 3D reconstruction.

- The wavelength selection workflow (Section 6.3) provides recommendations for how to select wavelengths in order to implement spectral-3D imaging to improve image-based 3D reconstruction.

8.6.3. Defining and mitigating DOF limitations

- A larger aperture diameter should be avoided due to the overall reduced image quality and the impact of the small DOF on the resulting 3D reconstruction. An optimal aperture provides a balance of DOF and image quality. Even though the diffraction was tolerated by the 3D reconstruction process using a smaller aperture diameter, high spatial frequency features may not be resolved because of the effect of diffraction on the 2D image quality.

8.6.4. Test objects and targets

- Imaging a flat plane can provide information about the maximum capabilities of an imaging system. The quality of the results can be assessed by using plane fitting.

- A target like the DICE target can provide metrics that could be used for comparing with other systems, which would be useful in monitoring an object over time and the changes in technology also over time.

- Custom built targets can be useful for recording heritage objects and testing the usability of an imaging system for specific collections or materials; however, these can be challenging to create.

- Test objects are limited, but it is important to be able to establish some of the capabilities of the imaging system as part of assessing accuracy.

8.6.5. Museum imaging

- Awareness of information coming from different categories and attention to the breadth and diversity that the different categories of museum imaging offer is important and can provide insight into the introduction of techniques, workflows, and processes. Advances in different categories and fields can provide benefits for other areas.

- Continued investigation and increased awareness of the limitations of accessible techniques through characterisation and accuracy assessment are important for the appropriate use and interpretation of imaging.

8.7.   Chapter summary

This chapter has tied together the experimental chapters by reviewing how the research questions were addressed, critiquing the methodology used, and concluding with recommendations for heritage professionals. The research sits at the intersection of the three museum imaging categories (collections photography, conservation documentation, and scientific imaging), and this chapter presented the research in the context of the state of the art for each category to connect the research outcomes with the needs of heritage professionals seeking to either use or benefit from image-based 3D reconstruction.

9. Conclusions, contributions, and further work

This chapter concludes the thesis by summarising the findings (Section 9.1) and contributions to knowledge (Section 9.2) and presenting directions for further work (Section 9.3).

9.1.   Thesis in review

The ease of creating 3D reconstructions using consumer imaging systems, both mass market digital cameras and readily available automated processing software, have brought 3D museum imaging into the mainstream. The availability, flexibility, and automation that make image-based 3D reconstruction an accessible process also increase the challenges of maintaining consistent, fit for purpose, 3D output. With the wider use is also the increased variability in the 3D output; however, conservation applications for image-based 3D reconstruction require scientific rigour to establish reliable and accurate models for monitoring and measuring change overtime. This thesis has demonstrated that image acquisition and data processing methods deployed with consumer imaging systems, combined with critical assessment throughout the 3D reconstruction process, can improve both the quality and consistency of resulting 3D reconstructions to the level needed for the most critical 3D museum imaging applications.

This thesis focussed on image-based 3D reconstruction for accurate and reliable scientific records for conservation documentation while seeking to maintain the accessibility of imaging and 3D model creation workflows. The quality of the output reconstruction is reliant on the quality and geometry of the input images, so the research focussed on scientific image acquisition specifically looking at local contrast, modified cameras and wavelength selection, sharpness, and focus. The thesis is written for the museum imaging professional with the overall aim of improving image-based 3D reconstruction as a tool to make accurate and reliable scientific records of small to medium sized heritage objects for conservation documentation.

Widening access requires better investigative methods to improve image-based 3D reconstruction and thereby ensure consistent high-quality outputs. Scientific model usage requires scientific rigour to establish the reliability and accuracy of the model and in the case of a temporal analysis, what types and levels of change can be recorded. The research presented in this thesis isolates and evaluates critical stages in the 3D reconstruction workflow. Quantifiable measures designed to increase confidence in image acquisition, processing, and analysis of image-based 3D reconstruction data in turn provide quantified

geometric evidence needed to answer questions of whether an object has changed over time (Chapter 4).

Two approaches for improving image-based 3D reconstruction were explored through laboratory based experiments, both focus on the qualities of the input imagery. The first concerned the quantifiable scientific use of a modified camera combined with wavelength selection, while the second addressed a gap in the state of the art, seeking to quantify DOF for 3D reconstruction with an associated automatic process of sharpness-based masking. These approaches were isolated and evaluated separately to reduce the variables being addressed.

Imaging using selected wavelengths within or beyond visible light can increase the image contrast of materials or features to provide an enhanced view. In turn, improved local detail and contrast through wavelength selection can improve image-based 3D reconstruction. While accurate and precise instruments exist for spectral imaging, these specialised devices can be too costly for many heritage professionals and institutions. Modified cameras provide inexpensive, easy to use, portable, and high-resolution options for spectral imaging and conservation documentation. The camera modification allows a low cost camera to approach the capabilities of a more expensive scientific imaging device while retaining usability; however, the raw image format and aspects of in-camera processing limit what can be achieved with this camera system. Addressing the second research question, a modified consumer digital camera can be paired with selected illumination and filtration to be used as a scientific method to improve the image-based 3D reconstruction of museum objects for conservation documentation.

The investigation of wavelength selection and improved 3D reconstruction presented a novel workflow and application for conservation documentation. Reflected IR images of a coyote and turtle sculpture increased the local contrast and reduced specular reflections (Section 6.2) providing evidence that a modified camera and wavelength selection can improve image-based 3D reconstruction. The developed wavelength selection workflow (Section 6.3) provides steps for selecting wavelengths to optimise the camera response, image quality, and object features to minimise the surface discrepancy for 3D reconstruction. The imaging study and wavelength selection workflow were informed by the camera characterisation (Chapter 5). The camera characterisation was essential for the use of the consumer camera as scientific tool in addition to understanding the limitations of the modified camera. The camera characterisation provided insight about the impact of the camera modification on the resulting 2D image quality, spectral response, and 3D reconstruction quality including the significance of the RAW processing workflow.

Image-based 3D reconstruction processing tools assume sharp focus across the entire object being imaged, but DOF can be a limitation for 2D and 3D imaging of small to medium sized objects. By restricting peripheral light rays passing through the lens optics to optimise DOF and hence 2D image quality within the limits of diffraction, lens aperture has a strong influence on the content of the network of images needed for a successful 3D reconstruction workflow. Addressing the third research question, quantifying DOF for 3D reconstruction and initial tests using sharpness to mask input images as image pre-processing are steps to mitigating limitations of optical DOF using consumer imaging systems for the 3D reconstruction of small to medium sized museum objects (Chapter 7). While DOF is well understood in the context of 2D imaging and it is considered with the acquisition of image-based 3D reconstruction, "acceptable" sharpness had not yet been quantified for image-based 3D reconstruction. Defining DOF in relation to 3D reconstruction can inform the setup and acquisition of an object in addition to sharpness-based masking as part of an image pre-processing step to optimise the processing performance for 3D reconstruction (Chapter 7). Results drew upon state of the art metrology capabilities to highlight the achievable surface recording capability of consumer imaging devices to define the range of acceptable image sharpness for 3D reconstruction.

9.2.   Contribution to knowledge

Overall this thesis contributed to achieving a higher level of consistency of the 3D model outputs that can be generated from consumer digital cameras and automated workflows accessible to heritage professionals making accurate and reliable scientific records for conservation documentation. This section brings together the contributions to knowledge identified in each of the experimental chapters.

Evidence of the contributions to knowledge of the research presented in this thesis is supported by the list of publications and presentations made by the author (Section 13). The audiences of the journals and conferences represent the three categories of museum imaging and thus illustrate the interdisciplinary nature of the research and outputs, in addition to the wide reach of the outputs and the interest in the research.

9.2.1.   Connecting across museum imaging

The defining of the three categories of museum imaging presented in this thesis is unique from other classifications of cultural heritage documentation. This definition involved investigating the techniques, applications, best practices, and standards for each to understand how these relate and overlap. The research was situated at the intersection of the

categories and demonstrated the translation of methods across disciplines to accomplish the research goals. The categorisation helps to define the heritage context for image-based 3D reconstruction which can in turn provide an understanding of and facilitate discussions about the direction of development and future growth in addition to accessibility and accuracy of techniques.

9.2.2. Ensuring consistent imaging quality capabilities

Characterisation of the modified camera and its associated imaging system aids in ensuring consistent imaging quality and capabilities by providing a better understanding of the modification, the use of the camera as a scientific tool, and the spectral capabilities for optimal use. There are early examples of camera characterisation for MSI that establish the limitations of the imaging system for example Casini et al. (1999), but these studies have not previously been linked to current uses of modified cameras for conservation documentation. The demonstration of these methods for conservation documentation combined established methods from collections photography and scientific imaging. Results provide an understanding of the possibilities and limitations of a modified consumer digital camera as a scientific tool, which has not previously been available for cultural heritage documentation. A better understanding of the device, through characterisation, provides improved results and an increased capability to measure and quantify the outcomes so that techniques can be further adapted for different heritage objects with differing geometries and optical surface properties. These methods are not limited to modified or low cost cameras but can be used for assessing other imaging sensors. The characterisation method is beneficial to ensuring quality and consistency across a wide range of imaging sensors and museum recording applications.

9.2.3. Wavelength selection for improved recording of fine detail

Imaging using a modified camera and selected wavelengths can improve the recording of fine detail for image-based 3D reconstruction. Increasing the local surface contrast and reducing specular reflection through wavelength selection can improve image-based 3D reconstruction as demonstrated by the imaging study of the coyote and turtle. While modified cameras are being used for broadband spectral imaging and MSI for conservation documentation, to the knowledge of the author, these devices have not been used for optimising image-based 3D reconstruction, so this thesis presents a novel workflow and application for conservation documentation. Other fields, like astrophysics and machine vision, have used selected wavelengths for improved recording; however, this has not been

done for conservation documentation for the increase of local contrast for improved surface recording of fine detail using a modified camera and optical filters.

9.2.4. Ensuring optimal sharpness and DOF as input to 3D reconstruction

This research contributed to the understanding and quantification of DOF and image-based 3D reconstruction by providing evidence of the influence and limitations of DOF and sharpness on the 3D reconstruction. DOF is well understood in the context of 2D imaging and it is considered with the acquisition of image-based 3D reconstruction, but DOF and the calculations for 2D imaging are not well connected with the required range of acceptable sharpness for 3D and resulting 3D reconstruction quality. A better understanding of the parameters relating to 3D ensures optimal sharpness and DOF as input for 3D reconstruction.

The thesis presented a novel approach of linking established aspects of 2D DOF using the DICE target and image quality assessment with 3D reconstruction to define DOF for 3D reconstruction. Aspects of the FADGI guidelines, the DICE target, and analysis software were used to assess 2D image quality using different wavelengths within and beyond visible light and also to link 2D image quality with 3D reconstruction. This assessment focused on sharpness and resolution using SFR and sampling efficiency to evaluate and compare results. The FADGI star rating was used as a point of reference for the quality of the image sets to link 2D image quality with 3D reconstruction results. By imaging and assessing the DICE target, the SFR analysis and sampling efficiency results were connected with the surface discrepancy maps assessing the 3D reconstructions. The lab-based experiments showed an optimal aperture (represented by f/11 in this research) balanced the limitations of DOF and image quality and the circle of confusion diameter, taking into consideration 3D reconstruction, would fall between the extremes of what would be required to achieve the FADGI star rating ($C = 0.01$ mm) and what is needed for the 3D reconstruction of the Panel ($C = 0.05$ mm).

9.2.5. Advances gained from the interdisciplinary nature of the wider 3D reconstruction community

There is a larger 3D reconstruction community that extends beyond museum imaging and conservation documentation, and the museum imaging community benefits from accessing knowledge and resources from this extended and interdisciplinary community. As one example, the literature review discussed the parallels of geomorphology and cultural heritage and the disconnect from the knowledge, experience, and literature within traditional

photogrammetry the field's traditionally associated with 3D reconstruction accuracy and reliability. Section 2.4.4 pointed to a disconnect between automated methods of image-based 3D reconstruction and some of the photogrammetric fundamentals relating to accuracy and citing the work of James et al. (2017) in the field of geomorphology. Following the lead of James et al., Chapter 4 demonstrated methods to improve acquisition, processing, and assessment contributing to the state of the art in museum imaging and conservation documentation.

9.3. Future work

There are several aspects of the research that could be pursued and developed as further work:

- Changes in techniques and technologies were discussed in the context of monitoring objects over time (Section 4.2.5). Monitoring an object requires modelling error of the 3D capture and it is unlikely that the same setup would be replicated or the same instrumentation in 5, 10, 15 years. Future studies could look into the development of a target as a reference over time to understand the uncertainty of the technique and calculate that uncertainty into the comparison of the models acquired over time.

- The implementation of the proposed MC-RAW workflow (Section 5.1) is limited as it is not yet an accessible solution. Future research will include investigating and testing a better correction for the residual pattern and increasing the usability of the processing.

- This thesis only presents the characterisation of a single manufacture and model of camera, and the spectral response cannot be generalized to other cameras. While characterisation methods were demonstrated in Chapter 5, not all heritage professionals working with modified cameras will be able to measure the spectral response of their devices. However, this information is beneficial to understand the range of camera sensitivity for spectral imaging and the wavelength selection process. It would be useful for spectral response measurements of several manufacturers and models of modified cameras were available to heritage professionals working with these devices. If a data set like this were to be assembled, it would be important to consider the uncertainties and accuracy of the measurement methods discussed in Section 3.3.3 and by Darrodi et al. (2015) and Manakov (2016).

- The imaging study provided one example using NIR wavelengths and improved image-based 3D reconstruction, but the one museum object is not representative of

all heritage objects. Additional imaging studies would provide more examples of materials and wavelengths that would benefit from the technique and those that would not, providing resources and references to heritage professionals interested in this workflow and technique. An upcoming project partnering with the Smithsonian's Freer|Sackler Galleries will investigate spectral-3D imaging of a collection of cylinder seals, specifically looking at blue light and UV radiation (Section 8.2.3). This project would investigate different materials and objects in addition to working with DOF as objects this size will present a more limited DOF than the objects in this thesis. This future project would provide additional examples, findings, and resources for spectral-3D and improved 3D reconstruction of heritage objects building on the research presented in this thesis.

- The initial tests for sharpness-based masking were not showing enough improvement to justify the investment of time to apply these approaches (Section 7.3). However, masking has proven beneficial for automation to improve the 3D reconstruction process (Section 2.5.3). Masking has been used to improve the quality of the alignment and decrease the reconstruction processing time, so by streamlining the methods initially tested there is still a potential for sharpness-based masking to improve the image-based 3D reconstruction. Future research could include testing with image stacking to improve the reliability of the camera calibration with the stacking workflow (Section 2.5.2), investigating focus measure operators from Shape From Focus (SFF) as a means for masking based on sharpness (Section 2.5.2), and even testing the Matlab toolbox presented by Verhoeven (2018) despite stated challenges and limitations (Section 2.5.3).

9.4. Concluding statements

This thesis has provided evidence that consumer imaging systems can be optimised to improve the quality of image-based 3D reconstruction of museum objects and that methods of acquisition, processing, and assessment of 3D reconstructions. The thesis contributed a more rigorous scientific approach for conservation applications of image-based 3D reconstruction that achieved a higher level of consistency of the 3D model outputs that can be generated from consumer digital cameras and automated workflows.

Imaging techniques and technologies are important in the heritage field as they offer non-invasive, non-destructive and in some cases portable techniques as options to support the research and conservation of cultural heritage objects. The research presented in this document focusing on consumer imaging systems can inform the improved documentation of heritage objects increasing the accuracy and reliability of image data as scientific records

and the support of caring and protecting our cultural heritage. Ultimately the goal for conservation and heritage science is the stewardship of our cultural heritage, protecting it for future generations. If we can optimise consumer imaging systems that are already being used for heritage documentation, then we can improve the recording, care, and understanding of these objects into the future.

10. References

3D Content in Europeana [WWW Document], n.d. URL https://pro.europeana.eu/project/3d-content-in-europeana (accessed 1.20.20).

3D-ICONS: 3D Digitisation of Icons of European Architectural and Archaeological Heritage [WWW Document], n.d. URL http://3dicons-project.eu/ (accessed 1.12.20).

Abate, D., Hermon, S., Eliades, I., 2016. Virtual and Physical Recomposition of Fragmented Ecclesiastical Frescoes Using a Photogrammetric Approach, in: 2016 XXIII ISPRS Congress. The International Archives of the Photogrammetry, Remote Sensing and Spatial Information Sciences, Prague, pp. 12–19. https://doi.org/10.5194/isprsarchives-XLI-B5-153-2016

Abate, D., Menna, F., Remondino, F., Gattari, M.G., 2014. 3D Painting documentation: Evaluation of conservation conditions with 3D imaging and ranging techniques, in: 2014 ISPRS Technical Commission V Symposium. The International Archives of the Photogrammetry, Remote Sensing and Spatial Information Sciences, Riva del Garda, pp. 1–8. https://doi.org/10.5194/isprsarchives-XL-5-1-2014

Agisoft [WWW Document], 2019. URL https://www.agisoft.com/about/ (accessed 11.25.15).

Agisoft PhotoScan User Manual [WWW Document], 2018. URL https://www.agisoft.com/pdf/photoscan-pro_1_4_en.pdf (accessed 4.9.19).

AIC Code of Ethics and Guidelines for Practice, 1994. URL http://www.conservation-us.org/our-organizations/association-(aic)/governance/code-of-ethics-and-guidelines-for-practice#.W_FwC5NKh-U (accessed 11.17.18).

Allen, E., Triantaphillidou, S. (Eds.), 2011. The Manual of Photography, 10th ed. Focal Press, Oxford.

Alsadik, B., Remondino, F., 2013. Robust extraction of image correspondences exploiting the image scene geometry and approximate camera orientation, in: 2013 3D-ARCH 2013 - 3D Virtual Reconstruction and Visualization of Complex Architectures. The International Archives of the Photogrammetry, Remote Sensing and Spatial Information Sciences, Trento, pp. 25–26. https://doi.org/10.5194/isprsarchives-XL-5-W1-1-2013

Andrews, D., Bedford, J., Bryan, P., 2015. Metric Survey Specifications for Cultural Heritage, 2nd ed. Historic England, Swindon.

Arbace, L., Sonnino, E., Callieri, M., Dellepiane, M., Fabbri, M., Iaccarino Idelson, A., Scopigno, R., 2013. Innovative uses of 3D digital technologies to assist the restoration of a fragmented terracotta statue. Journal of Cultural Heritage 14, pp. 332–345. https://doi.org/10.1016/j.culher.2012.06.008

Arnold, D., 2013. 3D-COFORM. D.1.5 - Project Final Report. Tools and Expertise for 3D Collection Formation. EU FP7 funded project. University of Brighton.

Arslanoglu, J., Centeno, S., Digney-Peer, S., Duvernois, I., 2013. 'Picasso in The Metropolitan Museum of Art': an investigation of materials and techniques. Journal of the American Institute for Conservation 52, pp. 140–155. https://doi.org/10.1179/1945233013Y.0000000007

Astrosurf, n.d. COMPARISON OF CANON 40D, 50D, 5D AND 5D Mark II [WWW Document]. URL http://astrosurf.com/buil/50d/test.htm (accessed 8.5.18).

Ballard, G., Delaney, J., Saunders, D., 2017. Looking Deeper: A Discussion about Imaging and Conservation [WWW Document]. Conservation Perspectives: The GCI Newsletter

Spring 2017. URL
https://www.getty.edu/conservation/publications_resources/newsletters/pdf/v32n1.pdf
(accessed 4.15.18).

Barazzetti, L., Scaioni, M., Remondino, F., 2010. Orientation and 3D modelling from
markerless terrestrial images: Combining accuracy with automation. Photogrammetric
Record 25, pp. 356–381. https://doi.org/10.1111/j.1477-9730.2010.00599.x

Bauer, P., Rottermann, R., 2010. How Sharp Images Are Formed [WWW Document]. Leica
Science Lab. URL https://www.leica-microsystems.com/science-lab/how-sharp-
images-are-formed/ (accessed 1.2.18).

Beraldin, J.A., Mackinnon, D., Cournoyer, L., 2015. Metrological characterization of 3D
imaging systems: progress report on standards developments, in: 17th International
Congress of Metrology. pp. 1–21. https://doi.org/10.1051/metrology/20150013003

Beraldin, J.A., Picard, M., Bandiera, A., Valzano, V., Negro, F., 2011. Best Practices for the
3D Documentation of the Grotta dei Cervi of Porto Badisco, Italy, in: Beraldin, J.
Angelo, Al, E. (Eds.), Proceedings of SPIE-IS&T Electronic Imaging: Three-
Dimensional Imaging, Interaction, and Measurement. SPIE-IS&T, pp. 1–15.
https://doi.org/10.1117/12.871211

Berra, E., Gibson-Poole, S., MacArthur, A., Gaulton, R., Hamilton, A., 2015. Estimation of
the spectral sensitivity functions of un-modified and modified commercial off-the-shelf
digital cameras to enable their use as a multispectral imaging system for UAVs, in:
International Conference on Unmanned Aerial Vehicles in Geomatics. The
International Archives of the Photogrammetry, Remote Sensing and Spatial
Information Sciences, Toronto, pp. 207–214. https://doi.org/10.5194/isprsarchives-XL-
1-W4-207-2015

Berrier, S., Tetzlaff, M., Ludwig, M., Meyer, G., 2015. Improved appearance rendering for
photogrammetrically acquired 3D models, in: 2015 Digital Heritage. IEEE, Granada,
pp. 255–262. https://doi.org/10.1109/DigitalHeritage.2015.7413879

Billiot, B., Cointault, F., Journaux, L., Simon, J.-C., Gouton, P., 2013. 3D Image Acquisition
System Based on Shape from Focus Technique. Sensors 13, pp. 5040–5053.
https://doi.org/10.3390/s130405040

Boer, J.R.J.V.A. De, 1969. Reflectography of Paintings Using an Infrared Vidicon
Television System. Studies in Conservation 14, pp. 96–118.

Bomarito, G.F., Ruggles, T.J., Hochhalter, J.D., Cannon, A.H., 2017. Investigation of
optimal digital image correlation patterns for deformation measurement. Conference
Proceedings of the Society for Experimental Mechanics Series.
https://doi.org/10.1007/978-3-319-51439-0_51

Bongiorno, D.L., Bryson, M., Dansereau, D.G., Williams, S.B., 2013. Spectral
characterization of COTS RGB cameras using a linear variable edge filter. IS&T/SPIE
Electronic Imaging 8660, pp. 1–10. https://doi.org/10.1117/12.2001460

Bossuyt, S., 2013. Optimized patterns for digital image correlation. Conference Proceedings
of the Society for Experimental Mechanics Series 3, pp. 239–248.
https://doi.org/10.1007/978-1-4614-4235-6_34

Bryan, P., Blake, B., Bedford, J., Mills, J., 2009. Metric Survey Specifications for Cultural
Heritage. English Heritage.

Burns, P.D., Williams, D., 2008. Sampling efficiency in digital camera performance
standards, in: Proceedings SPIE-IS&T Electronic Imaging Symposium. SPIE-IS&T,
San Jose, pp. 1–5. https://doi.org/10.1117/12.766359

Casini, A., Bacci, M., Cucci, C., Lotti, F., Porcinai, S., Picollo, M., Radicati, B., Poggesi,

M., Stefani, L., 2005. Fiber optic reflectance spectroscopy and hyper-spectral image spectroscopy: two integrated techniques for the study of the Madonna dei Fusi, in: Proceedings SPIE 5857: Optical Methods for Arts and Archaeology. SPIE.

Casini, A., Lotti, F., Picollo, M., Stefani, L., Buzzegoli, E., 1999. Image spectroscopy mapping technique for noninvasive analysis of paintings. Studies in Conservation 44, pp. 39–48. https://doi.org/10.1179/sic.1999.44.1.39

CHARISMA: Technical Imaging [WWW Document], 2017. CHARISMA Project Website. URL http://www.britishmuseum.org/research/research_projects/all_current_projects/charisma/technical_imaging.aspx (accessed 5.28.18).

CHI 4-Day Photogrammetry Training [WWW Document], 2018. Cultural Heritage Imaging Website. URL http://culturalheritageimaging.org/What_We_Offer/Training/photogram_training/index.html (accessed 9.5.18).

Christens-Barry, W.A., Boydston, K., France, F.G., Knox, K.T., Easton, J.R.L., Toth, M.B., 2009. Camera system for multispectral imaging of documents, in: Bodegom, E., Nguyen, V. (Eds.), Proceedings of SPIE-IS&T Electronic Imaging: Sensors Cameras and Systems for Industrial/Scientific Applications X. SPIE-IS&T, pp. 1–10. https://doi.org/10.1117/12.815374

Cignoni, P., Callieri, M., Corsini, M., Dellepiane, M., Ganovelli, F., Ranzuglia, G., 2008. MeshLab: an Open-Source Mesh Processing Tool, in: Scarano, V., Chiara, R. De, Erra, U. (Eds.), Sixth Eurographics Italian Chapter Conference. The Eurographics Association, Salerno, pp. 129–136.

CIPA Heritage Documentation [WWW Document], n.d. URL http://cipa.icomos.org/ (accessed 1.4.19).

Clini, P., Frapiccini, N., Mengoni, M., Nespeca, R., Ruggeri, L., 2016. SFM technique and focus stacking for digital documentation of archaeological artifacts, in: XXIII ISPRS Congress. International Archives of the Photogrammetry, Remote Sensing and Spatial Information Sciences - ISPRS Archives, Prague, pp. 229–236. https://doi.org/10.5194/isprsarchives-XLI-B5-229-2016

CloudCompare [WWW Document], 2018. URL http://www.danielgm.net/cc/ (accessed 12.16.18).

Coffin, D., 2009. Decoding raw digital photos in Linux [WWW Document]. URL http://www.cybercom.net/~dcoffin/dcraw/ (accessed 7.8.17).

Colour and Space in Cultural Heritage (COSCH) [WWW Document], n.d. URL http://cosch.info/home (accessed 8.1.17).

Coughlan, C.A., Cerussi, A.E., Kim, J., Ison, S., Bhandarkar, N.D., 2016. Near-Infrared Optical Imaging for Diagnosis of Maxillary Sinusitis. Otolaryngology -- Head and Neck Surgery 155, pp. 538–541. https://doi.org/10.1177/0194599816655309

Creating a Digital Smithsonian: Digitization Strategic Plan (2010-2015), 2010. Smithsonian Institution, Washington, DC. URL https://www.si.edu/content/pdf/about/2010_SI_Digitization_Plan.pdf (accessed 1.9.20).

CS3DP (Community Standards for 3D Data Preservation) [WWW Document], n.d. URL https://osf.io/ewt2h/ (accessed 1.20.20).

Cucci, C., Casini, A., Stefani, L., Picollo, M., Jussila, J., 2017. Bridging research with innovative products: a compact hyperspectral camera for investigating artworks: a feasibility study, in: Pezzati, L., Targowski, P. (Eds.), Proceedings SPIE 10331: Optics

for Arts, Architecture, and Archaeology VI. SPIE, Munich, pp. 1–13. https://doi.org/10.1117/12.2270015

Cucci, C., Delaney, J.K., Picollo, M., 2016. Reflectance Hyperspectral Imaging for Investigation of Works of Art : Old Master Paintings and Illuminated Manuscripts. Accounts of Chemical Research 49, pp. 2070–2079. https://doi.org/10.1021/acs.accounts.6b00048

Cucci, C., Webb, E.K., Casini, A., Ginanni, M., Prandi, E., Stefani, L., Vitorino, T., Picollo, M., 2019. Short-wave infrared reflectance hyperspectral imaging for painting investigations: A methodological study. Journal of the American Institute for Conservation 58, pp. 16–36. https://doi.org/10.1080/01971360.2018.1543102

Cultural Heritage Imaging, 2015. Scale Bars for Photogrammetry: User Guide. v1.0.

Darrodi, M.M., Finlayson, G., Goodman, T., Mackiewicz, M., 2015. Reference data set for camera spectral sensitivity estimation. Journal of the Optical Society of America A 32, pp. 381–391. https://doi.org/10.1364/JOSAA.32.000381

Davies, A., 2018. Digital Ultraviolet and Infrared Photography. Routledge, New York.

de la Rie, E.R., 1982. Fluorescence of paint and varnish layers (Part 1). Studies in Conservation 27, pp. 1–7.

De Reu, J., De Smedt, P., Herremans, D., Van Meirvenne, M., Laloo, P., De Clercq, W., 2014. On introducing an image-based 3D reconstruction method in archaeological excavation practice. Journal of Archaeological Science 41, pp. 251–262. https://doi.org/10.1016/j.jas.2013.08.020

Delaney, J.K., Thoury, M., Zeibel, J.G., Ricciardi, P., Morales, K.M., Dooley, K.A., 2016. Visible and infrared imaging spectroscopy of paintings and improved reflectography. Heritage Science 4. https://doi.org/10.1186/s40494-016-0075-4

Delaney, J.K., Zeibel, J.G., Thoury, M., Littleton, R., Palmer, M., Morales, K.M., de la Rie, E.R., Hoenigswald, A., 2010. Visible and Infrared Imaging Spectroscopy of Picasso's Harlequin Musician: Mapping and Identification of Artist Materials in Situ. Applied Spectroscopy 64, pp. 584–594.

Déliot, P., Duffaut, J., Lacan, A., 2006. Characterization and calibration of a high-resolution multi-spectral airborne digital camera, in: Proceedings SPIE 6031, ICO20: Remote Sensing and Infrared Devices and Systems, 603104. SPIE, Changchun, pp. 1–10. https://doi.org/10.1117/12.667894

Dellepiane, M., Dell'Unto, N., Callieri, M., Lindgren, S., Scopigno, R., 2013. Archeological excavation monitoring using dense stereo matching techniques. Journal of Cultural Heritage 14, pp. 201–210. https://doi.org/10.1016/j.culher.2012.01.011

Dooley, K.A., Lomax, S., Zeibel, J.G., Miliani, C., Ricciardi, P., Hoenigswald, A., Loew, M., Delaney, J.K., 2013. Mapping of egg yolk and animal skin glue paint binders in Early Renaissance paintings using near infrared reflectance imaging spectroscopy. The Analyst 138, pp. 4838–4848. https://doi.org/10.1039/c3an00926b

Dyer, J., Sotiropoulou, S., 2017. A technical step forward in the integration of visible - induced luminescence imaging methods for the study of ancient polychromy. Heritage Science 5, pp. 1–21. https://doi.org/10.1186/s40494-017-0137-2

Dyer, J., Tamburini, D., O'Connell, E.R., Harrison, A., 2018. A multispectral imaging approach integrated into the study of Late Antique textiles from Egypt. Plos One 13, pp. 1–33. https://doi.org/10.1371/journal.pone.0204699

Dyer, J., Verri, G., Cupitt, J., 2013. Multispectral Imaging in Reflectance and Photo-induced Luminescence modes: A User Manual [WWW Document]. URL https://www.britishmuseum.org/pdf/charisma-multispectral-imaging-manual-2013.pdf

Engel, J., 2011. 3D applications in museological context. Master's Thesis, The Royal Danish Academy of Fine Arts, Schools of Architecture, Design and Conservation, Copenhagen, Denmark.

European Machine Vision Association, 2012. EMVA Standard 1288: Standard for characterization of Image Sensors and Cameras. https://doi.org/10.1007/978-3-642-39360-0

Falco, C.M., 2009. High resolution digital camera for infrared reflectography. Review of Scientific Instruments 80. https://doi.org/10.1063/1.3174431

Fischer, C., Kakoulli, I., 2007. Multispectral and hyperspectral imaging technologies in conservation : current research and potential applications. Reviews in Conservation 7, pp. 3–16.

Fluorilon-99W [WWW Document], 2018. URL https://aviantechnologies.com/catalog/fluorilon-99w-2/ (accessed 12.7.18).

Flynn, T., 2019. Over 100,000 Cultural Heritage 3D Models on Sketchfab [WWW Document]. SketchFab blogBlog. URL https://sketchfab.com/blogs/community/over-100000-cultural-heritage-3d-models-on-sketchfab/ (accessed 11.21.19).

Foresta, M.A., 2004. At First Sight: Photography and the Smithsonian. Smithsonian Books, Washington, DC.

France, F.G., Toth, M.B., Christens-Barry, W.A., Boydston, K., 2010. Advanced Spectral Imaging for Microanalysis of Cultural Heritage. Microscopy and Microanalysis 16, pp. 728–729. https://doi.org/10.1017/S14319276100

Furukawa, Y., Ponce, J., 2010. Accurate, Dense, and Robust Multi-View Stereopsis. IEEE Transactions on Pattern Analysis and Machine Intelligence 32, pp. 1362–1376. https://doi.org/10.1109/FDL.2016.7880384

Gaiani, M., Remondino, F., Apollonio, F.I., Ballabeni, A., 2016. An advanced pre-processing pipeline to improve automated photogrammetric reconstructions of architectural scenes. Remote Sensing 8, pp. 1–27. https://doi.org/10.3390/rs8030178

Galeazzi, F., 2016. Towards the definition of best 3D practices in archaeology: Assessing 3D documentation techniques for intra-site data recording. Journal of Cultural Heritage 17, pp. 159–169. https://doi.org/10.1016/j.culher.2015.07.005

Gallo, A., Bruno, F., Muzzupappa, M., La Russa, M.F., 2012. Multi-view 3D reconstruction of small stone samples deteriorated by marine organisms, in: Proceedings of the 2012 18th International Conference on Virtual Systems and Multimedia, VSMM 2012: Virtual Systems in the Information Society. IEEE, pp. 181–187. https://doi.org/10.1109/VSMM.2012.6365923

Gallo, A., Muzzupappa, M., Bruno, F., 2014. 3D reconstruction of small sized objects from a sequence of multi-focused images. Journal of Cultural Heritage 15, pp. 173–182. https://doi.org/10.1016/j.culher.2013.04.009

Garcia, J.E., Wilksch, P.A., Spring, G., Philp, P., Dyer, A., 2014. Characterization of Digital Cameras for Reflected Ultraviolet Photography; Implications for Qualitative and Quantitative Image Analysis During Forensic Examination. Journal of Forensic Sciences 59, pp. 117–122. https://doi.org/10.1111/1556-4029.12274

Garland, K.M., Bernstein, J., Rogers, J., 2015. Raising Meret-It-Es: Examining and conserving an Egyptian anthropoid coffin from 380–250 BCE. Journal of the American Institute for Conservation 54, pp. 102–113. https://doi.org/10.1179/1945233015Y.0000000003

Gavrilov, D., Maeva, E., Grube, O., Vodyanoy, I., Maev, R., 2013. Experimental comparative study of the applicability of infrared techniques for non-destructive

evaluation of paintings. Journal of the American Institute for Conservation 52, pp. 48–60. https://doi.org/10.1179/0197136012Z.00000000002

Geffert, S., Loike, A., Ruiz-Molina, M., Serotta, A., 2018. A Workflow for Color and Tone Calibrated Multiband Imaging, Presentation at the American Institute for Conservation 46th Annual Meeting: Material Matters. Houston.

George, S., Hardeberg, J., Linhares, J., MacDonald, L., Montagner, C., Nascimento, S., Picollo, M., Pillay, R., Vitorino, T., Webb, E.K., 2017. A study of spectral imaging acquisition and processing for cultural heritage, in: Bentkowska-Kafel, A., MacDonald, L. (Eds.), Digital Techniques for Documenting and Preserving Cultural Heritage. The Applied Research Centre in the Humanities and Press Ltd, Kalamazzo, Michigan.

Gernoth, T., Grigat, R.-R., 2010. Camera characterization for face recognition under active near-infrared illumination, in: Farnand, S.P., Gaykema, F. (Eds.), Proceedings of SPIE-IS&T Electronic Imaging, SPIE Vol. 7529. SPIE-IS&T, pp. 1–9. https://doi.org/10.1117/12.839001

Gibson, A., Piquette, K.E., Bergmann, U., Christens-Barry, W., Davis, G., Endrizzi, M., Fan, S., Farsiu, S., Fitzgerald, A., Griffiths, J., Jones, C., Li, G., Manning, P.L., Maughan Jones, C., Mazza, R., Mills, D., Modregger, P., Munro, P.R.T., Olivo, A., Stevenson, A., Venugopal, B., Wallace, V., Wogelius, R.A., Toth, M.B., Terras, M., 2018. An assessment of multimodal imaging of subsurface text in mummy cartonnage using surrogate papyrus phantoms. Heritage Science 6, pp. 1–13. https://doi.org/10.1186/s40494-018-0175-4

GoldenThread User's Manual, n.d. . Image Science Associates, Rochester, NY.

GOM Inspect Professional V8 SR1 Basic Manual: Inspection 3D Metrology [WWW Document], 2015. URL http://www.gom.com/3d-software/gom-inspect/download.html (accessed 2.17.16).

Granshaw, S.I., 2016. Photogrammetric Terminology: Third Edition. Photogrammetric Record 31, pp. 210–252. https://doi.org/10.1111/phor.12146

Green, S., Bevan, A., Shapland, M., 2014. A comparative assessment of structure from motion methods for archaeological research. Journal of Archaeological Science 46, pp. 173–181. https://doi.org/10.1016/j.jas.2014.02.030

Guery, J., Hess, M., Mathys, A., 2017. Photogrammetry, in: Bentkowska-Kafel, A., MacDonald, L. (Eds.), Digital Techniques for Documenting and Preserving Cultural Heritage. ARC Humanities Press, Kalamazzo, pp. 229–235.

Guidi, G., Gonizzi, S., Micoli, L.L., 2014. Image pre-processing for optimizing automated photogrammetry performances, in: 2014 ISPRS Technical Commission V Symposium. ISPRS Annals of the Photogrammetry, Remote Sensing and Spatial Information Sciences, Riva del Garda, pp. 145–152. https://doi.org/10.5194/isprsannals-II-5-145-2014

Hawkins, D.S., Green, P., 2008. Spectral Characterisation of a Digital Still Camera Through a Single Integrating Exposure, in: Proceedings of 4th IS&T European Conference on Colour in Graphics, Imaging and Vision (CGIV). pp. 477–480.

Helicon Soft Ltd, n.d. Helicon Soft [WWW Document]. URL https://www.heliconsoft.com/ (accessed 6.7.19).

Hess, M., 2015a. A metric test object informed by user requirements for better 3D recording of cultural heritage artefacts. PhD Thesis, University College London, London, United Kingdom.

Hess, M., 2015b. Online Survey About Current Use Of 3D Imaging And Its User Requirements In Cultural Heritage Institutions, in: Digital Heritage 2015. IEEE, Granada, pp. 1–8.

Hess, M., Korenberg, C., Ward, C., Robson, S., Entwistle, C., 2015. Use of 3D laser scanning for monitoring the dimensional stability of a Byzantine ivory panel, in: Studies in Conservation. Maney Publishing and International Institute for Conservation of Historic and Artistic Artworks, Sharjah, pp. S126–S133.

Hess, M., MacDonald, L.W., Valach, J., 2018. Application of multi-modal 2D and 3D imaging and analytical techniques to document and examine coins on the example of two Roman silver denarii. Heritage Science pp. 1–22. https://doi.org/10.1186/s40494-018-0169-2

Hess, M., Robson, S., 2012. 3D imaging for museum artefacts: A portable test object for heritage and museum documentation of small objects, in: 2012 XXII ISPRS Congress. International Archives of the Photogrammetry, Remote Sensing and Spatial Information Sciences, Melbourne, pp. 103–108. https://doi.org/10.5194/isprsarchives-XXXIX-B5-103-2012

Hess, M., Robson, S., Millar, F.S., Were, G., Hviding, E., Berg, A.C., 2009. Niabara - The Western Solomon Islands war canoe at the british museum 3d documentation, virtual reconstruction and digital repatriation, in: 15th International Conference on Virtual Systems and Multimedia. IEEE, pp. 41–46. https://doi.org/10.1109/VSMM.2009.12

Hollinger, E., Partridge, N., 2017. 3D Technology May Revive this Ancient Hunting Tool [WWW Document]. Smithsonian Voices. URL https://www.smithsonianmag.com/blogs/national-museum-of-natural-history/2017/10/25/3d-technology-may-revive-ancient-hunting-tool/ (accessed 9.5.18).

Hollinger, R.E., Edwell John, J., Jacobs, H., Moran-Collins, L., Thome, C., Zastrow, J., Metallo, A., Waibel, G., Rossi, V., 2013. Tlingit-Smithsonian Collaborations with 3D Digitization of Cultural Objects. Museum Anthropology Review 7, pp. 201–253.

Hosseininaveh Ahmadabadian, A., Sargeant, B., Erfani, T., Robson, S., Shortis, M., Hess, M., Boehm, J., 2014. Towards fully automatic reliable 3D acquisition: From designing imaging network to a complete and accurate point cloud. Robotics and Autonomous Systems 62, pp. 1197–1207. https://doi.org/10.1016/j.robot.2014.04.001

IIIF 3D Community Group [WWW Document], n.d. URL https://iiif.io/community/groups/3d/ (accessed 1.20.20).

International Society for Photogrammetry and Remote Sensing [WWW Document], 2019. URL http://www.isprs.org/society/Default.aspx (accessed 1.3.19).

Interview with Fulvio Rinaudo: "Photogrammetry in Cultural Heritage: Is it only SfM software? [WWW Document], 2018. 2018 ISPRS TC II Mid-term Symposium "Towards Photogrammetry 2020". URL https://www.isprs.org/tc2-symposium2018/images/ISPRS-Interview-Rinaudo.pdf (accessed 4.14.19).

IR-UV Filters [WWW Document], 2015. URL http://www.ir-uv.com/iruv.html (accessed 11.8.17).

Jalandoni, A., Domingo, I., Taçon, P.S.C., 2018. Testing the value of low-cost Structure-from-Motion (SfM) photogrammetry for metric and visual analysis of rock art. Journal of Archaeological Science: Reports 17, pp. 605–616. https://doi.org/10.1016/j.jasrep.2017.12.020

James, M.R., Robson, S., 2014. Mitigating systematic error in topographic models derived from UAV and ground-based image networks. Earth Surface Processes and Landforms 39, pp. 1413–1420. https://doi.org/10.1002/esp.3609

James, M.R., Robson, S., Oleire-oltmanns, S., Niethammer, U., 2017. Optimising UAV topographic surveys processed with structure-from-motion: Ground control quality, quantity and bundle adjustment. Geomorphology 280, pp. 51–66. https://doi.org/10.1016/j.geomorph.2016.11.021

Janesick, J.R., 2001. Scientific Charge-Coupled Devices. SPIE Press, Bellingham, WA.

Jenoptik, n.d. UV-VIS-IR 60mm 1:4 Apo Macro Brochure [WWW Document]. URL https://www.jenoptik.com/cms/jenoptik.nsf/res/CoastalOpt 60mm UV-VIS-NIR SLR_V6.pdf/$file/CoastalOpt 60mm UV-VIS-NIR SLR_V6.pdf (accessed 2.21.18).

Ji, W., Rhodes, P.A., 2011. Spectral color characterization of digital cameras: a review, in: Galarneau, P., Liu, X., Li, P. (Eds.), Photonics and Optolectronics Meetings (POEM) 2011: Optoelectronic Sensing and Imaging. SPIE, pp. 1–8. https://doi.org/10.1117/12.915768

Jiang, J., Liu, D., Gu, J., Susstrunk, S., 2013a. What is the Space of Spectral Sensitivity Functions for Digital Color Cameras?, in: 2013 IEEE Workshop on Applications of Computer Vision (WACV). IEEE, pp. 168–179.

Jiang, J., Liu, D., Gu, J., Süsstrunk, S., 2013b. Camera Spectral Sensitivity Database [WWW Document]. URL http://www.gujinwei.org/research/camspec/db.html (accessed 9.11.17).

Kakoulli, I., Radpour, R., Lin, Y., Svoboda, M., Fischer, C., 2017. Application of forensic photography for the detection and mapping of Egyptian blue and madder lake in Hellenistic polychrome terracottas based on their photophysical properties. Dyes and Pigments 136, pp. 104–115. https://doi.org/10.1016/j.dyepig.2016.08.030

Kawakami, R., Zhao, H., Tan, R.T., Ikeuchi, K., 2013. Camera spectral sensitivity and white balance estimation from sky images. International Journal of Computer Vision 105, pp. 187–204. https://doi.org/10.1007/s11263-013-0632-1

Keck, S., 1941. A Use of Infra-red Photography in the Study of Technique. Technical Studies in the Field of the Fine Arts IX, pp. 145–152.

Kersten, T.P., Lindstaedt, M., 2012. Image-based low-cost systems for automatic 3D recording and modelling of archaeological finds and objects, in: Ioannides, M., Al., E. (Eds.), Proceedings of EuroMed 2012 Conference. Springer Berlin Heidelberg, pp. 1–10. https://doi.org/10.1007/978-3-642-34234-9_1

Kim, M.H., Kautz, J., 2008. Characterization for High Dynamic Range Imaging. Computer Graphics Forum 27, 2008.

Knox, K.T., 2008. Enhancement of overwritten text in the Archimedes Palimpsest, in: SPIE (Ed.), Proceedings SPIE 6810, Computer Image Analysis in the Study of Art. San Jose, California. https://doi.org/10.1117/12.766679

Koutsoudis, A., Vidmar, B., Arnaoutoglou, F., 2013. Performance evaluation of a multi-image 3D reconstruction software on a low-feature artefact. Journal of Archaeological Science 40, pp. 4450–4456. https://doi.org/10.1016/j.jas.2013.07.007

Koutsoudis, A., Vidmar, B., Ioannakis, G., Arnaoutoglou, F., Pavlidis, G., Chamzas, C., 2014. Multi-image 3D reconstruction data evaluation. Journal of Cultural Heritage 15, pp. 73–79. https://doi.org/10.1016/j.culher.2012.12.003

Labbé, S., Roux, B., Bégué, A., Lebourgeois, V., B Mallavan, 2007. An operational solution to acquire multispectral images with standard light cameras: Characterization and acquisition guidelines, in: ISPRS Workshop Airborne Digital Photogrammetric Sensor Systems. Newcastle, pp. 1–6.

Lebourgeois, V., Bégué, A., Labbé, S., Mallavan, B., Prévot, L., Roux, B., 2008. Can commercial digital cameras be used as multispectral sensors? A crop monitoring test. Sensors 8, pp. 7300–7322. https://doi.org/10.3390/s8117300

Lehmann, J.R.K., Nieberding, F., Prinz, T., Knoth, C., 2015. Analysis of unmanned aerial system-based CIR images in forestry-a new perspective to monitor pest infestation levels. Forests 6, pp. 594–612. https://doi.org/10.3390/f6030594

Lerma, J.L., Muir, C., 2014. Evaluating the 3D documentation of an early Christian upright stone with carvings from Scotland with multiples images. Journal of Archaeological Science 46, pp. 311–318. https://doi.org/10.1016/j.jas.2014.02.026

Levoy, M., 2006. Light fields and computational imaging. Computer 39, pp. 46–55. https://doi.org/10.1109/MC.2006.270

Liang, H., 2012. Advances in multispectral and hyperspectral imaging for archaeology and art conservation. Applied Physics A: Materials Science and Processing 106, pp. 309–323. https://doi.org/10.1007/s00339-011-6689-1

Liang, H., Lucian, A., Lange, R., Shing, C., Su, B., 2014. Remote spectral imaging with simultaneous extraction of 3D topography for historical wall paintings. ISPRS Journal of Photogrammetry and Remote Sensing 95, pp. 13–22. https://doi.org/10.1016/j.isprsjprs.2014.05.011

Luhmann, T., 2011. 3D imaging: How to achieve highest accuracy, in: Proc. SPIE 8085, Videometrics, Range Imaging, and Applications XI. SPIE, Munich, pp. 1–11. https://doi.org/10.1117/12.892070

Luhmann, T., Robson, S., Kyle, S., Boehm, J., 2014. Close-Range Photogrammetry and 3D Imaging, 2nd ed. De Gruyter, Berlin.

Lyon, R.A., 1934. Ultra-violet Rays as Aids to Restorers. Technical Studies in the Field of the Fine Arts 2, pp. 153–157.

MacDonald, L., 2010. The limits of resolution, in: Proceedings of Conference on Electronic Visualisation and the Arts (EVA). London, pp. 149–156.

MacDonald, L., Hindmarch, J., Robson, S., Terras, M., 2014. Modelling the appearance of heritage metallic surfaces, in: ISPRS Technical Commission V Symposium. The International Archives of the Photogrammetry, Remote Sensing and Spatial Information Sciences, Riva del Garda, pp. 371–377. https://doi.org/10.5194/isprsarchives-XL-5-371-2014

MacDonald, L.W., 2015. Determining Camera Spectral Responsivity with Multispectral Transmission Filters, in: Color and Imaging Conference. Society for Imaging Science and Technology, pp. 12–17.

Mahgoub, H., Chen, H., Gilchrist, J.R., Fearn, T., Strlič, M., 2017. Quantitative chemical near-infrared hyperspectral imaging of Islamic paper, in: Bridgland, J. (Ed.), ICOM-CC 18th Triennial Conference Proceedings. International Council of Museums, Copenhagen.

Manakov, A., 2016. Evaluation of computational radiometric and spectral sensor calibration techniques, in: Proceedings SPIE 9896, Optics, Photonics and Digital Technologies for Imaging Applications IV. SPIE, Brussels, pp. 1–14. https://doi.org/10.1117/12.2228071

Marchou, R., [WWW Document] 2017. Over 500 Cultural Institutions have joined Sketchfab. SketchFab blog. URL https://blog.sketchfab.com/500-cultural-institutions-joined-sketchfab/ (accessed 11.21.19).

Martinez, K., Cupitt, J., Saunders, D., Pillay, R., 2002. Ten Years of Art Imaging Research, in: Proceedings of the IEEE. IEEE, pp. 28–41. https://doi.org/10.1109/5.982403

Marziali, S., Dionisio, G., 2017. Photogrammetry and macro photography. The experience of the MUSINT II Project in the 3D digitizing process of small size archaeological artifacts. Studies in Digital Heritage 1, pp. 298–309. https://doi.org/10.14434/sdh.v1i2.23250

Matthews, N.A., 2008. Aerial and Close-Range Photogrammetric Technology: Providing Resource Decumentation, Interpretation, and Preservation, Technical Note 428. Denver, Colorado. https://doi.org/10.1017/CBO9781107415324.004

MaxMax Cameras [WWW Document], n.d. URL https://www.maxmax.com/maincamerapage (accessed 2.19.18).

McGlinchey Sexton, J., Messier, P., Chen, J.J., 2014. Development and Testing of a Fluorescence Standard for Documenting Ultraviolet Induced Visible Fluorescence, in: 42nd Annual American Institute for Conservation Meeting. American Institute for Conservation, San Francisco, pp. 1–42.

Menna, F., Nocerino, E., Remondino, F., 2018. Photogrammetric Modelling of Submerged Structures: Influence of Underwater Environment and Lens Ports on Three-Dimensional (3D) Measurements, in: Remondino, F., Georgopoulos, A., González-Aguilera, D., Agrafiotis, P. (Eds.), Latest Developments in Reality-Based 3D Surveying and Modelling. MDPI, pp. 279–303.

Menna, F., Nocerino, E., Remondino, F., Dellepiane, M., Callieri, M., Scopigno, R., 2016. 3D Digitization of an Heritage Masterpiece: A Critical Analysis on Quality Assessment, in: 2016 XXIII ISPRS Congress. The International Archives of the Photogrammetry, Remote Sensing and Spatial Information Sciences, Prague, pp. 675–683. https://doi.org/10.5194/isprsarchives-XLI-B5-675-2016

Menna, F., Rizzi, A., Nocerino, E., Remondino, F., Gruen, A., 2012. High Resolution 3D Modeling of the Behaim Globe, in: 2012 XXII ISPRS Congress. International Archives of the Photogrammetry, Remote Sensing and Spatial Information Sciences, Melbourne, pp. 115–120. https://doi.org/10.5194/isprsarchives-XXXIX-B5-115-2012

Mounier, A., Daniel, F., 2015. Hyperspectral imaging for the study of two thirteenth-century Italian miniatures from the Marcadé collection, Treasury of the Saint- Andre Cathedral in Bordeaux, France, in: Elnagger, A., Nevin, A., Castillejo, M., Strlič, M. (Eds.), LASERS IN THE CONSERVATION OF ARTWORKS. Maney Publishing and International Institute for Conservation of Historic and Artistic Artworks, Sharjah, pp. S200–S209.

Mudge, M., Malzbender, T., Chalmers, A., Scopigno, R., Davis, J., Wang, O., Gunawardane, P., Ashley, M., Doerr, M., Proenca, A., Barbosa, J., 2008. Image-Based Empirical Information Acquisition, Scientific Reliability, and Long-Term Digital Preservation for the Natural Sciences and Cultural Heritage. Eurographics.

Mulholland, R., Howell, D., Beeby, A., Nicholson, C.E., Domoney, K., 2017. Identifying eighteenth century pigments at the Bodleian library using in situ Raman spectroscopy, XRF and hyperspectral imaging. Heritage Science 5. https://doi.org/10.1186/s40494-017-0157-y

Nasse, H.H., 2010. Depth of Field and Bokeh [WWW Document]. URL https://dslrpro.net/wp-content/uploads/2013/02/Depth-of-Field-and-Bokeh.pdf (accessed 11.15.17).

Nayar, S.K., Nakagawa, Y., 1994. Shape from Focus. IEEE Transactions on Pattern Analysis and Machine Intelligence 16, pp. 824–831. https://doi.org/10.1109/34.308479

Ng, K.T., Zhu, Z.Y., Wang, C., Chan, S.C., Shum, H.Y., 2012. A multi-camera approach to image-based rendering and 3-D/Multiview display of ancient chinese artifacts. IEEE Transactions on Multimedia 14, pp. 1631–1641. https://doi.org/10.1109/TMM.2012.2199291

Ng, R., Levoy, M., Bredif, M., Duval, G., Horowitz, M., Hanrahan, P., 2005. Light Field Photography with a Hand-held Plenoptic Camera, Stanford Tech Report CTSR 2005-02. Palo Alto.

Nicolae, C., Nocerino, E., Menna, F., Remondino, F., 2014. Photogrammetry applied to Problematic artefacts, in: 2014 ISPRS Technical Commission V Symposium. The International Archives of the Photogrammetry, Remote Sensing and Spatial Information Sciences, Riva del Garda, pp. 451–456. https://doi.org/10.5194/isprsarchives-XL-5-451-2014

Nikon, 2017. Nikon D850 Brochure [WWW Document]. URL http://cdn-4.nikon-cdn.com/e/Q5NM96RZZo-YRYNeYvAi9beHK4x3L-8h09FYyKWnWU6L2l14O7STBw==/Misc/D850_brochure.pdf (accessed 1.2.18).

Nobel, J.J.I.-L., 2017. Buying a Focus Stacking Rail? [WWW Document]. The Extremist: Companion blog to extreme-macro.co.uk. URL http://extreme-macro.co.uk/extremist/buying-a-focus-stacking-rail/ (accessed 1.2.18).

Nocerino, E., Menna, F., Remondino, F., 2014. Accuracy of Typical Photogrammetric Networks in Cultural Heritage 3D Modeling Projects, in: 2014 ISPRS Technical Commission V Symposium. The International Archives of the Photogrammetry, Remote Sensing and Spatial Information Sciences, Riva del Garda, pp. 465–472. https://doi.org/10.5194/isprsarchives-XL-5-465-2014

Noya, N.C., García, Á.L., Ramírez, F.C., 2015. Combining photogrammetry and photographic enhancement techniques for the recording of megalithic art in north-west Iberia. Digital Applications in Archaeology and Cultural Heritage 2, pp. 89–101. https://doi.org/10.1016/j.daach.2015.02.004

Olympus America Inc., 2016. Revolutionary Camera Performance: The Olympus OM-D E-M1 Mark II Arrives [WWW Document]. URL http://www.olympusamerica.com/corporate/corp_presscenter_headline.asp?pressNo=2077 (accessed 1.2.18).

OSIRIS Camera [WWW Document], n.d. URL https://www.opusinstruments.com/products/osiris-camera/ (accessed 2.3.19).

Panasonic, n.d. Post Focus [WWW Document]. URL https://www.panasonic.com/au/consumer/lumix-cameras-video-cameras/lumix-g-cameras-learn/article/post-focus.html (accessed 1.2.18).

Percoco, G., Guerra, M.G., Sanchez Salmeron, A.J., Galantucci, L.M., 2017. Experimental investigation on camera calibration for 3D photogrammetric scanning of micro-features for micrometric resolution. The International Journal of Advanced Manufacturing Technology pp. 1–13. https://doi.org/10.1007/s00170-016-9949-6

Pertuz, S., Puig, D., Garcia, M.A., 2013. Analysis of focus measure operators for shape-from-focus. Pattern Recognition 46, pp. 1415–1432. https://doi.org/10.1016/j.patcog.2012.11.011

Photogrammetric Applications for Cultural Heritage: Guidance for Good Practice, 2017. Historic England, Swindon.

Pike, T.W., 2011. Using digital cameras to investigate animal colouration: Estimating sensor sensitivity functions. Behavioral Ecology and Sociobiology 65, pp. 849–858. https://doi.org/10.1007/s00265-010-1097-7

Plisson, H., Zotkina, L. V., 2015. From 2D to 3D at macro- and microscopic scale in rock art studies. Digital Applications in Archaeology and Cultural Heritage 2, pp. 102–119. https://doi.org/10.1016/j.daach.2015.06.002

Porter, S.T., Roussel, M., Soressi, M., 2016. A Simple Photogrammetry Rig for the Reliable Creation of 3D Artifact Models in the Field. Advances in Archaeological Practice 4, pp. 71–86. https://doi.org/10.7183/2326-3768.4.1.71

Prasad, D.K., Brown, M.S., 2013. Quick Approximation of Camera's Spectral Response from Casual Lighting, in: Proceedings of the IEEE International Conference on Computer Vision. IEEE Xplore, pp. 844–851. https://doi.org/10.1109/ICCVW.2013.116

Radley, J.A., Grant, J., 1959. Fluorescence Analysis in Ultra-violet Light, 4th ed. Chapman & Hall Ltd, London.

Radley, J.A., Grant, J., 1939. Fluorescence Analysis in Ultra-violet Light, 3rd ed. Chapman & Hall Ltd, London.

Radley, J.A., Grant, J., 1935. Fluorescence Analysis in Ultra-violet Light, 2nd ed. Chapman & Hall Ltd, London.

Radley, J.A., Grant, J., 1933. Fluorescence Analysis in Ultra-violet Light, 1st ed. Chapman & Hall Ltd, London.

Rawlins, F.I.G., 1942. The physics of paintings, Reports on Progress in Physics. London. https://doi.org/10.1088/0034-4885/9/1/320

Ray, S.F., 2002. Applied Photographic Optics, 3rd ed. Focal Press, Oxford.

Ray, S.F., 1999. Scientific Photography and Applied Imaging. Focal Press, Oxford.

Remondino, F., 2011a. Accurrate and Detailed Image-Based 3D Documentation of Large Sites and Complex Objects, in: Stanco, F., Battiato, S., Gallo, G. (Eds.), Digital Imaging for Cultural Heritage Preservation: Analysis, Restoration, and Reconstruction of Ancient Artworks. CRC Press, Boca Raton, pp. 127–157.

Remondino, F., 2011b. Advanced 3D Recording Techniques for the Digital Documentation and Conservation of Heritage Sites and Objects. Change Over Time 1, pp. 198–214. https://doi.org/10.1353/cot.2011.0012

Remondino, F., 2011c. Heritage recording and 3D modeling with photogrammetry and 3D scanning. Remote Sensing 3, pp. 1104–1138. https://doi.org/10.3390/rs3061104

Remondino, F., El-Hakim, S., 2006. Image-based 3D Modelling: A Review. The Photogrammetric Record 21, pp. 269–291.

Remondino, F., Gaiani, M., Apollonio, F., Ballabeni, A., Ballabeni, M., Morabito, D., Heritage, C., 2016. 3D Documentation of 40 Kilometers of Historical Porticoes – the Challenge, in: 2016 XXIII ISPRS Congress. The International Archives of the Photogrammetry, Remote Sensing and Spatial Information Sciences, Prague, pp. 12–19. https://doi.org/10.5194/isprsarchives-XLI-B5-711-2016

Remondino, F., Menna, F., 2008. Image-Based Surface Measurement for Close-Range Heritage Documentation, in: XXI ISPRS Congress. The International Archives of the Photogrammetry, Remote Sensing and Spatial Information Sciences, Beijing, pp. 199–206.

Remondino, F., Menna, F., Koutsoudis, A., Chamzas, C., El-Hakim, S., 2013. Design and implement a reality-based 3D digitisation and modelling project, in: Digital Heritage International Congress. IEEE, Marseilles, pp. 137–144. https://doi.org/10.1109/DigitalHeritage.2013.6743723

Remondino, F., Nocerino, E., Toschi, I., Menna, F., 2017. A critical review of automated photogrammetric processing of large datasets, in: 2017 26th International CIPA Symposium 2017. The International Archives of the Photogrammetry, Remote Sensing and Spatial Information Sciences, Ottawa, pp. 591–599. https://doi.org/10.5194/isprs-archives-XLII-2-W5-591-2017

Remondino, F., Pizzo, S. Del, Kersten, T.P., Troisi, S., 2012. Low-Cost and Open-Source Solutions for Automated Image Orientation – A Critical Overview, in: Ioannides, M., Fritsch, D., Leissner, J., Davies, R., Remondino, F., Caffo, R. (Eds.), Progress in Cultural Heritage Preservation: 4th International Conference EuroMed 2012. Springer, Limassol, pp. 40–54.

Remondino, F., Rizzi, A., Barazzetti, L., Scaioni, M., Fassi, F., Brumana, R., Pelagotti, A., 2011a. Review of geometric and radiometric analyses of paintings. Photogrammetric Record 26, pp. 439–461. https://doi.org/10.1111/j.1477-9730.2011.00664.x

Remondino, F., Rizzi, A., Barazzetti, L., Scaioni, M., Fassi, F., Brumana, R., Pelagotti, A., 2011b. Review of geometric and radiometric analyses of paintings. Photogrammetric Record 26, pp. 439–461. https://doi.org/10.1111/j.1477-9730.2011.00664.x

Remondino, F., Spera, M.G., Nocerino, E., Menna, F., Nex, F., 2014. State of the art in high density image matching. The Photogrammetric Record 29, pp. 144–166. https://doi.org/10.1111/phor.12063

Ribés, A., Schmitt, F., Pillay, R., Lahanier, C., 2005. Calibration and spectral reconstruction for CRISATEL: An art painting multispectral acquisition system. Journal of Imaging Science and Technology 49, pp. 563–573.

Ricciardi, P., Delaney, J.K., Facini, M., Zeibel, J.G., Picollo, M., Lomax, S., Loew, M., 2012. Near Infrared Reflectance Imaging Spectroscopy to Map Paint Binders In Situ on Illuminated Manuscripts. Angewandte Chemie International Edition 51, pp. 5607–5610. https://doi.org/10.1002/anie.201200840

Rieger, T. (Ed.), 2016. Technical Guidelines for Digitizing Cultural Heritage Materials : Creation of Raster Image Files, Federal Agencies Digital Guidelines Initiative. Rochester.

Robson, S., Bucklow, S., Woodhouse, N., Papadakia, H., 2004. Periodic photogrammetric monitoring and surface reconstruction of a historical wood panel painting for restoration purposes, in: XX ISPRS Congress. The International Archives of the Photogrammetry, Remote Sensing and Spatial Information Sciences, Istanbul, pp. 395–401.

Robson, S., MacDonald, L., Kyle, S., Shortis, M., 2014. Multispectral calibration to enhance the metrology performance of C-mount camera systems, in: 2014 ISPRS Technical Commission V Symposium. The International Archives of the Photogrammetry, Remote Sensing and Spatial Information Sciences, Riva del Garda, pp. 517–521. https://doi.org/10.5194/isprsarchives-XL-5-517-2014

Robson, S., MacDonald, S., Were, G., Hess, M., 2012. 3D recording and museums, in: Warwick, C., Terras, M., Nyhan, J. (Eds.), Digital Humanities in Practice. Facet, London, pp. 91–116. https://doi.org/10.29085/9781856049054.006

Rorimer, J.J., 1934. Ultra-violet Rays and a Mino da Fiesole Problem. Technical Studies in the Field of the Fine Arts 2, pp. 71–80.

Rorimer, J.J., 1931. Ultra-violet rays and their use in the examination of works of art, the Met Museum. The Metropolitan Museum of Art, New York.

Rossi, V., Blundell, J., Wiedemeier, R., 2019. Smithsonian 3D Open Source Pipeline (Conference Presentation), Presentation at the 2+3D Photography Conference 2019. Rijksmuseum, Amsterdam.

Rupnik, E., Daakir, M., Pierrot Deseilligny, M., 2017. MicMac – a free, open-source solution for photogrammetry. Open Geospatial Data, Software and Standards 2. https://doi.org/10.1186/s40965-017-0027-2

Sapirstein, P., 2018. A high-precision photogrammetric recording system for small artifacts. Journal of Cultural Heritage 31, pp. 33–45. https://doi.org/10.1016/j.culher.2017.10.011

Sapirstein, P., 2016. Accurate measurement with photogrammetry at large sites. Journal of Archaeological Science 66, pp. 137–145. https://doi.org/10.1016/j.jas.2016.01.002

Sapirstein, P., Murray, S., 2017. Establishing Best Practices for Photogrammetric Recording During Archaeological Fieldwork. Journal of Field Archaeology 42, pp. 337–350. https://doi.org/10.1080/00934690.2017.1338513

Sargeant, B., Hosseininaveh A., A., Erfani, T., Robson, S., Boehm, J., 2013. A webcam photogrammetric method for robot calibration, in: Remondino, F., Shortis, M.R., Beyerer, J., León, F.P. (Eds.), Proceedings SPIE 8791, Videometrics, Range Imaging, and Applications XII; and Automated Visual Inspection. SPIE, Munich, pp. 1–13. https://doi.org/10.1117/12.2020484

Sargeant, B., Robson, S., Szigeti, E., Richardson, P., El-Nounu, A., Rafla, M., 2016. A method to achieve large volume, high accuracy photogrammetric measurements through the use of an actively deformable sensor mounting platform, in: 2016 XXIII ISPRS Congress. The International Archives of the Photogrammetry, Remote Sensing and Spatial Information Sciences, Prague, pp. 123–129. https://doi.org/10.5194/isprsarchives-XLI-B5-123-2016

Saunders, D., Cupitt, J., 1993. Image Processing at the National Gallery: The VASARI Project, in: Roy, A. (Ed.), National Gallery Technical Bulletin. National Gallery Publications Limited, London, pp. 72–85.

Saunders, D., Cupitt, J., Padfield, J., 2006. Digital Imaging for Easel Paintings, in: MacDonald, L. (Ed.), Digital Heritage: Applying Digital Imaging to Cultural Heritage. Butterworth-Heinemann, Oxford, pp. 521–548.

Schroer, C., Mudge, M., Leisch, E., Doerr, M., 2017a. A Context Metadata Collection and Management Tool for Computational Photography Projects. Archiving 2017 Final Program and Proceedings pp. 99–104. https://doi.org/10.2352/issn.2168-3204.2017.1.0.99

Schroer, C., Mudge, M., Lum, M., 2017b. Photogrammetry Training: Practical, Scientific Use of Photogrammetry in Cultural Heritage.

Simon Chane, C., 2013. Integration of high resolution spatial and spectral data acquisition systems for monitoring purposes in cultural heritage applications. Université de Bourgogne.

Simon Chane, C., Schütze, R., Boochs, F., Marzani, F., 2013. Registration of 3D and Multispectral Data for the Study of Cultural Heritage Surfaces. Sensors 13, pp. 1004–1020. https://doi.org/10.3390/s130101004

Skarlatos, D., Kiparissi, S., 2012. Comparison of Laser Scanning, Photogrammetry and SFM-MVS Pipeline Applied in Structures and Artificial Surfaces, in: 2012 XXII ISPRS Congress. ISPRS Annals of the Photogrammetry, Remote Sensing and Spatial Information Sciences, Melbourne, pp. 299–304. https://doi.org/10.5194/isprsannals-I-3-299-2012

Smithsonian 2022 [WWW Document], 2017. URL https://www.si.edu/strategicplan (accessed 11.18.19).

Smithsonian Digitization Program Office: 3D Digitization [WWW Document], 2019. URL https://dpo.si.edu/3d-digitization-program (accessed 11.18.19).

Snavely, N., Seitz, S.M., Szeliski, R., 2006. Photo Tourism: Exploring Photo Collections in 3D, in: ACM Transactions on Graphics (Proceedings of SIGGRAPH 2006). https://doi.org/10.1145/1141911.1141964

Spectral Sensitivity Database [WWW Document], n.d. URL http://www.nae-lab.org/~rei/research/cs/zhao/database.html (accessed 8.5.18).

Sterzik, V., Bohnert, M., 2016. Reconstruction of crimes by infrared photography. International Journal of Legal Medicine 130, pp. 1379–1385. https://doi.org/10.1007/s00414-016-1343-2

Szeliski, R., 2011. Computer vision: Algorithms and applications. Springer, London.

Tallon, L., 2017. Digital Is More Than a Department, It Is a Collective Responsibility [WWW Document]. Now at the Met Blog. URL https://www.metmuseum.org/blogs/now-at-the-met/2017/digital-future-at-the-met (accessed 11.18.18).

Tools: OpenDICE and AutoSFR [WWW Document], 2018. FADGI. URL http://www.digitizationguidelines.gov/guidelines/digitize-OpenDice.html (accessed 11.14.18).

Toschi, I., Capra, A., De Luca, L., Beraldin, J.A., Cournoyer, L., 2014. On the evaluation of photogrammetric methods for dense 3D surface reconstruction in a metrological context, in: 2014 ISPRS Technical Commission V Symposium. ISPRS Annals of the Photogrammetry, Remote Sensing and Spatial Information Sciences, Riva del Garda, pp. 371–378. https://doi.org/10.5194/isprsannals-II-5-371-2014

Toschi, I., Nocerino, E., Hess, M., Menna, F., Sargeant, B., MacDonald, L., Remondino, F., Robson, S., 2015. Improving automated 3D reconstruction methods via vision metrology, in: Videometrics, Range Imaging, and Applications XIII. SPIE. https://doi.org/10.1117/12.2184974

Tragni, C.B., Chen, J., Kushel, D., 2005. The Use of Ultraviolet-Induced Visible Fluorescence for Examination of Photographs, Capstone Research Project, Advanced Residency Program in Photograph Conservation, George Eastman House/Image Permanence Institute. Rochester, NY.

Troisi, S., Del Pizzo, S., Gaglione, S., Miccio, A., Testa, R.L., 2015. 3D models comparison of complex shell in underwater and dry environments, in: 2015 Underwater 3D Recording and Modeling. The International Archives of the Photogrammetry, Remote Sensing and Spatial Information Sciences, Piano di Sorrento, pp. 215–222. https://doi.org/10.5194/isprsarchives-XL-5-W5-215-2015

van Dormolen, H., 2012. Metamorfoze Preservation Imaging Guidelines. the Hague.

Verhoeven, G.J., 2011. Taking Computer Vision Aloft Archaeological Three-dimensional Reconstructions from Aerial Photographs with PhotoScan. Archaeological Prospection 18, pp. 67–73.

Verhoeven, G.J., 2008. Imaging the invisible using modified digital still cameras for straightforward and low-cost archaeological near-infrared photography. Journal of Archaeological Science 35, pp. 3087–3100. https://doi.org/10.1016/j.jas.2008.06.012

Verhoeven, G.J., 2018. Focusing on Out-of-Focus: Assessing Defocus Estimation Algorithms for the Benefit, in: 2018 ISPRS TC II Mid-Term Symposium "Towards Photogrammetry 2020". The International Archives of the Photogrammetry, Remote Sensing and Spatial Information Sciences, Riva del Garda, pp. 1149–1156.

Verhoeven, G.J., Missinne, S.J., 2017. Unfolding Leonardo da Vinci's Globe (AD 1504) to Reveal its Historical World Map, in: 26th International CIPA Symposium 2017. ISPRS Annals of the Photogrammetry, Remote Sensing and Spatial Information Sciences, Ottawa, pp. 303–310. https://doi.org/10.5194/isprs-annals-IV-2-W2-303-2017

Verhoeven, G.J., Smet, P.F., Poelman, D., Vermeulen, F., 2009. Spectral characterization of a digital still camera's NIR modification to enhance archaeological observation. IEEE Transactions on Geoscience and Remote Sensing 47, pp. 3456–3468. https://doi.org/10.1109/TGRS.2009.2021431

Verhoeven, G.J., 2010. It's all about the format – unleashing the power of RAW aerial photography. International Journal of Remote Sensing 31, pp. 2009–2042. https://doi.org/10.1080/01431160902929271

Verri, G., 2017. "IT'S ALL IMAGING TO ME": Documentation, Investigation, Visualization, and Communication. [WWW Document]. Conservation Perspectives: The GCI Newsletter Spring 2017. URL https://www.getty.edu/conservation/publications_resources/newsletters/pdf/v32n1.pdf (accessed 4.15.18).

Verri, G., 2009a. The application of visible-induced luminescence imaging to the examination of museum objects, in: Pezzati, L., Salimbeni, R. (Eds.), Proceedings SPIE 7391: Optics for Arts, Architecture, and Archaeology II. SPIE, pp. 1–12. https://doi.org/10.1117/12.827331

Verri, G., 2009b. The spatially resolved characterisation of Egyptian blue, Han blue and Han purple by photo-induced luminescence digital imaging. Analytical and Bioanalytical Chemistry 394, pp. 1011–1021. https://doi.org/10.1007/s00216-009-2693-0

Verri, G., 2008. The use and distribution of Egyptian blue: a study by visible-induced luminescence imaging, in: The Nebamun Wall Paintings: Conservation, Scientific Analysis and Display at the British Museum. Archetype Publications Ltd., London, pp. 41–50.

Vitorino, T., Casini, A., Cucci, C., Melo, M.J., Picollo, M., Stefani, L., 2015. Non-invasive identification of traditional red lake pigments in fourteenth to sixteenth centuries paintings through the use of hyperspectral imaging technique. Applied Physics A: Materials Science and Processing 121, pp. 891–901. https://doi.org/10.1007/s00339-015-9360-4

Wachowiak, M.J., Karas, B.V., 2009. 3D Scanning And Replication for Museum and Cultural Heritage Applications. Journal of the American Institute for Conservation 48, pp. 141–158.

Wachowiak, M.J., Karas, B.V., Baltrusch, R.E., 2009. Reconstruction of a Nineteenth Century Plaster Piece Mold and Recreation of a Casting, in: Computer Applications to Archaeology. Williamsburg, pp. 1–8.

Wackrow, R., Chandler, J.H., 2008. A convergent image configuration for DEM extraction that minimises the systematic effects caused by an inaccurate lens model. Photogrammetric Record 23, pp. 6–18. https://doi.org/10.1111/j.1477-9730.2008.00467.x

Waldhäusl, P., Ogleby, C.L., 1994. 3×3-rules for simple photogrammetric documentation of architecture, in: Fryer, J.G., Shortis, M.R. (Eds.), Proceedings of the ISPRS Commission V Symposium. Close Range Techniques and Machine Vision. Australian Photogrammetric and Remote Sensing Society, Melbourne, Melbourne, Australia, pp. 426–429.

Warda, J., Frey, F., Heller, D., Kushel, D., Vitale, T., Weaver, G., 2017. The AIC Guide to Digital Photography and Conservation Documentation, 3rd ed. American Institute for Conservation of Historic and Artistic Works, Washington, DC.

Warda, J., Frey, F., Heller, D., Vitale, T., Weaver, G., 2011. The AIC Guide to Digital Photography and Conservation Documentation, 2nd ed. American Institute for Conservation of Historic and Artistic Works, Washington, DC.

Warda, J., Frey, F., Heller, D., Vitale, T., Weaver, G., 2008. The AIC Guide to Digital Photography and Conservation Documentation, 1st ed. American Institute for Conservation of Historic and Artistic Works, Washington, DC.

Webb, E.K., 2020. UV-induced visible luminescence for conservation documentation, in: Picollo, M., Stols-Witlox, M., Fuster-López, L. (Eds.), UV-Vis Luminescence Imaging Techniques. In-press for publication Spring 2020.

Webb, E.K., 2017. Reflected Infrared and 3D Imaging for Object Documentation. Journal of the American Institute for Conservation 56, pp. 1–14. https://doi.org/10.1080/01971360.2017.1359463

Webb, E.K., 2015. Infrared and 3D Imaging for Object Documentation. Master's Dissertation, University College London, London, United Kingdom.

Webb, E.K., Robson, S., Macdonald, L., Garside, D., Evans, R., 2018. Spectral and 3D Cultural Heritage Documentation Using a Modified Camera, in: 2018 ISPRS TC II Mid-Term Symposium "Towards Photogrammetry 2020". The International Archives of the Photogrammetry, Remote Sensing and Spatial Information Sciences, Riva del Garda, pp. 1183–1190.

Wu, C., 2013. Towards Linear-Time Incremental Structure from Motion, in: 2013 International Conference on 3D Vision. pp. 127–134. https://doi.org/10.1109/TSIPN.2018.2854669

Zerene Systems LLC, n.d. Zerene Stacker [WWW Document]. URL http://zerenesystems.com/ (accessed 1.2.18).

11. Standards

EMVA Standard 1288: Standard for characterization of Image Sensors and Cameras, European Machine Vision Association.

ISO 12233:2017 Photography — Electronic still-picture cameras — Resolution measurements, International Organization for Standardization, Geneva.

ISO 14524:2009 Photography — Electronic still picture imaging —Resolution and spatial frequency responses, International Organization for Standardization, Geneva.

ISO 15529:2010 Optics and photonics — Optical transfer function — Principles of measurement of modulation transfer function (MTF) of sampled imaging systems, International Organization for Standardization, Geneva.

ISO 15739: 2017 Photography — Electronic still picture imaging —Noise measurements, International Organization for Standardization, Geneva.

ISO 16067-1:2003 Photography — Spatial resolution measurements of electronic scanners for photographic images, Geneva: International Organizaiton for Standardization.

ISO 16067-2:2004 Photography — Electronic scanners for photographic images — Spatial resolution measurements, Geneva: International Organizaiton for Standardization.

ISO 17321-1:2012 Graphic technology and photography—Colour characterisation of digital still cameras (DSCs) Part 1: Stimuli, metrology and test, Geneva: International Organization for Standardization.

ISO 19263-1:2017 Photography—Archiving systems—Part 1: best practices for digital image capture of cultural heritage material, Geneva: International Organization for Standardization.

ISO 19264-1:2017 Photography—Archiving systems—Part 1: Reflective originals, Geneva: International Organization for Standardization.

12. Software

	Software	Purpose	URL
ACR	Adobe Camera RAW Adobe Inc San Jose, CA, USA	Image processing tool used for RAW conversion. ACR was used for standard RAW processing.	https://www.adobe.com/
PhotoScan	Agisoft PhotoScan Pro v. 1.3.3 Agisoft LLC St. Petersburg, Russia	SfM-MVS software for processing 3D reconstructions	Newest version is now called "Metashape" instead of PhotoScan https://www.agisoft.com/
DCRAW	Decoding RAW Digital Images Dave Coffin	RAW image decoder used to convert RAW images to TIFF as part of the proposed RAW processing workflow MC-RAW.	https://www.cybercom.net/~dcoffin/dcraw/
Geomagic Wrap	Geomagic Wrap 2017 3D Systems Rockhill, SC, USA	Averaging meshes for the averaged reference mesh introduced in Section 4.1.3.	https://www.3dsystems.com/software/geomagic-wrap
GoldenThread	GoldenThread, v. 6.5.1 Image Science Associates Rochester, NY, USA	Image quality software used to assess images of DICE target.	http://www.imagescienceassociates.com/mm5/merchant.mvc?Screen=PROD&Store_Code=ISA001&Product_Code=GTK&Category_Code=GT
GOM Inspect	GOM Inspect 2018 GOM GmbH Braunschweig, Germany	Evaluation software for 3D measurement that is PTB and NIST certified.	https://www.gom.com/3d-software/gom-inspect.html
Matlab	Matlab R 2016B Mathworks Natick, MA, USA	Computing environment and programming language that was used for image processing and assessing and visualising data.	https://uk.mathworks.com/products/matlab.html
Photoshop	Adobe Photoshop CC	Image processing tool used for image content masking in Chapter 8.	https://www.adobe.com/
sfrmat3	*sfrmat3* LosBurns Imaging Software Peter D. Burns	SFR analysis for digital cameras that calculates SFR from the slanted edge features	http://losburns.com/imaging/software/SFRedge/index.htm

13. Publications and presentations

13.1. Publications

The following papers are relevant to the topic of the thesis and were written and presented during the time period of the research project.

Forthcoming: Webb, E.K., 2020. UV-induced visible luminescence for conservation documentation, in: Picollo, M., Stols-Witlox, M., Fuster-López, L. (Eds.), UV-Vis Luminescence Imaging Techniques. In-press for publication Spring 2020.

Cucci, C., Webb, E.K., Casini, A., Ginanni, M., Prandi, E., Stefani, L., Vitorino, T., Picollo, M., 2019. Short-wave infrared reflectance hyperspectral imaging for painting investigations: A methodological study. Journal of the American Institute for Conservation 58, pp. 16–36. https://doi.org/10.1080/01971360.2018.1543102

Webb, E.K., Robson, S., MacDonald, L., Garside, D., Evans, R., 2018. Spectral and 3D Cultural Heritage Documentation Using a Modified Camera, in: 2018 ISPRS TC II Mid-Term Symposium "Towards Photogrammetry 2020". The International Archives of the Photogrammetry, Remote Sensing and Spatial Information Sciences, Riva del Garda, pp. 1183–1190.

George, S., Hardeberg, J., Linhares, J., MacDonald, L., Montagner, C., Nascimento, S., Picollo, M., Pillay, R., Vitorino, T., Webb, E.K., 2017. A study of spectral imaging acquisition and processing for cultural heritage, in: Bentkowska-Kafel, A., MacDonald, L. (Eds.), Digital Techniques for Documenting and Preserving Cultural Heritage. The Applied Research Centre in the Humanities and Press Ltd, Kalamazzo, Michigan.

Webb, E.K., 2017. Reflected Infrared and 3D Imaging for Object Documentation. Journal of the American Institute for Conservation 56, 1–14. https://doi.org/10.1080/01971360.2017.1359463

Webb, E.K., 2015. Reflected Infrared Imaging: Revisiting the Fundamentals, in: Guidi, G., Scopigno, R., Torres, J.C., Graf, H., Remondino, F., Duranti, L., Brunet, P., Hazan, S., Barcelo, J. (Eds.), Digital Heritage 2015. IEEE, Granada, Spain, pp. 51–54.

13.2. Conference and educational contributions

*Invited presentations

Imaging Panel Discussion. Panel moderator, American Institute for Conservation (AIC) 47th Annual Meeting, Uncasville, CT, USA. May 16, 2019.

Imaging Session: Imaging Tools, Techniques & Tactics. General session program committee and imaging session chair, American Institute for Conservation (AIC) 47th Annual Meeting, Uncasville, CT, USA. May 16, 2019.

*Webb, E.K. Integrating Spectral and 3D Imaging for Monitoring Cultural Heritage Objects. Invited presentation, 2+3D Photography – Practice and Prophecies Conference, Rijksmuseum, Amsterdam. May 8, 2019.

Geffert, S. Imaging standards: have we learned from our mistakes and what will the future bring, Invited panellists on panel discussion, 2+3D Photography – Practice and Prophecies Conference, Rijksmuseum, Amsterdam. May 8, 2019.

Webb, E.K., Scientific and Computational Imaging at the Smithsonian's Museum Conservation Institute. Invited presentation, Michelle Smith Collaboratory for Visual Culture, University of Maryland, Greenbelt, Maryland, USA. April 3, 2019.

*Webb, E.K. Digital Imaging for Conservation of the National Portrait Gallery's *Lansdowne Portrait of George Washington*. Invited presentation, Goddard Engineering Colloquium, NASA Goddard Space Flight Center, Greenbelt, Maryland, USA. December 3, 2018.

*Webb, E. K. Practical Applications for Integrating Spectral and 3D Revisited. Oral presentation, "Illumination of Material Culture Symposium II" session of Digital Heritage 2018 Congress, San Francisco, California, USA. October 26, 2018.

Webb, E.K. Supporting Conservation at the Smithsonian Institution with Digital Imaging Techniques. Oral presentation, "Digital Heritage Science and Infrastructures for Transatlantic Cooperation" session of Digital Heritage 2018 Congress, San Francisco, California, USA. October 28, 2018.

Webb, E.K. Spectral and 3D Cultural Heritage Documentation Using a Modified Camera. Poster, Gordon Research Seminar and Conference, Castelldefels, Spain. July 21-27, 2018.

Imaging Session: Imaging Technology. General session program committee and imaging session chair, American Institute for Conservation (AIC) 46th Annual Meeting, Houston, TX, USA. June 1, 2019.

Webb, E.K., Robson, S., MacDonald, L., Garside, D., and Evans, R. Spectral and 3D Cultural Heritage Documentation Using a Modified Camera. Oral presentation, ISPRS Technical Commission II Symposium, Riva del Garda, Italy. June 6, 2018.

Webb, E.K. Integrated Spectral and 3D Imaging to Monitor Cultural Heritage Objects. Oral presentation, SEAHA Seminar, University College London, London, UK. March 5, 2018.

*Webb, E.K. Integrated Spectral and 3D Imaging to Monitor Cultural Heritage Objects. Invited presentation for University of Bamberg Masters students from the "Digital Technologies in Heritage Conservation and 3D imaging metrology for cultural heritage", University College London, London, UK. February 19, 2018.

Webb, E.K., MacDonald, L., Garside, D., and Robson, S. Using a Modified Camera for Integrated Spectral and 3D Imaging to Monitor Cultural Heritage Objects. Oral presentation, 3D Imaging in Cultural Heritage Conference, British Museum, London, UK. November 9-10, 2017.

*Webb, E.K., Digital Documentation at the Smithsonian Institution. Guest Lecture for SEAHA Master's in Research Module 1, University College London, London, UK. October 24, 2017.

Webb, E.K., MacDonald, L., Garside, D., and Robson, S. Preliminary Results for the Characterisation of a Modified Digital Camera: Spectral Imaging for Cultural Heritage. Poster presentation, SEAHA Conference on Heritage Science, University of Brighton, Brighton, UK. June 19-20, 2017.

*Webb, E.K. Practical Applications for Integrating Spectral and 3D Imaging. Invited presentation, Illumination of Material Culture Symposium, the Metropolitan Museum of Art, New York, New York, USA. March 7, 2017.

*Webb, E.K. Summarizing coordinated and collaborative research on hyperspectral imaging devices and methods for cultural heritage documentation. COSCH Short Term Scientific Mission Presentation, COSCH Final Conference, i3Mainz, Mainz, Germany. October 11, 2016.

Webb, E.K. Reproducibility and comparability of spectral imaging: A European project and postgraduate research. Oral presentation, SEAHA Special Seminar on Multispectral and Hyperspectral Imaging, University of Oxford, Oxford, UK. June 30, 2016.

Webb, E.K. Reproducibility and comparability of imaging for monitoring cultural heritage objects. Oral presentation, SEAHA Conference on Heritage Science, University of Oxford, Oxford, UK. June 20, 2016.

Webb, E. K., Picollo, M., Casini, A., Cucci, C., Stefani, L., and Vitorino, T. Coordinated and collaborative research of imaging spectroscopy devices and methods for cultural heritage documentation. Poster presentation, SEAHA Conference on Heritage Science, University of Oxford, Oxford, UK. June 20, 2016.

Webb, E.K. The Future of Imaging the Past: New Research in Digital Imaging. Oral presentation, Topics in Museum Conservation Lecture, Smithsonian's Museum Conservation Institute, Suitland, Maryland, USA. May 26, 2016.

*Webb, E.K. Scientific and computational imaging at the Smithsonian's Museum Conservation Institute. Invited presentation, US Naval Observatory, Washington, DC, May 11, 2016.

Webb, E.K. Integrating Spectral and 3D Imaging for Monitoring Cultural Heritage Objects. Oral presentation, Cultural Informatics Research Group (CIRG) Seminar, University of Brighton, Brighton, UK. March 24, 2016.

Webb, E.K. Round Robin Test Data Processing and Finalization. COSCH Short Term Scientific Mission Presentation, COSCH Task Force Meeting, Florence, Italy. March 10, 2016.

*Webb, E.K. Elaboration of Hyperspectral Image Data from Round Robin Test Acquisition. COSCH Short Term Scientific Mission Presentation, COSCH Joint Working Group Meeting, Neuchatel, Switzerland. October 2015.

Webb. E.K. Reflected Infrared Imaging: Revisiting the Fundamentals, Oral presentation, Digital Heritage 2015 International Congress, Granada, Spain. September 2015.

Webb, E.K. Topics in Museum Conservation: Infrared and 3D Imaging for Object Documentation. Oral presentation, Smithsonian's Museum Conservation Institute, Suitland, Maryland, USA. July 2015.

Webb, E.K. 3D and infrared imaging for object documentation. Poster presentation, SEAHA Conference on Heritage Science, London, UK. July 2015.

14. Appendices

14.1. Circle of confusion table

Table 14-1 includes references and selected values for the circle of confusion both in mm and pixels. When the reference provided one (mm or pix), the other was calculated using the pixel size of 6.4 µm for the Canon 5D Mark II for the conversions. These values range from 1 pixel up to nearly 8 pixels. Even though 1 pixel was included in a couple of these references, this is beyond what the camera would be able to resolve, so the value needs to be at least 2 pixels or more.

Table 14-1. References and values for circle of confusion

References and values for circle of confusion (*C*)	*C* values (mm and pixels) * pixel count or length (right column) based on Canon 5D Mark II pixel size (6.4 um) when opposite value was provided by reference	
	mm	pixels
"In the 50s, the depth of field for 35 mm lenses was often calculated with a circle of confusion of 0.05 mm, meaning 1/865 of the picture diagonal" (Nasse, 2010, p. 20).	0.05 mm	7.8 px
".. in the early days of small-format photography, and conveniently for the time as a 50 mm lens was used as standard for the 24 x 36 mm format, a criterion of *f/*1000 was adopted for *C,* giving 0.05 mm for the 50 mm lens and correspondingly different values for different focal lengths…The idea of *C = f/*1000 is now deprecated, and instead the value of *C* is taken as constant for a range of lenses for a given format" (Ray, 2002, p. 216).	0.05 mm	7.8 px
"In practice, values from 0.025 to 0.033 mm are used for the 24 x 36 mm format to allow x8 enlargement." (Ray, 2002, pp. 216–217)	0.025 - 0.033 mm	3.9-5.2px
"Whenever we observe images in this way, then 1/3000 of the picture diagonal is the strictest sensible requirement for the circle of confusion diameter. A circle of confusion twice as large, 1/1500 of the diagonal, viewed at a visual angle of 2 arc minutes, still provides a satisfying sharpness even then; this requirement corresponds approximately to the often used 0.03 mm circle of confusion for the 35 mm format" (Nasse, 2010, p. 19).	0.030 mm	4.7 px
"the value of the circle of confusion was calculated as the ratio *GSD/S* that is equal to 8.3 µm on the sensor" (Menna et al., 2012, p. 117). (*S* is the scale number.)	0.0083 mm	1.3 px
"For the diameter of the circle of confusion, we will consider the value of the width of a pixel" (Billiot et al., 2013).	0.0064 mm	1 px

"The CoC can be evaluated with good approximation by the "Zeiss formula", by which is estimated as d/1500, where d is the diagonal measure of the sensor" (Gallo et al., 2014).	0.0288 mm	4.5 px
Luhmann et al. (2014, p. 116): $$u' \approx \frac{1}{2000}d'$$ where u' is the diameter of the circle of confusion and d' is the image diagonal	0.0216 mm	3.4 px
"An object point is observed by the human eye as sharply imaged if the diameter of the circle of confusion *u'* is under a resolution limit. For film cameras *u'* is normally taken as around 20-30 um and for digital cameras as around 1-3 pixels" (Luhmann et al., 2014, p. 116).	0.0064 - 0.0192 mm	1 – 3 px
"The computed DOF using a circle of confusion of 3 pixels (corresponding to a GSD of about 0.3 mm)…" (Menna et al., 2016, p. 679)		3 px

14.2. Description of Mango Vase test object

The Mango Vase test object (19 x 13 cm) was developed in order to experiment with the different techniques and parameters. The object had been used for preliminary research during a Masters in Research (MRes) at UCL with only Egyptian blue pigment providing capabilities of testing Visible Induced Infrared Luminescence (Figure 14-1) (Webb, 2015). The object was enhanced with line patterns and pigment patches (Figure 1-5) using materials that respond differently to different radiation (Figure 1-6) (Section 1.3.2). The test object was informed by the painted panel target from the COSCH RRT presented by George et al. (2017) and Cucci et al. (2019), and the considerations presented by Hess (2015a) in the creation of the metric test object.

Figure 14-1. First iteration of Mango Vase with Egyptian blue. Left to right: Visible light image, reflected IR image, and visible induced infrared luminescence image.

The line patterns were created using a ruler with 1 and 2 mm spacing (Figure 14-2). The pigment patches and bands were created with M. Graham & Co. Artists' Gouache and Cornelissen pigments (Table 14-2). The Cornelissen pigments required mixing with egg yolk and water. Two egg yolks were separated from whites by straining through hands and using a paper towel to dry each. A tack was used to pierce the membrane to separate the yolk from the membrane. Water was added to the yolk mixture using a straw to add a little bit at a time and mix. The pigments were not ground additionally from how they were provided in the jar; the azurite and madder lake had large particles that did not break down very far, which can be seen in the rough texture of the painted areas. Small amounts of the pigments were mixed with the yolk and water mixture in plastic paint cups using a straw to add a little bit of the yolk mixture and stirring with a paint brush. Precise measurements were not made, only estimations and mixing until the consistency seemed paint-like.
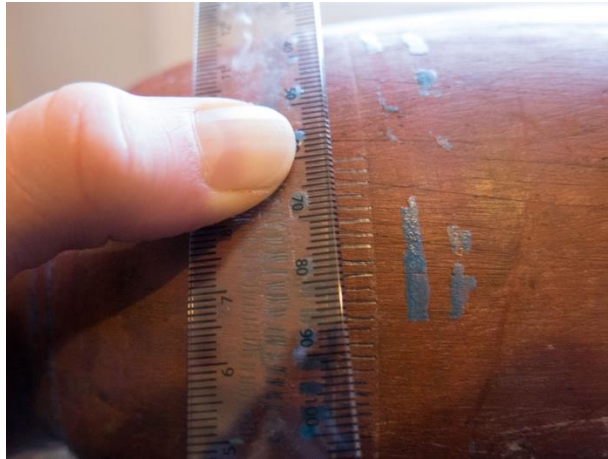
Figure 14-2. Creating line pattern on Mango Vase.

Table 14-2.Pigments and varnish used for Mango Vase

M. Graham & Co. Artists' Gouache (West Linn, OR, USA)	
Prussian Blue	Pigment: Ferriammonium Ferrocyanide (PB 27) Vehicle: Gum Arabic
Ivory Black	Pigment: Amorphous Carbon (PBk 9) Vehicle: Gum Arabic
Zinc White	Pigment: Zinc Oxide (PW 4) Vehicle: Gum Arabic
Titanium White (Permanent White)	Pigment: Titanium Dioxide (PW6) Vehicle: Gum Arabic

Cornelissen Pigments (105 Gt Russell St. London WC1)

Azurite
    Malachite
    Madder Lake Genuine

C. Roberson & Co. (1A Hercules St. London N7 6AT)
Shellac Varnish Clear   Picture Mastic Varnish Ordinary

14.3. Lens Comparison

The quality and detail needed for cultural heritage documentation requires high quality lenses often for close focusing applications (Rieger, 2016, p. 13). Apochromatic and macro lenses tend to outperform other lenses for close range applications (Rieger, 2016, p. 54). With the increasing pixel counts of digital cameras, the resolution of the digital camera can be limited by the lens performance making the selection of lens critical for the resulting image quality (Rieger, 2016, p. 54). The selection of lens and the quality of the optics influence the sharpness, contrast, and resolution with the potential of errors including aberrations like spherical aberrations and chromatic aberrations.

Macro lenses are important for close-up photography and the construction and correction of the lenses greatly minimises distortion (Warda et al., 2017, p. 37). Macro lenses are optimised for close-up work and high quality results. Macro lenses are recommended for small objects and high detail work for conservation documentation, but it is also recognized that the use of macro lenses and close-range photography presents limitations in depth of field (Warda et al., 2017). These challenges with DOF were discussed in Section 2.5 and were explored in the experimental work in Chapter 7.

Most lenses are optimised for visible light and not necessarily wavelengths beyond. Shorter wavelengths are refracted more than longer wavelengths, which causes spectral dispersion limiting the sharpness of an image resulting in axial chromatic aberrations (Allen and Triantaphillidou, 2011, p. 175). Lenses that are not corrected beyond visible light may have a focus shift from near UV to near IR (Allen and Triantaphillidou, 2011, p. 105). Axial chromatic aberrations can be corrected for through the construction of the lens by using different components and coatings. For example, apochromatic lenses can improve colour correction through a combination of three glass types (crown, short flint or lanthanum crown and dense flint glass) bringing three wavelengths into common focus (Ray, 2002, p. 117).

While macro and apochromatic lenses may be prioritised for 2D spectral imaging, there are also recommendations and considerations for lenses for image-based 3D reconstruction applications. The Agisoft PhotoScan manual recommends prime lenses and a 50 mm focal length (35 mm film equivalent) as the best choice for lens selection. Fisheye and ultra-wide angle lenses should be avoided as the distortion model used in PhotoScan poorly models these lenses. Cultural Heritage Imaging (CHI) recommends using a prime, wide angle lens with a focal length between 18-50 mm as wide angle lenses. Wide angle lenses provide better geometry by providing a better base:height ratio. If there are no restrictions for the data acquisition and the placement of the camera, Remondino et al. (2013) recommended a

medium focal length lens (50 mm on a full frame camera). These lenses have less geometric distortion and reproduce the scene close to what the human eye observes.

Macro and apochromatic lenses are prioritised for close-range focusing and 2D spectral imaging, while wide-angle (but not fisheye and ultra-wide angle) and a medium focal length are recommended for image-based 3D reconstruction. Based on these recommendations, three lenses were selected for this research: Canon 24 mm f/2.8, Canon 50 mm f/2.5 Compact Macro, and Coastal Optics 60 mm f/4 (Table 4-1 and Table 14-3). The 24 mm lens was selected in consideration for the image-based 3D reconstruction and recommendations for a wide angle for improved geometry. The 50 mm was selected as a macro lens for high quality, close-range conservation documentation for both 2D and 3D imaging. The 60 mm, an apochromatic lens, was selected as a high performing specialty lens for spectral imaging.

The Coastal Optics 60 mm UV-VIS-IR APO lens is advertised as a "high performance lens for forensics, science and fine art" without focus shift from UV into the IR, minimised flare and ghosting in the UV and IR regions and transmission from 290-1500nm (Jenoptik, n.d.). This performance from near UV to near IR is attributed to twelve layers of lens coatings to provide broad spectral transmission and five of its ten elements being made of calcium fluoride to help achieve an extreme level of chromatic correction. The combination of broad spectral transmission and no focal shift make this a useful lens for spectral imaging of heritage objects. The quality and performance of this lens comes at a high price. Despite being quite expensive, it has been the lens that is recommended with modified cameras for conservation documentation setups for spectral imaging.

Lens Performance

The performance of the three lenses were tested using the DICE target and GoldenThread software. The comparisons included here are qualitative and relative within acquisition sets and should not be compared reliably with other acquisition sets. The setup and acquisition parameters for the different sets are not consistent and therefore the results will not be comparable.

Table 14-3. Comparison of lenses

	Canon 24 mm f/2.8	Canon 50 mm f/2.5	Coastal Optics 60 mm (Jenoptik, n.d.)
Cost	$271.17[13]	$223.53[14]	$4495[15]
Aperture Range	f/2.8-f/22	f/2.5 – f/32	f/4- f/45
Closest focusing distance (m)	0.20	0.23	0.264
Maximum Magnification	0.23	0.5	1.5
Mounting Flange	Canon	Canon	Nikon F Mount

SFR analysis is used to compare the 50 mm and the 60 mm lenses with the Canon (unmodified) and mCanon (modified) cameras (Figure 14-3 and Figure 14-4). The modified camera images have been acquired with the Peca 916 filter (Figure 5-7) to restrict the wavelengths to visible for a comparable comparison between the unmodified and modified camera images. The images have been processed using a standard RAW processing workflow with ACR. The 60 mm lens has an improved performance compared to the 50 mm lens (Figure 14-3 and Figure 14-4). There is an increase in the sampling efficiency between the two lenses for both the unmodified and modified cameras, and the SFR curves are more consistent for the 60 mm lens results indicating that this lens is performing better across the field of view. The centre of the field of view for the 50 mm lens is showing the highest performance compared to the four corners of the field of view indicated by SFR measure of the central feature represented by the thicker black line.

---

[13] Average price on Fred and Miranda (http://www.fredmiranda.com/). Price accessed from http://www.fredmiranda.com/reviews/showproduct.php?product=21 on 21 February 2018.

[14] Average price on Fred and Miranda (http://www.fredmiranda.com/). Price accessed from http://www.fredmiranda.com/reviews/showproduct.php?product=45 on 21 February 2018.

[15] Price from DigiLlyod review (http://diglloyd.com/articles/CoastalOptics60f4/index.html) accessed 17 September 2016.
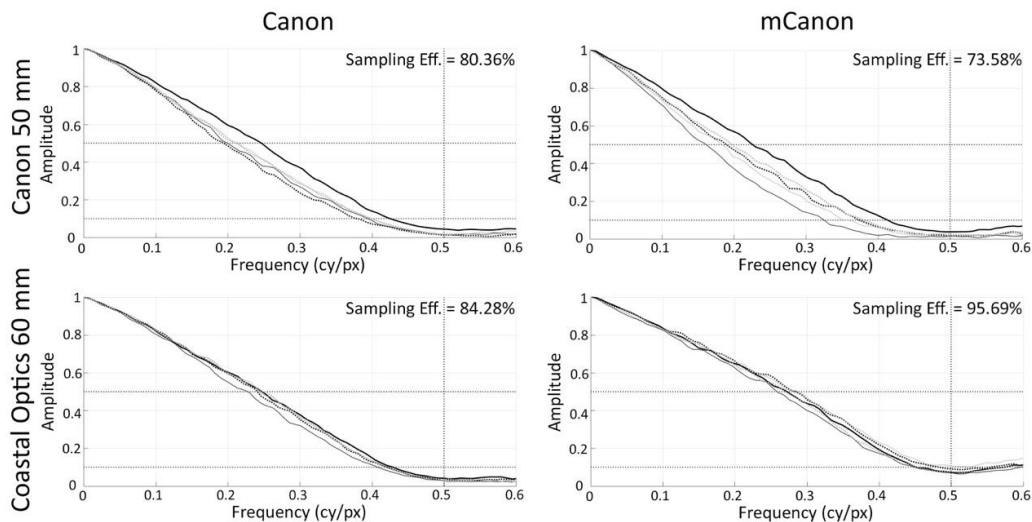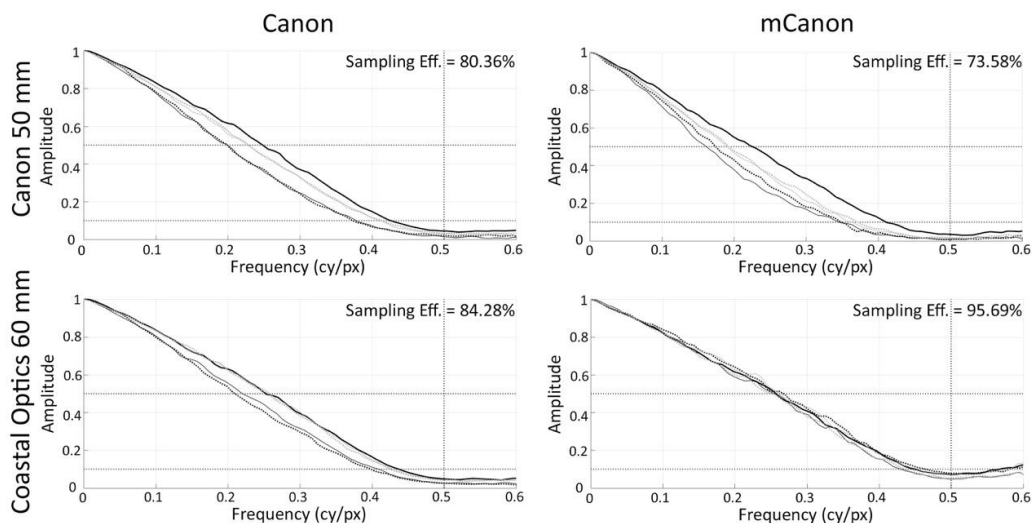
Figure 14-3. Horizontal SFR results comparing the performance of the 50 mm and 60 mm lenses with the unmodified camera ('Canon') and the modified camera ('mCanon'). Each plot includes five SFR measures from the five features on the DICE target in the centre and four corners. The thick black line is for the centre feature, the grey lines are the bottom features, the dotted lines are the right features, the black lines (with the exception of the thick black line) are the top features, and the solid lines (with the exception of the thick black line) are the left features. The sampling efficiency is included at the top right of each SFR plot.

Figure 14-4. Vertical SFR results comparing the performance of the 50 mm and the 60 mm lenses with the unmodified camera ('Canon') and the modified camera ('mCanon'). Each plot includes five SFR measures from the five features on the DICE target in the centre and four corners. The thick black line is for the centre feature, the grey lines are the bottom features, the dotted lines are the right features, the black lines (with the exception of the thick black line) are the top features, and the solid lines (with the exception of the thick black line) are the left features. The sampling efficiency is included at the top right of each SFR plot.

The sampling efficiencies (%) for the mCanon with three lenses (24 mm, 50 mm and 60 mm) and six apertures (f/4, f/5.6, f/8, f/11, f/16, f/22) are compared in Figure 14-5. The 60 mm lens has the highest performance from f/4-f/16 with diffraction decreasing the performance significantly at f/22. The 50 mm lens has the next best performance and then the 24 mm lens. The optimal apertures for the 60 mm are f/8 or f/11; f/5.6 and f/8 for the 50 mm lens; and f/8 for the 24 mm lens. Based on this comparison the performance of the 24 mm lens is about 10% lower than that of the 60 mm lens. To emphasis the point made
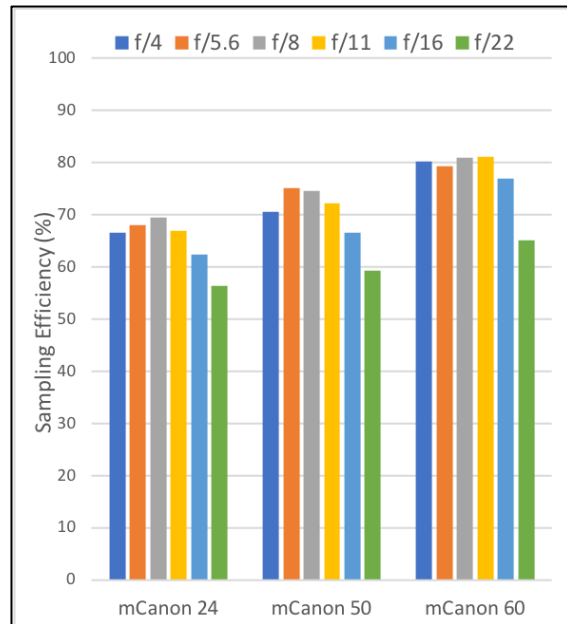
Figure 14-5. Sampling efficiency comparison of lenses paired with the modified camera ('mCanon'). The chart includes sampling efficiency calculations for three lenses (24 mm, 50 mm, and 60 mm) six apertures for each lens (f/5.6, f/8, f/11, f/16, f/22.

earlier, these comparisons are relative and qualitative. The value of the sampling efficiency for any given lens or aperture is less important here than the relative performance compared to the other lenses or apertures compared in the acquisition set. For this particular comparison, the takeaway is that the 60 mm performs the best with an optimal aperture around f/8-f/11.

The performance across the field of view for the different lenses is further investigated with Figure 14-6. Figure 14-3 and Figure 14-4 provided some information about the performance across the field of view for the 60 mm and the 50 mm lenses. Figure 14-6 includes the DPI values for the 10% SFR and 50% SFR for the three lenses. The top row are the 10% SFR results and the bottom row are the 50% SFR results presented for each aperture and colour coded for the five features in the centre and four corners of the DICE target (UL = upper left; UR = upper right; C = centre; LL = lower left; LR = lower right). The 60 mm lens (right column) is showing the most consistency across the field of view especially for apertures f/8-f/22. The largest discrepancies across the field of view are for the 24 mm lens indicated by the different bar heights for each of the aperture groupings.

The previous comparison has been based on a standard RAW processing workflow using ACR processing, so the results do not reflect the impact of the RAW processing or even the results without demosaicing. The impact of the RAW processing is discussed in Section 5.2.2.
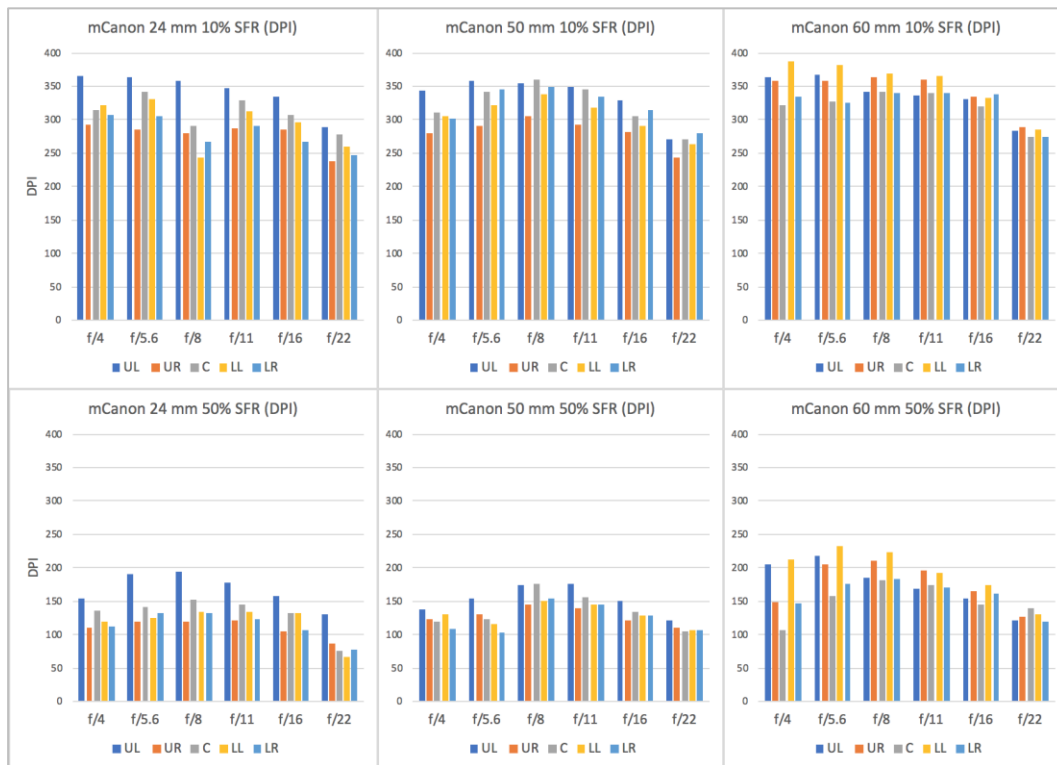
Figure 14-6. SFR analysis focusing on 10% SFR (top row) and 50% SFR (bottom row) for three lenses paired with the modified camera ('mCanon'). The three lenses are the 24 mm (left column), the 50 mm (middle column) and the 60 mm lens (right column). The 10% and 50% SFR are presented as DPI values for each aperture and colour coded for the five features in the centre and four corners of the DICE target (UL = upper left; UR = upper right; C = centre; LL = lower left; LR = lower right). The Coastal Optics 60 mm lens (left column).

In conclusion, the 60 mm lens performs the best based on SFR analysis and sampling efficiency. The 50 mm performs well and the 24 mm has the lowest performance of the three lenses. Additional strengths of the Coastal Optics 60 mm lens relate to its performance in the UV and IR. However, this assessment did not include wavelengths beyond visible or any assessment of resulting 3D reconstruction quality. The performance of the 60 mm lens was assessed beyond visible in Section 6.1.

14.4. Setup information for spectral response measurements

This section includes additional setup information for the spectral response measurements and different iterations of the measurements presented in Section 5.3.

Iteration #1: Tungsten lamps

Figure 14-7. Setup for spectral response measurement (Iteration#1) with tungsten lamps and copy stand.

Setup
The camera was mounted on the copy stand approximately 70 cm from the white target and the lights were positioned at about a 30° angle to the white target.

Lighting
    4 tungsten halogen lamps (Photolux 240V, 150W Frosted)

White target
    ColorChecker white card (X-Rite, Grand Rapids, MI, USA)

Camera Settings
    Canon: f/11 ISO 100 ¼"
    mCanon: f/11 ISO 100 1"

Iteration#2: Off-camera flashes

Figure 14-8. Setup for spectral response measurement (Iteration#2) with two Canon Speedlite flashes. The copy stand was positioned on a pelican case in order to have the flashes positioned on each side of the setup.

Setup
The use of the flashes required more space for the setup than the more compact setup with the tungsten lamps on the copy stand. The copy stand was positioned on a Pelican case in the centre of the lab in order to place two flashes on light stands at 45° angles to the target.

Lighting
    2 Canon Speedlite 580 EX II flashes
    Power level: ¼

White target
    Fluorilon-99W (Avian Technologies LLC, Sunapee, NH)

Camera Settings
    Canon: f/8 ISO 100 1/60
    mCanon: f/8 ISO 100 1/60

Iteration#3: Off-camera flash

Figure 14-9. Setup for spectral response measurement (Iteration#3) with a single Canon Speedlite flash.

Setup

The camera was mounted to the copy stand at a distance of 55 cm. The distance was closer than the previous setup because the white targets were smaller. The single flash was mounted onto a light stand and positioned at a high angle to reduce uneven illumination that might result from a single illumination source. The flash power was set of full power.

Lighting
    1 Canon Speedlite 580 EX II flash
    Power level: 1/1

White target
    ColorChecker Passport white card
    Spectralon 99% diffuse reflectance
        standard

Camera Settings
    mCanon: f/8 ISO 100 1/60

Iteration#4: Studio Strobe

Figure 14-10. Setup for spectral response measurement (Iteration#4) with a single Bowens strobe.

Setup

The copy stand was positioned on a Pelican case in the centre of the lab to position the single flash unit. The strobe was setup and tested to provide the best option for even illumination with a single illumination source. The camera was mounted to the copy stand at a distance of 67.5 cm from the white target. The white target used for this iteration was a.

Lighting
    1 Bowens Gemini GM400Rx studio
        strobe with Lumiair Softbox
    Power level: 5

White target
    Fluorilon-99W

Camera Settings
    Canon: f/8 ISO 100 1/60
    mCanon: f/8 ISO 100 1/60

14.5. Flash repeatability

This section includes additional results for the flash repeatability tests as part of the spectral response measurements presented in Section 5.3. The following results investigated different flash output settings for the Canon Speedlite flashes.
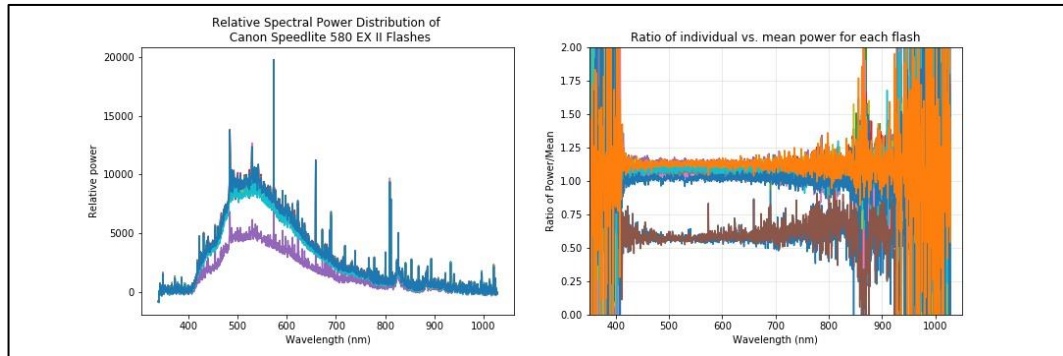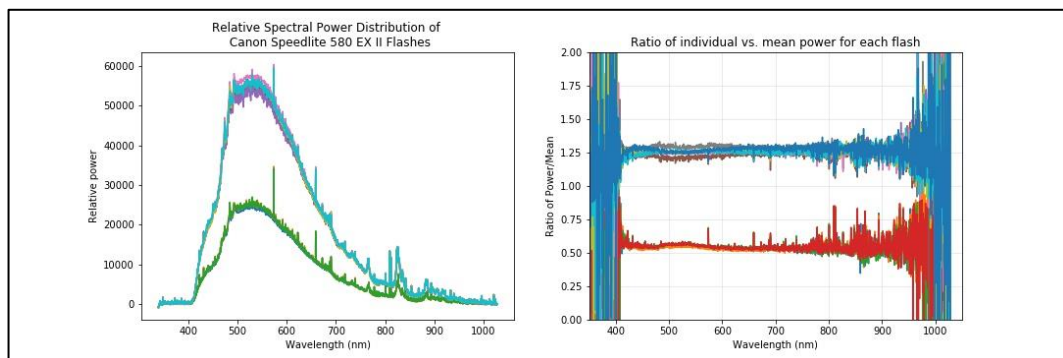

Figure 14-11. Repeatability test of Canon flash at 1/16 power. (left) Relative SPD (uncorrected) measured using the Ocean Optics USB2000+ spectrometer for twelve successive flashes with the flash set at 1/16 power. (right) Plot of the ratio of the individual vs mean power for each flash.

Figure 14-12. Repeatability test of Canon flash at full power. (left) Relative SPD (uncorrected) measured using the Ocean Optics USB2000+ spectrometer for eleven successive flashes with the flash set at full power with an umbrella. (right) Plot of the ratio of the individual vs mean power for each flash.

14.6. SFR Analysis and *sfrmat3*

While the GoldenThread software can be a straightforward method for SFR analysis and image quality assessment, in some instances, the target could not be read by the software due to the angle of the target or the defocus of the target features. The GoldenThread user manual includes specifics of capturing the target and the required target angle to ensure that the image does not have to be rotated for analysis as that would result in pixel interpolation and inaccurate values for the SFR analysis (*GoldenThread User's Manual*, n.d.). There is a 5 degree tolerance of acceptable orientations for 0/180 degrees or 90/270 degrees, otherwise the image will be rejected and cannot be used for assessment. This tolerance of acceptable orientation assumes the target is planar to the camera, which suggests that an image of an angled target would not be acceptable. The software locates four fiducials in order to select the regions of interest for the assessment and if the fiducials are not found the software cannot proceed with the measurements. Image defocus and the angling of the target would cause challenges for the software to locate the fiducials.

For the experiments where the target could not be read by GoldenThread, *sfrmat3* (Burns Digital Imaging) was used to calculate SFR from the slanted edge features.[16] Edge-based spatial frequency response (e-SFR) is outlined in ISO 12233:2017 as one of the methods for measuring sharpness using slanted edge features in a target. The software linked to this standard is from Burns Digital Imaging and includes *sfrmat3* as the Matlab code and *SFRedge_v6* for the Windows executable. *sfrmat3* is an executable file based in Matlab that computes ISO slanted edge SFR. The input for *sfrmat3* is an image file with a slanted edge feature (either horizontal or vertical) and the calculation results in an *.xls file providing an overall sampling efficiency percentage and an amplitude measure for each frequency. The region of interest (the location of the slanted edge feature) can be selected by the user using the mouse and clicking. However, the pixel dimension of the region of interest is not always consistent as different area sizes are selected each time. To be more consistent with the SFR analysis slanted edge features were extracted as 330x150 or 150x330 pixel areas (depending on horizontal or vertical orientation) before running *sfrmat3*. The extracted images were then processed independently using *sfrmat3*. The resulting *.xls format was not compatible with Microsoft Excel 2016, so the *.xls documents were converted to *.xlsx documents to be read and analysed using Matlab script.

---

[16] http://burnsdigitalimaging.com/software/sfredge-and-sftmat3/

The DOF-3D-Plane analysis (Section 7.1.1) required *sfrmat3* for the SFR measures because images beyond the first angle (0°) were not readable in GoldenThread due to the unsharpness of the image data. The horizontal and vertical values for the five features were kept separate, as opposed to averaging the values, in order to compare the results of the two sides and centre of the target as the angle changed.

The DOF-Sharp-SFR analysis (Section 7.1.2) also required *sfrmat3* due to the unsharpness of most of the images. The results for this test only used the central feature of the DICE target instead of all five features. While it could be beneficial to use all five features on the target for the SFR analysis, most of the images acquired for this test could not be analysed using the GoldenThread software and the SFR analysis required a much more manual process of extracting the slanted edge features and processing these with *sfrmat3*. There is a potential that the efficiency of this process could be improved and the manual components minimised with additional scripting assistance in Matlab. One of the challenges with an automated extraction of the features is that as the camera-object distance changes the positioning of the features also changes, so instead of indicating a consistent location for the extraction of slanted edge features there would need to be an adjustment as camera-object distance changed.

It was assumed that the SFR analysis with GoldenThread and *sfrmat3* would be comparable. The target from Image Science Associates is marketed as the "DICE Device Level Target" linking it to the Digital Image Conformance Evaluation (DICE) component of the FADGI guidelines and is "compliant with existing ISO standard's protocols"[17]. The open source alternative to the GoldenThread system is OpenDICE. Rieger (2016) cited that OpenDICE implemented the SFR analysis from ISO 12233:2000, an earlier version from IS0 12233:2017, which may use earlier versions of *sfrmat* or *SFRedge* or another SFR analysis software. According to the OpenDICE website, "The analysis methodology and results obtained have been confirmed by Image Science Associates as consistent with the results obtained with DICE and GoldenThread" ('Tools: OpenDICE and AutoSFR', 2018). Based on these statements, GoldenThread and OpenDICE should be linked back to ISO 12233 and *sfrmat3* providing comparable results.

To assess this assumption, DOF-3D-Plane experimental images of the DICE target (at 0º without any angling of the target, *a1*) were assessed using GoldenThread and *sfrmat3,* and

---

[17] http://www.imagescienceassociates.com/mm5/merchant.mvc?Screen=PROD&Store_Code=ISA001&Product_Code=OL1&Category_Code=TARGETS

the results were compared. This included three images of the target acquired with different apertures (f/5.6, f/11, and f/32). The DICE target includes five features for SFR analysis: centre, upper left, upper right, lower left, and lower right. Each feature of the DICE target has two horizontal and two vertical slanted edge features. The horizontal and vertical measures are separated for GoldenThread and *sfrmat3*. The *sfrmat3* results were averaged using a Matlab script with the top and bottom being averaged and the left and right being averaged for the horizontal and vertical results. The results for the comparison include SFR curves (plotting the modulation level versus spatial frequency, cy/px) for f/5.6 horizontal SFR analysis (Figure 14-13); f/5.6 vertical SFR analysis (Figure 14-14); f/11 horizontal SFR analysis (Figure 14-15); f/11 vertical SFR analysis (Figure 14-16); f/32 horizontal SFR analysis (Figure 14-17); and f/32 vertical SFR analysis (Figure 14-18). Figure 14-13-Figure 14-18 five graphs from the five DICE target SFR feature areas. The GoldenThread results are the blue lines, while the *sfrmat3* results are the grey lines.

The DICE target was imaged horizontal (on its side), so the features considered "upper left" in the GoldenThread analysis are in the lower left of the image frame. The figures below are based on how the target was positioned in the field of view, so the "upper left" or UL measures will be in the bottom left, the "upper right" or UR will be in the upper left, the "lower right" or LR will be in the upper right, etc. The figures are also quite small, but the main take away in each is whether the two curves are similar or show noticeable deviations.

The results for GoldenThread and *sfrmat3* are similar although not the same. The *sfrmat3* results show a slight rise in response consistently as compared to the GoldenThread results. In addition to comparing the SFR curves between the two processing options, the resulting sampling efficiencies were also compared (Table 14-4). The differences between sampling efficiencies are 0.7% for f/5.6; 0.14% for f/11; and 0.11% for f/32. Based on these results (SFR curves and sampling efficiency), it can be concluded that GoldenThread and *sfrmat3* are providing similar results for SFR analysis and the differences are not significant.

Table 14-4. Sampling efficiency results comparing GoldenThread and sfrmat3

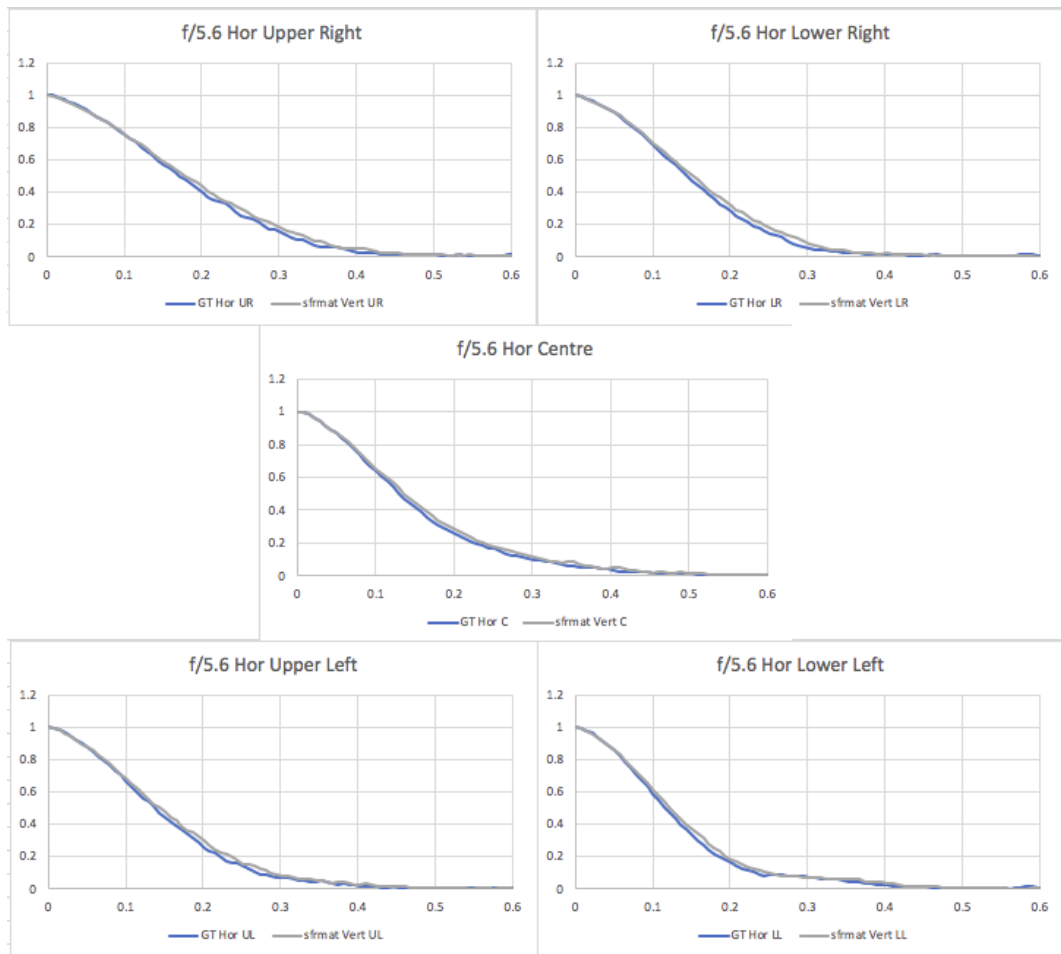|	f/5.6	f/11	f/32
GoldenThread	60.90 %	79.66 %	51.71 %
sfrmat3 vertical avg	56 %	79.6%	51 %
sfrmat3 horizontal avg	64.4 %	80%	52.2 %
sfrmat3 avg (vert & hor)	60. 2 %	79.8%	51.6 %

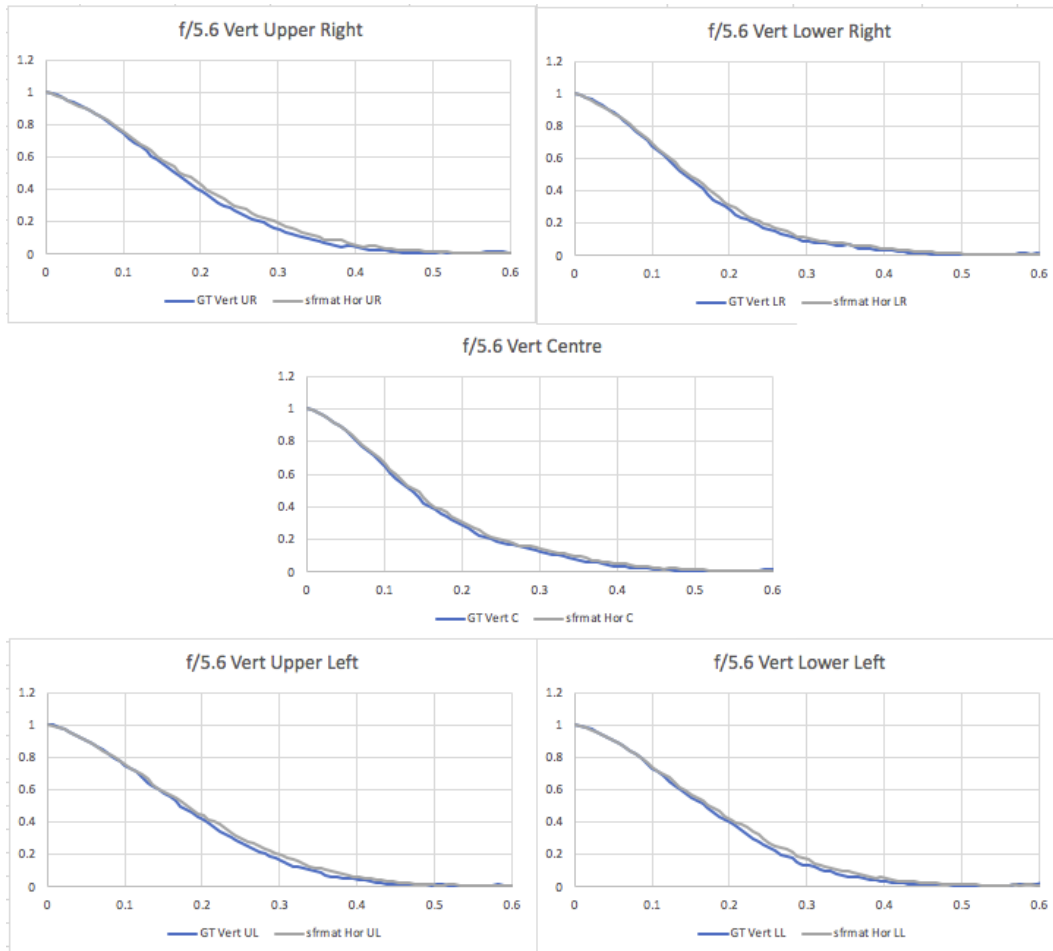*Figure 14-13. SFR analysis horizontal results for f/5.6 comparing GoldenThread and sfrmat3.*

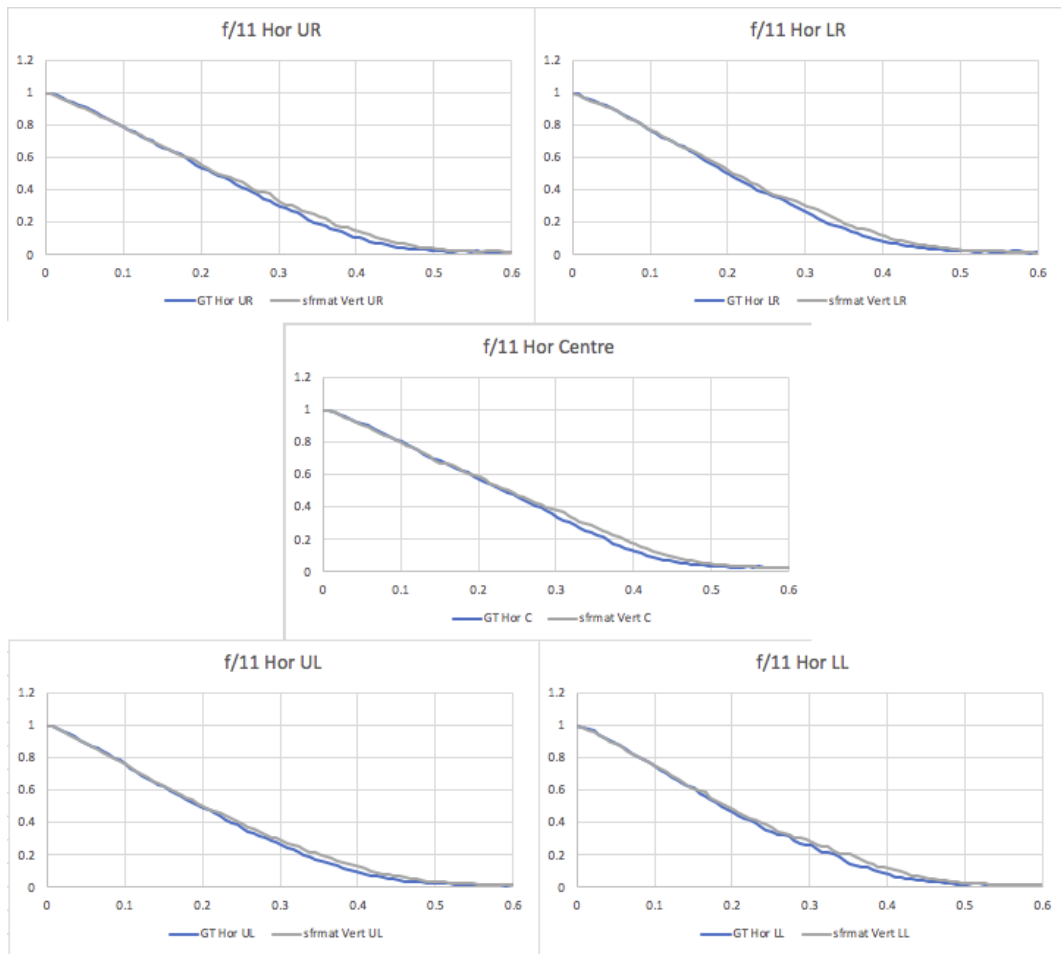*Figure 14-14. SFR analysis vertical results for f/5.6 comparing GoldenThread and sfrmat3.*

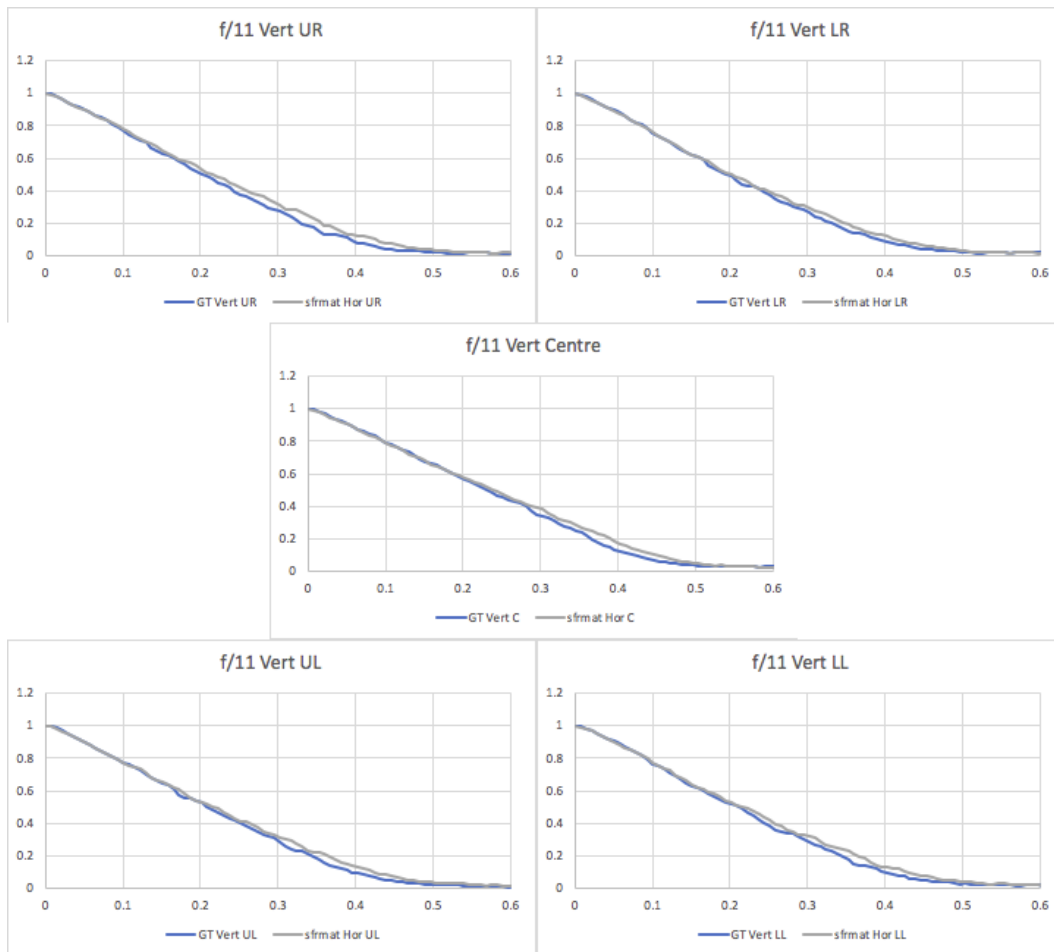*Figure 14-15. SFR analysis horizontal results for f/11 comparing GoldenThread and sfrmat3.*

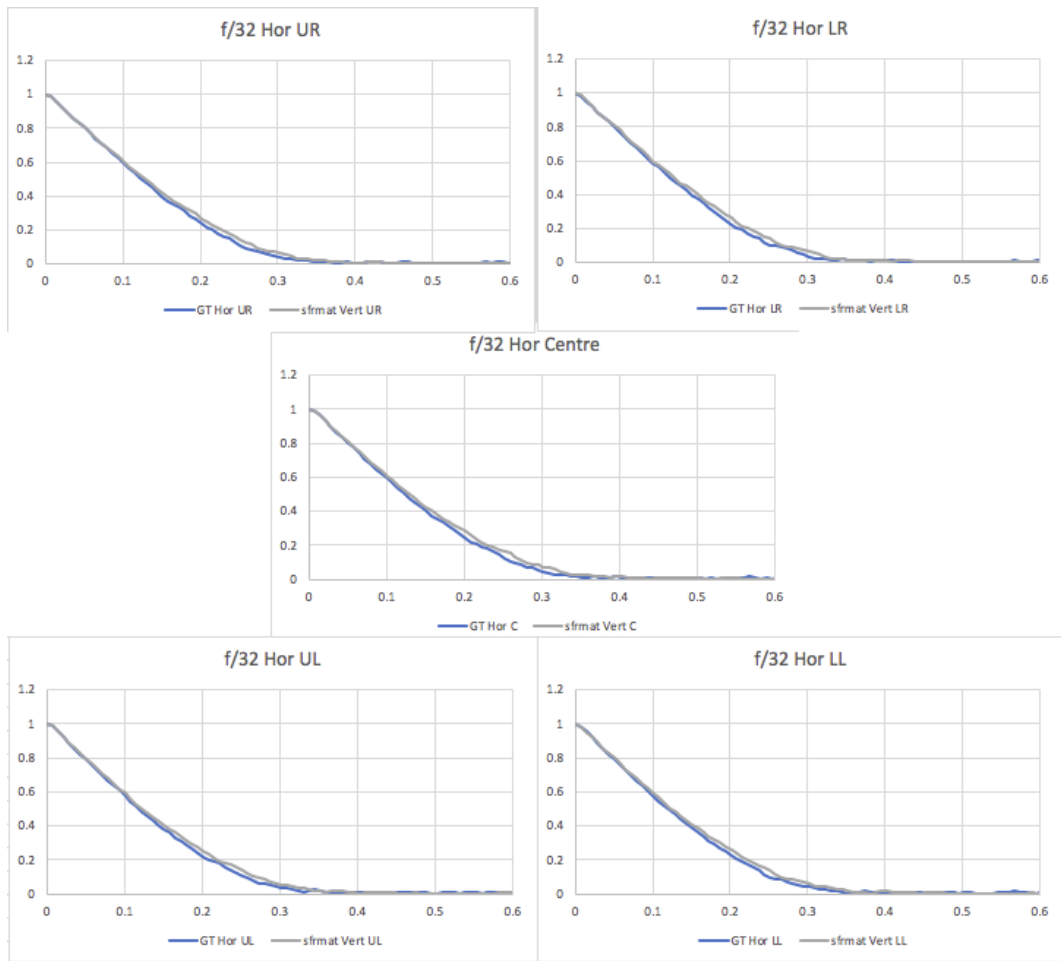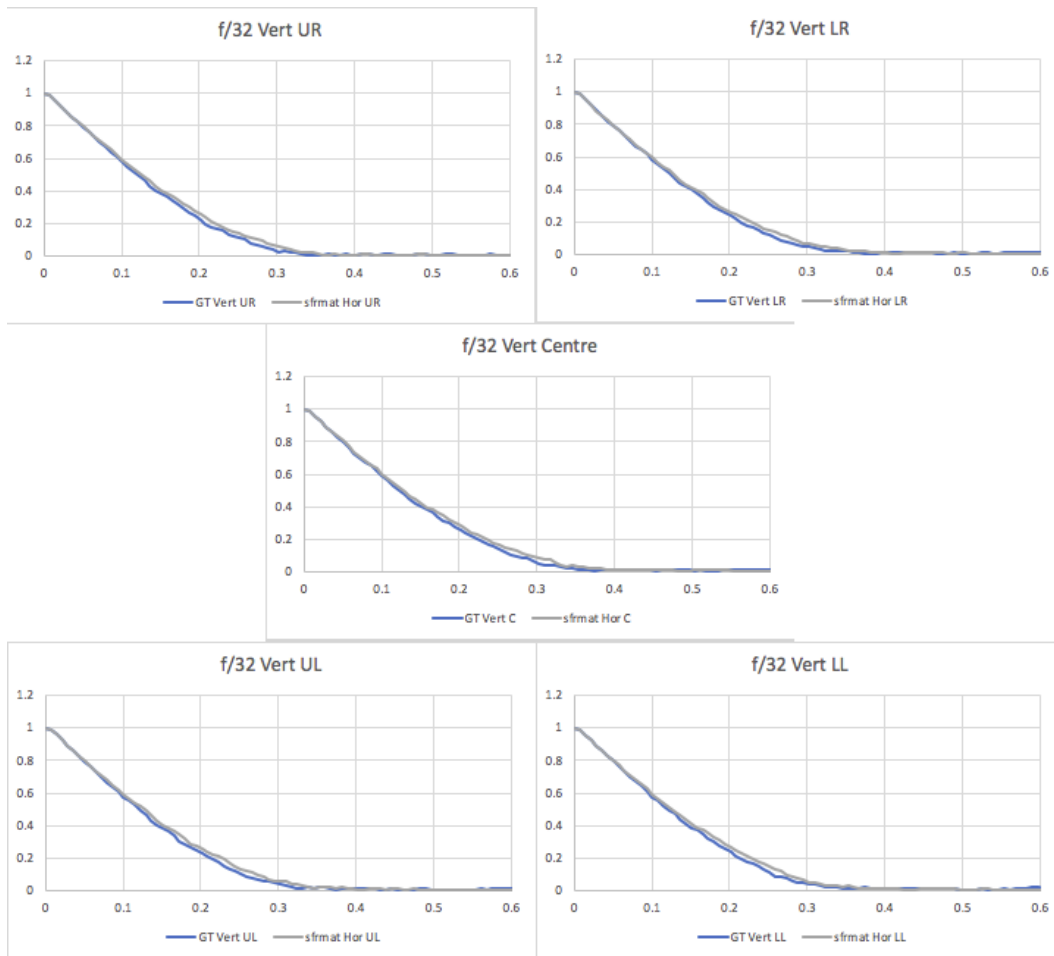*Figure 14-16. SFR analysis vertical results for f/11 comparing GoldenThread and sfrmat3.*

Figure 14-17. SFR analysis horizontal results for f/32 comparing GoldenThread and sfrmat3.

Figure 14-18. SFR analysis vertical results for f/32 comparing GoldenThread and sfrmat3.

14.7. Horizontal and vertical results presented together for SFR analysis

As specified by ISO 12233:2017, horizontal and vertical results for the SFR analysis should be presented together; however, due to space limitations only the horizontal results were included in Section 7.1.1 without the vertical results. The following figures include both the vertical and horizontal results from the SFR analysis for f/5.6, f/11, and f/32.
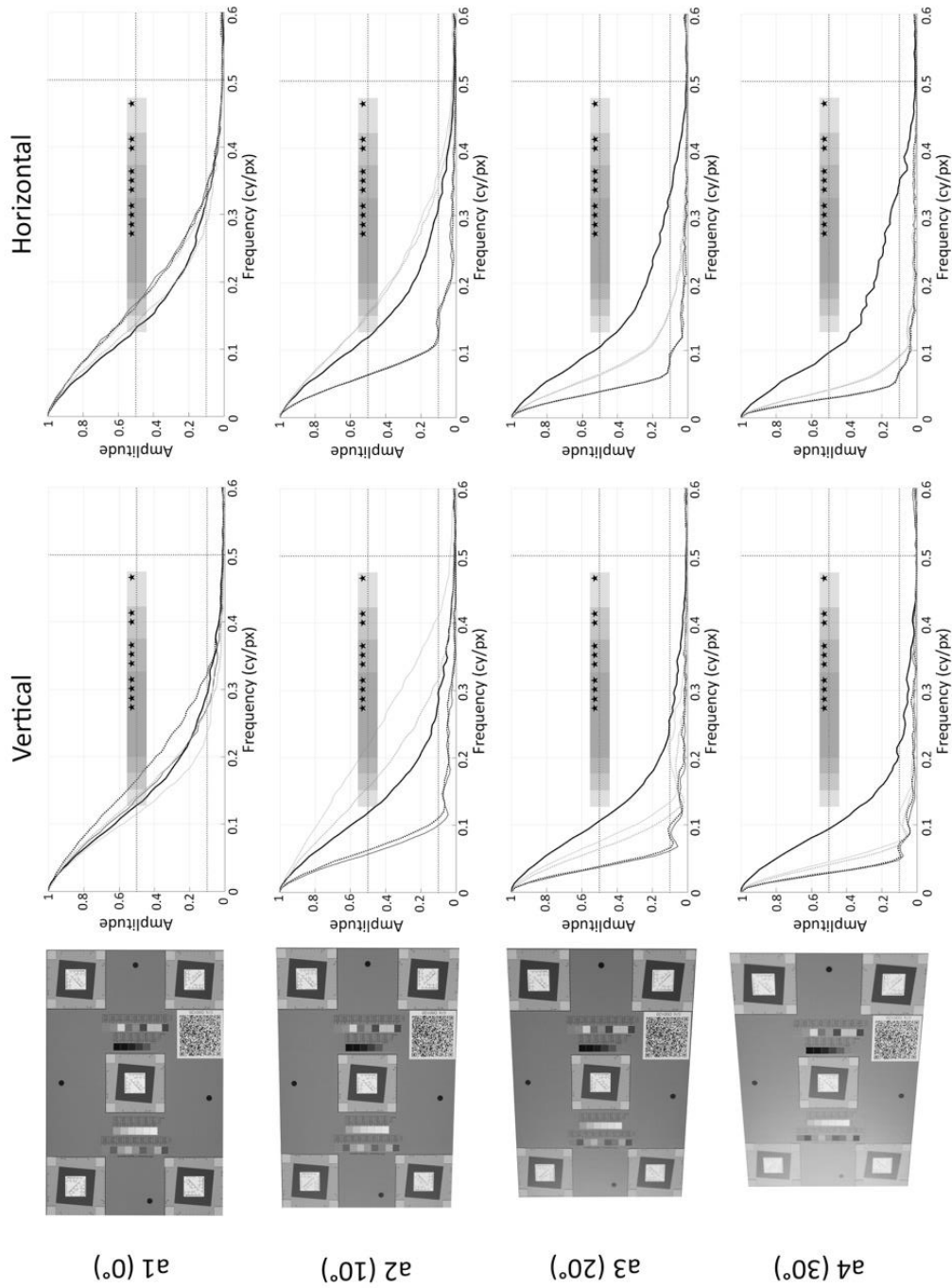

Figure 14-19. SFR analysis results presenting vertical and horizontal measures for f/5.6 from the four angles (a1, a2, a3, a4). The thick black line is for the centre feature, the grey lines are the right features, the dotted lines are the top feature, the solid lines (with the exception of the thick black line) are the bottom features.
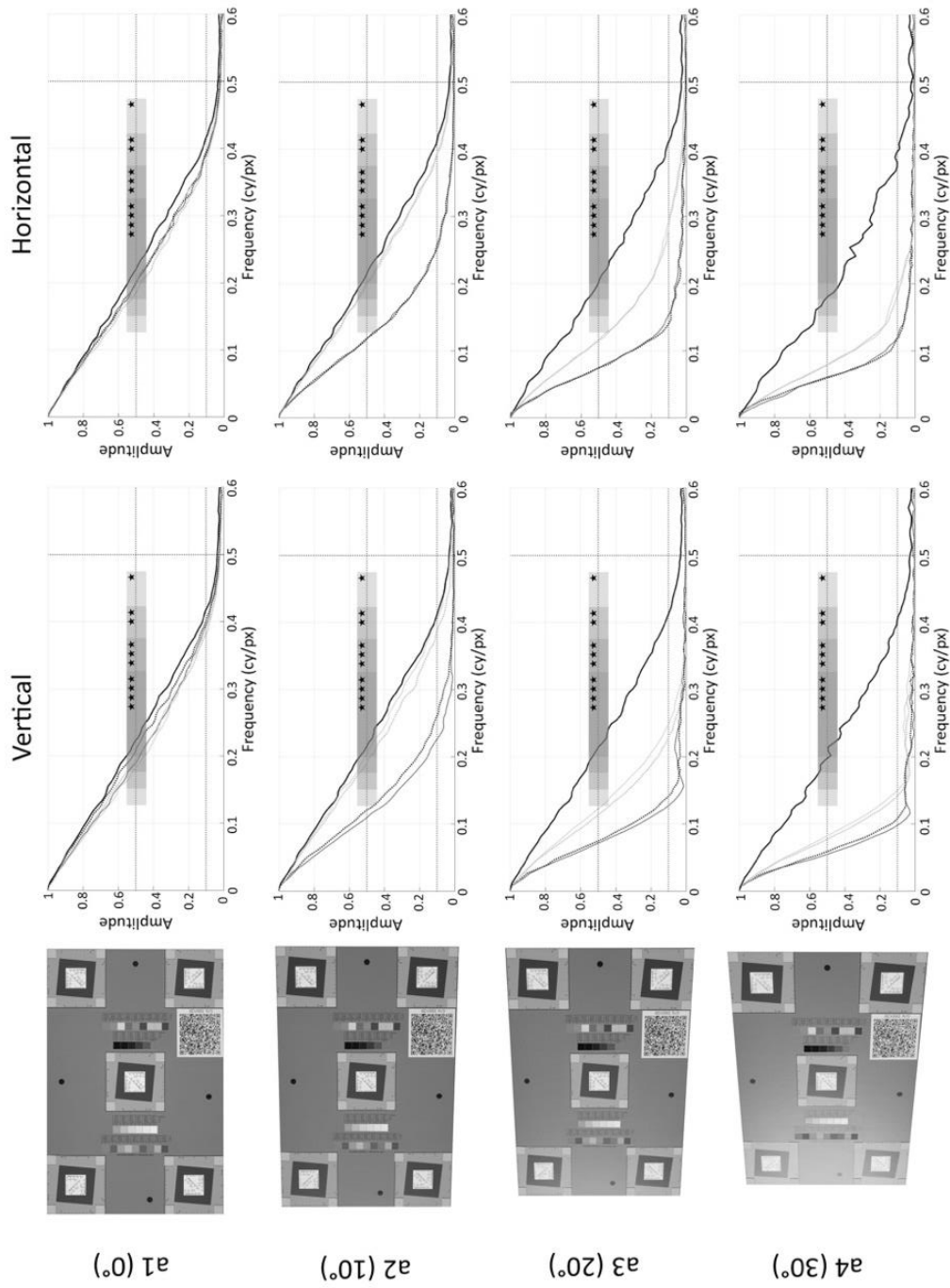
Figure 14-20. SFR analysis results presenting vertical and horizontal measures for f/11 from the four angles (a1, a2, a3, a4). The thick black line is for the centre feature, the grey lines are the right features, the dotted lines are the top feature, the solid lines (with the exception of the thick black line) are the bottom features.
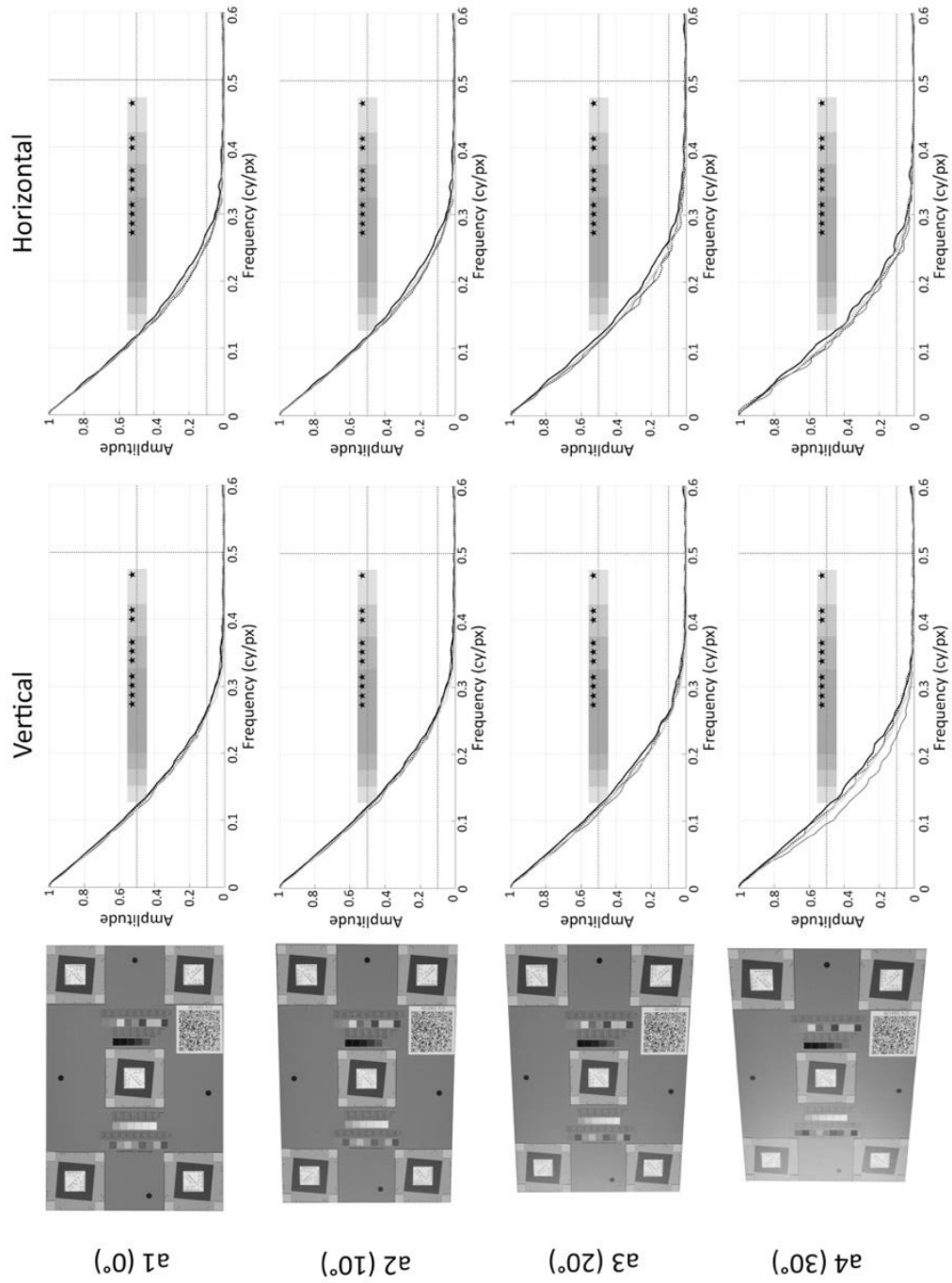
Figure 14-21. SFR analysis results presenting vertical and horizontal measures for f/32 from the four angles (a1, a2, a3, a4). The thick black line is for the centre feature, the grey lines are the right features, the dotted lines are the top feature, the solid lines (with the exception of the thick black line) are the bottom features.